ULB FACULTÉ DES SCIENCES

UNIVERSITÉ LIBRE DE BRUXELLES

Chemical and isotopic characterization of Antarctic meteorites: The chemical and isotopic effects of thermal processing and terrestrial weathering on the (re-)distributions of trace elements in chondrites

Thesis submitted by Ryoga MAEDA
in fulfilment of the requirements of the PhD Degree in Science
Academic year 2022-2023

Supervisor: Professor Dr. Vinciane DEBAILLE [a]
Co-supervisor: Professor Dr. Steven GODERIS [b]
Co-supervisor: Professor Dr. Philippe CLAEYS [b]
[a] Laboratoire G-Time, Université libre de Bruxelles
[b] Analytical-, Environmental-, and Geo-Chemistry (AMGC), Vrije Universiteit Brussel

VUB VRIJE UNIVERSITEIT BRUSSEL

Thesis jury:

Prof. Dr. Yue GAO (Vrije Universiteit Brussel, Chair)
Prof. Dr. Nadine MATTIELLI (Université libre de Bruxelles, Secretary)
Dr. Conel M. O'D. ALEXANDER (Carnegie Institution of Washington)
Prof. Dr. Martin R. LEE (University of Glasgow)

ET. HOME

Acknowledgements

One of the biggest adventures in my life ended, which took four and a half years in Belgium! Before coming to Belgium, I had significantly less experience in staying and even visiting abroad as my first visit abroad is to participate in the LPSC, U.S., when I was a master's student and the second one is to travel to Hawaii for vacation once my PhD position in Belgium was decided. Thus, coming to Belgium was the third time and even the first time for me to visit abroad and Europe, respectively. In addition, it was also the first time to live completely by myself, so you can imagine how big an adventure was to do PhD in Belgium for me…

However, once I visited AMGC, I felt a comfortable atmosphere in AMGC: everyone was so kind and welcomed me. And then I realized that I made a good decision in my life whether as a PhD or not. For making a great atmosphere in AMGC and surely many other reasons, foremost, I would like to thank Steven Goderis and Philippe Claeys. You have always left me free to do what I want without giving any pressure, making me a higher level as a scientist. I am so honored to be a part of AMGC and loved the atmosphere in terms of both working and socializing! Of course, the atmosphere was not created by only two, as such I would first thank Christophe Snoeck, the boss of archaeologists in AMGC. And also thank you my (ex-)colleagues at AMGC: Lawrence, Rachèl, Wendy, Niels, Matthias, David, Lisa, Juliette, Bastien, Alexandra, Marion, Marta, Mingyue, Delphine, Ellie, Koen, Marek, Camille, Johan, Ines, and the cool 7&8th floor gangs. It was a lot of fun to discuss, do science and parties, and have beers, together with you guys. In that sense, a special thank you to: Flore Van Maldeghem, my dear PhD buddy sharing the office, the birthday, the start of the PhD, and the research topic; (Dr.) Sietze de Graaff, my lekker roommate influenced me a lot in a good way (mostly); Pim Kaskes, the best Dutch geologist ever (expected) with a lovely family (thank you Nienke and lil' Jonas too); Thomas Dèhais, the kindest French guy left a "great" couch at my place; and Tom Boonants, our last hope of the AMGC party gangs. Thanks to you guys, I have become a true Dutch person hehe.

On the other part of my PhD research team, G-time, I would like to thank Vinciane Debaille for having discussions both scientifically and daily. I was honored to be invited and so fun to work in Antarctica with you. Naturally, I cannot forget to thank Nadine, Karen, Jérôme, Hamed, Geneviève, Maria, Julien, Valentin, Nina, Jeroen, Nora, Amanda, Ségolène, Aline, Wendy, and Sabrina. It was a great time to spend together with you, especially during the first and second years of my PhD.

As I collaboratively worked at other institutes than the VUB and ULB during my PhD duration, I am also grateful to whom worked and helped with my research there. First, thank you Ebihara-sensei, my bachelor's and master's supervisor, for suggesting and providing me with this great opportunity to do PhD in Belgium. And also thanks Thibaut, Stepan, and Frank for performing beautiful LA-ICP-TOF-MS mapping at the Atomic & Mass Spectrometry (A&MS) Research Unit, Ghent University. The (ex-)members in Antarctic meteorite research center, National Institute of Polar Research (NIPR), Japan, cannot be forgotten as I was awarded and participated in the NIPR International Internship Programs for Polar Science 2020 and 2021, so thank you Yamaguchi-sensei, Kanemaru-kun, Ojima-san, Kimura-sensei, Imae-san, and Mashino-san.

Importantly, of course, I would like to thank my family including my cutest niece and nephew for their grateful support and always understanding of whatever I want to do and for making me happy when I came back to Japan. And thanks to my friends for welcoming me when I was back. I also would like to thank the members in Kangaroos, the baseball club in Brussels, for playing together with me.

Lastly, I would like to acknowledge the financial support provided by the FWO/FNRS Excellence of Science (EoS) project ''ET-HoME" and VUB OZR extension grant of the doctoral trajectory.

Lay Summary (English)

Meteorites, any natural solid objects from interplanetary space that survived their passage through Earth's atmosphere and reached the surface, represent the only large volume of extraterrestrial material available on the Earth today. These precious extraterrestrial samples retain critical information regarding the Solar System processes, and thus they have been investigated from various research perspectives such as chemistry, mineralogy, and petrology, to refine our understanding of the history of the Solar System. Since the first systematic search for meteorites in Antarctica was successfully conducted in 1969, more than 41,000 meteorites have been collected in Antarctica, which today constitute more than 60% of the population of meteorites by number. Moreover, Antarctic meteorites include many "rare" types of meteorites such as martian and lunar meteorites, and hence the Antarctic meteorite collection plays a pivotal role for cosmochemistry. Before these meteorites were collected in Antarctica, they were buried in the ice sheets for a long time, on average on the order of hundreds of thousands of years. This burial and the cold and dry environment in Antarctica better protect them from terrestrial weathering relative to residence in hot desert environments, where meteorites generally retain for tens of thousands of years or less. Nevertheless, following their long residence time, even Antarctic meteorites can be still altered mineralogically and chemically to some extent, which means that information on their parent bodies and the processes they underwent was modified and lost. Therefore, the effects of Antarctic weathering have been assessed extensively to determine whether or not the results obtained represent the original information. However, as the mechanisms and processes involved vary widely from environment to environment, the underlying mechanisms of the alteration and weathering affecting meteorites remain relatively poorly constrained.

My PhD research aims to encompass a detailed chemical and isotopic characterization of "well-preserved" Antarctic meteorites to improve our understanding of the (re-)distribution of various trace elements in specific meteorite types and the effects of the (re-)distribution on radiogenic isotope systematics. As Antarctic meteorites can be affected by alteration, prior to the investigation of the elemental distribution in meteorites and the isotopic effects of the (re-)distribution, the first task of this work has been dedicated to assessing the effects of Antarctic alteration on the chemical and isotopic compositions of ordinary chondrites, the most abundant class of meteorites, and more specifically on H group of ordinary chondrites. The main focus is placed on the systematic study of rare earth elements including their isotope systematics such as Sm-Nd and Lu-Hf.

This PhD thesis first demonstrates that the effects of Antarctic alteration on the Sm-Nd and Lu-Hf systems in bulk H chondrites are generally limited and thus the Sm-Nd and Lu-Hf systems preserve their original compositions during Antarctic alteration. Secondly, the underlying mechanism of Antarctic alteration observed in the first part of the PhD study is investigated using *in-situ* measurement techniques including state-of-the-art laser ablation-inductively coupled plasma-time of flight-mass spectrometry (LA-ICP-TOF-MS). Simultaneously, the potential of LA-ICP-TOF-MS as a novel technique to study the elemental distribution is examined and evaluated. Finally, the distribution of lithophile elements among the constituent minerals in H chondrites is documented at the microscale and their re-distribution during thermal metamorphism in the parent body(ies), *i.e.*, the thermal effects of the lithophile element distribution are quantified and discussed, with a direct link to the heterogeneity recorded in the Sm-Nd and Lu-Hf isotope systematics of bulk chondrites. Overall, this thesis confirms the generally pristine nature of Antarctic meteorites and describes the thermal processes that took place in the parent bodies of ordinary chondrites.

Lay Summary (French)

Une météorite est tout objet solide et naturel provenant de l'espace interplanétaire qui a survécu à son passage dans l'atmosphère terrestre avant de venir s'écraser à la surface. Il s'agit presqu'exclusivement des uniques matériaux extraterrestres que nous pouvons acquérir de nos jours. Ces précieux échantillons extraterrestres contiennent des informations sur les processus ayant eu lieu dans le système solaire et ont par conséquent été étudiés de diverses façons : chimique, minéralogique, et pétrographique, ceci afin de comprendre l'histoire du système solaire. Depuis la première mission de collecte systématique en Antarctique, plus de 41,000 ont été collectées en Antarctique, ce qui représente aujourd'hui plus de 60% de la collection mondiale. De plus, la collection antarctique contient certaines météorites « rares » telles que des martiennes et lunaires, prouvant ainsi l'importance de son rôle dans le domaine de la cosmochimie. Avant d'être collectées en Antarctique, les météorites étaient enfuies dans les couches de glace pendant plusieurs centaines de milliers d'années en moyenne et ont été de ce fait protégées de l'altération terrestre. Cependant, dû à leur longue exposition au climat extrême antarctique, les météorites ont pu être malgré tout altérées minéralogiquement et chimiquement, ce qui implique une perte d'information quant à l'histoire du système solaire. Les effets de l'altération sur les météorites antarctiques ont été étudiés à de nombreuses reprises pour vérifier si les résultats obtenus sur ces échantillons représentaient bien encore l'information originale. Néanmoins, ces études sont, à ce jour, encore incomplètes et particulièrement au niveau des mécanismes fondamentaux de l'altération qui restent peu compris.

Cette thèse de doctorat vise à apporter une caractérisation chimique et isotopique détaillée des météorites antarctiques considérées comme « bien conservées" afin d'améliorer notre compréhension de la (re-)distribution de divers éléments en traces dans des types de météorites spécifiques ainsi que pour les systèmes isotopiques radiogéniques. Comme les météorites antarctiques peuvent être affectées par l'altération, avant l'étude de la distribution élémentaire dans les météorites et les effets isotopiques de la (re-)distribution, la première tâche de ce travail a été consacrée à l'évaluation des effets de l'altération antarctique sur les compositions chimiques et isotopiques des chondrites ordinaires, la classe la plus abondante de météorites, et plus précisément du groupe H des chondrites ordinaires. L'accent est mis sur l'étude systématique des éléments des terres rares, y compris leur systématique isotopique Sm-Nd et Lu-Hf.

Ce travail démontre d'abord que les effets de l'altération antarctique pour les systèmes Sm-Nd et Lu-Hf dans les chondrites de type H sont généralement limités et donc que ces systèmes conservent leurs compositions d'origine lors de l'altération antarctique. Deuxièmement, le mécanisme sous-jacent de l'altération antarctique a été étudié à l'aide de techniques de mesure in situ, notamment l'ablation laser et la spectrométrie de masse plasma-temps de vol à couplage inductif (LA-ICP-TOF-MS). Simultanément, le potentiel du LA-ICP-TOF-MS en tant que nouvelle technique pour étudier la distribution élémentaire a été examiné et évalué. Enfin, la distribution des éléments lithophiles parmi les minéraux constitutifs des chondrites H est documentée à l'échelle microscopique et leur redistribution lors du métamorphisme thermique dans le ou les corps parents. Ainsi, les effets thermiques de la distribution des éléments lithophiles sont quantifiés et discutés, avec un lien direct avec l'hétérogénéité enregistrée dans la systématique isotopique Sm-Nd et Lu-Hf des chondrites. Dans l'ensemble, cette thèse confirme la nature généralement intacte des météorites antarctiques et identifie les processus thermiques qui ont eu lieu sur les corps parents des chondrites ordinaires.

Lay Summary (Dutch)

Een *meteoriet*, elk natuurlijk, vast object uit de interplanetaire ruimte dat de doorgang door de atmosfeer van de aarde overleefde en het aardoppervlak heeft bereikt, is het (bijna) enige extraterrestrisch materiaal dat we vandaag de dag kunnen bemachtigen. Deze waardevolle extraterrestrische stalen bevatten kritische informatie over specifieke processen die zich afspelen in het zonnestelsel, en worden dus onderzocht vanuit verschillende perspectieven gebaseerd op chemie, mineralogie en petrologie om de geschiedenis van het zonnestelsel in kaart te brengen. Sinds de eerste systematische zoektocht naar meteorieten op Antarctica in 1969, werden meer dan 41.000 meteorieten verzameld op, wat vandaag meer dan 60% van de meteorietpopulatie omvat in absolute aantallen. Meer nog, tot de Antarctische meteorieten behoren veel 'zeldzame' meteorieten zoals meteorieten van Mars en de Maan, en zodoende speelt de Antarctische meteorietcollectie een cruciale rol in de cosmochemie. Voordat deze meteorieten werden verzameld op Antarctica, waren ze begraven onder de ijskappen voor een lange tijd, gemiddeld voor enkele honderdduizenden jaren. Deze afscherming en koude en droge omgeving in Antarctica beschermt hen beter tegen terrestrische verwering in vergelijking met de bewaring in hete woestijnomgevingen, waar meteorieten gewoonlijk enkele tienduizenden jaren kunnen bewaard blijven. Nochtans, door hun lange verblijfstijden, worden zelfs de Antarctische meteorieten enigszins mineralogisch en chemisch gewijzigd, wat ertoe leidt dat een deel van de informatie over hun moederlichamen en de processen die deze ondergingen is veranderd en verloren. Daarom werden de effecten van Antarctische verwering grondig onderzocht om te zien of de verkregen resultaten nog steeds de originele informatie weergeven. Helaas zijn de onderliggende mechanismen van verwering nog niet goed begrepen, aangezien de betrokken mechanismen en processen sterk variëren van omgeving tot omgeving.

Mijn doctoraatsonderzoek focusseert op een gedetailleerde chemische en isotopische karakterisering van goed bewaarde Antarctische meteorieten om ons begrip van de herverdeling van verschillende spoorelementen in specifieke meteoriettypes en de effecten van deze herverdeling op radiogene isotopensystemen te verbeteren. Aangezien Antarctische meteorieten kunnen worden aangetast door alteratie, dienen als eerste taak, vóór de studie van de elementdistributie in meteorieten en de isotopische effecten van mogelijke herverdelingen, de gevolgen van Antarctische alteratie op de chemische en isotopische samenstelling op *ordinary chondrites*, de meest voorkomende klasse meteoriet, en meer specifiek de H groep *ordinary chondrites* te worden geëvalueerd. De focus wordt hierbij voornamelijk geplaatst op de systematische studie van de zeldzame aardelementen, met inbegrip van hun isotopische systemen zoals Sm-Nd en Lu-Hf.

Dit PhD project toont voor het eerst aan dat de effecten van Antarctische alteratie op de Sm-Nd en Lu-Hf systemen in bulk H chondrieten in het algemeen beperkt blijven en dus dat de Sm-Nd en Lu-Hf systemen hun oorspronkelijke samenstelling bewaren tijdens Antarctische alteratie. Ten tweede wordt het onderliggende mechanisme van Antarctische alteratie onthuld aan de hand van *in-situ* meettechnieken inclusief een van de nieuwste instrumenten op de markt *laser ablation-inductively coupled plasma-time of flight-mass spectrometry* (LA-ICP-TOF-MS). Tegelijkertijd wordt het potentieel van LA-ICP-TOF-MS als een nieuwe techniek om de verdeling van elementen te bestuderen onderzocht en geëvalueerd. Tot slot wordt de verdeling van lithofiele elementen in de samenstellende mineralen van H chondrieten gedocumenteerd op de microschaal en hun herverdeling tijdens thermisch metamorfisme op hun moederlicha(a)m(en) besproken. Dit zijn de thermische effecten op de verdeling van de lithofiele elementen, die direct gelinkt worden met de heterogeniteiten waargenomen voor de Sm-Nd en Lu-Hf isotopensamenstelling van bulk chondrieten. Samen genomen, bevestigt dit werk de over het algemeen goed bewaarde aard van Antarctische meteorieten en documenteert het de thermische processen die plaatsvonden op de moederlichamen van *ordinary chondrites*.

Table of Contents

Chapter 1 "*Introduction: Do we need a time machine to reveal the history of our Solar System?*"

"The farther backward you can look, the farther forward you are likely to see"

- *Winston Churchill*

Meteorites: windows on the Solar System

As we human beings largely base our knowledge and experiences on historical events, their documentation plays a pivotal role to study and reveal human and natural history. In the framework of studying natural history, we as a species have conducted research not only on Earth's history but also on the history of the Solar System. The Solar System fundamentally consists of the Sun, eight planets, five dwarf planets, and plenty of asteroids (on the order of several million: The International Astronomical Union Minor Planet Center: https://minorplanetcenter.net/, accessed 03 December 2022) since the Sun and the Solar System were formed ~4.568 billion years ago (Bouvier and Wadhwa, 2010). Due to materials ejected from the surface of planets and asteroids and the collapse of asteroids following large-scale impact events, we have been able to obtain solid bodies of extraterrestrial material here on the Earth when these objects penetrate the atmosphere and reach the Earth's surface, in the form of *meteorites* (*e.g.*, Krot *et al.*, 2003). Meteorites retain information regarding their parent bodies as they are representative of the physical and chemical conditions of the parent bodies, and thus have been extensively used as an important source of information on the history of the Solar System. Although we have succeeded in sampling from planets and asteroids so far (Apollo program, NASA: National Aeronautics and Space Administration, U.S.; Genesis, NASA; Hayabusa, JAXA: Japan Aerospace Exploration Agency, Japan; Hayabusa 2, JAXA), cosmochemistry still relies heavily on meteorite studies (total mass: ~400 kg vs. ~700,000 kg for the sample return missions and meteorites, respectively: NASA; Meteoritical Bulletin Database: http://www.lpi.usra.edu/meteor/metbull.php, accessed 03 December 2022). As such, meteorites are precious extraterrestrial materials providing highly valuable information to understand Solar System formation and evolution.

Classification of meteorites

Meteorites exist in various types as they derive from various parent bodies and thus have been classified based on several points of view, such as their mineral and chemical compositions. There are two major classifications: one is based on the ratio of metal and silicate contents and the other on whether or not they underwent differentiation, *i.e.*, describing them as primitive or evolved (Krot *et al.*, 2003; Weisberg *et al.*, 2006). Following the former classification, meteorites are classified into three categories in descending order of metal content: iron meteorite, stony-iron meteorite, and stony meteorite. In the case of the latter classification, the stony meteorites are divided into two categories: chondritic meteorites (chondrites), which contain primitive materials such as chondrules, and achondritic meteorites (achondrites), which underwent differentiation such as lunar and Martian meteorites. The iron meteorites and stony-iron meteorites are classified into the differentiated meteorites as well as achondrites. Although there are meteorites that are described as primitive achondrites exhibiting features in-between those of chondrites and differentiated meteorites, and differentiated meteorites come

in various types, only chondrites will be described in detail in the following sections as my PhD work focused on them.

Most meteorites that we have collected are chondrites (> 90% by number: estimated from the Meteoritical Bulletin Database: http://www.lpi.usra.edu/meteor/metbull.php, accessed 03 December 2022), which are primitive rocks that have non-volatile element abundances close to those observed in the solar photosphere (McSween and Huss, 2010). Chondrites fundamentally consist of chondrules, Fe-Ni metal, refractory inclusions, and a fine-grained matrix (Krot *et al.*, 2003). Chondrules are primitive spherical materials that are 1-2 mm in diameter and formed by the rapid cooling of silicates in space, and the name "chondrites" is derived from these chondrules. Chondrites are classified further into classes and then groups based on their chemical and petrological features (*e.g.*, oxygen isotopes and mineralogy). Based on their bulk chemical features, chondrites are classified into carbonaceous chondrites (CCs), ordinary chondrites (OCs), enstatite chondrites (ECs), Rumuruti-like chondrites (R chondrites), and Kakangari-like chondrites (K chondrites). The first three classes can be further divided in nine groups (CI, CM, CR, CH, CB, CV, CK, CO, and CL) for CCs, three groups (H, L, and LL) for OCs, and two groups (EH and EL) for ECs (Krot *et al.*, 2003; Metzler *et al.*, 2021). On the other hand, chondrites can be also classified based on their petrologic features providing a guide to the degree of thermal and aqueous alteration that chondrites underwent, following a scheme introduced by Van Schmus and Wood (1967). In this classification, chondrites are divided into petrologic (metamorphic) types 1-7. With decreasing types from 3 to 1, the degree of aqueous alteration that chondrites underwent in their parent bodies increases. With increasing number for types 3 to 7, chondrites underwent more thermal metamorphism in their parent bodies and the resulting chemical equilibration and textural recrystallization proceeded to a larger extent. Due to this equilibration, type 3 chondrites are commonly named unequilibrated chondrites and types 4-7 chondrites are labelled equilibrated chondrites. As such, type 3 chondrites are generally regarded the least secondary-metamorphosed meteorites. The heat source of this thermal metamorphism in the parent bodies is considered the decay heat from short-lived radioactive nuclides such as ^{26}Al (half-life: 0.72 Myr; Lee *et al.*, 1976) and ^{60}Fe (half-life: 1.5 Myr; Kutschera *et al.*, 1984). In the classification of meteorites, the chemical and petrologic classifications described above are typically combined. For example, the Allende meteorite, one of the most studied meteorites, is labelled CV3 as it is a CV chondrite of type 3. See Figure 1 for the overview of the classification of meteorites.

The OCs are the most abundant meteorite class (~ 85% by number: estimated from the Meteoritical Bulletin Database: http://www.lpi.usra.edu/meteor/metbull.php, accessed 03 December 2022) among all meteorite classes collected so far, and that is why the name "ordinary" was given. The OCs display a wide range in degree of metamorphism from type 3 to 7, while some type-3 OCs are further subdivided into 10 subtypes ranging from 3.0 to 3.9. In this array, type 3.0 represents the least metamorphosed OCs, based on the bulk thermoluminescence (TL) sensitivity, cathodoluminescence (CL), or other petrologic features (*e.g.*, Sear *et al.*, 1991; Huss *et al.*, 2006). As described above, OCs are divided into H, L and LL groups based on their bulk iron contents. H chondrites have high total iron contents, L chondrites display low total iron contents, and LL chondrites have low metallic iron relative to total iron as well as low total iron contents (Figure 2). They are fundamentally the same in terms of their bulk chemical compositions, except for elements concentrated to a high degree in Fe-Ni metals (Kallemeyn *et al.*, 1989). In addition, their mineralogy is also comparable, consisting of olivine, low-Ca pyroxene, Ca-rich pyroxene, and feldspar as silicates, kamacite and taenite as metals, troilite as sulfides,

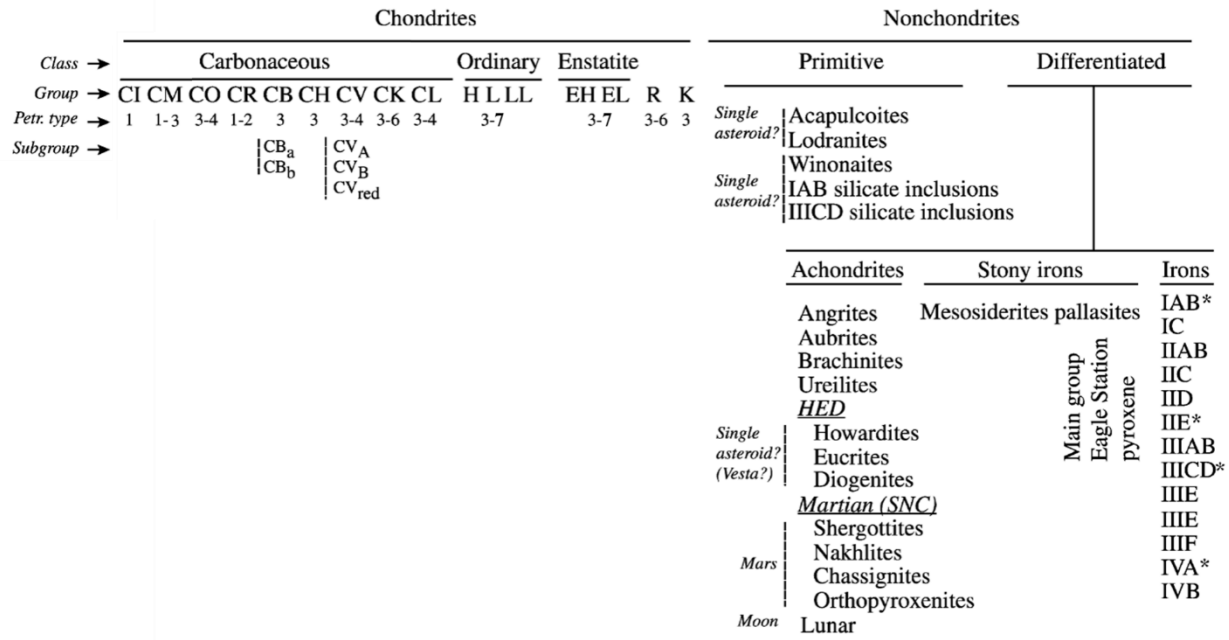

Figure 1 Classification of meteorite updated from Krot *et al.* (2003) for chondrites.

chromite and ilmenite as oxides, and merrillite and chlorapatite as phosphates (Van Schmus, 1969; McSween *et al.*, 1991). Because their oxidation states increase accordingly from H to LL (Figure 2), however, there are differences in the mineral modal abundances and the mean mineral compositions among the OC groups (Table 1).

Relative mobility of the elements and its relative importance

When the elements condensed from the solar nebular with primary phases in chondrites, they behaved differently mainly due to their varying chemical properties. These different chemical properties of elements combined with their parent body processes produced variable chemical compositions in chondrites (*e.g.*, Palme and Jones, 2003). Based on the chemical properties of elements, there are two major classifications of elements in cosmochemistry. One of them is based on their affinity, *i.e.*, whether the element tends to concentrate in silicate phases or metal/sulfide phases, which is fundamentally equivalent to Goldschmidt's classification. Elements favoring silicate phases are called lithophile elements (*e.g.*, Al, Ca, and Sc) and those partitioning into metal or sulfide phases are labelled siderophile or chalcophile elements (*e.g.*, Co, Cu, and Ir), respectively (Palme and Jones, 2003). The other classification is based on their volatility, more specifically their equilibrium 50% condensation temperature (Lodders, 2003). Following to this classification, elements that condensed from the Solar nebular in the first phase with a condensation temperature at a pressure of 10^{-4} bar (T_c) in the range of 1850 to 1400 K are named refractory elements (*e.g.*, rare earth elements, Hf, and Os), those that condensed with T_c = 1350-640 K are labelled moderately volatile elements (*e.g.*, P, Mn, and Ga), and those that condensed during the last phase with T_c = < 640 K are called highly volatile elements (*e.g.*, Cl, In, and Pb: Palme and Jones, 2003; Davis, 2006). Combining these two classifications, for example, Ca, which concentrates in silicate phases and has a T_c of 1517 K (Lodders, 2003), is classified as a refractory lithophile element. This cosmochemical classification of elements is summarized in Figure 3.

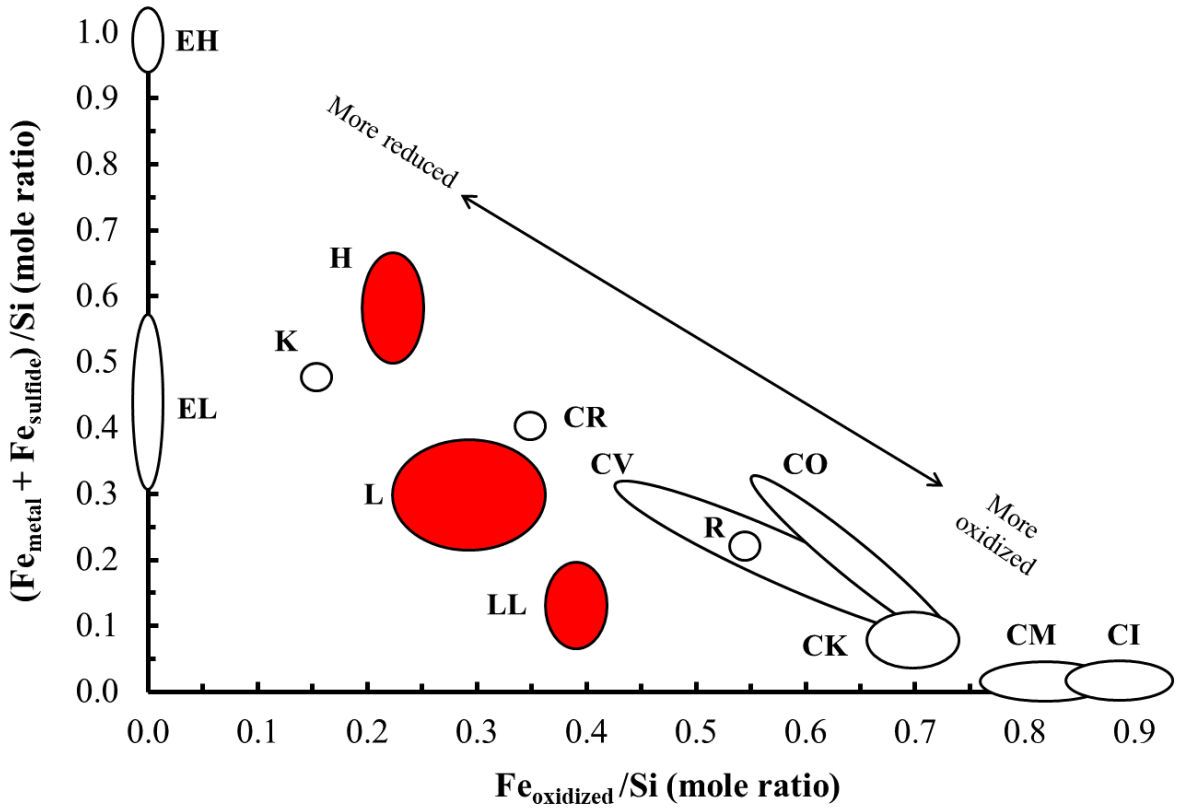

Figure 2 Urey-Craig diagram showing relative iron contents and oxidation states of the chondrite groups. Iron present in metal and sulfide phases is plotted versus iron present in silicate and oxide phases, for bulk chondrite compositions (Brearley and Jones, 1998). Ordinary chondrites are highlighted by coloring.

Thanks to these different elemental behaviors, analyzing the chemical compositions of and studying their relative abundances in chondrites but also in terrestrial materials can help to better understand their geochemical history within their parent bodies. Among the elements, rare earth elements (REEs) in particular represent critical elements universally used for understanding geochemical processes in both the geochemical and cosmochemical fields of research due to their similar chemical properties. Moreover, the REEs include radioactive isotopes such as ^{146}Sm (half-life ~ 103 Myr), ^{147}Sm (half-life ~ 106 Gyr), and ^{176}Lu (half-life ~ 37.1 Gyr). Their isotope systematics form the basis of important chronometers and tracers of chemical differentiation processes. The broad definition of the REE group comprises 17 elements including Sc, Y, and lanthanides, but the REEs commonly only indicate the lanthanoids in the Earth sciences and cosmochemistry, as the term will be applied in this work. The first four lanthanoids La to Nd (Pm is a radioelement) will be defined as the light REEs (LREEs), the next five lanthanoids Sm to Dy are the middle REEs (MREEs), and the last five lanthanoids Ho to Lu are the heavy REEs (HREEs). In cosmochemistry, the abundances and isotopic compositions of the REEs in bulk chondrites have been studied and analyzed in detail so far, and these studies demonstrate that the REEs are not fractionated in bulk chondrites in most cases (*e.g.*, Nakamura, 1974; Jacobsen and Wasserburg, 1980). However, looking at the mineral scale instead of the bulk scale, the REEs are fractionated strongly among the constituent minerals in chondrites depending on their chemical properties. For example, REEs are concentrated in Ca-phosphates or oldhamite (a unique sulfide CaS) among the minerals in the case of OCs or ECs, respectively (*e.g.*, Crozaz, 1974; Murrell and Burnett, 1983; Ebihara and Honda, 1983). The information regarding these elemental distributions among the constituent minerals has significantly improved our

understanding of the conditions of equilibration induced by thermal metamorphism in their parent bodies (*e.g.*, McIntire, 1963). It also led to better insights into the variations of isotopic compositions and elemental abundances in bulk rock that we have observed so far (*e.g.*, Bouvier *et al.*, 2008; Dauphas and Pourmand, 2015; Debaille *et al.*, 2017). As such, several studies focusing on elemental distribution have been conducted using physical mineral separation, *in-situ* measurements, and chemical leaching techniques for various classes of chondrites (*e.g.*, Mason and Graham, 1970; Martin *et al.*, 2013; Barrat *et al.*, 2014). Nevertheless, some improvements, notably a more detailed study of the elemental distribution are still required especially in the case of OCs, mainly due to the instrumental limitations when the previous studies were conducted.

The effects of weathering on the Earth

Humankind has been collecting meteorites from various places on the Earth, at the least since the 19th of May in 861 when the Nogata meteorite fell in Japan (Shima *et al.*, 1980), which is regarded as the oldest documented fall so far. In 1969, a Japanese expedition found nine meteorites on the bare ice fields near the Yamato Mountains in Antarctica, which in 1973 led to the first systematic meteorite recovery expedition on the Southern continent (Yamaguchi *et al.*, 2021), and was followed by expeditions until the present (*e.g.*, Goderis *et al.*, 2021). The reasons why we have collected many meteorites from Antarctica are the following. First of all, meteorites reaching the Earth's surface look the same as common terrestrial rocks to the untrained eye, thus it is hard to distinguish whether a rock found in most places on the Earth is a meteorite or not without further analyses. However, there are almost no such terrestrial rocks on the ice fields in Antarctica, hence it is highly likely that any rocks found on the ice fields are meteorites. Moreover, this glacial ice in Antarctica has been moving very slowly (~several - tens of m/year for the inland; NIPR: National Institute of Polar Research, Japan), and meteorites accumulate at certain points near mountain ranges following transport by the ice (Figure 4).

Table 1

Mineral modal abundances (MA in wt.%) and the mean mineral compositions (comp.) among the equilibrated OC groups.

	H group		L group		LL group	
	MA	comp.	MA	comp.	MA	comp.
Olivine	33-37	$Fo_{81}Fa_{19}$	45-49	$Fo_{75}Fa_{25}$	56-60	$Fo_{69}Fa_{31}$
Low-Ca pyroxene	23-27	$En_{82}Fs_{17}Wo_{2}$	21-25	$En_{77}Fs_{21}Wo_{2}$	14-18	$En_{73}Fs_{25}Wo_{2}$
Ca-rich pyroxene	4-5	$En_{49}Fs_{6}Wo_{45}$	4-5	$En_{48}Fs_{8}Wo_{45}$	4-5	$En_{47}Fs_{10}Wo_{44}$
Feldspar	9-10	$Or_{6}An_{12}Ab_{82}$	9-10	$Or_{6}An_{10}Ab_{84}$	9-10	$Or_{4}An_{11}Ab_{86}$
Kamacite	15-17		6-8		1-2	
Taenite	2-3		2-3		2-4	
Troilite	5-6		5-6		5-6	
Chromite	0.5	$Fe_{83}Mg_{14}Mn_{3}$	0.5	$Fe_{87}Mg_{11}Mn_{2}$	0.5	$Fe_{91}Mg_{9}Mn_{2}$
Ca-phosphates	0.6		0.6		0.6	

See Van Schmus (1969) for more details, especially for the mineral compositions.

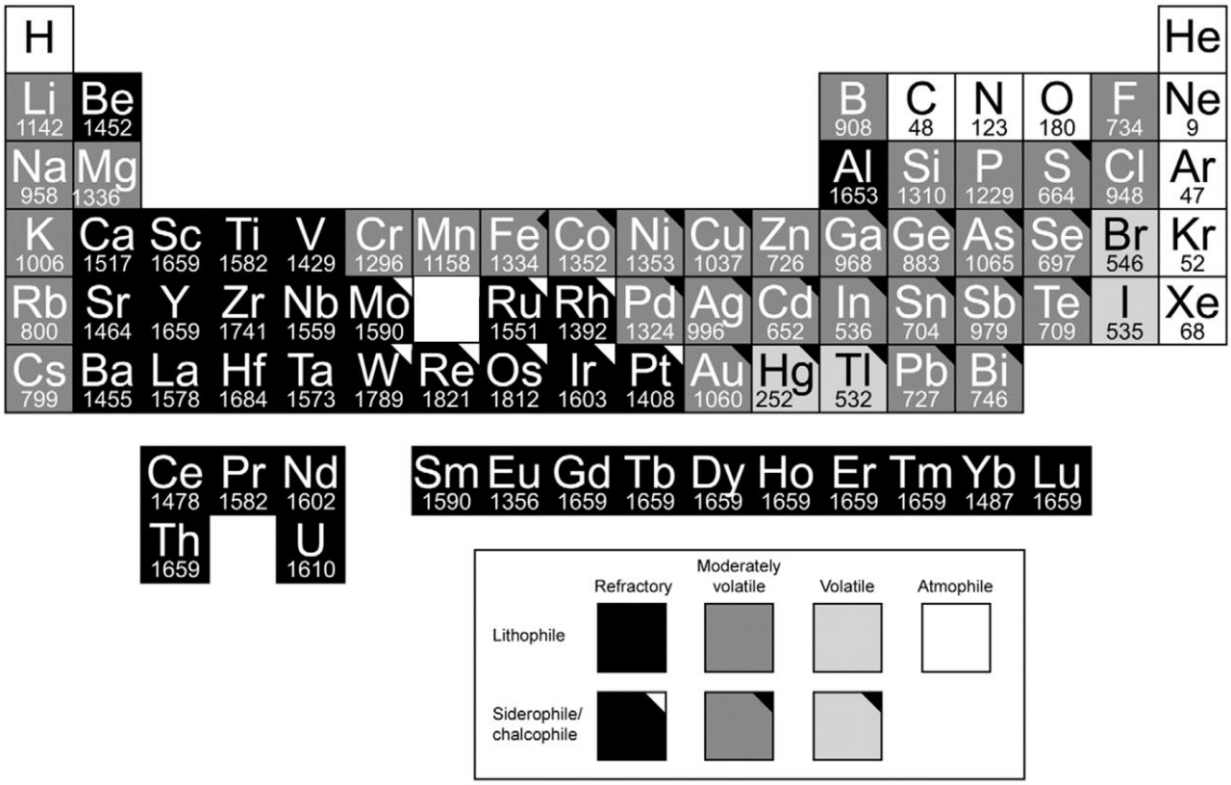

Figure 3 A cosmochemical periodic table of the elements modified from Daivs (2006). Only stable or very long-lived unstable elements (Th and U) are shown. Under each element is given the equilibrium 50% condensation temperature (K) calculated by Lodders (2003) for a gas of solar composition at 10^{-4} atm total pressure. The elements are shaded by cosmochemical classification, with siderophile/chalcophile elements indicated by a small triangle at the upper right. Iron is given a half-triangle, because it has lithophile, siderophile, and chalcophile tendencies.

As such, we can readily collect many meteorites by searching at such a site labelled "blue ice field" in Antarctica (*e.g.*, Bischoff, 2001). Today, Antarctic meteorites constitute by number more than 60% of the population of meteorites and include many rare meteorites such as ungrouped, martian, and lunar meteorites (Meteorite Newsletter, NIPR; Antarctic Meteorite Newsletter, NASA); hence the Antarctic meteorite collection plays a pivotal role for cosmochemistry. Meteorites collected from hot deserts such as Sahara and Atacama also contribute to the population of meteorites in a significant manner (> 20% by number: estimated from the Meteoritical Bulletin Database: http://www.lpi.usra.edu/meteor/metbull.php, accessed 03 December 2022), as meteorites can also be identified more easily in hot desert environments. Depending on how meteorites were recovered, they are divided into falls and finds: falls are recovered after observed fall events, sometimes days after, while finds cannot be associated with observed falls such as Antarctic meteorites and meteorites collected from hot deserts. As falls are usually collected shortly after the fall events, they are in general considerably fresher than finds, as the latter have been subjected to weathering on the Earth to various degrees during their terrestrial residence (roughly on the order of tens of kyr: *e.g.*, Al-Kathiri *et al.*, 2005). Such terrestrial weathering may change the original mineralogy and chemical compositions of meteorites due to the alteration to mineral phases that are more stable at the Earth's surface depending on environmental factors such as humidity and temperature (*e.g.*, Koeberl and Cassidy, 1991; Lee and Bland, 2004; Bland *et al.*, 2006; van Ginneken *et al.*, 2022). This process can take place relatively rapidly, particularly in temperate and tropical zones, as well as in hot deserts

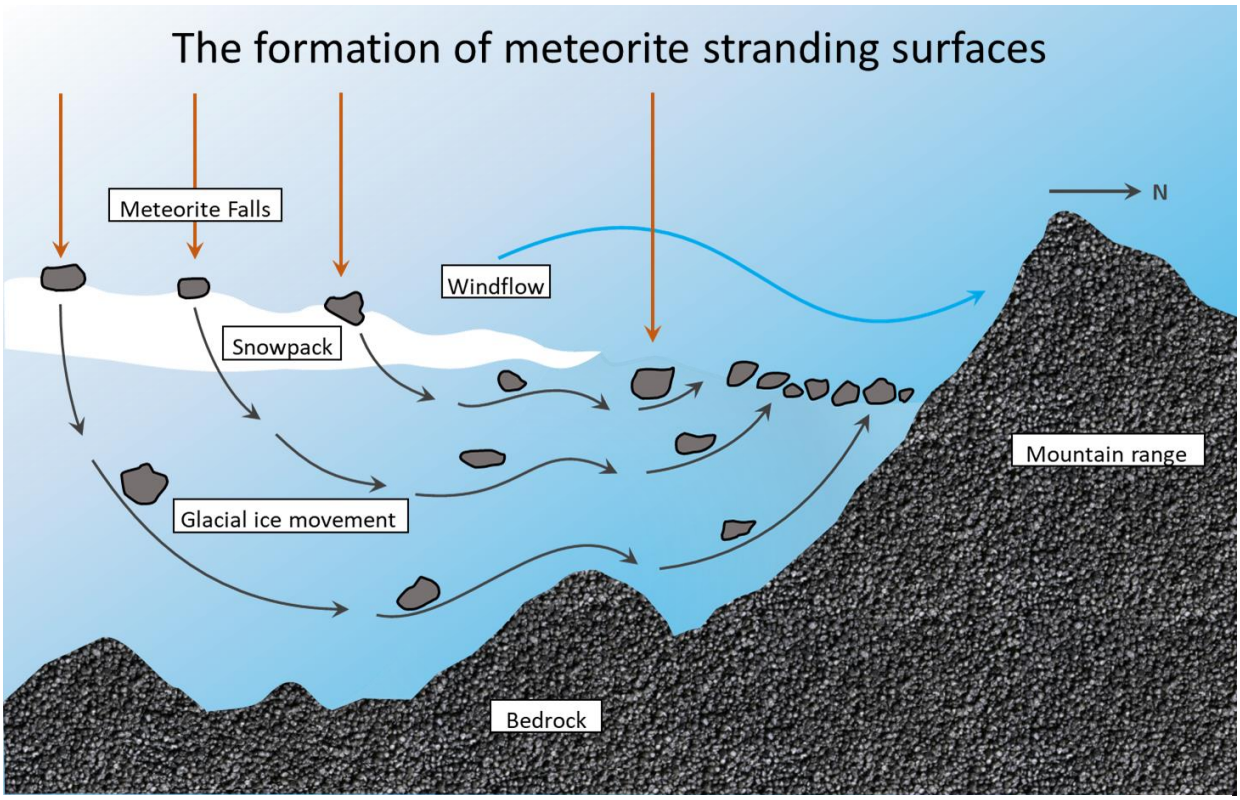

Figure 4 Meteorite Stranding Surface - Whillans and Cassidy Model from The Field Museum, Chicago, U.S., illustrated by Ruthie A. Smith and modified by Maria Valdes.

(Lee and Bland, 2004; Bland *et al*., 2006; Pourkhorsandi *et al*., 2021), thus finds collected from such a site are fundamentally weathered to some extent. Antarctic meteorites have been buried in and shielded by the ice since their fall, exhibiting old terrestrial ages on the order of hundreds of kyr (Whillans and Cassidy, 1983; Cassidy and Whillans, 1990; Nishiizumi *et al.*, 1989). Despite better protection of the burial from terrestrial weathering relative to the residence in hot desert environments, the exposure of Antarctic meteorites to the extreme Antarctic climate during such an extended period of time can lead to mineralogical and chemical alteration (*e.g.*, Koeberl and Cassidy, 1991; Lee and Bland, 2004; Bland *et al.*, 2006).

Research aims

My PhD work aims to characterize Antarctic meteorites chemically and isotopically, and then to improve our understanding of the distribution of various trace elements in specific meteorite classes/groups as well as the effects of such elemental distributions on radiogenic isotope systematics. However, terrestrial alteration can modify their original compositions even in the case of "well-preserved" Antarctic meteorites. In this context, it is essential to confirm if such terrestrial weathering affects the original features of the target meteorite, *i.e.*, if the meteorite still records the history of its parent body after the terrestrial residence. Otherwise, data obtained may already be modified and cannot be used to discuss the planetesimal or planetary history. To archive the aims, H chondrites were chosen for this PhD work due to their largest number of samples in all meteorite classes (~40%: estimated from the Meteoritical Bulletin Database: http://www.lpi.usra.edu/meteor/metbull.php, accessed 03 December 2022), no systematic study regarding the Antarctic alteration effect on chondrites, and their various metamorphic degrees from type 3 to type 7. Table 2 lists the information of the samples used in

Table 2

List of H chondrites analyzed in this PhD study (n.d.: not determined; NIPR: National Institute of Polar Research, Japan; RBINS: Royal Belgian Institute of Natural Sciences, Belgium).

Sample name	Type	Find/Fall	Weathering index	Shock stage	ID # for section / fragments	Mass for fragments (mg)	Source	Sampling location	Coordinate
Asuka 880941	H3.3	Find	A/B	S1-2[b]	51-A / 48	538	NIPR	Antarctica	72°50'S, 24°30'E
Yamato 793574	H3.5	Find	n.d.	n.d.	51-A / 56	789	NIPR	Antarctica	71°30'S, 35°40'E
Yamato 790461	H3.7	Find	B	S3[b]	91-A / 100	795	NIPR	Antarctica	71°30'S, 35°40'E
Allan Hills 78084	H3.9	Find	B/Ce	n.d.	81-A / 89	634	NIPR	Antarctica	76°43'S, 159°40'E
Asuka 881258	H3.9[a]	Find	B	n.d.	71-A / 82	553	NIPR	Antarctica	72°50'S, 24°30'E
Asuka 09436	H3	Find	C	n.d.		731	RBINS	Antarctica	72°50'S, 24°30'E
Northwest Africa 6752	H3	Find	W2	S1		478	RBINS	Tabelbala area, Morocco/Algeria	30°5'N, 4°35'W
Asuka 09387	H4	Find	B/C	n.d.		857	RBINS	Antarctica	72°50'S, 24°30'E
Northwest Africa 6771	H4	Find	W1	S1		552	RBINS	Chaanba - Tademaït, Algeria	29°15'N, 3°30'E
Jilin	H5	Fall	n.d.	S3			RBINS	Jilin (Kirin), China	44°0'N, 126°30'E
Nuevo Mercurio	H5	Fall	n.d.	n.d.			RBINS	Nuevo Mercurio, Mexico	24°18'N, 102°8'W
Richardton	H5	Fall	n.d.	n.d.			RBINS	Richardton, U.S.	46°53'N, 102°19'W
Asuka 09618	H5	Find	C	n.d.		982	RBINS	Antarctica	72°50'S, 24°30'E
Sahara 97035	H5	Find	W2	S1		916	RBINS	Sahara	y+0°03'33"N, x+0°30'50"W[c]
Butsura	H6	Fall	n.d.	n.d.			RBINS	Butsura, India	27°5'N, 84°5'E
Asuka 09516	H6	Find	C	n.d.		606	RBINS	Antarctica	72°50'S, 24°30'E
Yamato 790960	H7	Find	B	S3[b]	63-A / 62	542	NIPR	Antarctica	71°30'S, 35°40'E

The type, weathering index, shock stage, and coordinate are based on the Meteoritical Bulletin Database (http://www.lpi.usra.edu/meteor/metbull.php).

[a] Ninagawa *et al.* (2005).

[b] The shock stages are estimated from descriptions of the shock degree in Meteorite Newsletter, NIPR, based on Stöffler *et al.* (1991).

[c] Listed is the offset relative to a secret origin at (x°W longitude, y°N latitude, where x and y are integers).

the PhD study. Therefore, in my PhD work, the effects of terrestrial alteration on the Sm-Nd and Lu-Hf isotope systematics and the elemental abundances in bulk H chondrites are firstly examined by comparison with chondrite falls, which is discussed in **Chapter 2**. This work also confirms the usefulness of Antarctic meteorites for isotope studies. Although Chapter 2 demonstrates that Antarctic meteorites generally preserve their original Sm-Nd and Lu-Hf isotopic compositions, the underlying mechanism of Antarctic alteration remained, especially when the alteration was severe. Thus, the potential of state-of-the-art laser ablation-inductively coupled plasma-time of flight-mass spectrometry to reveal the detailed mechanism of terrestrial alteration as well as the elemental distributions is evaluated by comparison with more conventional spot analysis in **Chapter 3**. Chapter 3 shows a deposition of REEs in a crack of a weathered sample, leading us to a comprehensive characterization of cracks using various *in-situ* measurements. This work is described in **Chapter 4** and links to the remaining question from chapter 2, which reveals the underlying mechanism of Antarctic alteration. Finally, in **Chapter 5**, the elemental distributions in chondrites and their thermal processes in the parent bodies are discussed in a systematic manner, combining the bulk and *in-situ* data. Chapter 5 demonstrates that re-distribution of refractory lithophile elements occurred in the parent body(ies), which is completely consistent with what we expected and discussed based on the heterogeneity observed for the Sm-Nd and Lu-Hf systems in chapter 2.

This research fell within the framework of the Excellence of Science (EoS) ET-HoME project that aims at investigating the Evolution and Tracers of the Habitability of Mars and Earth, and was conducted through the collaboration of four research groups: (1) Analytical-, Environmental-, and Geo-Chemistry (AMGC), Vrije Universiteit Brussel, Belgium, (2) Laboratoire G-Time, Université libre de Bruxelles, Belgium, (3) Atomic & Mass Spectrometry (A&MS) Research Unit, Ghent University, Belgium, and (4) Antarctic meteorite research center, National Institute of Polar Research (NIPR), Japan. The highly interdisciplinary research summarized in this work demonstrates that by combining different expertise critical new insights can be acquired.

References

Al-Kathiri A., Hofmann B.A., Jull J.T. and Gnos E. (2005) Weathering of meteorites from Oman: Correlation of chemical and mineralogical weathering proxies with ^{14}C terrestrial ages and the influence of soil chemistry. *Meteorit. Planet. Sci.* **40**, 1215-1239.

Barrat J.A., Zanda B., Jambon A. and Bollinger C. (2014) The lithophile trace elements in enstatite chondrites. *Geochim. Cosmochim. Acta* **128**, 71-94.

Bischoff A. (2001) Meteorite classifcation and the defnition of new chondrite classes as a result of successful meteorite search in hot and cold deserts. *Planet. Space Sci.* **49**, 769-776.

Bland P.A., Zolensky M.E., Benedix G.K. and Sephton M.A. (2006) Weathering of chondritic meteorites. In *Meteorites and the Early Solar System II* (eds. Lauretta D.S. and McSween Jr. H.Y.). The University of Arizona Press, Tucson, pp. 853-867. in collaboration with Lunar and Planetary Institute, Houston.

Bouvier A. and Wadhwa M. (2010) The age of the Solar System redefined by the oldest Pb–Pb age of a meteoritic inclusion. *Nat. Geosci.* **3**, 637–641.

Bouvier A., Vervoort J.D. and Patchett P.J. (2008) The Lu–Hf and Sm–Nd isotopic composition of CHUR: Constraints from unequilibrated chondrites and implications for the bulk composition of terrestrial planets. *Earth Planet. Sci. Lett.* **273**, 48-57.

Brearley A.J. and Jones R.H. (1998) Chondritic meteorites. In *Planetary Materials*, Reviews in Mineralogy (ed. J.J. Papike). Mineralogical Society of America, Washington, DC, vol. 36, chap. 3, pp. 3-1-3-398.

Cassidy W.A. and Whillans I.M. eds. (1990) *Workshop on Anturctic Meteorite Stranding Surfaces; LPI Tech. Rept. 90-03*. Lunar and Planetary Institute, Houston.

Crozaz G. (1974) U, Th and extinct ^{244}Pu in the phosphates of the St. Severin meteorite. *Earth Planet. Sci. Lett.* **23**, 164-169.

Dauphas N. and Pourmand A. (2015) Thulium anomalies and rare earth element patterns in meteorites and Earth: Nebular fractionation and the nugget effect. *Geochim. Cosmochim. Acta* **163**, 234-261.

Davis A.M. (2006) Volatile evolution and loss. In *Meteorites and the Early Solar System II* (eds. Lauretta D.S. and McSween Jr. H.Y.). The University of Arizona Press, Tucson, pp. 295-307. in collaboration with Lunar and Planetary Institute, Houston.

Debaille V., Orman J.V., Yin Q.Z. and Amelin Y. (2017) The role of phosphates for the Lu–Hf chronology of meteorites. *Earth Planet. Sci. Lett.* **473**, 52-61.

Ebihara M. and Honda M. (1983) Rare earth abundances in chondritic phosphates and their implications for early stage chronologies. *Earth and Planet. Sci. Lett.* **63**, 433-445.

Goderis S., Yesiltas M., Pourkhorsandi H., Shirai N., Poudelet M., Martin L., Yamaguchi A., Debaille V. and Claeys P. (2021) Detailed record of the BELARE 2019-2020 meteorite recovery expedition on the Nansen Ice Field, East Antarctica. *Antarctic Rec.* **65**, 1-20.

Huss G.R., Rubin A.E. and Grossman J.N. (2006) Thermal metamorphism in chondrites. In *Meteorites and the Early Solar System II* (eds. Lauretta D.S. and McSween Jr. H.Y.). The University of Arizona Press, Tucson, pp. 567-586. in collaboration with Lunar and Planetary Institute, Houston.

Jacobsen S.B. and Wasserburg G.J. (1980) Sm–Nd isotopic evolution of chondrites. *Earth Planet. Sci. Lett.* **50**, 139-155.

Kallemeyn G.W., Rubin A.E., Wang D. and Wasson J.T. (1989) Ordinary chondrites: Bulk compositions, classification, lithophile-element fractionations, and composition-petrographic type relationships. *Geochim. Cosmochim. Acta* **53**, 2747-2767.

Koeberl C. and Cassidy W.A. (1991) Differences between Antarctic and non-Antarctic meteorites: An assessment. *Geochim. Cosmochim. Acta* **55**, 3-18.

Krot A.N., Keil K., Scott E.R.D., Goodrich C.A. and Weisberg M.K. (2003) Classification of meteorites. In *Meteorites, Comets, and Planets*, Treatise on Geochemistry (ed. Davis A.M.). Elsevier, Amsterdam, vol. 1, chap. 1.05, pp. 83-128.

Kutschera W., Billquist P.J., Frekers D., Henning W., Jensen K.J., Xiuzeng M., Pardo R., Paul M., Rehm K.E., Smither R.K. and Yntema J.L. (1984) Half-life of ^{60}Fe. *Nucl. Instrum. Methods* **B5**, 430-435.

Lee M.R. and Bland P.A. (2004) Mechanism of weathering of meteorites recovered from hot and cold deserts and the formation of phyllosilicates. *Geochim. Cosmochim. Acta* **68**, 893-916.

Lee T., Papanastassiou D.A. and Wasserburg G.J. (1976) Demonstration of ^{26}Mg excess in Allende and evidence for ^{26}Al. *Geophys. Res. Lett*. **3**, 41-44.

Lodders K. (2003) Solar system abundances and condensation temperatures of the elements. *Astrophys. J.* **591**, 1220–1247.

Martin C., Debaille V., Lanari P., Goderis S., Vandendael I., Vanhaecke F., Vidal O. and Claeys P. (2013) REE and Hf distribution among mineral phases in the CV–CK clan: A way to explain present-day Hf isotopic variations in chondrites. *Geochim. Cosmochim. Acta* **120**, 496-513.

Mason B. and Graham A.L. (1970) Minor and trace elements in meteoritic minerals. *Smithson. Contrib. Earth Sci.* **3**, 1-17.

McIntire W.L. (1963) Trace element partition coefficients—a review of theory and applocations to geology. *Geochim. Cosmochim. Acta* **27**, 1209-1264.

McSween Jr. H.Y. and Huss G.R. (2010) Cosmochemistry. Cambridge University Press, pp. 1-549.

McSween Jr. H.Y., Bennett III M.E. and Jarosewich E. (1991) The mineralogy of ordinary chondrites and implications for asteroid spectroscopy. *Icarus* **90**, 107-116.

Metzler K., Hezel D.C., Barosch J., Wölfer E., Schneider J.M., Hellmann J.L, Berndt J., Stracke A., Gattacceca J., Greenwood R.C., Franchi I.A., Burkhardt C. and Kleine T. (2021) The Loongana (CL) group of carbonaceous chondrites. *Geochim. Cosmochim. Acta* **304**, 1-31.

Murrell M.T. and Burnett D.S. (1983) Actinide microdistributions in the enstatite meteorites. *Geochim. Cosmochim. Acta* **46**, 2453-2460.

Nakamura N. (1974) Determination of REE, Ba, Fe, Mg, Na and K in carbonaceous and ordinary chondrites. *Geochim. Cosmochim. Acta* **38**, 757-775.

Ninagawa K., Mieda Y., Ueda H., Imae N., Kojima H. and Yanai K. (2005) Thermoluminescence studies of ordinary chondrites in the Japanese Antarctic meteorite collection IV: Asuka ordinary chondrites. *Antarct. Meteor. Res.* **18**, 1-16.

Nishiizumi K., Elmore D. and Kubik P.W. (1989) Update onterrestrial ages of Antarctic meteorites. *Earth Planet. Sci. Lett.* **93**, 299-313.

Palme H. and Jones A. (2003) Solar system abundances of the elements. In *Meteorites, Comets, and Planets*, Treatise on Geochemistry (ed. Davis A.M.). Elsevier, Amsterdam, vol. 1, chap. 1.03, pp. 41-61.

Pourkhorsandi H., Debaille V., Armytage R.M.G., van Ginneken M., Rochette P. and Gattacceca J. (2021) The effects of terrestrial weathering on samarium-neodymium isotopic composition of ordinary chondrites. *Chem. Geol.* **562**, 120056.

Sears D.W.G., Hasan F.A., Batchelor J.D. and Lu J. (1991) Chemical and physical studies of type 3 chondrites: XI. Metamorphism, pairing, and brecciation of ordinary chondrites. *Proc. Lunar Planet. Sci. Conf.* **21**, 493–512.

Shima M., Murayama S., Yabuki H. and Okada A. (1980) Petrography, mineralogy and chemical composition on the chondrite Nogata, Nogata-shi, Fukuoka-ken, Japan: Oldest observed fall in the world. *Meteoritics* **15**, 365-366 (abstract).

Stöffler D., Keil K. and Scott E.R.D. (1991) Shock metamorphism of ordinary chondrites. *Geochim. Cosmochim. Acta* **55**, 3845– 3867.

van Ginneken M., Debaille V., Decrée S., Goderis S., Woodland A.B., Wozniakiewicz P., De Ceukelaire M., Leduc T. and Claeys P. (2022) Artificial weathering of an ordinary chondrite: Recommendations for the curation of Antarctic meteorites. *Meteorit. Planet. Sci.* **57**, 1247-1266.

Van Schmus W.R. (1969) The mineralogy and petrology of chondritic meteorites. *Earth Sci. Rev.* **5**, 145-184.

Van Schmus W.R. and Wood J.A. (1967) A chemical-petrologic classification for the chondritic meteorites. *Geochim. Cosmochim. Acta* **31**, 747-765.

Weisberg M.K., McCoy T.J. and Krot A.N. (2006) Systematics and Evaluation of Meteorite Classification. In *Meteorites and the Early Solar System II* (eds. Lauretta D.S. and McSween Jr. H.Y.). The University of Arizona Press, Tucson, pp. 19-52. in collaboration with Lunar and Planetary Institute, Houston.

Whillans I.M. and Cassidy W.A. (1983) Catch a falling star: Meteorites and old ice. *Science* **222**, 55-57.

Yamaguchi A., Shiraishi K. and Harvey R. (2021) The discovery of meteorites near the Yamato Mountains: how the 1969 discoveries changed planetary science. *Meteorit. Planet. Sci.* **56**, 11–12.

Chapter 2 "*The effects of Antarctic alteration and sample heterogeneity on Sm-Nd and Lu-Hf systematics in H chondrites*" (Published in GCA 2021)

Chapter introduction

In this chapter, we first chemically and isotopically characterized various petrologic types of H chondrites (HCs) collected in Antarctica as well as from hot deserts. Samples were allocated from the Royal Belgian Institute of Natural Sciences (RBINS), Belgium, and the NIPR, Japan, and their mineral modal abundances, elemental abundances, and Sm-Nd and Lu-Hf systematics, were determined using both *in-situ* measurements and bulk wet chemistry. The effects of terrestrial alteration, especially in the Antarctic environment, on bulk HCs were extensively and systematically evaluated by comparison of the data obtained in this study with the results obtained for fresh falls.

Based on our results, Antarctic HCs commonly retain their original chemical and mineralogical compositions regardless of their degrees of weathering, although exceptions exist in the case of severe alteration. Once pristine nature was confirmed the heterogeneity observed in the elemental and isotopic compositions at bulk sample scale is discussed, based on the re-distribution scenario of REEs during thermal metamorphism in their parent bodies. Our interpretations contribute to the usefulness of Antarctic meteorites in the context of isotope studies and to the determination of well-constrained average Sm-Nd and Lu-Hf isotopic compositions for individual chondrite groups as well as robust values for the Chondritic Uniform Reservoir. However, following this chapter, two questions remained: (1) what is the detailed mechanism of Antarctic alteration by fluids that severely affected Asuka 09516? and (2) what is the Hf distribution among the constituent minerals in chondrites?

Contributions to this paper

This study was led by RM, and the AMGC and G-Time teams. All *in-situ* measurements, bulk analyses including elemental and isotopic measurements, interpretations, and writing were done by RM.

This chapter is published as:

Ryoga Maeda, Steven Goderis, Vinciane Debaille, Hamed Pourkhorsandi, Geneviève Hublet and Philippe Claeys (2021) The effects of Antarctic alteration and sample heterogeneity on Sm-Nd and Lu-Hf systematics in H chondrites. *Geochimica et Cosmochimica Acta* **305**, 106–129. DOI: 10.1016/j.gca.2021.05.005.

Supplementary data for this chapter can be found at: https://doi.org/10.1016/j.gca.2021.05.005.

Available online at www.sciencedirect.com

ScienceDirect

Geochimica et Cosmochimica Acta 305 (2021) 106–129

Geochimica et Cosmochimica Acta

www.elsevier.com/locate/gca

The effects of Antarctic alteration and sample heterogeneity on Sm-Nd and Lu-Hf systematics in H chondrites

Ryoga Maeda [a,b,*], Steven Goderis [a], Vinciane Debaille [b], Hamed Pourkhorsandi [b], Geneviève Hublet [b], Philippe Claeys [a]

[a] *Analytical-, Environmental-, and Geo-Chemistry, Vrije Universiteit Brussel, Pleinlaan 2, BE-1050 Brussels, Belgium*

[b] *Laboratoire G-Time, Universite´ libre de Bruxelles, CP 160/02, 50, Av. F.D. Roosevelt, BE-1050 Brussels, Belgium*

Received 26 September 2020; accepted in revised form 3 May 2021; Available online 12 May 2021

Abstract

Long-lived radioactive isotope systematics, such as Sm-Nd and Lu-Hf, are useful tools as important chronometers and tracers for chemical differentiation processes. Even though Antarctic meteorites include rare meteorites such as ungrouped meteorites, the effects of Antarctic alteration on the Sm-Nd and Lu-Hf systems in chondrites have not yet been evaluated in detail. Moreover, the heterogeneity of Sm-Nd and Lu-Hf data in bulk chondrites prevents the determination of precise average Sm-Nd and Lu-Hf values (*e.g.*, for individual chondrite groups). To examine the effects of Antarctic alteration and sample heterogeneity on the Sm-Nd and Lu-Hf isotope systematics, ten Antarctic H chondrites (HCs) and three HCs from hot deserts were characterized for their modal abundances, elemental abundances, and Sm-Nd and Lu-Hf isotopic compositions. Regardless of the classical weathering index for Antarctic meteorites and the normalized Rb abundance used as a chemical alteration indicator in this study, the modal and elemental abundances in Antarctic HCs appear to be in good agreement with those in non-Antarctic HCs. The Sm-Nd and Lu-Hf isotopic compositions of the characterized H chondrites fall within the range measured for both HC falls and for falls of other chondrite groups, except in the case of the most heavily altered sample. Consequently, the effects of Antarctic alteration processes on the Sm-Nd and Lu-Hf systematics in HCs appear to be limited, except in the case of Asuka 09516. The latter meteorite exhibits severe mineralogical and chemical alteration, with considerable losses of even the rare earth elements (REEs), which are considered relatively immobile. The $^{147}Sm/^{144}Nd$, $^{143}Nd/^{144}Nd$, $^{176}Lu/^{177}Hf$, and $^{176}Hf/^{177}Hf$ of bulk HCs correlate with their P/Mg and Y/Mg. Furthermore, the Lu-Hf ratios correlate strongly with their P/Ca and Y/Ca as well as their P/Mg and Y/Mg. Thus, the distribution of the elements between constituent minerals in ordinary chondrites (OCs) may control the heterogeneity observed for the bulk Sm-Nd and Lu-Hf data. In this context, the weight ratio of Ca-phosphates to Ca-pyroxene, or at least that of Ca-phosphates to silicates, may be a key factor leading to the observed elemental and isotopic variations. This observation indicates that the nugget effect of Ca-phosphates in OCs as the result of insufficient homogenization or terrestrial alteration leads to the heterogeneities displayed by the Sm-Nd and Lu-Hf data. Moreover, it also indicates that the use of equilibrated OCs for the determination of Sm-Nd and Lu-Hf data is affected more by sample heterogeneity, especially with respect to Ca-phosphates, than is the case for unequilibrated OCs, based on the re-distribution of REEs during thermal metamorphism on their parent

* Corresponding author at: Analytical-, Environmental-, and Geo-Chemistry, Vrije Universiteit Brussel, Pleinlaan 2, BE-1050 Brussels, Belgium.

E-mail address: Ryoga.Maeda@vub.be (R. Maeda).

https://doi.org/10.1016/j.gca.2021.05.005

bodies. This study demonstrates that Antarctic meteorites commonly preserve their original Sm-Nd and Lu-Hf isotopic compositions as much as chondrite falls, although exceptions are possible in the case of severe alteration. Similar to previous studies, we recommend the use of unequilibrated chondrites, for which the re-distribution of REEs is less extensive, for the determination of well-constrained average Sm-Nd and Lu-Hf isotopic compositions for individual chondrite groups as well as their robust Chondritic Uniform Reservoir values.

Keywords: Sm-Nd; Lu-Hf; H chondrite; Chondrite; Antarctic alteration; Sample heterogeneity; Rare earth element

1. INTRODUCTION

In 1969, a Japanese expedition found nine meteorites in Antarctica, which in 1973 led to the first systematic meteorite recovery expedition on the Southern continent (Yamaguchi *et al*., 2021), which was followed by expeditions until the present (*e.g.*, Goderis *et al*., 2021). Today, Antarctic meteorites constitute by number more than half of all known meteorites and include many rare varieties such as ungrouped chondrites and achondrites, shergottites-nakhlites-chassignites, and lunar meteorites (Meteorite Newsletter, NIPR; Antarctic Meteorite Newsletter, NASA). Hence, the Antarctic meteorite collection plays a pivotal role in understanding the history of the Solar System. Meteorites recovered after observed fall events are termed "falls"; those that cannot definitely be associated with observed falls, such as Antarctic meteorites, are named "finds." Finds are generally characterized by a much longer terrestrial residence time than falls (roughly of the order of tens of kyr: *e.g.*, Al-Kathiri *et al*., 2005). Many finds become weathered during this long residence time, and this process can take place relatively rapidly, particularly in temperate and tropical zones, as well as in hot deserts (Bland *et al*., 2006; Pourkhorsandi *et al.*, 2021). On average, Antarctic meteorites exhibit old terrestrial ages, on the order of hundreds of kyr (*e.g.*, Nishiizumi *et al.*, 1989), and these are better protected from terrestrial weathering while buried in the ice compared to finds collected from hot deserts (Whillans and Cassidy, 1983; Cassidy and Whillans, 1990). However, these meteorites were exposed to the extreme Antarctic climate during an extended period of time, leading to significant mineralogical and chemical alteration (*e.g.*, Koeberl and Cassidy, 1991; Bland *et al*., 2006).

Rare earth elements (REEs) are refractory lithophile elements that share similar chemical properties due to their electron configurations, implying that they should not have been fractionated by condensation and volatilization processes in the early Solar System or by metal-silicate separation during core formation in differentiated planets. Therefore, REEs are universally used for understanding specific planetary processes, such as silicate differentiation. The REEs include long-lived radioactive isotopes such as ^{147}Sm and ^{176}Lu, which decay to ^{143}Nd (half-life ~ 106 Gyr; Lugmair and Marti, 1978) and ^{176}Hf (half-life ~ 37.1 Gyr; Patchett *et al*., 2004), respectively. Their isotope systematics form the basis of important chronometers and tracers of chemical differentiation processes. The Sm-Nd and Lu-Hf isotope systematics of chondritic meteorites are particularly important as the Chondritic Uniform Reservoir (CHUR), which constitutes the average reference for undifferentiated planetary material in the Solar System (DePaolo and Wasserburg, 1976). Bouvier *et al.* (2008) determined the currently most precise CHUR values of the Sm-Nd and Lu-Hf data as well as the respective isochrons by utilizing unequilibrated carbonaceous, ordinary, and enstatite chondrites of petrologic types 1–3, mostly from falls, since scatter increases when using equilibrated chondrites. Consequently, the Sm-Nd and Lu-Hf CHUR values are regarded as the equivalents of the composition of Bulk Silicate Earth. As Bouvier *et al.* (2008) discussed, the heterogeneity of Sm-Nd and Lu-Hf data in bulk chondrites is one of the largest problems when willing to determine precise average values (i.e., CHUR values or an average of a group of chondrites), as the observed spread leads to larger uncertainties on the mean. For example, such heterogeneity occurs even on a duplicate analysis of Lu-Hf values in an H4 chondrite (^{176}Lu/^{177}Hf = 0.0301 ± 0.0002 and 0.0334 ± 0.0002, ^{176}Hf/^{177}Hf = 0.282444 ± 0.000009 and 0.282761 ± 0.000016 in Ochansk; Patchett *et al*., 2004).

Previous studies regarding the Sm-Nd and Lu-Hf systems in bulk chondrites have focused on falls to avoid any possible weathering occurring during long terrestrial residence (*e.g.*, Jacobsen and Wasserburg, 1984; Blichert-Toft and Albarède,

1997; Patchett *et al*., 2004; Bouvier *et al*., 2008). Terrestrial weathering can affect REEs, although they are often considered to be relatively immobile (*e.g.*, Shimizu *et al*., 1983; Crozaz *et al*., 2003; Al-Kathiri *et al*., 2005; Pourkhorsandi *et al*., 2017). The effects of Antarctic alteration on REE abundances were only examined for achondrites, and more specifically for eucrites (Shimizu *et al*., 1983; Mittlefehldt and Lindstrom, 1991; Crozaz *et al*., 2003). Today, few studies exist for chondrites (Tatsumoto *et al*., 1981; Nishikawa *et al*., 1990). In particular, the effects of Antarctic alteration on the Sm-Nd and Lu-Hf systems in bulk chondrites remain poorly understood.

As such, even though the Antarctic collection includes meteorite groups and clans found only in Antarctica, the effects of Antarctic alteration on the Sm-Nd and Lu-Hf systems in chondrites have not been assessed on a systematic way. Therefore, in this study, the results of the Sm-Nd and Lu-Hf isotope systematics in Antarctic HCs are examined in a methodical manner to evaluate weathering effects induced by extended residence times within the Antarctic ice. Moreover, this work also investigates the constituent minerals that control the heterogeneity of these isotope systems in bulk HC by combining the isotope ratios and elemental abundance ratios, which can aid in determining average Sm-Nd and Lu-Hf isotopic compositions with limited uncertainty (*i.e*., precise average Sm-Nd and Lu-Hf isotopic compositions) for individual chondrite groups.

2. EXPERIMENTAL

2.1. Samples

Ten Antarctic HCs and three HCs collected from hot deserts have been characterized for their modal abundances, and elemental and isotopic compositions. Four of the Antarctic HCs, Asuka (A) 09436 (H3), A 09387 (H4), A 09618 (H5), and A 09516 (H6), and the three hot desert HCs, northwest Africa (NWA) 6752 (H3), NWA 6771 (H4), and Sahara 97035 (H5), were provided by the Royal Belgian Institute of Natural Sciences (RBINS), Belgium. Meteorites A-881258 (H3.0), A-880941 (H3.3), Yamato (Y-)793574 (H3.5), Y-790461 (H3.7), Allan Hills (ALH) 78084 (H3.9), and Y-790960 (H7) were allocated by the National Institute of Polar Research (NIPR), Japan. Available information on the meteorites is listed in Table 1. To clarify any potential effect of terrestrial weathering on the inner portions of these chondrites - even if the sample visually appears fresh -, only the interior portions were used to avoid as much as possible fusion crust or sample fragments directly affected by terrestrial weathering.

Table 1

List of H chondrites analyzed in this study.

Meteorite	Section Number		Type[a, b]	Weathering[a, b] index	Shock stage	Sources
	PTS	Powder				
A-881258	71-A	82	H3.0	B	?	NIPR
A-880941	51-A	48	H3.3	A/B	S1-2*	NIPR
Y-793574	51-A	56	H3.5	?	?	NIPR
Y-790461	91-A	100	H3.7	B	S3*	NIPR
ALH 78084	81-A	89	H3.9	B/Ce	?	NIPR
A 09436	-	-	H3	C	?	RBINS
A 09387	-	-	H4	B/C	?	RBINS
A 09618	-	-	H5	C	?	RBINS
A 09516	-	-	H6	C	?	RBINS
Y-790960	63-A	62	H7	B	S3*	NIPR
NWA 6752	-	-	H3	W2	S1	RBINS
NWA 6771	-	-	H4	W1	S1	RBINS
Sahara 97035	-	-	H5	W2	S1	RBINS

*The shock stages are estimated from descriptions of the shock degree in Meteorite Newsletter, NIPR, based on Stöffler *et al*. (1991).

[a] Meteorite Newsletter, NIPR. [b] Antarctic Meteorite Newsletter, NASA.

2.2. In-situ measurement

Polished thick sections (PTSs) were prepared for all of the meteorites, except in the case of NWA 6752 (H3) when a polished thin section was used. These polished thick and thin sections were analyzed using a Bruker M4 Tornado micro-X-ray fluorescence (μXRF) scanner equipped with a Rh source and two XFlash 430 Silicon Drift detectors at the Vrije Universiteit Brussel (VUB), Belgium. The M4 set up is described in detail in Winter and Claeys (2017), and for each sample, elemental maps of 16 elements (Na, Mg, Al, Si, P, Cl, K, Ca, Ti, Cr, Mn, Fe, Ni, and Zn) were obtained. To produce the element maps, the 25 μm X-ray beam was applied under vacuum conditions (20 mbar), with 10 lm step size, 1 ms dwell time per point and maximized source energy settings (50 kV, 600 μA) without a source filter. Constituent minerals in the samples were identified from the elemental maps and their modal abundances were determined using the ImageJ image analysis program, while confirming the nature of these phases using a JEOL JSM-IT300 scanning electron microscope (SEM) equipped with an Oxford energy dispersive spectrometer (EDS) at the SURF research unit of VUB. Uncertainties for the modal abundances determined using this method are estimated to be better than 10% relative.

2.3. Bulk analyses

To examine the effects of sample heterogeneity as well as

Antarctic weathering on the Sm-Nd and Lu-Hf systems, a relatively small sample volume was preferred in this study to amplify sample heterogeneity caused by sampling. Approximately 200 mg of fragments of each sample were homogenized using an agate mortar and pestle dedicated to chondrites. No leaching to remove terrestrial materials was applied, even in the case of the three hot desert HCs. Approximately 100 mg of each powdered sample, which is the smallest possible amount to measure the elemental abundances and the isotopic compositions based on their detection limits, was dissolved in Teflon beakers using a mixture of ultrapure concentrated HF-HNO_3 (1:3) at 120 °C overnight. Because undigested residue remained in the beakers, possibly including acid-resistant phases such as oxides, the residues were then transferred into Teflon bombs for high-pressure dissolution, using the same acid mixture at 150 °C for 2 days. During the high-pressure dissolution, the supernatants remaining in the first Teflon beaker were evaporated. After the high-pressure dissolution, the solutions in the bombs were added to the Teflon beakers containing the residues of the supernatants. Following evaporation, the residues were dissolved in concentrated HCl and evaporated again. After re-dissolution in 1.5 M HCl with a trace amount of concentrated HF, a 2% aliquot of each solution was taken for the determination of major and trace elemental abundances. Similarly, a 5% aliquot of each solution was spiked with mixed ^{148}Nd-^{150}Sm and ^{176}Lu-^{179}Hf spikes. The spiked aliquots were heated on a hotplate for at least 1 day for spike-sample equilibration.

The REEs and Hf were separated from the main fraction by cation exchange chromatography using 2 mL of AG50W-X8 resin (100–200 mesh for the spiked aliquots, 200–400 mesh for the unspiked aliquots). The Hf cut was collected first during the loading of the sample and the following rinsing step using 1.5 M HCl with a trace amount of concentrated HF, while the REE cut was subsequently collected using 6 M HCl. The REE cuts were loaded onto a column with 2 mL of HDEHP resin to separate Nd for both the unspiked and spiked aliquots, and Sm and Lu for the spiked aliquots. The Hf cuts were further purified from Fe by anion exchange chromatography in 6 M HCl using 2 mL of AG1X8 resin (100–200 mesh for the spiked aliquots, 200–400 mesh for the unspiked aliquots), and the remaining matrix, especially Ti, was removed on 2 mL of Eichrom LN-Spec resin using 6 M HCl with a trace amount of H_2O_2. Finally, Hf was collected in 4 M HF. The yields of Nd, Sm, Lu, and Hf are estimated to be better than 90%, 95%, 95%, and 90% respectively, for both unspiked and spiked aliquots (Debaille *et al*., 2007). Total procedural blanks were determined to be 26 pg and 10 pg for Nd and Sm, respectively, and 4.5 pg and 20 pg for Lu and Hf, respectively. No blank correction was applied due to these negligible blank levels, even on the spiked aliquots (the blank-to-sample rations of more than 1%) because they represent insignificant contributions. The chemical procedures outlined here were performed at the Université libre de Bruxelles (ULB), Belgium, and are based on procedures described in detail in Armytage *et al*. (2018) and Debaille *et al*. (2007, 2017). Reference basalt BHVO-2 of the United States Geological Survey was subjected to the same procedures and measured in duplicate to validate the analytical accuracy and reproducibility during the following measurements using inductively coupled plasma-optical emission spectrometry (ICP-OES), quadrupole-ICP-mass spectrometry (Q-ICP-MS), and multiple collector-ICP-MS (MC-ICPMS). Approximately 50 mg of BHVO-2 was weighed and prepared at similar concentrations for measurement to the chondrite samples for both unspiked and spiked aliquots. Samples A 09436 (H3) and A 09516 (H6) were also analyzed in duplicate. All duplicate analyses were carried out on different powder subsamples.

2.3.1. Measurements of major and trace elemental abundances using ICP-OES and Q-ICP-MS

The major elemental abundances (Na, Mg, Al, P, K, Ca, Ti, Cr, Mn, Fe, Co, and Ni) were determined using a Thermo Scientific iCAP 7000 Plus Series ICP-OES at ULB. Yttrium was used as the internal standard, and the dilution factors (DFs) for the meteorite samples and the reference basalt were set to be 15,000 and 10,000 respectively, using 5% HNO_3.

The trace elemental abundances (Cu, Zn, Rb, Sr, Y, Zr, Nb, Ba, REEs, Hf, Th, and U) were determined using an Agilent 7700 ICP-MS at ULB. Measurement solutions were prepared with 5% HNO_3 and all of the measured elements including the high field strength elements were analyzed in 5% HNO_3 without HF. For Q-ICP-MS analysis, In was used as the internal standard, and the DFs for the meteorite samples and the geological reference materials were set to be 2,000 and 6,000, respectively, in order to minimize the influence of non-spectral matrix effects (Ebihara *et al*., 2020). Although slight analyte loss has been observed during dissolution (Ebihara *et al*., 2020), no correction for such analyte loss was applied here. Individual single element standards of Ba, Ce, Pr, and Nd were used to correct isobaric interferences from their oxide molecules. The results for the

Table 2

Elemental abundances and isotopic compositions in BHVO-2 (ID: isotope dilution, n.a.: not analyzed).

	This work		Preferred values[a-c]
(%)			
Na	1.79 ± 0.00	1.59 ± 0.02	1.646 ± 0.036
Mg	4.74 ± 0.03	4.44 ± 0.02	4.376 ± 0.025
Al	7.79 ± 0.05	6.87 ± 0.03	7.113 ± 0.032
P	0.115 ± 0.002	0.114 ± 0.003	0.1172 ± 0.0022
K	0.439 ± 0.005	0.416 ± 0.001	0.4259 ± 0.0031
Ca	8.15 ± 0.02	7.66 ± 0.03	8.148 ± 0.043
Ti	1.68 ± 0.01	1.57 ± 0.00	1.637 ± 0.011
Cr	0.0310 ± 0.0008	0.0335 ± 0.0004	0.02872 ± 0.00031
Mn	0.129 ± 0.002	0.130 ± 0.002	0.1309 ± 0.0015
Fe	8.73 ± 0.01	8.30 ± 0.01	8.666 ± 0.063
(ppm)			
Ni	127 ± 31	127 ± 4	119.8 ± 1.2
Co	80.8 ± 1.7	76.5 ± 1.9	44.89 ± 0.32
Cu	123 ± 1	119 ± 1	129.3 ± 1.4
Zn	97.9 ± 0.5	123 ± 1	103.9 ± 1.0
Rb	9.91 ± 0.10	8.24 ± 0.19	9.261 ± 0.096
Sr	370 ± 2	354 ± 5	394.1 ± 1.7
Y	25.7 ± 0.1	24.3 ± 0.2	25.91 ± 0.28
Zr	165 ± 1	157 ± 1	171.2 ± 1.3
Nb	16.9 ± 0.1	16.4 ± 0.1	18.10 ± 0.20
Ba	126 ± 1	121 ± 2	130.9 ± 1.0
La	15.7 ± 0.2	15.2 ± 0.2	15.20 ± 0.08
Ce	37.7 ± 0.4	36.5 ± 0.5	37.53 ± 0.19
Pr	5.20 ± 0.03	5.08 ± 0.08	5.339 ± 0.028
Nd	24.7 ± 0.2	23.7 ± 0.4	24.27 ± 0.25
Sm	6.01 ± 0.13	5.75 ± 0.1	6.023 ± 0.057
Eu	2.02 ± 0.03	1.98 ± 0.03	2.043 ± 0.012
Gd	6.47 ± 0.11	6.18 ± 0.12	6.207 ± 0.038
Tb	0.914 ± 0.012	0.876 ± 0.020	0.9392 ± 0.0053
Dy	5.29 ± 0.05	5.11 ± 0.08	5.280 ± 0.028
Ho	0.980 ± 0.015	0.940 ± 0.020	0.9887 ± 0.0053
Er	2.57 ± 0.03	2.43 ± 0.04	2.511 ± 0.014
Tm	0.335 ± 0.004	0.315 ± 0.012	0.3349 ± 0.0031
Yb	2.00 ± 0.06	1.93 ± 0.01	1.994 ± 0.027
Lu	0.278 ± 0.005	0.256 ± 0.008	0.2754 ± 0.0024
Hf	4.40 ± 0.04	4.06 ± 0.12	4.470 ± 0.025
Th	1.38 ± 0.06	1.14 ± 0.05	1.224 ± 0.016
U	0.412 ± 0.007	0.377 ± 0.012	0.412 ± 0.035
Nd (ID)	n.a.	22.5 ± 0.1	24.27 ± 0.18
Sm (ID)		5.63 ± 0.03	6.023 ± 0.038
Lu (ID)		0.249 ± 0.001	0.2754 ± 0.0018
Hf (ID)		4.04 ± 0.02	4.470 ± 0.020
$^{147}Sm/^{144}Nd$	n.a.	0.1515 ± 0.0011	0.1501 ± 0.0010
$^{143}Nd/^{144}Nd$	0.512965 ± 0.000008 0.512961 ± 0.000007	0.512971 ± 0.000008 0.512988 ± 0.000007	0.512984 ± 0.000011
$(^{143}Nd/^{144}Nd)_{mean}$	0.512971 ± 0.000012 (n = 4)		
$^{176}Lu/^{177}Hf$	n.a.	0.0088 ± 0.0001	0.00878 ± 0.00006
$^{176}Hf/^{177}Hf$	0.283104 ± 0.000010 0.283103 ± 0.000009	0.283102 ± 0.000014 (n = 8)*	0.283105 ± 0.000011
$(^{176}Hf/^{177}Hf)_{mean}$	0.283103 ± 0.000011 (n = 10)		

The uncertainties of elemental abundances (1SD), $^{143}Nd/^{144}Nd$, and $^{176}Hf/^{177}Hf$ (2SE) reflect internal reproducibilities during the measurements by ICP-OES, Q-ICP-MS, and MC-ICP-MS. The uncertainties of the elemental abundances (ID), $^{147}Sm/^{144}Nd$, and $^{176}Lu/^{177}Hf$ (2SE) reflect the maximum uncertainties due to spike calibrations (see Section 2.3.2).

* The uncertainty of the $^{176}Hf/^{177}Hf$ value (2SE) reflects external reproducibilities during the measurements of MC-ICP-MS.

[a] Jochum *et al.* (2016) for elemental abundances including those determined by isotope dilution, $^{147}Sm/^{144}Nd$, and $^{176}Lu/^{177}Hf$. [b] Weis *et al.* (2006) for $^{143}Nd/^{144}Nd$. [c] Weis *et al.* (2007) for $^{176}Hf/^{177}Hf$.

elemental abundances of BHVO-2 (n=2) are shown in Table 2, together with their preferred values (Jochum *et al*., 2016).

2.3.2. Isotope ratio measurement using MC-ICP-MS

All of the unspiked and spiked cuts were analyzed in 0.05 M HNO_3 (with 0.05 M HF for the Hf cuts) using the Nu instruments MC-ICP-MS Nu-Plasma Ⅱ equipped with an Aridus Ⅱ desolvating nebulizer at ULB. For isotope measurements of Nd, the unspiked Nd cuts were diluted to 20 ppb. The isobaric interference of ^{144}Sm on ^{144}Nd was monitored on mass ^{147}Sm, but no Sm was detected. Measured Nd isotope ratios were normalized to ^{146}Nd/^{144}Nd = 0.7219 using an exponential law following Debaille *et al*. (2007) to correct for instrumental mass fractionation. Measurements of the meteorite samples and BHVO-2 were bracketed by the measurement of a 20 ppb Rennes in-house Nd standard. The measured ^{143}Nd/^{144}Nd values of the standard were re-calculated to the accepted ^{143}Nd/^{144}Nd value of the Rennes in-house Nd standard (0.511961; Chauvel and Blichert-Toft, 2001). For isotope measurements of Hf, the unspiked Hf cuts were prepared at 5 ppb. Isobaric interferences for Hf from Yb, Lu, and W were monitored on masses ^{172}Yb, ^{175}Lu, and ^{182}W, respectively. No detectable Yb, Lu, or W were found in the unspiked Hf cuts. Measured Hf isotope ratios were normalized to ^{179}Hf/^{177}Hf = 0.7325 using the exponential law to correct for instrumental mass fractionation. A 5 ppb JMC-475 Hf standard was used to bracket each sample during the runs. The measured ^{176}Hf/^{177}Hf values of the Hf standard were re-calculated to the accepted ^{176}Hf/^{177}Hf value of the JMC-475 Hf standard (0.282163; Blichert-Toft *et al*., 1997). Internal reproducibilities of Nd and Hf are better than 32 ppm and 31 ppm for all standards, respectively. The means of ^{143}Nd/^{144}Nd values and ^{176}Hf/^{177}Hf values in BHVO-2 are 0.512971 ± 0.000012 (2SE, n = 4) and 0.283102 ± 0.000011 (2SE, n = 10), as shown in Table 2. These values overlap within uncertainty with published reference values (0.512984 ± 0.000011; Weis *et al*., 2006 and 0.283105 ± 0.000011; Weis *et al*., 2007, respectively).

For spiked cuts, the mass fractionation for each element was corrected using an exponential law followed by spike stripping using an iterative method (Debaille *et al*., 2007). Comparing to standard solutions, the total amounts of Nd, Sm, Lu, and Hf in the spiked cuts, *i.e.*, spiked + natural Nd, correspond to 6 ng, 2 ng, 0.20 ng, and 1.5 ng, respectively, which are 45 (Lu) to 230 (Nd) times more than the blank values. Hence, no blank correction was applied on spiked measurements. The same isotopes as in unspiked Nd and Hf analyses were monitored to check for isobaric interferences during spiked Nd and Hf analyses. No detectable contributions of these isotopes were observed in the spiked Nd and Hf cuts. During Sm measurement, ^{147}Sm, ^{150}Sm, ^{152}Sm, and ^{154}Sm were measured. Here, ^{150}Sm is included due to the use of the ^{150}Sm enriched spike despite the isobaric interference by ^{150}Nd. The presence of Nd and Gd in the Sm cuts was monitored on masses ^{146}Nd and ^{156}Gd, and the presence of Gd was corrected mathematically. Even though a trace of Nd was observed in the Sm cuts, the contribution was considered negligible. The isobaric interference of ^{176}Hf was monitored on mass ^{177}Hf during Lu analysis, but no Hf was detected in the Lu cuts. Because Lu possesses only two stable isotopes, a mass fractionation correction for Lu must be applied, for example by using Yb (Blichert-Toft *et al*., 1997). The uncertainties on the Nd, Sm, Lu, and Hf concentrations are dominated by the uncertainty of the spike calibration, which is estimated to be better than 0.5% (2SE). Therefore, the uncertainties on the concentrations are estimated to be 0.5% as a maximum and are presented in Tables 2 and 4. The obtained ^{147}Sm/^{144}Nd and ^{176}Lu/^{177}Hf values for BHVO-2 are 0.1515 ± 0.0011 (2SE) and 0.0088 ± 0.0001 (2SE), shown in Table 2, which are in good agreement with their preferred values of 0.1501 ± 0.0010 and 0.00878 ± 0.00006, respectively (Jochum *et al*., 2016).

3. RESULTS

3.1. Modal abundances

Table 3 summarizes the modal abundances in all samples obtained using the μXRF, including the mean values of unequilibrated H chondrites (UHCs; n = 7) and equilibrated H chondrites (EHCs; n = 6), together with the published modal abundances of EHCs (Van Schmus, 1969; McSween *et al*., 1991). According to the mineral observation using SEM-EDS in this study, forsterite, silica, and a few accessory minerals (Table 3) can be found in a limited number of samples. Also, H chondrites generally contain ilmenite (0.2 wt.%: *e.g.*, McSween *et al*., 1991). However, the mapping using μXRF is not sufficiently quantitative and the minimum spot size (25 μm) used in this study is larger than the size of some mineral phases (*e.g.*, silica and ilmenite), which does not allow distinguishing forsterite from low-Ca pyroxene (especially enstatite), silica from feldspar, or ilmenite from chromite. Therefore, the modal abundances of low-Ca pyroxene, feldspar, and chromite obtained in this study may include the abundances of forsterite, silica, and ilmenite, respectively.

Table 3

Modal abundances in H chondrites: vol. % at left; wt.% at right (UHC: unequilibrated H chondrite, EHC: equilibrated H chondrite).

Name	A-881258		A-880941		Y-793574		Y-790461		ALH 78084		A 09436		A 09387		A 09618		A 09516		Y-790960	
Area (mm^2)	71.294		52.706		61.594		104.907		81.524		190.921		89.756		152.775		177.284		34.607	
Olivine	40.7	38.9	36.8	33.4	34.4	32.2	38.0	35.9	35.8	33.5	35.4	33.1	36.8	35.4	38.0	35.6	36.8	33.4	38.7	36.0
Low-Ca pyroxene*	30.7	27	24.1	20	27.4	24	26.8	23	29.7	26	32.8	28	29.2	26	30.6	26	30.8	26	29.0	25
Ca-pyroxene	1.15	1.1	6.26	5.6	7.88	7.2	5.53	5.1	5.51	5.0	4.52	4.1	4.86	4.6	2.26	2.1	3.94	3.5	5.02	4.6
Feldspar*	14.8	10.7	14.5	9.91	14.6	10.3	14.7	10.5	14.1	9.91	13.1	9.22	14.3	10.3	13.6	9.58	10.9	7.45	14.0	9.77
Kamacite	6.01	13	3.52	7.2	5.76	12	6.05	13	6.64	14	6.09	13	4.81	10	7.23	15	7.35	15	6.46	14
Taenite	1.59	3.49	8.85	18.5	3.49	7.51	2.67	5.82	2.86	6.17	3.15	6.76	2.91	6.44	2.06	4.45	4.40	9.19	2.59	5.54
Troilite	3.59	4.55	3.12	3.75	4.33	5.36	3.93	4.92	3.47	4.30	3.74	4.62	4.04	5.15	3.97	4.94	3.50	4.20	3.79	4.67
Chlorapatite	0.05	0.04	0.09	0.07	0.11	0.10	0.05	0.04	0.29	0.25	0.16	0.14	0.03	0.02	0.30	0.26	0.14	0.11	0.35	0.30
Merrillite	0.47	0.41	0.37	0.30	0.38	0.32	0.41	0.35	0.32	0.27	0.36	0.30	0.90	0.78	0.33	0.28	0.78	0.64	0.43	0.36
Total Ca-phosphates	0.52	0.45	0.46	0.38	0.49	0.41	0.46	0.39	0.61	0.51	0.52	0.44	0.93	0.80	0.63	0.53	0.92	0.75	0.78	0.66
Chromite*	0.59	0.74	0.97	1.2	1.05	1.3	0.81	1.0	0.72	0.89	0.60	0.74	0.77	0.97	0.79	0.98	0.63	0.76	0.28	0.35
Iron oxide	-		trace		trace		-		trace		trace		-		-		-		-	
Silica	-		-		-		trace		-		-		trace		-		-		-	
(Mg, Fe)-spinel	-		trace		-		trace		-		-		-		-		-		-	
Hibonite	-		-		-		trace		-		-		-		-		-		-	
(Zn, Fe)S	-		-		-		-		-		trace		trace		-		-		-	
Total	99.6		98.6		99.3		99.0		99.3		100.0		98.6		99.0		99.3		100.7	

(*continued on next page*)

Table 3 (*continued*)

Name	NWA 6752		NWA 6771		Sahara 97035		UHC mean (this study)		EHC mean (this study)		EHC mean (literature data; in wt. %)	
Area (mm^2)/ n / Ref.	496.441		94.315		100.041		n = 7		n = 6		Van Schmus (1969)	McSween *et al*. (1991), n = 25
Olivine	38.0	34.5	39.3	36.4	35.3	33.7	37.0 ± 1.9	34.5 ± 2.4	37.5 ± 1.5	35.1 ± 1.3	33 - 37	35.7 ± 1.5
Low-Ca pyroxene*	31.2	26	26.4	22	30.1	26	29.0 ± 2.8	25 ± 3	29.4 ± 1.7	25 ±2	23 - 27	26.3 ± 1.2
Ca-pyroxene	2.02	1.8	5.55	5.0	5.50	5.1	4.70 ± 2.19	4.3 ± 2.0	4.52 ± 1.31	4.1 ± 1.2	4 - 5	4.1 ± 0.2
Feldspar*	9.00	6.15	12.1	8.40	13.8	9.89	13.5 ± 1.9	9.52 ± 0.58	13.1 ± 1.4	9.24 ± 1.14	9 - 10	9.6 ± 0.2
Kamacite	7.30	15	7.21	15	6.88	15	5.91 ± 1.09	13 ± 3	6.65 ± 1.01	14 ± 2	15 - 17	18.2 ± 0.6
Taenite	4.54	9.48	2.88	6.13	1.51	3.32	3.88 ± 2.19	8.25 ± 4.64	2.72 ± 1.03	5.84 ± 2.10	2 - 3	
Troilite	4.88	5.86	3.95	4.85	4.06	5.14	3.86 ± 0.54	4.77 ± 0.47	3.89 ± 0.22	4.82 ± 0.37	5 - 6	5.5 ± 0.2
Chlorapatite	0.06	0.05	0.42	0.35	trace		0.12 ± 0.08	0.10 ± 0.07	0.21 ± 0.17	0.17 ± 0.14	-	-
Merrillite	0.14	0.12	0.41	0.34	0.89	0.76	0.35 ± 0.10	0.29 ± 0.08	0.62 ± 0.27	0.53 ± 0.24	-	-
Total Ca-phosphates	0.20	0.17	0.83	0.69	0.89	0.76	0.47 ± 0.12	0.39 ± 0.09	0.83 ± 0.12	0.70 ± 0.10	0.6	0.65 ± 0.03
Chromite*	0.83	0.99	0.80	0.98	0.48	0.60	0.79 ± 0.16	0.98 ± 0.20	0.63 ± 0.22	0.77 ± 0.27	0.5	0.76 ± 0.02
Iron oxide	trace		-		-							
Silica	-		-		-							
(Mg, Fe)-spinel	-		-		-							
Hibonite	-		-		-							
(Zn, Fe)S	-		-		-							
Total	98.0		98.9		98.5							

wt.% is calculated from vol. % using the following estimated mineral specific gravities and normalized to 100%: olivine (3.48), low-Ca pyroxene (3.2). Ca-pyroxene (3.4), feldspar (2.62), kamacite (7.9), taenite (8.01), troilite (4.61), chlorapatite (3.16), merrillite (3.12), chromite (4.6).

The uncertainties for the mean values from this study are 95% confidence interval, and those for McSween *et al*., (1991) are 2SE calculated from their data.

* The modal abundances of low-Ca pyroxene, feldspar, and chromite obtained in this study may include forsterite, silica, and ilmenite, respectively (see Section 3.1).

Table 4

Elemental abundances and isotopic compositions in H chondrites (UHC: unequilibrated H chondrite, EHC: equilibrated H chondrite, ID: isotope dilution, n.d.: not determined).

Name	A-881258	A-880941	Y-793574	Y-790461	ALH 78084
(%)					
Na	0.56 ± 0.03	0.54 ± 0.04	0.68 ± 0.04	0.61 ± 0.01	0.62 ± 0.03
Mg	14 ± 0	13 ± 0	15 ± 0	14 ± 0	14 ± 0
Al	0.99 ± 0.00	0.92 ± 0.00	1.1 ± 0.0	1.1 ± 0.0	1.0 ± 0.00
P	0.11 ± 0.00	0.11 ± 0.00	0.13 ± 0.00	0.12 ± 0.00	0.10 ± 0.00
K	0.065 ± 0.001	0.050 ± 0.001	0.071 ± 0.002	0.065 ± 0.002	0.065 ± 0.001
Ca	0.98 ± 0.00	0.94 ± 0.01	1.2 ± 0.0	1.0 ± 0.0	1.0 ± 0.0
Ti	0.057 ± 0.01	0.050 ± 0.002	0.061 ± 0.002	0.062 ± 0.001	0.055 ± 0.000
Cr	0.38 ± 0.00	0.34 ± 0.00	0.41 ± 0.00	0.40 ± 0.00	0.35 ± 0.00
Mn	0.23 ± 0.00	0.22 ± 0.00	0.25 ± 0.00	0.23 ± 0.00	0.23 ± 0.00
Fe	23 ± 1	22 ± 0	27 ± 0	23 ± 0	22 ± 0
Ni	1.6 ± 0.0	1.6 ± 0.0	1.6 ± 0.1	1.5 ± 0	1.5 ± 0.0
Co	0.064 ± 0.001	0.066 ± 0.000	0.085 ± 0.001	0.060 ± 0.000	0.065 ± 0.01
(ppm)					
Cu	88.0 ± 0.6	80.0 ± 1.6	78.0 ± 1.4	90.5 ± 1.8	75.2 ± 1.7
Zn	63.9 ± 0.8	52.1 ± 1.3	61.4 ± 0.9	61.2 ± 0.7	54.8 ± 1.3
Rb	2.45 ± 0.08	1.29 ± 0.05	2.29 ± 0.05	2.67 ± 0.07	2.26 ± 0.08
Sr	8.77 ± 0.13	8.76 ± 0.14	8.53 ± 0.14	9.42 ± 0.12	8.66 ± 0.23
Y	1.90 ± 0.02	1.97 ± 0.06	1.87 ± 0.04	1.98 ± 0.05	2.08 ± 0.05
Zr	4.78 ± 0.08	4.79 ± 0.10	4.69 ± 0.08	5.28 ± 0.09	5.31 ± 0.02
Nb	0.358 ± 0.014	0.356 ± 0.008	0.375 ± 0.007	0.370 ± 0.015	0.382 ± 0.008
Ba	3.19 ± 0.07	3.17 ± 0.07	3.06 ± 0.01	3.38 ± 0.02	3.18 ± 0.02
(ppb)					
La	299 ± 10	330 ± 8	324 ± 4	333 ± 10	317 ± 15
Ce	788 ± 19	833 ± 24	830 ± 21	850 ± 22	820 ± 40
Pr	116 ± 4	121 ± 8	119 ± 2	125 ± 4	113 ± 2
Nd	549 ± 19	602 ± 53	618 ± 14	581 ± 42	615 ± 60
Sm	177 ± 15	216 ± 12	181 ± 6	208 ± 12	188 ± 18
Eu	72.9 ± 3.4	73.8 ± 4.8	74.3 ± 3.0	76.6 ± 5.4	65.3 ± 4.8
Gd	257 ± 15	283 ± 17	292 ± 8	289 ± 19	285 ± 17
Tb	45.1 ± 2.7	47.2 ± 3.2	49.8 ± 0.9	46.9 ± 2.6	47.5 ± 2.5
Dy	324 ± 8	335 ± 11	337 ± 17	338 ± 20	365 ± 15
Ho	67.5 ± 3.0	75.0 ± 2.7	75.8 ± 1.5	74.3 ± 2.6	77.6 ± 2.3
Er	206 ± 3	215 ± 9	226 ± 7	232 ± 3	229 ± 4
Tm	30.2 ± 0.7	32.1 ± 1.7	34.6 ± 2.0	32.3 ± 1.4	31.5 ± 1.6
Yb	210 ± 12	210 ± 5	226 ± 8	211 ± 13	220 ± 9
Lu	30.1 ± 3.1	31.7 ± 4.3	34.3 ± 2.1	32.8 ± 2.7	30.0 ± 0.6
Hf	123 ± 9	135 ± 3	140 ± 10	147 ± 14	149 ± 7
Th	42.7 ± 1.4	38.1 ± 0.9	42.4 ± 0.6	43.0 ± 2.5	39.7 ± 1.9
U	11.4 ± 1.1	9.99 ± 0.64	12.4 ± 0.4	10.8 ± 0.5	12.0 ± 0.7

(*continued on next page*)

Table 4 (*continued*)

Name	A-881258	A-880941	Y-793574	Y-790461	ALH 78084
Nd (ID)	585 ± 3	609 ± 3	527 ± 3	604 ± 3	543 ± 3
Sm (ID)	190 ± 1	196 ± 1	172 ± 1	197 ± 1	178 ± 1
Lu (ID)	28.9 ± 0.1	29.7 ± 0.1	32.4 ± 0.2	29.2 ± 0.1	31.0 ± 0.2
Hf (ID)	123 ± 1	125 ± 1	152 ± 1	136 ± 1	140 ± 1
$^{147}Sm/^{144}Nd$	0.1958 ± 0.0014	0.1949 ± 0.0014	0.1977 ± 0.0014	0.1971 ± 0.0014	0.1986 ± 0.0014
$^{143}Nd/^{144}Nd$	0.512604 ± 0.000007	0.512570 ± 0.000014	0.512712 ± 0.000009	0.512585 ± 0.000008	0.512619 ± 0.000008
$^{176}Lu/^{177}Hf$	0.0336 ± 0.0002	0.0338 ± 0.0002	0.0304 ± 0.0002	0.0306 ± 0.0002	0.0315 ± 0.0002
$^{176}Hf/^{177}Hf$	0.282825 ± 0.000015	0.282868 ± 0.000016	0.282825 ± 0.000038	0.282689 ± 0.000019	0.282702 ± 0.000013

Name	A 09436-1	A 09436-2	A 09387	A 09618	A 09516-1
(%)					
Na	0.65 ± 0.02	0.59 ± 0.02	0.57 ± 0.02	0.59 ± 0.02	0.50 ± 0.04
Mg	15 ± 0	14 ± 0	13 ± 0	13 ± 0	12 ± 0
Al	1.1 ± 0.0	1.1 ± 0.0	1.0 ± 0.0	0.88 ± 0.00	1.1 ± 0.0
P	0.12 ± 0.00	0.11 ± 0.00	0.099 ± 0.003	0.097 ± 0.001	0.067 ± 0.003
K	0.070 ± 0.001	0.068 ± 0.000	0.070 ± 0.002	0.068 ± 0.001	0.054 ± 0.001
Ca	1.2 ± 0.0	1.1 ± 0.0	1.2 ± 0.0	1.1 ± 0.0	0.94 ± 0.00
Ti	0.064 ± 0.000	0.059 ± 0.002	0.057 ± 0.003	0.057 ± 0.002	0.053 ± 0.003
Cr	0.42 ± 0.00	0.39 ± 0.00	0.36 ± 0.00	0.37 ± 0.00	0.34 ± 0.00
Mn	0.24 ± 0.00	0.23 ± 0.00	0.23 ± 0.00	0.23 ± 0.00	0.19 ± 0.00
Fe	23 ± 0	25 ± 0	22 ± 0.0	24 ± 0	27 ± 0
Ni	1.4 ± 0.0	1.6 ± 0.0	1.3 ± 0.0	1.5 ± 0.0	1.9 ± 0.0
Co	0.065 ± 0.001	0.078 ± 0.001	0.063 ± 0.000	0.075 ± 0.001	0.097 ± 0.001
(ppm)					
Cu	87.9 ± 0.6	92.6 ± 1.1	77.2 ± 0.6	79.0 ± 0.00	80.0 ± 1.1
Zn	53.8 ± 0.5	56.7 ± 0.5	61.8 ± 0.7	48.4 ± 0.1	41.3 ± 0.6
Rb	2.05 ± 0.04	1.99 ± 0.05	3.03 ± 0.07	1.94 ± 0.02	0.717 ± 0.031
Sr	9.43 ± 0.11	9.25 ± 0.10	8.60 ± 0.11	8.06 ± 0.02	6.97 ± 0.17
Y	1.80 ± 0.04	1.80 ± 0.03	1.87 ± 0.04	1.67 ± 0.02	1.09 ± 0.02
Zr	5.05 ± 0.03	5.13 ± 0.05	5.05 ± 0.05	4.42 ± 0.01	4.23 ± 0.05
Nb	0.390 ± 0.006	0.382 ± 0.005	0.356 ± 0.003	0.356 ± 0.003	0.271 ± 0.006
Ba	3.56 ± 0.12	3.53 ±0.07	3.12 ± 0.06	2.90 ± 0.03	2.56 ± 0.08
(ppb)					
La	349 ± 8	351 ± 6	297 ± 2	278 ± 4	211 ± 5
Ce	824 ± 9	833 ± 8	767 ± 13	707 ± 8	493 ± 11
Pr	124 ± 3	121 ± 2	110 ± 4	104 ± 2	74.2 ± 1.4
Nd	626 ± 17	608 ± 23	599 ± 9	537 ± 9	380 ± 11
Sm	198 ± 9	203 ± 4	187 ± 4	168 ± 5	109 ± 4
Eu	79.7 ± 1.4	73.7 ± 3.3	72.8 ± 1.0	67.6 ± 1.1	56.4 ± 1.8
Gd	271 ± 11	274 ± 7	271 ± 10	242 ± 8	156 ± 2
Tb	48.5 ± 0.8	47.8 ± 1.0	48.6 ± 1.0	43.9 ± 0.3	28.8 ± 1.0
Dy	329 ± 9	331 ± 5	333 ± 14	294 ± 8	185 ± 10

(*continued on next page*)

Table 4 (*continued*)

Name	A 09436-1	A 09436-2	A 09387	A 09618	A 09516-1
Ho	73.1 ± 2.2	71.9 ± 1.5	74.4 ± 1.1	66.2 ± 0.4	45.0 ± 1.2
Er	213 ± 6	217 ± 8	216 ± 2	200 ± 8	134 ± 2
Tm	32.1 ± 0.7	34.0 ± 1.4	34.0 ± 2.0	30.3 ± 0.2	20.8 ± 0.8
Yb	218 ± 7	218 ± 6	221 ± 2	197 ± 4	138 ± 4
Lu	33.8 ± 1.7	36.1 ± 0.9	34.7 ± 1.0	30.6 ± 0.7	23.8 ± 1.2
Hf	152 ± 5	159 ± 2	155 ± 9	136 ± 4	134 ± 3
Th	46.6 ± 0.7	46.4 ± 1.4	44.6 ± 0.9	40.0 ± 3.5	47.3 ± 1.5
U	15.7 ± 1.6	15.5 ± 1.4	10.5 ± 0.3	13.0 ± 0.9	13.8 ± 0.5
Nd (ID)	620 ± 3	577 ± 3	574 ± 3	568 ± 3	357 ± 2
Sm (ID)	197 ± 1	187 ± 1	190 ± 1	187 ± 1	112 ± 1
Lu (ID)	30.1 ± 0.2	32.4 ± 0.2	33.8 ± 0.2	30.7 ± 0.2	22.9 ± 0.1
Hf (ID)	149 ± 1	151 ± 1	158 ± 1	147 ± 1	122 ± 1
$^{147}Sm/^{144}Nd$	0.1926 ± 0.0014	0.1971 ± 0.0014	0.1998 ± 0.0014	0.1988 ± 0.0014	0.1900 ± 0.0013
$^{143}Nd/^{144}Nd$	0.512596 ± 0.000010	0.512572 ± 0.000008	0.512679 ± 0.000007	0.512747 ± 0.000008	0.512767 ± 0.000008
$^{176}Lu/^{177}Hf$	0.0288 ± 0.0002	0.0305 ± 0.0002	0.0305 ± 0.0002	0.0299 ± 0.0002	0.0268 ± 0.0002
$^{176}Hf/^{177}Hf$	0.282495 ± 0.000054	0.282520 ± 0.000030	0.282645 ± 0.000013	0.282675 ± 0.000008	n.d.

Name	A 09516-2	Y-790960	NWA 6752	NWA 6771	Sahara 97035
(%)					
Na	0.46 ± 0.02	0.64 ± 0.03	0.55 ± 0.03	0.51 ± 0.02	0.59 ± 0.01
Mg	12 ± 0	15 ± 0	14 ± 0	13 ± 0	12 ± 0
Al	0.84 ± 0.00	1.0 ± 0.0	1.1 ± 0.0	1.1 ± 0.0	0.56 ± 0.00
P	0.070 ± 0.003	0.10 ± 0.00	0.11 ± 0.00	0.11 ± 0.00	0.10 ± 0.00
K	0.051 ± 0.000	0.071 ± 0.001	0.071 ± 0.001	0.080 ± 0.001	0.091 ± 0.002
Ca	0.82 ± 0.01	0.99 ± 0.01	1.2 ± 0.0	1.4 ± 0.0	1.4 ± 0.0
Ti	0.049 ± 0.002	0.058 ± 0.002	0.061 ± 0.002	0.062 ± 0.000	0.059 ± 0.002
Cr	0.32 ± 0.00	0.42 ± 0.00	0.39 ± 0.00	0.35 ± 0.00	0.37 ± 0.00
Mn	0.20 ± 0.00	0.24 ± 0.00	0.24 ± 0.00	0.22 ± 0.00	0.22 ± 0.00
Fe	23 ± 0	26 ± 0	26 ± 0	24 ± 0	23 ± 0
Ni	1.7 ± 0.0	1.7 ± 0.1	1.5 ± 0.0	1.4 ± 0.0	1.1 ± 0.0
Co	0.072 ± 0.001	0.076 ± 0.000	0.081 ± 0.001	0.077 ± 0.000	0.060 ± 0.001
(ppm)					
Cu	81.0 ± 1.7	84.5 ± 1.9	78.1 ± 1.2	78.6 ± 0.7	75.2 ± 1.4
Zn	54.0 ± 1.0	64.6 ± 1.1	51.3 ± 0.9	48.2 ± 0.6	34.3 ± 0.5
Rb	0.840 ± 0.040	2.61 ± 0.18	2.07 ± 0.06	2.49 ± 0.04	2.28 ± 0.06
Sr	7.99 ± 0.25	8.72 ± 0.15	21.8 ± 0.3	16.9 ± 0.2	70.9 ± 1.2
Y	1.32 ± 0.03	1.86 ± 0.04	1.80 ± 0.03	2.09 ± 0.05	1.82 ± 0.03
Zr	4.61 ± 0.06	4.63 ± 0.15	5.08 ± 0.10	9.22 ± 0.14	4.90 ± 0.08
Nb	0.324 ± 0.005	0.364 ± 0.017	0.381 ± 0.017	0.568 ± 0.010	0.409 ± 0.004
Ba	3.41 ± 0.18	3.07 ± 0.20	166 ± 3	17.8 ± 0.3	29.5 ± 0.5
(ppb)					
La	265 ± 6	307 ± 15	390 ± 8	840 ± 17	609 ± 12

(*continued on next page*)

Table 4 (*continued*)

Name	A 09516-2	Y-790960	NWA 6752	NWA 6771	Sahara 97035
Ce	614 ± 13	777 ± 20	905 ± 17	(1.824 ± 0.03) × 10^3	(1.63 ± 0.02) × 10^3
Pr	85.0 ± 1.0	115 ± 10	131 ± 6	231 ± 4	179 ± 3
Nd	406 ± 28	558 ± 27	631 ± 18	(1.04 ± 0.03) × 10^3	853 ± 17
Sm	122 ± 9	183 ± 20	190 ± 4	265 ± 10	227 ± 7
Eu	59.5 ± 5.1	67.3 ± 4.3	61.0 ± 3.2	86.8 ± 3.2	78.3 ± 3.1
Gd	187 ± 11	257 ± 6	274 ± 5	344 ± 16	317 ± 3
Tb	31.7 ± 1.2	46.7 ± 2.3	49.3 ± 1.0	57.4 ± 0.5	52.5 ± 0.8
Dy	220 ± 11	306 ± 5	329 ± 5	388 ± 14	333 ± 6
Ho	46.8 ± 2.3	66.9 ± 2.4	71.3 ± 2.9	82.1 ± 3.5	71.8 ± 1.1
Er	151 ± 7	208 ± 14	215 ± 9	247 ± 5	220 ± 5
Tm	23.5 ± 1.7	31.1 ± 1.1	33.3 ± 0.8	37.0 ± 0.5	33.5 ± 1.4
Yb	156 ± 7	205 ± 6	215 ± 4	247 ± 9	217 ± 5
Lu	22.4 ± 2.6	29.7 ± 0.6	33.6 ± 0.6	37.8 ± 1.3	33.8 ± 1.0
Hf	136 ± 2	135 ± 2	151 ± 2	269 ± 5	147 ± 2
Th	39.8 ± 2.3	33.4 ± 1.0	55.2 ± 0.9	194 ± 2	128 ± 2
U	13.2 ± 0.4	8.47 ± 0.28	75.7 ± 1.5	84.5 ± 0.7	105 ± 2
Nd (ID)	340 ± 2	450 ± 2	639 ± 3	1073 ± 5	865 ± 4
Sm (ID)	107 ± 1	148 ± 1	197 ± 1	280 ± 1	242 ± 1
Lu (ID)	22.3 ± 0.1	28.9 ± 0.1	26.0 ± 0.1	36.2 ± 0.2	34.8 ± 0.2
Hf (ID)	125 ± 1	126 ± 1	133 ± 1	274 ± 1	154 ± 1
$^{147}Sm/^{144}Nd$	0.1910 ± 0.0014	0.1987 ± 0.0014	0.1866 ± 0.0013	0.1578 ± 0.0011	0.1694 ± 0.0012
$^{143}Nd/^{144}Nd$	0.512647 ± 0.000010	0.512648 ± 0.000008	0.512540 ± 0.000008	0.512312 ± 0.000007	0.512525 ± 0.000008
$^{176}Lu/^{177}Hf$	0.0254 ± 0.0002	0.0327 ± 0.0002	0.0278 ± 0.0002	0.0188 ± 0.0001	0.0321 ± 0.0002
$^{176}Hf/^{177}Hf$	0.282174 ± 0.000013	0.282756 ± 0.000025	0.282431 ± 0.000085	0.282444 ± 0.000012	0.282691 ± 0.000011

Name	Antarctic UHC mean (n = 7)	Antarctic EHC mean* (n = 3)	Antarctic HC mean* (n = 10)	Hot desert HC mean (n = 3)	Non-Antarctic HC mean (literature data)[a-f]
(%)					
Na	0.61 ± 0.05	0.60 ± 0.9	0.60 ± 0.03	0.55 ± 0.11	0.638 ± 0.012
Mg	14 ± 1	14 ± 2	14 ± 0	13 ± 2	14.0 ± 0.1
Al	1.0 ± 0.1	0.98 ± 0.23	1.0 ± 0.1	0.90 ± 0.74	1.13 ± 0.03
P	0.11 ± 0.01	0.10 ± 0.01	0.11 ± 0.01	0.11 ± 0.01	0.118 ± 0.005
K	0.065 ± 0.006	0.070 ± 0.005	0.066 ± 0.004	0.081 ± 0.024	0.0747 ± 0.0033
Ca	1.1 ± 0.1	1.1 ± 0.3	1.1 ± 0.1	1.3 ± 0.3	1.24 ± 0.03
Ti	0.058 ± 0.004	0.057 ± 0.002	0.058 ± 0.003	0.060 ± 0.004	0.0719 ± 0.0024
Cr	0.38 ± 0.03	0.38 ± 0.08	0.38 ± 0.02	0.37 ± 0.04	0.356 ± 0.008
Mn	0.23 ± 0.01	0.23 ± 0.02	0.23 ± 0.01	0.23 ± 0.03	0.240 ± 0.006
Fe	24 ± 2	24 ± 6	24 ± 1	24 ± 3	27.5 ± 0.3
Ni	1.5 ± 0.1	1.5 ± 0.6	1.5 ± 0.1	1.4 ± 0.5	1.74 ± 0.04
Co	0.069 ± 0.008	0.071 ± 0.018	0.070 ± 0.006	0.073 ± 0.028	0.0810
(ppm)					
Cu	84.6 ± 6.3	80.2 ± 9.5	83.3 ± 4.4	77.3 ± 4.5	82

(*continued on next page*)

Table 4 (*continued*)

Name	Antarctic UHC mean (n = 7)	Antarctic EHC mean* (n = 3)	Antarctic HC mean* (n = 10)	Hot desert HC mean (n = 3)	Non-Antarctic HC mean (literature data)[a-f]
Zn	57.7 ± 4.1	58.3 ± 21.6	57.9 ± 3.9	44.6 ± 22.5	47
Rb	2.14 ± 0.41	2.53 ± 1.37	2.26 ± 0.34	2.28 ± 0.52	2.9
Sr	8.97 ± 0.35	8.46 ± 0.87	8.82 ± 0.31	36.5 ± 74.2	10
Y	1.92 ± 0.10	1.80 ± 0.28	1.88 ± 0.08	1.90 ± 0.40	2.20
Zr	5.01 ± 0.23	4.70 ± 0.80	4.91 ± 0.21	6.40 ± 6.06	6.30
Nb	0.373 ± 0.012	0.359 ± 0.012	0.369 ± 0.009	0.453 ± 0.250	0.360
Ba	3.30 ± 0.18	3.03 ± 0.29	3.22 ± 0.15	71.2 ± 205.3	4.2
(ppb)					
La	329 ± 17	294 ± 36	319 ± 17	613 ± 559	309 ± 26
Ce	825 ± 17	750 ± 94	803 ± 31	(1.45 ± 1.20) × 10^3	816 ± 68
Pr	120 ± 4	109 ± 14	117 ± 5	180 ± 124	
Nd	600 ± 25	565 ± 78	589 ± 22	841 ± 509	588 ± 37
Sm	196 ± 13	179 ± 24	191 ± 11	227 ± 93	189 ± 11
Eu	73.7 ± 4.1	69.3 ± 7.8	72.4 ± 3.2	75.4 ± 32.6	71.5 ± 2.4
Gd	279 ± 11	257 ± 36	272 ± 11	312 ± 87	255 ± 14
Tb	47.6 ± 1.4	46.4 ± 5.9	47.2 ± 1.2	53.1 ± 10.1	
Dy	337 ± 12	311 ± 49	329 ± 14	350 ± 83	320 ± 17
Ho	73.6 ± 3.0	69.2 ± 11.3	72.3 ± 2.9	75.1 ± 15.0	
Er	220 ± 9	208 ± 19	216 ± 7	227 ± 43	210 ± 11
Tm	32.4 ± 1.4	31.8 ± 4.8	32.2 ± 1.1	34.6 ± 5.2	
Yb	216 ± 6	208 ± 30	214 ± 6	226 ± 45	207 ± 11
Lu	32.7 ± 2.1	31.7 ± 6.6	32.4 ± 1.6	35.1 ± 5.9	32.0 ± 1.5
Hf	144 ± 11	142 ± 28	143 ± 8	189 ± 173	180
Th	42.7 ± 2.9	39.3 ± 13.9	41.7 ± 2.9	126 ± 172	41.5 ± 17.4
U	12.5 ± 2.1	10.6 ± 5.6	12.0 ± 1.7	88.2 ± 36.8	11.8 ± 6.1
Nd (ID)	581 ± 32	531 ± 174	566 ± 36	859 ± 539	613 ± 36
Sm (ID)	188 ± 9	175 ± 58	184 ± 11	240 ± 103	198 ± 12
Lu (ID)	30.5 ± 1.3	31.1 ± 6.2	30.7 ± 1.2	32.3 ± 13.7	33.0 ± 0.8
Hf (ID)	140 ± 11	144 ± 41	141 ± 9	187 ± 189	143 ± 4
$^{147}Sm/^{144}Nd$	0.1963 ± 0.0019	0.1991 ± 0.0016	0.1971 ± 0.0016	0.1713 ± 0.0360	0.1953 ± 0.0006
$^{143}Nd/^{144}Nd$	0.512608 ± 0.000045	0.512691 ± 0.000126	0.512633 ± 0.000044	0.512459 ± 0.000317	0.512623 ± 0.000009
$^{176}Lu/^{177}Hf$	0.0313 ± 0.0017	0.0310 ± 0.0038	0.0312 ± 0.0012	0.0262 ± 0.0168	0.0328 ± 0.0007
$^{176}Hf/^{177}Hf$	0.282703 ± 0.000138	0.282692 ± 0.000143	0.282700 ± 0.000090	0.282522 ± 0.000364	0.282730 ± 0.000060

The uncertainties for each sample reflect the same as those in Table 2 and the number of digits is based on the reproducibility of the reference material. The uncertainties for the mean values are 95% confidence interval. The elemental abundances (ID) and the isotope ratios for non-Antarctic HC are mean values of H chondrite falls from the following literatures (see Supplementary data-1).

* The data of A 09516 (H6) are excluded from the means (see Section 3.2).

Jarosewich (1990) for Na-Ni. [b] Wasson and Kallemeyn (1988) for Cu-Ba and Hf. [c] Nakamura (1974) for REEs. [d] Tatsumoto *et al.* (1973) for Th and U. [e] Jacobsen and Wasserburg (1980, 1984); Patchett *et al.* (2004); Boyet and Carlson (2005); Carlson *et al.* (2007); Bouvier *et al.* (2008); Gannoun *et al.* (2011); Burkhardt *et al.* (2016); and Fukai and Yokoyama (2017) for Nd and Sm isotopic compositions. [f] Blichert-Toft and Albarède (1997); Bizzarro *et al.* (2003); Patchett *et al.* (2004); Bouvier *et al.* (2008); and Dauphas and Pourmand (2011) for Lu and Hf isotopic compositions.

Moreover, grains smaller than 5 μm, such as tiny Ca-phosphates especially present in UHCs, might have been missed because of this limitation. However, forsterite and silica are only observed in some UHCs (for forsterite: A-881258, Y-793574, Y790461, and NWA 6752; for silica: Y-790461 and A 09436) and A 09387 (H4), and these were confirmed to be present in the HCs in trace abundances only. Based on this work, there is no resolvable difference in the modal abundances between Antarctic HCs and hot desert HCs, thus the mean values of UHCs and EHCs are calculated from the combined data for Antarctic and hot desert HCs (Fig. 1). Most of the mean modal abundances in UHCs and EHCs are in good agreement with each other (Table 3 and Fig. 1). These mean modal abundances also compare well with the published values listed in Table 3. The mean modal abundance of total Ca-phosphates in EHCs is 0.70 ± 0.10 wt.% at the 95% confidence interval (95% CI) and agrees within uncertainty with previously published values. In addition, the mean modal abundances of chlorapatite and merrillite in UHCs and EHCs overlap within uncertainty (0.10 ± 0.07 wt.% vs. 0.17 ± 0.14 wt.% and 0.29 ± 0.08 wt.% vs. 0.53 ± 0.24 wt.%, respectively at the 95% CI; Table 3). However, the mean modal abundance of total Ca-phosphates in UHCs is 0.39 abundance of total Ca-phosphates in UHCs is 0.39 ± 0.09 wt.% (95% CI), which is significantly lower than the abundance in EHCs (Fig. 1).

3.2. Elemental abundances

The major and trace elemental abundances in bulk samples measured using ICP-OES and ICP-MS are summarized in Table 4, with mean values for the Antarctic UHCs (n = 7), Antarctic EHCs (n = 3), Antarctic HCs (n = 10) and hot desert HCs (n = 3), and literature values for non-Antarctic HCs (Jarosewich, 1990 for Na. Mg, Al, P, K, Ca, Ti, Cr, Mn, Fe, and Ni; Wasson and Kallemeyn, 1988 for Cu, Zn, Rb, Sr, Y, Zr, Nb, Ba, and Hf; Nakamura, 1974 for REEs; Tatsumoto *et al.*, 1973 for Th and U). The data of A 09516 (H6) are excluded from the mean values of Antarctic EHCs and Antarctic HCs because of the anomalous depletions in various elements, including the REEs, displayed by this sample as the result of chemical alteration in Antarctica (*e.g.*, Lipschutz and Samuels, 1991). This sample also exhibits a positive Eu anomaly, as often observed in heavily weathered Antarctic chondrites (*e.g.*, Y-74014: Ebihara, 1987; Y-74492: Nishikawa *et al.*, 1990). The characteristics of this sample are described in detail in Section 4.1.2.

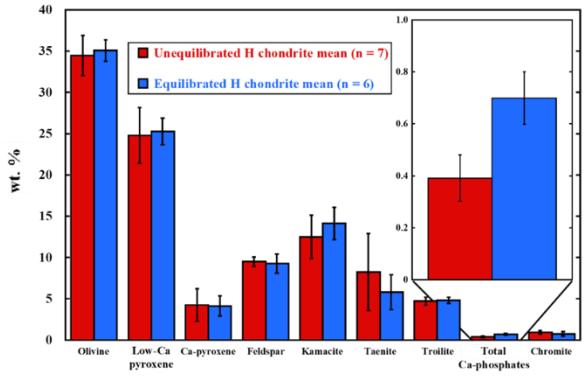

Fig. 1. The mean modal abundances (wt.%) in UHC and EHC obtained in this study (n = 7 and 6, respectively). The mean modal abundances of low-Ca pyroxene, feldspar, and chromite may include forsterite, silica, and ilmenite, respectively (see Section 3.1). The uncertainties represent 95% confidence interval of the mean values.

3.2.1. Major elements

The abundances of major elements for individual samples obtained using ICP-OES were determined with 2% relative standard deviation (RSD; 1SD) on average, while the individual RSDs ranged from 0.05% to 8%. Although most of the mean values for major elemental abundances in Antarctic HCs are in good agreement with the literature values, the mean values of K, Ti, Fe, and Ni are 15% lower than those reported in literature. However, the mean Ti abundance in Antarctic HCs is in excellent agreement with the published Ti abundance in HCs determined using the isotope dilution method (0.0549 ± 0.0015 wt.% at the 95% CI; calculated from Shima, 1979). According to these results, there is almost no difference in the abundances of major elements between Antarctic and hot desert HCs, although the K and Ca abundances in hot desert HCs are 20% higher than those in Antarctic HCs possibly due to either mobilization of these elements by chemical alteration in Antarctica (Velbel *et al.*, 1991) or terrestrial contamination in hot deserts (Al-Kathiri *et al.*, 2005; Pourkhorsandi *et al.*, 2019).

3.2.2. Trace elements

The trace elemental abundances for individual samples obtained using Q-ICP-MS are reproducible within 3% RSD (1SD) on average. The abundances of Lu and U in some samples display larger uncertainties, due to their lower absolute abundances, on the order of 10% RSD. The abundances of Lu and U in some samples display larger uncertainties, due to their lower absolute abundances, on the order of 10% RSD. The CI- normalized REE, Th, and U abundances in each

sample are shown in Fig. 2, and their mean REE, Th and U abundances in Antarctic UHCs, EHCs, and HCs are compared with the literature values in Fig. 3 (CI values are from Anders and Grevesse, 1989). No resolvable difference is observed between the trace elemental abundances of bulk Antarctic UHCs and EHCs, which is consistent with the conclusion of Huss *et al.* (2006). Most of the mean trace elemental abundances in Antarctic HCs, especially for REEs, Th, and U, are in good agreement with the literature values for non-Antarctic HC listed in Table 4. The mean values for Sr and Ba in Antarctic HCs deviate from the literature values (8.82 ± 0.31 ppm vs. 10 ppm and 3.22 ± 0.15 ppm vs. 4.20 ppm at the 95% CI, respectively). However, Sr and Ba are strongly affected by terrestrial weathering as their abundances in the hot desert HCs characterized in this study are high (16.9–70.9 ppm and 17.8–166 ppm, respectively). Moreover, the mean values for Sr and Ba in Antarctic HCs are in agreement within uncertainty with their published values for Antarctic HCs determined by the isotope dilution method (9.29 ± 0.93 ppm and 2.69 ± 0.75 ppm at the 95% CI; Nishikawa *et al.*, 1990). Thus, the observed deviations may only reflect a difference between Antarctic and non-Antarctic meteorites. For hot desert HCs, the mean values of Cu, Zn, Rb, and Y agree within uncertainty with those for Antarctic HCs in this study and with the literature values for non-Antarctic HC, with the exception of Rb. However, other trace elements are enriched compared with the values of Antarctic HCs and non-Antarctic HCs, especially in the case of Sr, Ba, the light REEs (LREEs), Th, and U. In addition, negative Eu anomalies are observed in the CI-normalized REE patterns of hot desert HCs (Fig. 2).

3.3. Isotopic compositions

The Nd, Sm, Lu, and Hf abundances determined by the isotope dilution method, and Sm-Nd and Lu-Hf isotopic compositions in the bulk samples measured using MCICP-MS are summarized in Table 2 (for BHVO-2) and Table 4 (for meteorites) as well as in Figs. 4 and 5. The $^{143}Nd/^{144}Nd$ and $^{176}Hf/^{177}Hf$ values in most of the samples were determined within 20 ppm relative standard error (RSE) and 60 ppm RSE (2SE), respectively. This relatively large standard error for $^{176}Hf/^{177}Hf$ values compared with that for $^{143}Nd/^{144}Nd$ values clearly results from the difference in the adjusted concentrations in the measurement solutions (see Section 2.3.2). This relatively large standard error for $^{176}Hf/^{177}Hf$ values compared with that for $^{143}Nd/^{144}Nd$ values clearly results from the difference in the adjusted concentrations in the measurement solution (see Section 2.3.2). Furthermore, the actual Hf concentration in the measurement solutions for most of the meteorite sample was less than 5 ppb, leading to larger standard errors for the $^{176}Hf/^{177}Hf$ values. On the other hand, the differences in these elemental abundances between those determined

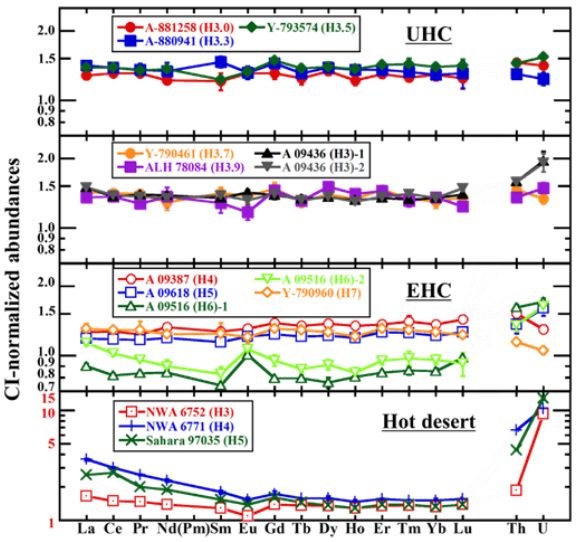

Fig. 2. CI-normalized REE, Th, and U abundances in each Antarctic and hot desert HC. The uncertainties represent 1SD of the measurements by Q-ICP-MS. Error bars are often smaller than the symbol size. Note that the scale of y-axis for hot desert is different from the other. CI values are from Anders and Grevesse (1989).

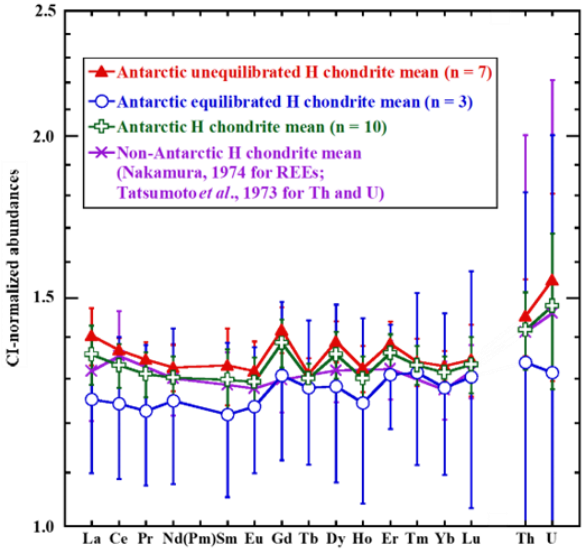

Fig. 3. Mean CI-normalized REE, Th, and U abundances of Antarctic UHCs, Antarctic EHCs, and Antarctic HCs (n = 7, 3, and 10, respectively). The mean values of non-Antarctic HCs are also shown for comparison (Nakamura, 1974 for REEs; Tatsumoto *et al.*, 1973 for Th and U). The uncertainties are 95% confidence interval of the mean values. CI values from Anders and Grevesse (1989).

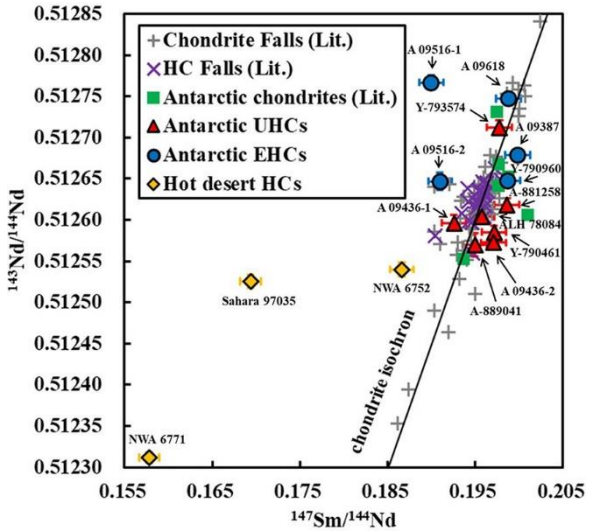

Fig. 4. Sm-Nd isotopic compositions of Antarctic UHCs, Antarctic EHCs, and HCs collected from hot deserts. The isotopic compositions of chondrite falls, HC falls, and Antarctic chondrites from literatures are shown for comparison (Jacobsen and Wasserburg, 1980, 1984; Patchett *et al*., 2004; Boyet and Carlson, 2005; Carlson *et al*., 2007; Bouvier *et al*., 2008; Gannoun *et al*., 2011; Burkhardt *et al*., 2016; Fukai and Yokoyama, 2017; see Supplementary data-1 for the details). The uncertainties for the $^{143}Nd/^{144}Nd$ values are 2SE of the internal reproducibility, and the uncertainties for the $^{147}Sm/^{144}Nd$ are 2SE of the total uncertainty derived from the uncertainty of the spike calibration (see Section 2.3.2). Error bars are often smaller than the symbol size. The analytical uncertainties for the literature data are not shown. The chondrite isochron is from Bouvier *et al*. (2008).

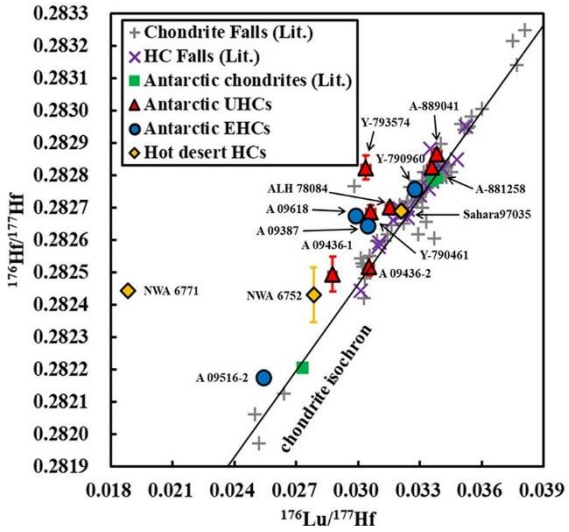

Fig. 5. Lu-Hf isotopic compositions of Antarctic UHCs, Antarctic EHCs, and HCs collected from hot deserts. The isotopic compositions of chondrite falls, HC falls, and Antarctic chondrites from literature are also shown for comparison (Blichert-Toft and Albarède, 1997; Bizzarro *et al*., 2003; Patchett *et al*., 2004; Bouvier *et al*., 2008; Dauphas and Pourmand, 2011; see Supplementary data-1 for the details). Note that Blichert-Toft and Albarède (1997) did not use high-pressure vessels during the sample digestion. The data of Farmington (L5), Adhi Kot (EH4), and Jajh Deh Kot Lalu (EL6) from Dauphas and Pourmand (2011) plot outside the range of the figure. The uncertainties for the $^{176}Hf/^{177}Hf$ values are 2SE of the internal reproducibility, and the uncertainties for the $^{176}Lu/^{177}Hf$ values are 2SE of the total uncertainty derived from the uncertainty of the spike calibration (see Section 2.3.2). Error bars are often smaller than the symbol size. The analytical uncertainties for the literature data are not shown. The chondrite isochron is from Bouvier *et al*. (2008).

using the isotope dilution method (MC-ICP-MS) and calibration line method (Q-ICP-MS) are less than 5% on average, which is in excellent agreement.

The mean values of the elemental abundances determined using the isotope dilution method in Antarctic HCs are in excellent agreement with those in HC falls (Table 4). Most of the Sm-Nd and Lu-Hf data for Antarctic HCs are within the range of chondrite fall data and several of them plot on the respective chondrite isochrons within uncertainty (for Sm-Nd data: Jacobsen and Wasserburg, 1980, 1984; Patchett *et al*., 2004; Boyet and Carlson, 2005; Carlson *et al*., 2007; Bouvier *et al*., 2008; Gannoun *et al*., 2011; Burkhardt *et al*., 2016; Fukai and Yokoyama, 2017; for Lu-Hf data: Blichert-Toft and Albarède, 1997; Bizzarro *et al*., 2003; Patchett *et al*., 2004; Bouvier *et al*., 2008; Dauphas and Pourmand, 2011; for chondrite isochrons: Bouvier *et al*., 2008). The mean values of $^{147}Sm/^{144}Nd$, $^{143}Nd/^{144}Nd$, $^{176}Lu/^{177}Hf$, and $^{176}Hf/^{177}Hf$ for

Antarctic HCs overlap with those of HC falls within uncertainties (Table 4). There are no resolvable differences in the mean values of Antarctic UHC and EHC. In the case of hot desert HCs, the $^{147}Sm/^{144}Nd$ and $^{143}Nd/^{144}Nd$ values (0.1578–0.1866 and 0.512312–0.512540, respectively) are significantly lower than the mean values reported in literature for HC falls (0.1953 ± 0.0006 and 0.512623 ± 0.000009 at 2SE, respectively; Table 4) and the mean values determined here for Antarctic HCs (0.1971 ± 0.0016 and 0.512633 ± 0.000044 at the 95% CI, respectively; Table 4), chondrite plotting as far from the isochron as falling out of the range of chondrite fall data (Fig. 4). In contrast, it seems that the $^{176}Lu/^{177}Hf$ and $^{176}Hf/^{177}Hf$ values of hot desert HCs fall within the ranges determined in literature and measured for Antarctic HCs (Table 4 and Fig. 5), except in the case of NWA 6771 (H4), which is characterized by an anomalously high Hf abundance (269 ppb).

4. DISCUSSION

4.1. Assessment of weathering effects on the Sm-Nd and Lu-Hf systems in Antarctic HCs

For the assessment of weathering effects on Antarctic meteorites, the classical ABC index system is commonly used: A—minor rustiness (*e.g.*, rust stains along fractures are minor); B—moderate rustiness (*e.g.*, 7.5–35% of metal particles are weathered to limonite); C—severe rustiness (*e.g.*, most metal particles are weathered to limonite); and e—evaporite minerals are visible to the naked eye (Antarctic Meteorite Newsletter, NASA; Meteorite Newsletter, NIPR). However, this index may not be sufficient as an indicator especially in terms of chemical alteration (Koeberl and Cassidy, 1991), as it is determined based on mineralogy. Velbel (1988) and Nishikawa *et al.* (1990) found that bulk Rb abundances in some Antarctic ordinary chondrites (OCs) and heavily weathered non-Antarctic HCs are anomalously low and do not covary with the weathering index. Velbel (1988) concluded that Rb loss could be due to chemical leaching during the residence of the meteorite in Antarctica, indicating that relative loss of Rb may be a better indicator of chemical alteration than the weathering index. The results presented here display remarkable deviations in the Rb abundances of both Antarctic and hot desert HCs relative to those reported in literature (Table 4). The mean Rb abundance of Antarctic HCs is significantly lower than the literature value (2.26 ± 0.34 ppm vs. 2.9 ppm at the 95% CI) with extremely low Rb abundances in A-880941 (H3.3) and A 09516 (H6), implying a loss of Rb during Antarctic alteration. However, these lower Rb abundances may just reflect heterogeneity in the amount of feldspar in the samples, which may be induced as the result of a sampling bias (*i.e.*, sampling heterogeneity), as Rb is mostly distributed in feldspar (Shima and Honda, 1967; Mason and Graham, 1970). The average Na and Al abundances in the bulk samples are used as an indicator for the amount of feldspar in the sample, and the respective Rb abundances normalized to the indicator are listed in Table 5. Even considering the heterogeneous distribution of feldspar based on these normalized Rb abundances, the samples displaying extremely low Rb abundances also show low normalized Rb abundances. Thus, any possible effect on the bulk Rb abundance by sampling

Table 5
Elemental abundance ratios in H chondrites (UHC: unequilibrated H chondrite, EHC: equilibrated H chondrite).

Name	Rb / (Na + Al)/2	Sr / (Na + Al)/2	Ba / (Na + Al)/2
A-881258	3.16 ± 0.12	11.3 ± 0.3	4.11 ± 0.14
A-880941	1.77 ± 0.09	12.0 ± 0.5	4.35 ± 0.18
Y-793574	2.56 ± 0.09	9.55 ± 0.32	3.43 ± 0.15
Y-790461	3.19 ± 0.09	11.3 ± 0.2	4.04 ± 0.24
ALH 78084	2.80 ± 0.13	10.7 ± 0.4	3.94 ± 0.24
A 09436-1	2.32 ± 0.05	10.7 ± 0.2	4.04 ± 0.15
A 09436-2	2.38 ± 0.07	11.1 ± 0.2	4.23 ± 0.11
A 09387	3.77 ± 0.11	10.7 ± 0.3	3.88 ± 0.11
A 09618	2.65 ± 0.06	11.0 ± 0.2	3.96 ± 0.08
A 09516-1	0.895 ± 0.049	8.71 ± 0.35	3.19 ± 0.15
A 09516-2	1.29 ± 0.07	12.3 ± 0.5	5.24 ± 0.31
Y-790960	3.11 ± 0.22	10.4 ± 0.3	3.65 ± 0.25
NWA 6752	2.51 ± 0.09	26.5 ± 0.7	202 ± 6
NWA 6771	3.21 ± 0.08	21.8 ± 0.5	22.9 ± 0.5
Sahara 97035	3.96 ± 0.13	123 ± 3	51.4 ± 1.3
Antarctic UHC mean (n = 7)	2.60 ± 0.50	11.0 ± 0.8	4.02 ± 0.29
Antarctic EHC mean* (n = 3)	3.17 ± 0.56	10.7 ± 0.3	3.83 ± 0.16
Antarctic HC mean* (n = 10)	2.77 ± 0.56	10.9 ± 0.7	3.96 ± 0.27
Hot desert HC mean (n = 3)	3.23 ± 3.23	57.2 ± 57.4	92.1 ± 96.3
Non-Antarctic HC mean[a, b]	3.28 ± 0.09	11.3 ± 0.3	4.74 ± 0.13
Antarctic HC mean[a, c]	3.24 ± 0.48	10.5 ± 1.1	3.04 ± 0.85

The uncertainties are derived from the uncertainties of the respective elemental abundances. The uncertainties for the mean values are 95% confidence interval. The mean values of non-Antarctic HC and Antarctic HC are calculated from the following literatures.

* The data of A 09516 (H6) are excluded from the means (see Section 3.2).

[a] Jarosewich (1990) for Na and Al. [b] Wasson and Kallemeyn (1988) for Rb, Sr, and Ba. [c] Nishikawa *et al.* (1990) for Rb, Sr, and Ba.

biases alone can be ruled out. The normalized Rb abundances can also be compared with the normalized abundances of Sr, which is especially concentrated in feldspar (Shima and Honda, 1967; Mason and Graham, 1970) but generally considered less mobile than Rb. The data from this study are compared with calculated values for non-Antarctic HC (Table 4) and Antarctic HCs from Nishikawa *et al.* (1990), in Fig. 6. The normalized Sr abundances in most of the samples are in good agreement with the literature values, but in various samples the normalized Rb abundances are lower than those reported in literature and display a wider range than the Sr abundances. A similar trend emerges when comparing the normalized abundance of Rb and that of Ba, which is concentrated in feldspar as well (Table 5). The low normalized Rb abundances (< 2.7) in some Antarctic HCs co-vary to some degree with their weathering grades although exceptions exist. A-880941 (H3.3) is categorized as A/B but contains a low normalized Rb abundance (1.77 ± 0.09), which may reflect a difference in the weathering degree implied by elemental ratios versus that inferred based on petrographic observation. In any case, the low Rb abundances clearly reflect the loss of Rb during the terrestrial residence of the meteorites in Antarctica or elsewhere in the world (Nishikawa *et al.*, 1990), possibly because of chemical leaching. Therefore, the normalized Rb abundances are taken here as a potential indicator for chemical alteration in the following discussions.

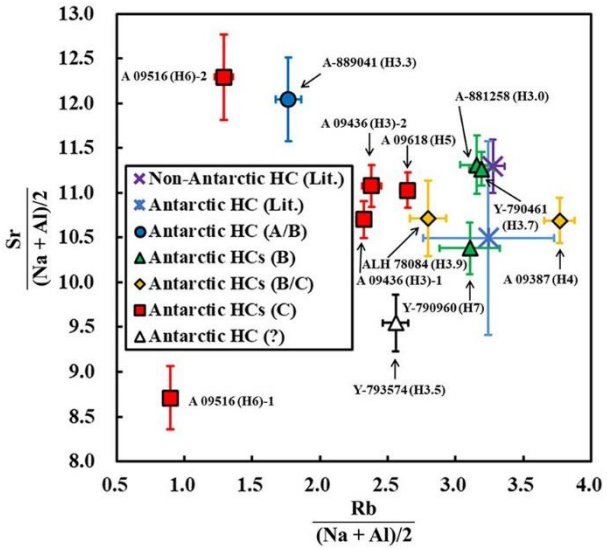

Fig. 6. Comparison of Rb and Sr abundances normalized by the mean Na and Al abundances, as a measure for the amount of feldspar in the sample. The plotted groups are divided based on their weathering index. The values for Non-Antarctic HC (Lit.) and Antarctic HC (Lit.) are calculated from Wasson and Kallemeyn (1988); Jarosewich (1990); and Nishikawa *et al.* (1990), shown in Table 5. The uncertainties are derived from the individual uncertainties of each elemental abundance, and those for literature values are 95% confidence interval of the mean values. Error bars are often smaller than the symbol size.

4.1.1. Weathering effects on bulk Sm-Nd and Lu-Hf systems

The Sm-Nd and Lu-Hf data of a few Antarctic HCs (*e.g.*, A 09516) plot away from the respective chondrite isochrons (Figs. 4 and 5). This may reflect an effect of weathering on the Sm-Nd and Lu-Hf systems in bulk chondrites in Antarctica. However, it remains unclear whether the parent isotope ratios $^{147}Sm/^{144}Nd$ and $^{176}Lu/^{177}Hf$ or the daughter isotope ratios $^{143}Nd/^{144}Nd$ and $^{176}Hf/^{177}Hf$ have been affected by Antarctic weathering. Alternatively, it is also possible that both ratios were disturbed. Therefore, we need to consider one by one which of the following processes affected the Sm-Nd and Lu-Hf systems: i) sample heterogeneity, ii) thermal metamorphism on the parent body or bodies, iii) contamination with terrestrial material, and iv) chemical alteration during residence on the Earth.

(i) Based on the results of this study and previous works, REEs in bulk chondrites are largely unfractionated (*e.g.*, Huss *et al.*, 2006). On the other hand, REEs in individual constituent minerals are highly fractionated depending on their partition coefficients (*e.g.*, Curtis and Schmitt, 1979). This fractionation of REEs between the constituent minerals affects not only their abundances but also their radiogenic isotope systems (*e.g.*, Jacobsen and Wasserburg, 1984). Thus, a loss of constituent mineral(s) due to terrestrial weathering, as observed in Antarctic eucrites (Mittlefehldt and Lindstrom, 1991), or a nonrepresentative sampling bias may induce minor variation in the elemental compositions and radiogenic isotope data of bulk chondrites. According to Amelin and Rotenberg (2004); Amelin (2005); and Debaille *et al.* (2017), the Sm-Nd and Lu-Hf data in individual minerals are indeed different from those in bulk chondrites. However, both data of individual minerals and bulk chondrites plot on the same chondrite isochron when considering the uncertainties. Therefore, the heterogeneous distribution of constituent mineral(s) due to a sampling bias or terrestrial weathering, *i.e.*, sample

heterogeneity may result in heterogeneity of the Sm-Nd and Lu-Hf data of bulk chondrites, but the isotope data will always plot along the isochrons.

(ii) Thermal metamorphism can affect the Sm-Nd and Lu-Hf systems at the bulk scale as a re-distribution due to crystallization of REE-rich minerals such as Ca-phosphates, can take place during metamorphism (Bouvier *et al.*, 2008; Martin *et al.*, 2013; Debaille *et al.*, 2017; Bloch *et al.*, 2017, 2018). The nugget effect, in which the REE-rich Ca-phosphates are heterogeneously distributed, can lead to sampling biases due to non-representative sample volumes, while such Ca-phosphate phases may also be preferentially weathered during the terrestrial residence of the meteorite of interest. These processes may produce wider ranges in the Sm-Nd and Lu-Hf data in bulk equilibrated chondrites than in bulk unequilibrated chondrites (Bouvier *et al.*, 2008; Dauphas and Pourmand, 2011, 2015). However, as mentioned above, unequilibrated and equilibrated chondrites do not show any fractionation or change in the bulk REE abundances in most of the cases. If unequilibrated and equilibrated chondrites had originally the exact same bulk elemental composition, the bulk Sm-Nd and Lu-Hf data in these chondrites should exhibit the same values. This is consistent with the observation that the mean Sm-Nd and Lu-Hf values in bulk unequilibrated and equilibrated chondrites are in agreement with each other, both based on this study and literature values (Jacobsen and Wasserburg, 1980, 1984; Blichert-Toft and Albarède, 1997; Bizzarro *et al.*, 2003; Patchett *et al.*, 2004; Boyet and Carlson, 2005; Carlson *et al.*, 2007; Bouvier *et al.*, 2008; Dauphas and Pourmand, 2011; Gannoun *et al.*, 2011; Burkhardt *et al.*, 2016; Fukai and Yokoyama, 2017). Therefore, thermal metamorphism emphasizes the heterogeneity of the Sm-Nd and Lu-Hf data in bulk chondrites at the scale of the individual sample. Theoretically, the isotope data in bulk unequilibrated and equilibrated chondrites should have the same values as long as these have the same elemental compositions.

(iii) Considering the higher Nd, Sm, Lu, and Hf abundances and lower $^{147}Sm/^{144}Nd$ and $^{176}Lu/^{177}Hf$ in the upper continental crust (26 ppm, 4.5 ppm, 0.32 ppm, 5.8 ppm, 0.10, and 0.0079, respectively; Taylor and McLennan, 1995) as potential contaminating material relative to the lower REE concentrations in chondrites, the Sm-Nd and Lu-Hf data in bulk chondrites display lower values in most of the cases when terrestrial contamination occurred (Bast *et al.*, 2017a, b; Pourkhorsandi *et al.*, 2017, 2021). As the hot desert HCs used in this study exhibit enrichments in Sr, Ba, LREEs, Th, and U and negative Eu anomalies (Table 4 and Fig. 2), these enrichments must result from terrestrial contamination (*e.g.*, Al-Kathiri *et al.*, 2005; Pourkhorsandi *et al.*, 2017). Thus, the low $^{147}Sm/^{144}Nd$ and $^{143}Nd/^{144}Nd$ values in the hot desert HCs (Table 4 and Fig. 4) must also be explained by mixing with terrestrial material. However, the absolute Lu abundance in the upper continental crust is only 10 times higher than that in HCs and Hf is highly immobile during terrestrial alteration, while the absolute abundances of Nd and Sm in the upper continental crust are 45 and 25 times higher than those in HCs, respectively (Taylor and McLennan, 1995), and these elements are also considered to be more mobile than Hf (Middelburg *et al.*, 1988). In this way, because it is more difficult for the Lu-Hf system to be affected by terrestrial contamination than the Sm-Nd system, the $^{176}Lu/^{177}Hf$ and $^{176}Hf/^{177}Hf$ values in the hot desert HCs used in this study do not deviate as far from the isochron as observed for the $^{147}Sm/^{144}Nd$ and $^{143}Nd/^{144}Nd$ values (Table 4 and Fig. 5). This is consistent with the observation of Al-Kathiri *et al.* (2005) who showed that Hf abundances in HCs collected from hot deserts do not deviate from the literature value listed in Table 4 (0.15–0.18 ppm vs. 0.18 ppm), while their corresponding Nd and Sm abundances are 10–30% higher than the literature values (0.66–0.75 ppm vs. 0.59 ppm and 0.21– 0.24 ppm vs. 0.19 ppm, respectively). Therefore, although the extent of terrestrial contamination on chondrites strongly depends on where the sample was collected (Pourkhorsandi *et al.*, 2017, 2021), this process can produce deviations from the Sm-Nd and Lu-Hf isochrons in the case of chondrites (Bast *et al.*, 2017b). These deviations should be accompanied by additional indications of terrestrial contamination, such as higher abundances of Sr, Ba, LREEs, Th, and U.

(iv) Chemical alteration during terrestrial residence, such as leaching, occurs anywhere on Earth in the presence of water, either in the form of rain or humidity. Even

in Antarctica, melting of ice can trigger sample alteration (Mittlefehldt and Lindstrom, 1991). Chemical alteration is commonly divided into two main types: the first type encompasses alteration affecting minerals, such as the loss of Ca-phosphates (Mittlefehldt and Lindstrom, 1991), while the second type reflects alteration that depends on the mobility of the element, as in the case of Rb loss (Velbel, 1988; Nishikawa *et al*., 1990). For the former type of alteration, the effect on the Sm-Nd and Lu-Hf systems is similar to the effect of sample heterogeneity. Thus, even if this alteration occurs, the affected Sm-Nd and Lu-Hf data would plot on their respective isochrons assuming no prior disturbance. The latter type of alteration can disturb these systems because the parent nuclide and the daughter nuclide may have different chemical characteristics, which is consistent with the observations of Nishikawa *et al*. (1990) although based on the Rb-Sr system. Thus, if this alteration occurred during the residence of the meteorite at the Earth's surface, the $^{147}Sm/^{144}Nd$ and $^{176}Lu/^{177}Hf$ values would be disturbed producing deviations from the Sm-Nd and Lu-Hf isochrons. This type of alteration does not influence the $^{143}Nd/^{144}Nd$ and $^{176}Hf/^{177}Hf$ values at the bulk scale.

In summary, thermal metamorphism amplifies the nugget effect of REE-rich minerals such as Ca-phosphates on the Sm-Nd and Lu-Hf isotope systems. Sample heterogeneity also affects the Sm-Nd and Lu-Hf data in bulk chondrites, but the measured data continue to plot on the respective chondrite isochrons. In addition, $^{143}Nd/^{144}Nd$ and $^{176}Hf/^{177}Hf$ values are not affected by chemical alteration at the bulk scale or at least such isotopic fractionation is not yet resolvable. Thus, the $^{143}Nd/^{144}Nd$ and $^{176}Hf/^{177}Hf$ values obtained likely reflect the original values of the bulk HC sample, unless this sample was contaminated by terrestrial material. Because the Asuka, Yamato, and Allan Hill samples used in this study are collected from blue ice fields, it is unlikely that the samples were contaminated during their residence in Antarctica. Therefore, the deviations from the isochrons on the Sm-Nd and Lu-Hf data that are apparent in a small set of samples (Figs. 4 and 5) have likely been produced by disturbance of the $^{147}Sm/^{144}Nd$ and $^{176}Lu/^{177}Hf$ values during the chemical alteration that depends on the elemental mobility.

Based on the assumption above, to evaluate the effects of Antarctic weathering on the Sm-Nd and Lu-Hf data in bulk chondrites, the differences in $^{147}Sm/^{144}Nd$ and $^{176}Lu/^{177}Hf$ values between the measured values and the respective chondrite isochrons are expressed as $\delta^{147}Sm/^{144}Nd$ (‰) and $\delta^{176}Lu/^{177}Hf$ (‰) respectively, calculated following the equations (in the case of the Sm-Nd system):

$$\delta\frac{^{147}Sm}{^{144}Nd} = \left[\left(\frac{^{147}Sm}{^{144}Nd}\right)_{measured} - \left(\frac{^{147}Sm}{^{144}Nd}\right)_{ideal}\right] \times 1{,}000\,[‰]$$

and

$$\left(\frac{^{147}Sm}{^{144}Nd}\right)_{ideal} = \frac{\left(\frac{^{143}Nd}{^{144}Nd}\right)_{measured} - b}{a}$$

where a is the slope of the isochron and b is the intercept of the isochron, which is the initial $^{143}Nd/^{144}Nd$ value. The values for the isochrons and the initial isotope ratios in the Sm-Nd and Lu-Hf systems are from Bouvier *et al*. (2008). These calculated differences for Antarctic HCs reflect the extent of the disturbance on the $^{147}Sm/^{144}Nd$ and $^{176}Lu/^{177}Hf$ values by Antarctic alteration. The calculated differences are shown in Fig. 7, with a range of differences in chondrite falls since the Sm-Nd and Lu-Hf data in chondrite falls also show a deviation from the isochron (Figs. 4 and 5). According to Fig. 7, the $\delta^{147}Sm/^{144}Nd$ values of Antarctic HCs, except for A 09436 (H3)-2, ALH 78084 (H3.9), and A 09516 (H6), fall within the range of HC falls taking into account the associated uncertainty. The $\delta^{176}Lu/^{177}Hf$ of Antarctic HCs, except for Y-793574 (H3.5), Y-790461 (H3.7), A 09387 (H4), and A 09618 (H5), also fall within the range of HC falls. Although the $\delta^{147}Sm/^{144}Nd$ or $\delta^{176}Lu/^{177}Hf$ values of the samples excluded above do not fall within the range of HC falls, the $\delta^{147}Sm/^{144}Nd$ and $\delta^{176}Lu/^{177}Hf$ values of all Antarctic HCs, except for A 09516 (H6)-1, do plot within the range of other chondrite falls. The values of Antarctic HCs that do not fall within the range of HC falls could indicate disturbance of the systems by chemical alteration in Antarctica. However, this disturbance can be considered minor as most of the values fall within the range of other chondrite falls. The $\delta^{147}Sm/^{144}Nd$ and $\delta^{176}Lu/^{177}Hf$ values in A-880941 (H3.3), which displays the lowest weathering index but the second highest Rb loss in this study, fall close to 0. Similar $\delta^{147}Sm/^{144}Nd$ and $\delta^{176}Lu/^{177}Hf$ values are observed for heavily weathered

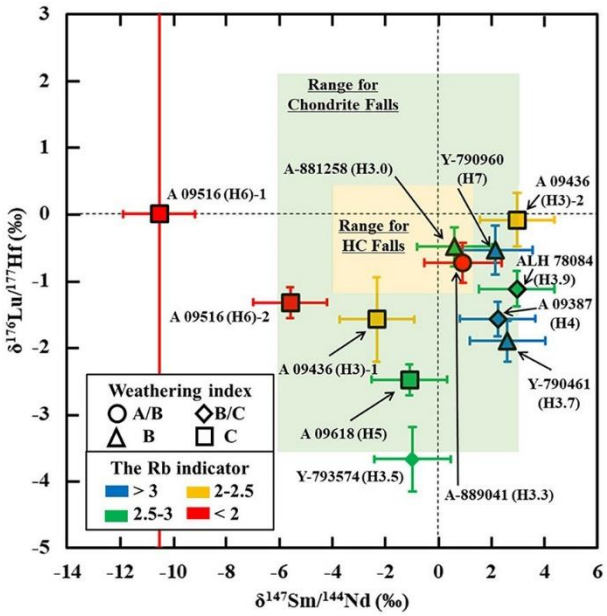

Fig. 7. Deviations of $^{147}Sm/^{144}Nd$ and $^{176}Lu/^{177}Hf$ from the respective chondrite isochron on the Sm-Nd and Lu-Hf systems. The symbols of each plot reflect the weathering index and the Rb indicator (Table 5) by shape and color, respectively. Note that no weathering index for Y-793574 (H3.5) and $^{176}Hf/^{177}Hf$ of A 09516 (H6)-1 have been determined, hence the symbol of Y-793574 (H3.5) is not surrounded by black line and the $\delta^{176}Lu/^{177}Hf$ of A 09516 (H6)-1 was not determined. The ranges for chondrite falls and HC falls are calculated from the literature values shown in Figs. 4 and 5 (Supplementary data-1), and are shown by light green and light red, respectively. The respective isochrons used for the calculations are from Bouvier *et al*. (2008). The uncertainties except for the $\delta^{176}Lu/^{177}Hf$ of A 09516 (H6)-1 are derived from the uncertainties of each isotope ratios. The uncertainties of the isochrons are not considered. (For interpretation of the references to color in this figure legend, the reader is referred to the web version of this article.)

(sub)samples A 09618 (H5) and A 09436 (H3)-2 respectively, and for A-881258 (H3.0) that indicates no Rb loss. Furthermore, $\delta^{147}Sm/^{144}Nd$ and $\delta^{176}Lu/^{177}Hf$ values of all published data for Antarctic chondrites (Figs. 4 and 5), except for ALHA 77295 (EH3) with a high $\delta^{147}Sm/^{144}Nd$ (5.66‰), range from 1.96 to 1.94‰ and from 0.02 to 0.18‰, respectively, falling within the range of chondrite falls also regardless of their weathering index. Therefore, it can be concluded that Antarctic chondrites display limited effects of weathering on their isotopic values, and the extent of the disturbance on $^{147}Sm/^{144}Nd$ and $^{176}Lu/^{177}Hf$ in Antarctic chondrites would be of a level similar to that measured for chondrite falls even if Antarctic weathering occurred. In addition, there seems to be no correlation between the $\delta^{147}Sm/^{144}Nd$ and $\delta^{176}Lu/^{177}Hf$ values and the weathering indicators, suggesting that both the Sm-Nd and Lu-Hf systems are fairly robust against Antarctic weathering relative to the Rb-Sr system (Nishikawa *et al*., 1990). However, the most weathered sample in this study, as indicated by the weathering index C and the lowest normalized Rb abundance (Table 5), A 09516 (H6), shows the largest absolute $\delta^{147}Sm/^{144}Nd$ values in this study and an atypical CI-normalized REE signature that is characterized by subchondritic values and a positive Eu anomaly (Figs. 2 and 7). Therefore, the Sm-Nd and Lu-Hf systems are generally unaffected by Antarctic weathering except in the case of anomalous CI-normalized REE abundances, as all samples except A 09516 (H6) display normal chondritic REE patterns and low $\delta^{147}Sm/^{144}Nd$ and $\delta^{176}Lu/^{177}Hf$ values.

4.1.2. Loss of REEs in Asuka 09516 (H6)

As described above, A 09516 clearly underwent a significant degree of alteration, both mineralogically and chemically. Since this sample was analyzed in duplicate and the low elemental abundances are observed for this sample twice, significant sample losses during acid decomposition can be ruled out. Moreover, no other sample analyzed in this study exhibits such low abundances. Given that the weathering mechanism that affected A 09516 appears considerably more complicated than that of any other sample, this H6 chondrite is excluded from the previous discussions and is discussed here separately.

The low P and REE abundances and the low P/Mg of A 09516 relative to the other HCs (Table 4) may imply a loss of Ca-phosphates, known to take place during the alteration of eucrites in Antarctica (Mittlefehldt and Lindstrom, 1991). However, the characteristic LREE depletion and Ce anomaly typical for alteration of Antarctic eucrites are not observed A 09516 (Fig. 2). Considering the CI-normalized REE abundance in Ca-phosphates of HCs (Ebihara and Honda, 1983; Ward *et al*., 2017), HCs that have lost Ca-phosphates should display lower CI-normalized LREE abundances relative to the heavy REE (HREE) abundances, which indicates that the CI-normalized REE abundances in A 09516 cannot be explained only by a loss of Ca-phosphates, as is the case for the weathered Antarctic eucrites (Mittlefehldt and Lindstrom, 1991). Normal chondritic Th and U abundances in A 09516 (Table 4 and Fig. 2) support that this sample did not lose considerable Ca-phosphate, simply because Th and U are also concentrated in Ca-phosphates of OCs (Pellas and Störzer, 1975; Crozaz,

1979). Generally, OCs, including HCs, contain chlorapatite and merrillite as Ca-phosphates (*e.g.*, Van Schmus, 1969). The CI-normalized REE abundances in merrillite are relatively flat, while those in chlorapatite are more enriched in LREEs than in HREEs in OCs (Crozaz *et al.*, 1989; Ward *et al.*, 2017). In addition, the Th and U abundances in merrillite are considerably lower (3 ppm and 0.3 ppm, respectively) than those in chlorapatite (11 ppm and 7.5 ppm, respectively) for OCs (Crozaz, 1974, 1979), implying that a loss of merrillite from bulk OCs affects the bulk Th and U abundances significantly less than a loss of chlorapatite. Thus, the REE abundances in A 09516 might be explained by the selective or more rapid dissolution of merrillite rather than chlorapatite during Antarctic alteration. However, the solubilities of merrillite and chlorapatite are comparable under acidic conditions (Adcock *et al.*, 2013), and selective or rapid dissolution of merrillite is hence unlikely. Therefore, a simple loss of Ca-phosphates by alteration cannot explain the elemental composition of A 09516.

Alternatively, chemical leaching depending on the solubility of an element, for example taking place at grain boundaries, could explain the elemental losses observed for A 09516. It is assumed that this mechanism does not strongly affect the mineralogy of the OCs, as highly mobile elements are leached more during this type of alteration. According to studies dealing with the mobility of REEs during weathering (Nesbitt, 1979; Middelburg *et al.*, 1988; van der Weijden and van der Weijden, 1995; Hannigan and Sholkovitz, 2001; Su *et al.*, 2017), the middle REEs (MREEs) and HREEs can more strongly be leached than the LREEs by alteration depending on the redox conditions, which could produce the observed REE abundances in A 09516. This can leave immobile elements such as Hf and Th in this sample. Moreover, the solubility difference explains the large deviation from the isochron on the Sm-Nd plots for A 09516 (Figs. 4 and 7) because any weathering mechanism affecting the modal abundance of the constituent minerals, such as a loss of Ca-phosphates, could not induce this divergence. However, the positive Eu anomaly in A 09516 cannot be produced by this leaching mechanism because the sample would exhibit no or rather a negative Eu anomaly if leaching occurred following their solubilities only. In addition, the Lu/Hf data in A 09516 display only a limited deviation (δLu/Hf = 1.32 ± 0.23 ‰; Figs. 5 and 7) from the isochron while the Sm-Nd data show a larger deviation (δSm/Nd = 5.58 ± 1.40 ‰ and 10.5 ± 1.4 ‰; Figs. 4 and 7), which is inconsistent with their relative mobility. Therefore, the chemical leaching depending on the solubility of an element can also not fully explain the characteristics of A 09516.

Lastly, two speculative possibilities remain to explain the REE abundances in A 09516: either some Ca-phosphates were partially leached during Antarctic alteration, or some Ca-phosphates were completely leached during Antarctic alteration, but the sample was at a later stage contaminated by terrestrial material. Similar scenarios have been proposed by Bast *et al.* (2017b) to explain the observed discrepancies from the reference isochron for bulk Lu-Hf data in eucrites and angrites. In the case of the former scenario, Ca-phosphates are fractured to some extent by an interruption in the ionic bonding between cations, especially impurity cations, and $(PO_4)^{2-}$ in the Ca-phosphates as the result of Antarctic alteration, but the Ca-phosphates are not completely broken due to insufficiencies in time, in the amount of fluid, or in the pH of the fluid during the leaching. This leads to selective leaching of more soluble trace elements from Ca-phosphates. In this case, the losses of MREEs and HREEs are more remarkable than those of LREEs, while the positive Eu anomaly and the normal Th and U abundances in A 09516 remain. Moreover, this incomplete dissolution of Ca-phosphates can produce the disturbance on the Sm-Nd plots for A 09516. However, the observation of a lack of disturbance for the Lu/Hf in A 09516 still remains to be explained. In the case of the latter scenario, contamination by terrestrial material during residence in Antarctica (Delisle *et al.*, 1989; Welten *et al.*, 2001) or during the experimental procedure such as sample crushing cannot be ruled out completely, although the contamination during Antarctic residence is unlikely because other samples, collected in the vicinity of A 09516, show no traces of contamination based on the results in this study. In both cases of contamination, some Ca-phosphates are removed by leaching during Antarctic alteration entirely, but the abundances of LREEs, Th, and U in A 09516 remain elevated because of terrestrial contamination. This can also explain the disturbance of Sm/Nd, the presence of the positive Eu anomaly and even the absence of any disturbance of the Lu/Hf because of less pronounced effects from terrestrial contamination on the Lu and Hf abundances. However, the observation that the Th and U abundances are still chondritic limits the possible admixture of terrestrial material. In any case, both possibilities including the loss of Ca-phosphates are inconsistent with a high modal abundance of Ca-phosphates in this sample (0.75 wt.%; Table 3), although their mass scales need to be considered. Therefore, A 09516 may have lost some amount of Ca-phosphates,

but the way this HC lost Ca-phosphates appears to be different from how Antarctic eucrites are affected (Mittlefehldt and Lindstrom, 1991), indicating that Antarctic alteration may be significantly more complicated than what is expected based on heavily altered samples.

4.2. Control of heterogeneity on bulk Sm-Nd and Lu-Hf data by Ca-phosphates and Ca-pyroxene

The isotopic heterogeneity mostly depends on the sample heterogeneity unless the sample is affected by terrestrial weathering, as discussed above. Thus, it is important to constrain which minerals mainly affect the Sm-Nd and Lu-Hf data of bulk chondrites. To do this, elemental abundance ratios in Antarctic HCs were compared with their isotope ratios, and their correlation coefficients r are shown in Table 6. If a constituent mineral controls the heterogeneity in bulk Sm-Nd and Lu-Hf data, elements accommodated in the mineral should display co-variation with the isotope data, if no selective removal or addition of elements occurred during weathering. According to the correlation coefficients for all samples, P/Mg and Y/Mg display strong positive correlations with $^{147}Sm/^{144}Nd$, $^{176}Lu/^{177}Hf$, and $^{176}Hf/^{177}Hf$ (r = 0.5–0.8) and strong negative correlations with $^{143}Nd/^{144}Nd$ (r = 0.6 and 0.7, respectively). If A 09516 (H6) is excluded, because its $^{147}Sm/^{144}Nd$ is the most disturbed by Antarctic weathering among the samples studied in this work, the P/Mg displays a strong negative correlation with $^{147}Sm/^{144}Nd$ instead of a positive correlation (r = 0.6; Table 6). In the case of OCs, Y is distributed in Ca-phosphates (*e.g.*, Mason and Graham, 1970), and Ca-phosphates have lower $^{147}Sm/^{144}Nd$ and $^{143}Nd/^{144}Nd$ values and higher $^{176}Lu/^{177}Hf$ and $^{176}Hf/^{177}Hf$ values compared to bulk samples (Amelin and Rotenberg, 2004; Amelin, 2005; Debaille *et al.*, 2017). Thus, these correlations indicate that the isotope ratios in bulk samples highly depend on the Ca-phosphates-to-silicates weight ratio in the sample, because the P/Mg and Y/Mg can be considered as indicators of the Ca-phosphates/silicates.

The correlation coefficients excluding A 09516 (H6) are shown in Table 6, not only because of the reasons outlined above but also because this sample is characterized by an abnormally low abundance of Ca-phosphates as discussed in the Section 4.1.2. When A 09516 (H6) is excluded, the P/Mg no longer correlates with the $^{176}Lu/^{177}Hf$ and $^{176}Hf/^{177}Hf$. Because the Y/Mg still correlates with these ratios and P is in part distributed in metals especially in unequilibrated chondrites (Murrell and Burnett, 1983; Zanda *et al.*, 1994), this may be caused by a disturbance of the bulk P abundance through the accommodation of P in metal. On the other hand, Al/Mg, Ca/Mg, and Ti/Mg display negative correlations with $^{176}Lu/^{177}Hf$ and $^{176}Hf/^{177}Hf$ (r = 0.8 to 0.4), although the correlations with Al/Mg are relatively weak (r = 0.4 and 0.5, respectively). According to in-situ analyses and Hf partition coefficients of minerals (Alexander, 1994; Righter and Shearer, 2003; Martin *et al.*, 2013), Hf is distributed in chondrule glass and Ca-pyroxene for unequilibrated chondrites and in Ca-pyroxene for equilibrated chondrites. Aluminum, Ca, and Ti are distributed in these silicate minerals as well, although Al is mostly distributed in feldspar in EOCs (Curtis and Schmitt, 1979; Alexander, 1994). Considering the REE distribution in EOCs, Lu is not only distributed in Ca-phosphates but also partitioned to a large degree into Ca-pyroxene, while Sm and Nd are mostly distributed in Ca-phosphates (*e.g.*, Curtis and Schmitt, 1979). In the case of UOCs, Lu is distributed in chondrule glass and Ca-pyroxene (Alexander, 1994; Shinotsuka, 1997). In addition, chondrule glass has the lowest Lu/Hf among silicates and Ca-phosphates for unequilibrated chondrites and Ca-pyroxene has the lowest Lu/Hf among these

Table 6

Correlation coefficients (r) between elemental ratios and isotope ratios in Antarctic HCs.

	Correlation coefficients for all samples				Correlation coefficients excluding A 09516 (H6)			
	$^{147}Sm/^{144}Nd$	$^{143}Nd/^{144}Nd$	$^{176}Lu/^{177}Hf$	$^{176}Hf/^{177}Hf$	$^{147}Sm/^{144}Nd$	$^{143}Nd/^{144}Nd$	$^{176}Lu/^{177}Hf$	$^{176}Hf/^{177}Hf$
Al/Mg	-0.50	0.29	-0.42	-0.12	-0.21	-0.47	-0.36	-0.51
P/Mg	0.48	-0.57	**0.64**	**0.62**	**-0.60**	-0.45	-0.04	0.09
Ca/Mg	0.19	0.40	-0.24	-0.01	0.14	0.45	**-0.74**	-0.54
Ti/Mg	-0.42	0.28	**-0.63**	-0.43	-0.23	-0.01	**-0.79**	**-0.73**
Y/Mg	**0.65**	**-0.65**	**0.78**	**0.66**	0.04	-0.48	0.56	0.40
P/Ca	0.33	**-0.74**	**0.74**	**0.60**	-0.47	**-0.63**	0.58	0.50
Y/Ca	0.41	**-0.71**	**0.75**	0.49	-0.06	-0.55	**0.80**	0.58

Strong and no correlations are defined as $|r| > 0.6$ and $0.4 > |r|$, and are shown in bolded and underlined, respectively.

minerals for equilibrated chondrites (Alexander, 1994; Martin *et al*., 2013). Therefore, the negative correlations of Al/Mg, Ca/ Mg, and Ti/Mg with $^{176}Lu/^{177}Hf$ and $^{176}Hf/^{177}Hf$ indicate that the amount of Ca-pyroxene, which is a major host phase of Hf and a partial carrier of Lu, affects the heterogeneity of bulk Lu-Hf data. Moreover, the negative correlations are also produced by the heterogeneity in the amount of chondrule glass, which is a major host phase of Lu and Hf in UHCs. The negative correlation between Ti/Mg and Lu-Hf data may also be affected by the amount of ilmenite, which can have lower Lu/Hf than that in Ca-pyroxene according to their partition coefficients (Green, 1994; Kleine *et al*., 2008). However, considering the budget of Hf between constituent minerals in the whole rock, the correlation mostly depends on the weight ratio of Ca-pyroxene to silicates (or Ca-pyroxene and chondrule glass to silicates).

According to Table 6, P/Ca and Y/Ca exhibit negative correlations with Sm-Nd data and positive correlations with Lu-Hf data, both when including and excluding A 09516 (H6), although $^{147}Sm/^{144}Nd$ still displays positive correlations possibly because of the disturbance by weathering. Most of these correlations are stronger than those for the P/Mg and Y/Mg. For OCs, REEs including Y are mostly distributed among the two phases of Ca-phosphate and Ca-pyroxene (Ebihara and Honda, 1984). Among silicates and Ca-phosphates in chondrites, Ca-phosphates have the highest P/Ca, Y/Ca, and Lu/Hf and the lowest Sm/Nd (*e.g.*, Curtis and Schmitt, 1979; Amelin, 2005). In contrast, Ca-pyroxene has the lowest P/Ca, Lu/Hf, and Y/Ca and the highest or second highest Sm/Nd (Curtis and Schmitt, 1979; Alexander, 1994; Martin *et al*., 2013). Thus, Ca-phosphates and Ca-pyroxene are considered to be the endmembers of the bulk P/Ca, Y/Ca, Sm/Nd, and Lu/Hf, indicating that the correlations of the P/Ca and Y/Ca reflect the Ca-phosphates-to-Ca-pyroxene weight ratio. Therefore, the heterogeneity of Sm-Nd and Lu-Hf data in bulk OCs is mainly controlled by the weight ratio of Ca-phosphates to Ca-pyroxene in the sample. For UOCs, the amount of chondrule glass also affects the overall REE budget and isotopic values.

4.3. Relationship between the distributions of REEs and Hf and the heterogeneities of bulk Sm-Nd and Lu-Hf data

According to the result of the in-situ measurement in this study, the modal abundance of Ca-phosphates in UHCs is significantly lower than that in EHCs (Fig. 1). This increase in the modal abundances of Ca-phosphates from UHCs to EHCs must result from thermal metamorphism on their parent body or bodies (Huss *et al*., 2006). On the other hand, the bulk REE and P abundances overlap within uncertainty between UHCs and EHCs, which is consistent with previous works (*e.g*., Jarosewich, 1990). Murrell and Burnett (1983) reported that Ca-phosphate grains in UOCs are very fine (<10 μm). Perron *et al*. (1992) found phosphate, chromite, silica, and silica inclusions as secondary minerals in some UOCs. However, Semarkona (LL3.00), which is one of the least metamorphosed chondrites, does not contain such grains. Based on these observations, combining the bulk P abundances and the modal abundances of Ca-phosphates between UHCs and EHCs used in this study, Ca-phosphates must have formed and grown in a closed system during thermal metamorphism on the parent body or bodies. Ebihara (1989) and Shinotsuka (1997) analyzed REE abundances in acid residues of OCs with lower and higher degrees of metamorphism, which were leached using HCl or HNO_3. Because REEs are enriched in chondrule glass in UOCs (Alexander, 1994), Shinotsuka (1997) suggested that the REEs are re-distributed mainly from chondrule glass to Ca-phosphates during thermal metamorphism. Since the bulk REE abundances are the same between UOCs and EOCs, the re-distribution of REEs may have occurred in a closed system with the growth of Ca-phosphates. This REE re-distribution in a closed system can explain the observation that the Sm-Nd and Lu-Hf data of each constituent mineral in chondrites are plotted on the respective chondrite isochrons (Amelin and Rotenberg, 2004; Amelin, 2005; Debaille *et al*., 2017). In this way, because REEs are more distributed to Ca-phosphates in EOCs than UOCs, the nugget effect of Ca-phosphates for EOCs produces larger isotopic variabilities of the Sm-Nd and Lu-Hf systematics than that for UOCs, which reinforces the conclusions by Bouvier *et al*. (2008) and Dauphas and Pourmand (2011, 2015). Moreover, sampling effects on bulk Lu-Hf data due to a heterogeneous distribution of Ca-pyroxene may be larger in EOCs than in UOCs because Lu is hosted in Ca-pyroxene as well as Ca-phosphates, while Hf seems to be re-distributed from chondrule glass to Ca-pyroxene based on their initial distribution and their re-distribution after metamorphism (Curtis and Schmitt, 1979; Alexander, 1994; Righter and Shearer, 2003; Martin *et al*., 2013), although no data exist on the Hf distribution in OCs and the mobility of Hf during thermal metamorphism. These larger contributions to bulk Sm-Nd and Lu-Hf data by the sampling heterogeneities of Ca-phosphates and

Ca-pyroxene in EOCs in terms of the distributions of REE and Hf are complementary to the correlations between the elemental abundance ratios and the isotope ratios obtained in this study (Table 6). Therefore, unequilibrated chondrites in which the re-distributions have not proceeded in the case of OCs should be used for the determination of precise average Sm-Nd and Lu-Hf isotopic compositions to limit the effects of the sampling heterogeneities, reinforcing the conclusions by Bouvier *et al*. (2008) and Debaille *et al.* (2017). Even in this case, the sampling heterogeneity of chondrule glass can still lead to heterogeneity in the bulk Sm-Nd and Lu-Hf data although the effect on the isotope data by the heterogeneous distribution of chondrule glass appears to be less than that by the heterogeneous distribution of Ca-phosphates. Theoretically, equilibrated chondrites could also be useful for the determination of precise average isotopic compositions as aimed for the CHUR values if a sufficiently large amount of the sample is homogenized (speculatively more than a few grams at least), because the heterogeneity of bulk Sm-Nd and Lu-Hf data only results from the sample heterogeneity, provided that re-distributions occurred in a closed system. Based on Patchett *et al*. (2004) and Bouvier *et al*. (2008), the mean values and uncertainties of bulk Sm-Nd data in equilibrated chondrites are almost the same as those in unequilibrated chondrites when a few grams of equilibrated chondrite are homogenized ($^{147}Sm/^{144}Nd$ = 0.1960 ± 0.0006 and 0.1960 ± 0.0004; $^{143}Nd/^{144}Nd$ = 0.512634 ± 0.000012 and 0.512630 ± 0.000011, respectively) On the other hand, the homogenization with even a few grams of equilibrated chondrite seems to be insufficient for the determination of bulk average Lu-Hf isotopic compositions for the purpose of CHUR determination ($^{176}Lu/^{177}Hf$ = 0.0324 ± 0.0009 and 0.0336 ± 0.0001; $^{176}Hf/^{177}Hf$ = 0.282693 ± 0.000078 and 0.282785 ± 0.000011, the same order as above), as also concluded by Patchett *et al*. (2004). Thus, equilibrated chondrites may provide representative Sm-Nd isotopic compositions in individual samples as long as more than a few grams of the sample is homogenized to remove the nugget effect, and such data would be useful for the determination of precise average Sm-Nd isotopic compositions for individual chondrite groups. However, because of the uncertainty related to the essential mass to be actually representative, only unequilibrated chondrites should be used for the determination of the precise Lu-Hf CHUR values, probably applied to the determination of precise average Lu-Hf isotopic compositions for individual chondrite groups as well. This difference in sufficient sample amounts for homogenization may be because the variation in Sm-Nd data largely depends on the sampling heterogeneity of Ca-phosphates, while the variation in Lu-Hf data depends not only on the sampling heterogeneity of Ca-phosphates but also on that of Ca-pyroxene and chondrule glass.

The distributions of REEs and Hf and the redistribution of these elements during parent body processes differ between the various groups of chondrites as the major hosts of those elements and their parent body processes vary, as shown in Table 7, although the distribution and the mobility of Hf remain poorly understood. Sampling biases involving these major hosts are largely responsible for the observed variations in Sm-Nd and Lu-Hf isotope ratios. For example, CV and CO chondrites contain abundant Ca, Al-rich inclusions (CAIs; 2.98 vol.% and 0.99 vol. %, respectively; Hezel *et al*., 2008), producing variable REE abundances and probably variable Hf abundance as well, as the result of a heterogeneous distribution of CAIs in samples of these meteorites. However, CI-normalized abundances of REEs in bulk CAIs are only 20 × CI (*e.g.*, El Goresy *et al.*, 2002), while bulk oldhamite in enstatite chondrites and bulk Ca-phosphates in R chondrites contain 100 × CI and 200 × CI of REEs, respectively (Larimer and Ganapathy, 1987; Maeda *et al*., 2017). Moreover, other refractory components such as amoeboid olivine aggregates contain much less REE and Hf abundances (Krot *et al*., 2004). Thus, based on mass balance considerations, the nugget effects of CAIs or other refractory components on the Sm-Nd and Lu-Hf isotopic heterogeneities are not as much as those of Ca-phosphates or oldhamite. In the cases of enstatite and Rumuruti chondrites, the modal abundances of the REE host phases are only less than 2 wt.% and about 0.4 wt.%, respectively (Crozaz and Lundberg, 1995; Bischoff *et al*., 2011). Moreover, Barrat *et al.* (2014) and Maeda *et al.* (2017) concluded that the REEs of both chondrite groups were re-distributed between the respective host phases during thermal metamorphism. Thus, similar to OCs, the unequilibrated counterparts of these other chondrite groups should be preferred to determine the precise average Sm-Nd and Lu-Hf isotopic compositions for enstatite and Rumuruti chondrites to avoid strong nugget effects of the respective host phases. This may also apply to CK chondrites because these experienced thermal metamorphism and contain < 1 vol.% of Ca-phosphates as one of the hosts of REEs (Martin *et al*., 2013). Kakangari, CV, and CO chondrites underwent aqueous alteration but simultaneously also underwent a limited degree of thermal metamorphism on their parent bodies. However, their thermal

Table 7

Correlation coefficients (r) between elemental ratios and isotope ratios in Antarctic HCs

Chondrite	Major hosts of REEs	Major hosts of Hf	Alteration type
H, L, LL	Ca-phosphates[a]	Ca-pyroxene (silicates)[f]	
EH, EL	Oldhamite (CaS)[b]	Sulfides and silicates[g]	Thermal metamorphism[h]
CK	Ca-phosphates and silicates[c]	Silicates[c]	
CV	Ca, Al-rich inclusions (CAIs)[d]	?	Aqueous alteration and
CO	?	?	weak thermal metamorphism[h]
CI, CM, CR, CH, CB	?	?	Aqueous alteration[h]
Rumuruti	Ca-phosphates[e]	?	Thermal metamorphism[h]
Kakangari	?	?	Aqueous alteration and weak thermal metamorphism[i]

[a] Curtis and Schmitt (1979) and Ebihara and Honda (1983). [b] Larimer and Ganapathy (1987) and Ebihara (1988). [c] Martin *et al*. (2013). [d] Ebihara and Honda (1987). [e] Maeda *et al*. (2017). [f] Alexander (1994) and Mason and Graham (1970). [g] Barrat *et al*. (2014). [h] Krot *et al*. (2003) and Huss *et al*. (2006). [i] Weisberg *et al*. (1996) and Barosch *et al*. (2020).

metamorphism occurred within the unequilibrated range, implying the effect of elemental re-distribution by thermal metamorphism is almost negligible. For many groups of carbonaceous chondrites that underwent aqueous alteration, it is unclear whether heavily altered samples can be used for the determination of the precise average isotopic compositions because the re-distribution of REEs and Hf during aqueous alteration remains poorly constrained. According to Bouvier *et al*. (2008), aqueously altered samples produce fewer heterogeneities of bulk Sm-Nd and Lu-Hf data than metamorphosed samples. Therefore, the use of unequilibrated chondrites not only for OCs but also for most other groups of chondrites can reduce the effect of variability in the isotope data stemming from the sample heterogeneity, which is required for the determination of precise average Sm-Nd and Lu-Hf isotopic compositions for individual chondrite groups.

5. CONCLUSIONS

In this study, we analyzed ten Antarctic HCs and three HCs from hot deserts in a systematic manner to determine their modal mineral abundances, major and trace elemental abundances, and Sm-Nd and Lu-Hf isotopic compositions. The following conclusions can be drawn.

Firstly, by calculating the Rb abundances normalized to the average Na and Al abundances for each sample to evaluate Antarctic chemical alteration, our results indicate that not all weathered samples categorized as C according to the weathering index display a loss of Rb. Conversely, samples categorized as A/B may exhibit a high Rb loss. Thus, the normalized Rb abundance can be a good indicator for the assessment of Antarctic alteration chemically but only indicates the relative intensity of the chemical weathering in Antarctica.

Secondly, the effects of Antarctic alteration on the Sm-Nd and Lu-Hf systems in bulk HCs are evaluated using the $\delta^{147}Sm/^{143}Nd$ and $\delta^{176}Lu/^{177}Hf$ notations. These values do not correlate with the weathering index or the Rb indicator, except in the case of a single heavily weathered sample A 09516 (H6), which displays various element losses, including for the REEs. This result suggests that the Sm-Nd and Lu-Hf systems preserve their original compositions during Antarctic alteration. However, when a sample is heavily affected by Antarctic weathering and has lost many elements, the isotope systems may also be disturbed. Such high elemental losses might reflect partial dissolution of Ca-phosphates during alteration. Therefore, unless the sample is clearly heavily weathered, most Antarctic meteorites, including rare meteorites such as ungrouped meteorites, shergottites-nakhlites-chassignites, and lunar meteorites can be used for the investigation of their Sm-Nd and Lu-Hf isotopic compositions.

Finally, we confirm that the Sm-Nd and Lu-Hf data in bulk HCs are correlated with the weight ratio of Ca-phosphates to silicates. The weight ratio of Ca-phosphates to Ca-pyroxene may correlate stronger with the isotope ratios, especially in the case of the Lu-Hf system. Sample heterogeneity of Ca-phosphates in HCs may thus lead to heterogeneities in the bulk Sm-Nd and Lu-Hf data. Since REEs in OCs are redistributed to Ca-phosphates in a closed system during thermal metamorphism on the parent bodies, the nugget effect of Ca-phosphates on the heterogeneities of bulk Sm-Nd and Lu-Hf isotope data is larger for EOCs than for UOCs. Therefore,

the use of UOCs should be preferred for the determination of well-constrained average Sm-Nd and Lu-Hf isotopic compositions such as CHUR values unless at least a few grams of EOCs are used, which reinforces the conclusion by Bouvier *et al*. (2008). The preferred use of unequilibrated specimens may also be extended to the other groups of chondrites, but the optimal sample amount for homogenization to obtain representative Sm-Nd and Lu-Hf isotopic compositions in a sample is expected to differ for each group because the host phases of REEs and Hf and their re-mobilization during parent body processes are distinct. For the analysis of bulk isotope data, major and trace elemental abundances should be determined together with the isotope data in order to evaluate the sample heterogeneity and to assess the effects of weathering. A better understanding of the Hf distribution on the bulk meteorite scale, the Hf mobilization during thermal metamorphism, and the re-distribution of REEs and Hf during aqueous alteration on meteorite parent bodies may help to determine the sample sizes required to overcome sample heterogeneity and to measure representative Sm-Nd and Lu-Hf isotopic compositions in individual samples, leading to precise average Sm-Nd and Lu-Hf isotopic compositions for individual chondrite groups.

Declaration of Competing Interest

The authors declare that they have no known competing financial interests or personal relationships that could have appeared to influence the work reported in this paper.

ACKNOWLEDGMENTS

We would like to thank S. Cauchies and W. Debouge for assistance in the lab, J. De Jong for helping with the isotope analysis, and N. J. de Winter for guidance with the μXRF. We also thank the Royal Belgian Institute of Natural Sciences, Belgium, and the National Institute of Polar Research, Japan, for the loan of the Antarctic meteorites and meteorites collected from hot deserts used in this study. RM, SG, VD, and PhC acknowledge support from the Excellence of Science (EoS) project "ET-HoME". SG, VD, and GH thank the BRAIN-Be Belgian Science Policy (BELSPO) project "BAMM". VD thanks the ERC StG ISoSyC and FRSFNRS for support. HP acknowledges receiving funding from the European Union's Horizon 2020 research and innovation program under the Marie Skłodowska-Curie grant agreement No 801505. PhC acknowledges support from the VUB Strategic Research Program and the Research Foundation Flanders (FWO Hercules grant) for the purchase of the μXRF instrument. Finally, we are grateful to Audrey Bouvier for her editorial work and insightful comments during the review process. We also thank Erik Scherer, Minako Righter, and an anonymous reviewer for their constructive and detailed reviews.

APPENDIX A. SUPPLEMENTARY MATERIAL

Supplementary data to this article can be found online at https://doi.org/10.1016/j.gca.2021.05.005.

REFERENCES

Adcock C. T., Hausrath E. M. and Forster P. M. (2013) Readily available phosphate from minerals in early aqueous environments on Mars. *Nat. Geosci.* **6**, 824–827.

Alexander C. M. O'D. (1994) Trace element distributions within ordinary chondrite chondrules: implications for chondrule formation conditions and precursors. *Geochim. Cosmochim. Acta* **58**, 3451–3468.

Al-Kathiri A., Hofmann B. A., Jull J. T. and Gnos E. (2005) Weathering of meteorites from Oman: Correlation of chemical and mineralogical weathering proxies with ^{14}C terrestrial ages and the influence of soil chemistry. *Meteorit. Planet. Sci.* **40**, 1215–1239.

Amelin Y. (2005) Meteorite phosphates show constant ^{176}Lu decay rate since 4557 million years ago. *Science* **310**(5749), 839–841.

Amelin Y. and Rotenberg E. (2004) Sm–Nd systematics of chondrites. *Earth Planet. Sci. Lett.* **223**, 267–282.

Anders E. and Grevesse N. (1989) Abundances of the elements: meteoritic and solar. *Geochim. Cosmochim. Acta* **53**, 197–214.

Armytage R. M. G., Debaille V., Brandon A. D. and Agee C. B. (2018) A complex history of silicate differentiation of Mars from Nd and Hf isotopes in crustal breccia NWA 7034. *Earth and Planet. Sci. Lett.* **502**, 274–283.

Barosch J., Ebel D. S., Hezel D. C., Alpert S. and Palme H. (2020) Formation of chondrules and matrix in Kakangari chondrites. *Earth Planet. Sci. Lett.* **542**, 116286.

Barrat J. A., Zanda B., Jambon A. and Bollinger C. (2014) The lithophile trace elements in enstatite chondrites. *Geochim. Cosmochim. Acta* **128**, 71–94.

Bast R., Scherer E. E. and Bischoff A. (2017a) The ^{176}Lu-^{176}Hf systematics of ALM-A: a sample of the recent Almahata Sitta meteorite fall. *Geochem. Pers. Lett.* **3**, 45–54.

Bast R., Scherer E. E., Sprung P., Mezger K., Fischer-Go¨dde M., Taetz S., Bo¨hnke M., Schmid-Beurmann H., Mu¨nker C., Kleine T. and Srinivasan G. (2017b) Reconciliation of the excess ^{176}Hf conundrum in meteorites: recent disturbances of the Lu-Hf and Sm-Nd isotope systematics. *Geochim. Cosmochim. Acta* **212**, 303–323.

Bischoff A., Vogel N. and Roszjar J. (2011) The Rumuruti chondrite group. *Chemie der Erde* **71**(2), 101–133.

Bizzarro M., Baker J. A., Haack H., Ulfbeck D. and Rosing M. (2003) Early history of the Earth's crust–mantle system inferred from hafnium isotopes in chondrites. *Nature* **421**, 931–933.

Bland P. A., Zolensky M. E., Benedix G. K. and Sephton M. A. (2006) Weathering of chondritic meteorites. In *Meteorites and the Early Solar System II* (eds. Lauretta D. S. and McSween Jr. H. Y.). The University of Arizona Press, Tucson, pp. 853–867. In collaboration with Lunar and Planetary Institute, Houston.

Blichert-Toft J. and Albarède F. (1997) The Lu–Hf isotope geochemistry of chondrites and the evolution of the mantle– crust system. *Earth Planet. Sci. Lett.* **148**, 243–258.

Blichert-Toft J., Chauvel C. and Albarède F. (1997) Hf and Lu for high-precision isotope analysis of rock samples by magnetic sector-multiple collector ICP-MS. *Contrib. Mineral. Petrol.* **127**, 248–260.

Bloch E., Watkins J. and Ganguly J. (2017) Diffusion kinetics of lutetium in diopside and the effect of thermal metamorphism on Lu–Hf systematics in clinopyroxene. *Geochim. Cosmochim. Acta* **204**, 32–51.

Bloch E., Watkins J. and Ganguly J. (2018) Comment on "Reconciliation of the excess ^{176}Hf conundrum in meteorites: Recent disturbances of the Lu-Hf and Sm-Nd isotope systematics" [*Geochim. Cosmochim. Acta* **212** (2017) 303–323]. *Geochim. Cosmochim. Acta* **230**, 190–192.

Bouvier A., Vervoort J. D. and Patchett P. J. (2008) The Lu–Hf and Sm–Nd isotopic composition of CHUR: Constraints from unequilibrated chondrites and implications for the bulk composition of terrestrial planets. *Earth Planet. Sci. Lett.* **273**(1-2), 48–57.

Burkhardt C., Borg L. E., Brennecka G. A., Shollenberger Q. R., Dauphas N. and Kleine T. (2016) A nucleosynthetic origin for the Earth's anomalous ^{142}Nd composition. *Nature* **537**(7620), 394–398.

Boyet M. and Carlson R. W. (2005) Chondrite barium, neodymium, and samarium isotopic heterogeneity and early Earth differentiation. *Science* **316**, 1175–1178.

Carlson R. W., Boyet M. and Horan M. (2007) ^{142}Nd evidence for early (>4.53 Ga) global differentiation of the silicate. *Science* **309**, 576–581.

Cassidy W.A. and Whillans I.M. eds. (1990) Workshop on Antarctic Meteorite Stranding Surfaces; LPI Tech. Rept. 90– 03. Lunar and Planetary Institute, Houston.

Chauvel C. and Blichert-Toft J. (2001) A hafnium isotope and trace element perspective on melting of the depleted mantle. *Earth Planet. Sci. Lett.* **190**, 137–151.

Crozaz G. (1974) U, Th and extinct ^{244}Pu in the phosphates of the St. Severin meteorite. *Earth Planet. Sci. Lett.* **23**, 164–169.

Crozaz G. (1979) Uranium and thorium microdistributions in stony meteorites. *Geochim. Cosmochim. Acta* **43**, 127–136.

Crozaz G. and Lundberg L. L. (1995) The origin of oldhamite in unequilibrated enstatite chondrites. *Geochim. Cosmochim. Acta* **59**, 3817–3831.

Crozaz G., Pellas P., Bourot-Denise M., de Chazal S. M., Fieni C., Lundberg L. L. and Zinner E. (1989) Plutonium, uranium and rare earths in the phosphates of ordinary chondrites— The quest for a chronometer. *Earth Planet. Sci. Lett.* **93**, 157–169.

Crozaz G., Floss C. and Wadhwa M. (2003) Chemical alteration and REE mobilization in meteorites from hot and cold deserts. *Geochim. Cosmochim. Acta* **67**, 4727–4741.

Curtis D. B. and Schmitt R. A. (1979) The petrogenesis of L-6 chondrites: insights from the chemistry of minerals. *Geochim. Cosmochim. Acta* **43**, 1091–1103.

Dauphas N. and Pourmand A. (2011) Hf–W–Th evidence for rapid growth of Mars and its status as a planetary embryo. *Nature* **473**(7348), 489–492.

Dauphas N. and Pourmand A. (2015) Thulium anomalies and rare earth element patterns in meteorites and Earth: Nebular fractionation and the nugget effect. *Geochim. Cosmochim. Acta* **163**, 234–261.

Debaille V., Brandon A. D., Yin Q. Z. and Jacobsen B. (2007) Coupled ^{142}Nd–^{143}Nd evidence for a protracted magma ocean in Mars. *Nature* **450**(7169), 525–528.

Debaille V., Orman J. V., Yin Q. Z. and Amelin Y. (2017) The role of phosphates for the Lu–Hf chronology of meteorites. *Earth Planet. Sci. Lett.* **473**, 52–61.

Delisle G., Schultz L., Spettel B., Weber H. W., Wlotzka F., Hofle H. C., Thierbach R., Vogt S., Herpers U., Bonani G. and Suter M. (1989) Meteorite finds near the Frontier Mountain Range in North Victoria Land. *Geol. Jb.* **38**, 483–513.

DePaolo D. J. and Wasserburg G. J. (1976) Nd isotopic variations and petrogenetic models. *Geophys. Res. Lett.* **3**, 249–252.

Ebihara M. (1987) Determination of ten lanthanoids in chondritic meteorites by radiochemical neutron activation analysis using coaxial and planar type pure Ge detectors. *J. Radioanal. Nucl. Chem.* **111**, 385–397.

Ebihara M. (1988) Trace element composition and distribution of Yamato-691, an unequilibrated enstatite chondrite. *Proc. NIPR Symp. Antract. Meteorites* **1**, 102–112.

Ebihara M. (1989) Rare earth and some other elements in acidresidues od unequilibrated ordinary chondrites. *Proc. NIPR Symp. Antract. Meteorites* **2**, 279–287.

Ebihara M., Hayano K. and Shirai N. (2020) Determination of trace rare earth elements in rock samples including meteorites by ICP-MS coupled with isotope dilution and comparison methods. *Anal. Chim. Acta* **1101**, 81–89.

Ebihara M. and Honda M. (1983) Rare earth abundances in chondritic phosphates and their implications for early stage chronologies. *Earth Planet. Sci. Lett.* **63**, 433–445.

Ebihara M. and Honda M. (1984) Distribution of rare earth elements and uranium in various components of ordinary chondrites. *Meteoritics* **19**(2), 69–77.

Ebihara M. and Honda M. (1987) Rare earth elements in Caphosphates of Allende carbonaceous chondrite. *Meteoritics* **3**, 179–190.

El Goresy A., Zinner E., Matsunami S., Palme H., Spettel B., Lin Y. and Nazarov M. (2002) Efremovka 101.1: a CAI with ultrarefractory REE patterns and enormous enrichments of Sc, Zr, and Y in Fassaite and Perovskite. *Geochim. Cosmochim. Acta* **66**(8), 1459–1491.

Fukai R. and Yokoyama T. (2017) Neodymium isotope heterogeneity of ordinary and carbonaceous chondrites and the origin of non-chondritic ^{142}Nd compositions in the Earth. *Earth Planet. Sci. Lett.* **474**, 206–214.

Gannoun A., Boyet M., Rizo H. and El Goresy A. (2011) ^{146}Sm–^{142}Nd systematics measured in enstatite chondrites reveals a heterogeneous distribution of ^{142}Nd in the solar nebula. *Proc. Natl. Acad. Sci.* **108**, 7693–7697.

Goderis S., Yesiltas M., Pourkhorsandi H., Shirai N., Poudelet M., Martin L., Yamaguchi A., Debaille V. and Claeys P. (2021) Detailed record of the BELARE 2019–2020 meteorite recovery expedition on the Nansen Ice Field, East Antarctica. *Antarctic Rec.* **65**, 1–20.

Green T. H. (1994) Experimental studies of trace-element partitioning applicable to igneous petrogenesis — Sedona 16 years later. *Chem. Geol.* **117**, 1–36.

Hannigan R. E. and Sholkovitz E. R. (2001) The development of middle rare earth element enrichments in freshwaters: weathering of phosphate minerals. *Chem. Geol.* **175**(3-4), 495–508.

Hezel D. C., Russell S. S., Ross A. J. and Kearsley A. T. (2008) Modal abundances of CAIs: implications for bulk chondrite element abundances and fractionations. *Meteorit. Planet. Sci.* **43**, 1879–1894.

Huss G. R., Rubin A. E. and Grossman J. N. (2006) Thermal metamorphism in chondrites. In *Meteorites and the Early Solar System II* (eds. Lauretta D. S. and McSween Jr. H. Y.). The University of Arizona Press, Tucson, pp. 567–586. In collaboration with Lunar and Planetary Institute, Houston.

Jacobsen S. B. and Wasserburg G. J. (1980) Sm–Nd isotopic evolution of chondrites. *Earth Planet. Sci. Lett.* **50**, 139–155.

Jacobsen S. B. and Wasserburg G. J. (1984) Sm–Nd isotopic evolution of chondrites and achondrites, II. *Earth Planet. Sci. Lett.* **67**, 137–150.

Jarosewich E. (1990) Chemical analyses of meteorites: a compilation of stony and iron meteorite analyses. *Meteoritics* **25**(4), 323–337.

Jochum M. P., Weis U., Scwager B., Stoll B., Wilson S. A., Haug G. H., Andreae M. O. and Enzweiler J. (2016) Reference values following ISO guidelines for frequently requested rock reference materials. *Geostand. Geoanal. Res.* **40**, 333–350.

Kleine T., Touboul M., Van Orman J. A., Bourdon B., Maden C., Mezger K. and Halliday A. N. (2008) Hf–W thermochronometry: closure temperature and constraints on the accretion and cooling history of the H chondrite parent body. *Earth Planet. Sci. Lett.* **270**(1-2), 106–118.

Koeberl C. and Cassidy W. (1991) Differences between Antarctic and non-Antarctic meteorites: an assessment. *Geochim. Cosmochim. Acta* **55**, 3–18.

Krot A. N., Keil K., Scott E. R. D., Goodrich C. A. and Weisberg M. K. (2003) Classification of meteorites. In *Meteorites, Comets,*

and Planets, Treatise on Geochemistry, vol 1 (ed. Davis A.M.). Elsevier-Pergamon, Oxford, chap. 1.05, pp. 83–128.

Krot A. N., Petaev M. I., Russell S. S., Itoh S., Fagan T. J., Yurimoto H., Chizmadia L., Weisberg M. K., Komatsu M., Ulyanov A. A. and Keil K. (2004) Amoeboid olivine aggregates and related objects in carbonaceous chondrites: records of nebular and asteroid processes. *Chemie der Erde* **64**(3), 185–239.

Larimer J. W. and Ganapathy R. (1987) The trace element chemistry of CaS in enstatite chondrites and some implications regarding its origin. *Earth Planet. Sci. Lett.* **84**, 123–134.

Lipschutz M. E. and Samuels S. M. (1991) Ordinary chondrites; multivariate statistical analysis of trace element contents. *Geochim. Cosmochim. Acta* **55**, 9–34.

Lugmair G. W. and Marti K. (1978) Lunar initial $^{143}Nd/^{144}Nd$: differential evolution of the lunar crust and mantle. *Earth Planet Sci. Lett.* **39**, 349–357.

Maeda R., Shirai N. and Ebihara M. (2017) Distribution of rare earth elements, Th and U in R chondrite. In *Lunar Plant. Sci.* **XLVIII**. Lunar and Planetary Institute, Houston. #2370 (abstract).

Martin C, Debaille V., Lanari P., Goderis S., Vandendael I., Vanhaecke F., Vidal O. and Claeys P. (2013) REE and Hf distribution among mineral phases in the CV–CK clan: a way to explain present-day Hf isotopic variations in chondrites. *Geochim. Cosmochim. Acta* **120**, 496–513.

Mason B. and Graham A. L. (1970) Minor and trace elements in meteoritic minerals. *Smithson. Contrib. Earth Sci.* **3**, 1–17.

McSween, Jr., H. Y., Bennett, III, M. E. and Jarosewich E. (1991) The mineralogy of ordinary chondrites and implications for asteroid spectroscopy. *Icarus* **90**, 107–116.

Middelburg J. J., van der Weijden C. H. and Woittiez J. R. W. (1988) Chemical processes affecting the mobility of major, minor and trace elements during weathering of granitic rocks. *Chem. Geol.* **68**, 253–273.

Mittlefehldt D. W. and Lindstrom M. M. (1991) Generation of abnormal trace element abundances in Antarctic eucrites by weathering processes. *Geochim. Cosmochim. Acta* **55**, 77–87.

Murrell M. T. and Burnett D. S. (1983) The behavior of actinides, phosphorus, and rare earth elements during chondrite metamorphism. *Geochim. Cosmochim. Acta* **47**, 1999–2014.

Nakamura N. (1974) Determination of REE, Ba, Fe, Mg, Na and K in carbonaceous and ordinary chondrites. *Geochim. Cosmochim. Acta* **38**, 757–775.

Nesbitt H. W. (1979) Mobility and fractionation of rare earth elements during weathering of a granodiorite. Nature 279 (5710), 206–210.

Nishiizumi K., Elmore D. and Kubik P. W. (1989) Update on terrestrial ages of Antarctic meteorites. *Earth Planet. Sci. Lett.* **93**, 299–313.

Nishikawa Y., Nakamura N., Misawa K., Okano O., Kagami H. and Yamamoto K. (1990) Investigation of the weathering effect on rb-sr systematics and trace element abundances in Antarctic and Non-Antarctic meteorites: a case of H-Chondrites. *Mass Spectrosc.* **38**(3), 115–123.

Patchett P. J., Vervoort J. D., Soderlund U. and Salters V. J. M. (2004) Lu–Hf and Sm–Nd isotopic systematics in chondrites and their constraints on the Lu–Hf properties of the Earth. *Earth Planet. Sci. Lett.* **222**, 29–41.

Pellas P. and Störzer D. (1975) Uranium and plutonium in chondritic phosphates. Meteoritics 10, 471 (abstract).

Perron C., Zanda B., Bourot-Denise M. and Mostefaoui S. (1992) Bishunpur and Semarkona: new clues to the origin of inclusions in metal. *Meteoritics* **27**, 275–276.

Pourkhorsandi H., D'Orazio M., Rochette P., Valenzuela M., Gattacceca J., Mirnejad H., Sutter B., Hutzler A. and Aboulahris M. (2017) Modification of REE distribution of ordinary chondrites from Atacama (Chile) and Lut (Iran) hot deserts: insights into the chemical weathering of meteorites. *Meteorit. Planet. Sci.* **52**, 1843–1858.

Pourkhorsandi H., Gattacceca J., Rochette P., D'Orazio M., Kamali H., de Avillez R., Letichevsky S., Djamali M., Mirnejad H., Debaille V. and Jull A. J. T. (2019) Meteorites from the Lut Desert (Iran). *Meteorit. Planet. Sci.* **54**, 1737–1763.

Pourkhorsandi H., Debaille V., Armytage R. M. G., van Ginneken M., Rochette P. and Gattacceca J. (2021) The effects of terrestrial weathering on samarium-neodymium isotopic composition of ordinary chondrites. *Chem. Geol.* **562**, 120056.

Righter K. and Shearer C. K. (2003) Magmatic fractionation of Hf and W: Constraints on the timing of core formation and differentiation in the Moon and Mars. *Geochim. Cosmochim. Acta* **67**(13), 2497–2507.

Shima M. (1979) The abundances of titanium, zirconium and hafnium in stony meteorites. *Geochim. Cosmochim. Acta* **43**, 353–362.

Shima M. and Honda M. (1967) Distributions of alkali, alkaline earth and rare earth elements in component minerals of chondrites. *Geochim. Cosmochim. Acta* **31**, 1995–2006.

Shimizu H., Masuda A. and Tanaka T. (1983) Cerium anomaly in REE pattern of Antarctic eucrite. *Mem. Nat. Inst. Polar Res. Tokyo. Spec Issue* **30**, 341–348.

Shinotsuka K. (1997) Abundances of rare earth elements, thorium and uranium in chondritic meteorites. Ph. D. Thesis, Tokyo Metropolitan University, Tokyo, Japan. DOI: 10.11501/ 3126008.

Stöffler D., Keil K. and Scott E. R. D. (1991) Shock metamorphism of ordinary chondrites. *Geochim. Cosmochim. Acta* **55**, 3845–3867.

Su N., Yang S., Guo Y., Yue W., Wang X., Yin P. and Huang X. (2017) Revisit of rare earth element fractionation during chemical weathering and river sediment transport. *Geochem. Geophys. Geosyst.* **18**(3), 935–955.

Tatsumoto M., Knight R. J. and Allegre C. J. (1973) Time differences in the formation of meteorites as determined from the ratio of lead-207 to lead-206. *Science* **180**(4092), 1279–1283.

Tatsumoto M., Unruh D. M. and Patchett P. J. (1981) U-Pb and Lu-Hf systematics of Antarctic meteorites. *Mem. Nat. Inst. Polar Res Tokyo. Spec Issue* **20**, 237–249.

Taylor S. R. and McLennan S. M. (1995) The geochemical evolution of the continental crust. *Rev. Geophys.* **33**, 241–265.

van der Weijden C. H. and van der Weijden R. D. (1995) Mobility of major, minor and some redox-sensitive trace elements and rare-earth elements during weathering of four granitoids in central Portugal. *Chem. Geol.* **125**(3-4), 149–167.

Van Schmus W. R. (1969) The mineralogy and petrology of chondritic meteorites. *Earth Sci. Rev.* **5**, 145–184.

Velbel M. A. (1988) The distribution and significance of evaporitic weathering products on Antarctic meteorites. *Meteoritics* **23**(2), 151–159.

Velbel M. A., Long D. T. and Gooding J. L. (1991) Terrestrial weathering of Antarctic stone meteorites: Formation of Mgcarbonates on ordinary chondrites. *Geochim. Cosmochim. Acta* **55**(1), 67–76.

Ward D., Bischoff A., Roszjar J., Berndt J. and Whitehouse M. J. (2017) Trace element inventory of meteoritic Ca-phosphates. *Am. Mineral.* **102**(9), 1856–1880.

Wasson J. T. and Kallemeyn G. W. (1988) Compositions of chondrites. *Philos. Trans. R. Soc. Lond* **A 325**, 535–544.

Weis D., Kieffer B., Maerschalk C., Barling J., de Jong J., Williams G. A., Hanano D., Pretorius W., Mattielli N., Scoates J. S., Goolaerts A., Friedman R. M. and Mahoney J. B. (2006) Highprecision isotopic characterization of USGS reference materials by TIMS and MC-ICP-MS. *Geochem. Geophys. Geosyst.* **7**(8).

Weis D., Kieffer B., Hanano D., Silva I. N., Barling J., Pretorius W., Maerschalk C. and Mattielli N. (2007) Hf isotope compositions of US Geological Survey reference materials. *Geochem. Geophys. Geosyst.* **8**, Q06006.

Weisberg M. K., Prinz M., Clayton R. N., Mayeda T. K., Grady M. M., Franchi I., Pillinger C. T. and Kallemeyn G. W. (1996) The K (Kakangari) chondrite grouplet. *Geochim. Cosmochim. Acta* **60**, 4253–4263.

Welten K. C., Nishiizumi K., Masarik J., Caffee M. W., Jull A. J. T., Klandrud S. E. and Wieler R. (2001) Cosmic-ray exposure history of two Frontier Mountain H-chondrite showers from spallation and neutron-capture products. *Meteorit. Planet. Sci.* **36**, 301–317.

Whillans I. M. and Cassidy W. A. (1983) Catch a falling star: meteorites and old ice. *Science* **222**(4619), 55–57.

de Winter N. J. and Claeys P. (2017) Micro X-ray fluorescence (μXRF) line scanning on Cretaceous rudist bivalves: a new method for reproducible trace element profiles in bivalve calcite. *Sedimentology* **64**, 231–251.

Yamaguchi A., Shiraishi K. and Harvey R. (2021) The discovery of meteorites near the Yamato Mountains: how the 1969 discoveries changed planetary science. *Meteorit. Planet. Sci.* **56**, 11– 12.

Zanda B., Bourot-Denise M., Perron C. and Hewins R. H. (1994) Origin and metamorphic redistribution of silicon, chromium and phosphorus in the metal of chondrites. *Science* **265**(5180), 1846–1849.

Associate editor: Audrey Bouvier

Chapter 3 "*Quantitative elemental mapping of chondritic meteorites using Laser Ablation-Inductively Coupled Plasma-Time of Flight-Mass Spectrometry (LA-ICP-TOF-MS)*" (Published in JAAS 2023)

Chapter introduction

In this chapter, we investigate the advantages of analytical development in analyzing meteorites and meteorite phases in an accurate and precise manner. In 2019, a collaborator research group of the AMGC group, the A&MS research unit at Ghent University, installed a state-of-the-art instrument Laser Ablation-Inductively Coupled Plasma-Time of Flight-Mass Spectrometry (LA-ICP-TOF-MS) as the first in Europe. LA-ICP-TOF-MS provides rapid quasi-simultaneous detection of nearly the entire elemental mass spectrum for each individual laser pulse and thus is an ideal tool for fast elemental mapping applications including trace elements in a (semi-)quantitative manner. We have invested significantly in applying this mapping to meteorite samples for examining and improving the potential of LA-ICP-TOF-MS mapping, *i.e.*, to fundamentally constrain how fast LA-ICP-TOF-MS mapping works on chondrite samples containing relatively small mineral grains in terms of the spatial resolution and the ability for quantification. As such, we applied this mapping approach to 12 HC samples including 4 falls and the LA-ICP-TOF-MS mapping provided a number of unexpected and interesting results, exhibiting the potential as a great screening tool for particular geological samples and future and past sample-return space mission (*e.g.*, Hayabusa 2, JAXA, and OSIRIS-REx, NASA).

This chapter demonstrates the potential of fast elemental mapping on HCs using LA-ICP-TOF-MS by comparison with conventional spot analyses using an electron probe micro analyzer (EPMA) and LA-ICP-sector field (SF)-MS. LA-ICP-TOF-MS mapping visualizes elemental distributions among the constituent minerals, while major and trace element abundances determined using LA-ICP-TOF-MS are overall in good agreement with up to 30% relative uncertainty compared to the values obtained based on the spot analyses and relative to literature values. In particular, the main host phase(s) of an element can readily be identified and the major and trace element abundances in the phase(s) can be quantified at an accuracy level approaching that of the spot analyses. Furthermore, the trace element maps also identify a local accumulation of REEs, Th, and U, likely resulting from terrestrial weathering. Thus, we conclude that fast LA-ICP-TOF-MS is highly efficient for visualizing and revealing the elemental distribution in chondrites, including the re-distribution related to terrestrial alteration in detail. The spot analyses using EPMA and LA-ICP-SF-MS at NIPR were conducted within the framework of the NIPR International Internship Program for Polar Science 2020.

Contributions to this paper

This study was led by RM and the AMGC, A&MS, NIPR, and G-Time teams. All *in-situ* measurements, interpretations, and writing were done by RM. LA-ICP-TOF-MS mapping was performed with the assistance of Thibaut Van Acker.

This chapter is published as:

Ryoga Maeda, Thibaut Van Acker, Frank Vanhaecke, Akira Yamaguchi, Vinciane Debaille, Phillippe Claeys and Steven Goderis (2023) Quantitative elemental mapping of chondritic meteorites using Laser Ablation-Inductively Coupled Plasma-Time of Flight-Mass Spectrometry (LA-ICP-TOF-MS). *Journal of Analytical Atomic Spectrometry* **38**, 369-381. DOI: 10.1039/d2ja00317a.

Electronic Supplementary Information (ESI) for this chapter can be found at: https://doi.org/10.1039/d2ja00317a.

JAAS

PAPER

Quantitative elemental mapping of chondritic meteorites using Laser Ablation-Inductively Coupled Plasma-Time of Flight-Mass Spectrometry (LA-ICP-TOF-MS)†

Ryoga Maeda,[*a,b] Thibaut Van Acker,[c] Frank Vanhaecke,[c] Akira Yamaguchi,[d] Vinciane Debaille,[b] Phillippe Claeys[a] and Steven Goderis[a]

Fast elemental mapping using laser ablation-inductively coupled plasma–time of flight–mass spectrometry (LA-ICP-TOF-MS) was applied to a set of chondritic meteorite samples, more specifically H chondrites. LA-ICP-TOF-MS enables element distribution maps for both major and trace elements to be obtained at µm-order spatial resolution (5×5 µm square pixels in this study) in a (semi-)quantitative manner. To assess the reliability of the quantitative data as obtained using LA-ICP-TOF-MS mapping, the accuracy and precision as obtained using this fast elemental mapping approach were compared to those of the data obtained using the more conventional spot analysis with an electron probe micro analyzer and LA-ICP-sector field (SF)-MS for major and trace elements, respectively. The maps obtained using LA-ICP-TOF-MS visualize elemental distributions among the constituent minerals, while major and trace element abundances determined using LA-ICP-TOF-MS are overall in good agreement within up to 30% relative uncertainty with those obtained based on the spot analyses and with literature values. Yet, some analytical limitations of LA-ICP-TOF-MS mapping remain due to the limited ablated yield when using a small laser spot size for high spatial resolution mapping, while ICP-TOF-MS shows a lower sensitivity and narrower linear dynamic range than does ICP-SF-MS. On the other hand, the main host phase(s) of an element can be readily identified and the major and trace element abundances in the phase(s) can be quantified with an accuracy approaching that of the spot analyses. As such, this study demonstrates the potential of LA-ICP-TOF-MS for fast quantitative imaging of various types of samples, in particular geological samples.

Introduction

In-situ spot analysis and elemental mapping in geological and geochemical research are commonly based on electron probe micro analysis (EPMA), scanning electron microscopy in combination with energy-dispersive X-ray spectrometry, micro-X-ray fluorescence spectrometry (µXRF), or secondary ion mass spectrometry (SIMS). Most of these techniques are valuable in the context of major element concentrations (generally > 0.1 % m/m level) for both spot analysis and mapping, but their application is more limited in relation to trace element analysis due to their relatively high limits of detection. For the determination of trace elemental abundances, laser ablation-inductively coupled plasma-mass spectrometry (LA-ICP-MS) is now widely used as a direct solid sampling micro-analytical technique.[1-3] LA-ICP-MS technique not only determines the trace elemental abundances in mineral phases, but also provides spatially resolved information under the form of elemental maps for major, minor, and trace elements.[4,5] Recently, hardware developments focusing on low-dispersion ablation cells and aerosol transport systems, which reduce the duration of single pulse response profiles and boost the signal-to-noise ratio and speed of analysis, significantly improved the analytical capabilities of LA-ICP-MS elemental mapping.[6,7] Moreover, the launch of commercially available time-of-flight (TOF) based ICP-mass spectrometers, providing rapid quasi-simultaneous detection of nearly the entire elemental mass spectrum for each individual laser pulse, has boosted the use of LA-ICP-MS for elemental mapping applications in a wide variety of research fields. ICP-TOF-MS instruments can handle the short transient signals produced with low-dispersion LA setups and provide fast multi-elemental detection in contrast to sequential scanning-type ICP-mass spectrometers such as quadrupole (Q) or sector field (SF)-based mass analyzers.[7-10] TOF-based mass analyzers have also been developed for SIMS.[11,12] TOF-SIMS and LA-ICP-TOF-MS are complementary in terms of mapping: TOF-SIMS is capable of achieving a higher spatial resolution at the order of tens of nm and a higher depth resolution, but with a limited range in terms of analysis area up to about tens of µm, while LA-ICP-TOF-MS is capable of handling mm-cm ranges of analysis area with µm-order spatial resolution. To reveal

[a] Analytical-, Environmental-, and Geo-Chemistry, Vrije Universiteit Brussel, Pleinlaan 2, 1050 Brussels, Belgium. E-mail: ryoga.maeda@vub.be
[b] Laboratoire G-Time, Université libre de Bruxelles, CP 160/02, 50, Av. F.D. Roosevelt, 1050 Brussels, Belgium.
[c] Atomic & Mass Spectrometry (A&MS) Research Unit, Department of Chemistry, Ghent University, Campus Sterre, Krijgslaan, 281 – S12, 9000 Ghent, Belgium.
[d] National Institute of Polar Research, 10-3 Midori-cho, Tachikawa-shi, Tokyo 190-8518, Japan.
† Electronic Supplementary Information (ESI) available: See DOI: https://doi.org/10.1039/d2ja00317a

elemental distributions among the constituent minerals in geological samples in a (semi-)quantitative manner, LA-ICP-TOF-MS is preferred due to the larger range of analysis area (cm order) and significantly lower matrix effects than TOF-SIMS.

Meteorites are divided into two major categories, chondritic and non-chondritic meteorites based on their bulk compositions and textures.[13] Chondritic meteorites generally consist of chondrules embedded in a very fine-grained matrix (< 5 µm). LA-ICP-TOF-MS mapping is an ideal tool for studying such samples because their elemental distributions among the constituent minerals, especially in the case of trace elements, remain poorly understood due to the small size of minerals. To date, however, the application of LA-ICP-TOF-MS to geological samples has been limited.[10,14-23] In addition, the technique has so far been applied to meteorite samples in few studies.[15] Therefore, in this study, LA-ICP-TOF-MS mapping is applied to a set of H group of ordinary chondrites (H chondrites), which are the most abundant of all meteorite classes (~40% by number: based on the Meteoritical Bulletin Database, http://www.lpi.usra.edu/meteor/metbull.php, accessed 27 September 2022), with the aim of assessing the potential of state-of-the-art LA-ICP-TOF-MS instrumentation in terms of speed, spatial resolution, LODs, and accuracy and precision For this purpose, the quantitative data obtained were compared with those using with more conventional EPMA and LA-ICP-SF-MS spot drilling approaches.

Experimental

Samples

The same polished thick sections (PTSs) as those studied in Maeda *et al.* (2021)[24] were used for the analyses described below. Additionally, PTSs for Jilin (H5), Nuevo Mercurio (H5), Richardton (H5), and Butsura (H6) were allocated by the Royal Belgian Institute of Natural Sciences (RBINS), Belgium, and prepared for these analyses. Petrographic information on the meteorite samples is listed in Table 1. Note that the following results of two samples, A 09618 (H5) and Y-790960 (H7), of a larger 16-sample collection that was studied in a systematic manner are fundamentally shown in this study. Note that for reasons of conciseness, only the results for two samples, A 09618 (H5) and Y-790960 (H7) out of the larger 16-sample collection, are shown in this fundamental study.

LA-ICP-TOF-MS mapping

Prior to LA-ICP-TOF-MS mapping, all PTSs were analyzed using a Bruker M4 Tornado µXRF scanner equipped with a Rh source and two XFlash 430 Silicon Drift detectors at the Vrije Universiteit Brussel (VUB), Belgium, to obtain major element maps. These analyses have been described in detail in Maeda *et al.* (2021).[24] The PTSs of 12 samples (A-880941, A-881258, A 09436, A 09387, NWA 6771, Jilin, Nuevo Mercurio, Richardton, A 09618, Butsura, A 09516, and Y-790960) were analyzed using pulse-resolved multi-elemental LA-ICP-TOF-MS mapping at Ghent University, Belgium. Two LA-units equipped with a 193 nm ArF* excimer-based nanosecond lasing system were used: a customized Teledyne Photon Machines Analyte G2 and a commercially available Teledyne Photon Machines Iridia LA-unit equipped with a prototype and commercially available version of the Cobalt ablation chamber, respectively.

Table 1 List of chondritic meteorite samples analyzed in this study (n.d.: not determined).

Meteorite	Type	Weathering
A-880941	H3.3	A/B
Y-793574	H3.5	n.d.
Y-790461	H3.7	B
ALH 78084	H3.9	B/Ce
A-881258	H3.9[a]	B
A 09436	H3	C
A 09387	H4	B/C
NWA 6771	H4	W1
Jilin	H5	n.d.
Nuevo Mercurio	H5	n.d.
Richardton	H5	n.d.
A 09618	H5	C
Sahara 97035	H5	W2
Butsura	H6	n.d.
A 09516	H6	C
Y-790960	H7	B

See Maeda *et al.* (2021)[24] for the details of the type and weathering index.

[a] Ninagawa *et al.* (2005).[25]

Table 2 Instrument settings and data acquisition conditions for LA-ICP-TOF-MS mapping.

Analyte G2 and Iridia LA-units	
Laser energy density (J/cm²)	4.00
Repetition rate (Hz)	100 or 200*
Spot size (µm)	5
Mask shape	square
Lateral scan speed (µm/s)	500 or 1000*
He carrier gas flow rate (L/min)	0.50
icpTOF 2R ICP-mass spectrometer	
RF power (W)	1580
Ar plasma gas flow rate (L/min)	15
Ar auxiliary gas flow rate (L/min)	0.90
Ar make-up gas flow rate (L/min)	0.96
Integrated TOF spectra per data point	103-206

* Either 100 Hz with 500 µm/s or 200 Hz with 1000 µm/s for the repetition rate and the lateral scan speed.

Both systems were equipped with low-dispersion tube cell-type ablation cells.[6,7,26,27] The LA-units were coupled to a TOFWERK icpTOF 2R ICP-TOF-MS unit equipped with a 1 mm inner diameter torch injector via a low-dispersion aerosol transport system, named "aerosol rapid introduction system" (ARIS), developed at Ghent University, and commercialized by Teledyne Photon Machines.[28] The instrumental setups provide fast quasi- simultaneous detection across almost the entire elemental mass range (14-256 amu), which is highly beneficial for pulse-resolved multi-elemental mapping applications as mentioned above.[9,15,29] Daily tuning of the instrument settings and data acquisition conditions was performed while ablating NIST SRM 612 glass reference material aiming at low laser-induced elemental fractionation ($^{238}U^{+}/^{232}Th^{+} \approx 1$), high sensitivity across the elemental mass range and low levels of oxide formation ($^{238}U^{16}O^{+}/^{238}U^{+} < 0.5\%$). All instrument settings and data acquisition conditions for the fast LA-ICP-TOF-MS mapping approach are listed in Table 2.

The regions of interest for LA-ICP-TOF-MS mapping were selected based on the major element X-ray maps. For each sample, these X-ray maps were imported into Chromium v2.7, the operating software of the LA-unit, and were aligned to the live camera view, *i.e.*, to the actual position and orientation of the samples in the ablation chamber. For quantification purposes, 13 external calibration standards (MPI-DING glass reference materials: ATHO-G, GOR128-G, KL2-G, ML3B-G, StHs6/80-G, and T1-G; USGS glass reference materials: BCR-2G, BHVO-2G, BIR-1G, GSD-1G, GSE-1G, and NKT-1G; and in-house Durango apatite) were analyzed before and after mapping the regions of interest in the meteorite samples. Ablation was performed according to consecutive edge-to-edge line scans over regions of interest of 1-10 mm^2 using a square laser spot size of 5×5 µm and the data/pixel acquisition rate was matched to the laser repetition rate of either 100 or 200 Hz.

The elemental mass spectra were recorded using the TOFWERK Tofpilot v2.8 software and stored in HDF5 files, an open-source hierarchal data format. The data analysis package Tofware v3.1.1 was used for data post-processing including time-dependent mass calibration, modeling and subtracting baseline signal intensities, and peak shape determination and integration.[30] Subsequently, Teledyne HDIP software v.1.6 was used for further data post-processing steps, such as external calibration based on a sum normalization approach and exporting the quantitative elemental maps.[31] Once the quantitative elemental maps were obtained, each constituent mineral in a sample was systematically identified using "clustering zones", which is a k-means clustering algorithm automatically identifying the phases based on the levels of selected elements in the HDIP software. Given the constituent minerals in H chondrites, the automatic clustering was performed based on the following elements: Na, Mg, Al, Si, P, S, Ca, Sc, Ti, Cr, and Fe. Images identified using the automatic clustering approach are shown in Figure 4 and discussed together with the results of the elemental maps. Note that two phosphate phases in the meteorite samples, apatite and merrillite, were masked manually because the clustering did not effectively distinguish between these phases. Finally, the elemental abundances in the constituent minerals were determined by taking an average of the elemental abundances in the corresponding regions. To avoid matrix effects as much as possible, especially in the case of the phosphate phases, phases of silicates, phosphates, and the others were differently calibrated using all the MPI-DING and USGS glasses, the Durango apatite only, and all the MPI-DING and USGS glasses combined with the Durango apatite, respectively. The following nuclides were used for the quantification: ^{23}Na, ^{24}Mg, ^{27}Al, ^{28}Si, ^{31}P, ^{39}K, ^{43}Ca, ^{45}Sc, ^{49}Ti, ^{51}V, ^{52}Cr, ^{55}Mn, ^{57}Fe, ^{59}Co, ^{60}Ni, ^{63}Cu, ^{66}Zn, ^{85}Rb, ^{88}Sr, ^{89}Y, ^{137}Ba, ^{90}Zr, ^{93}Nb, ^{139}La, ^{140}Ce, ^{141}Pr, ^{143}Nd, ^{147}Sm, ^{153}Eu, ^{157}Gd, ^{159}Tb, ^{163}Dy, ^{165}Ho, ^{167}Er, ^{169}Tm, ^{173}Yb, ^{175}Lu, ^{178}Hf, ^{181}Ta, ^{208}Pb, ^{232}Th, and ^{238}U. BHVO-2G, GOR128-G, and the Durango apatite were also quantified using the same procedures for the validation of this analysis. Incidentally, BHVO-2G and GOR128-G were calibrated as silicate phase while the Durango apatite was calibrated as phosphate phase.

Electron probe microanalysis

First, all the samples to be analyzed using LA-ICP-TOF-MS were slightly polished and subjected to the following analyses. Back-scattered electron (BSE) images of all PTSs were generated using a JEOL JSM-7100F field emission-scanning electron microscope (FE-SEM) equipped with an Oxford energy-dispersive spectrometer at the National Institute of Polar Research (NIPR), Japan. By combining the BSE images with the X-ray maps obtained using µXRF, the constituent minerals in the samples were identified. Based on the constituent minerals identified, the major and minor elemental abundances of the constituent minerals in the PTSs were determined using a JEOL JXA-8200 electron micro probe analyzer at the NIPR. All analyses were carried

Table 3 EPMA experimental conditions for each mineral phase.

Mineral phase	Beam current (nA)	Beam size (µm)	Monitored elements
Phosphate	5	5	F, Na, Ma, Si, P, Cl, Ca, and Fe
Olivine, pyroxene, and oxide	30	<1	Na, Mg, Al, Si, P, Ca, Ti, V, Cr, Mn, Fe, Ni, and Zn
Feldspar	10	<1 or 1	Na. Mg, Al, Si, P, K, Ca, Ti, Cr, Mn, and Fe

out using a 15 kV accelerating voltage. Different measurement conditions were used depending on the mineral phase, and these conditions are listed in Table 3. Counting times ranged from 10 to 100 s on peaks for each mineral. Correction procedures are based on the ZAF method. As a result of the occurrence of overlapping signals, the intensity of V was mathematically corrected for the intensity of Ti. Natural and synthetic silicates, oxides, and metals with well-known chemical compositions were used as standards. A fluorapatite standard was used for the quantification of F.

Spot drilling analysis using LA-ICP-SF-MS

The trace element abundances of Ca-phosphates and silicates in the samples were determined using LA-SF-ICP-MS in single-point drilling mode. These measurements were performed using a Teledyne CETAC LSX-213 G2+ LA-system coupled to a Thermo Element XR ICP-SF-MS unit at the NIPR. The laser system provides an output wavelength of 213 nm and 100 shots were fired per spot analysis at a laser repetition of 10 Hz and a laser energy density of 36 J/cm^2. Oxide formation was set to a low level by tuning the parameters while ablating NIST SRM 612 glass reference material ($^{232}Th^{16}O^+/^{232}Th^+ < 0.5\%$). All nuclide peaks were collected at low mass resolution (M/ΔM = ~300) with triple mode detection and the following nuclides were monitored for the major elements: ^{23}Na, ^{24}Mg, ^{27}Al, ^{29}Si, ^{31}P, ^{39}K, ^{43}Ca, ^{44}Ca, and ^{57}Fe; and for the trace elements: ^{45}Sc, ^{51}V, ^{55}Mn, ^{66}Zn, ^{85}Rb, ^{88}Sr, ^{89}Y, ^{137}Ba, ^{139}La, ^{140}Ce, ^{141}Pr, ^{146}Nd, ^{147}Sm, ^{151}Eu, ^{157}Gd, ^{159}Tb, ^{161}Dy, ^{165}Ho, ^{166}Er, ^{169}Tm, ^{173}Yb, ^{175}Lu, ^{178}Hf, ^{208}Pb, ^{232}Th, and ^{238}U. All peaks were acquired by peak jumping between peak tops with 10% mass window (average of 5 peaks on the peak top) and 50–100 milliseconds of acquisition time on the peak top. Depending on the target phase, nuclides monitored were selected among those mentioned above and laser spot sizes were selected so that detectable intensities were obtained, especially in the case of the rare earth elements (REEs). This information is summarized in Table 4.

Elemental abundances were calculated using average relative sensitivity factors (RSFs) obtained from triplicate analysis of the in-house Durango apatite for phosphate phases (except for Rb and Hf) and BCR2-G, BHVO2-G, and ML3B-G for all other phases as well as for Rb and Hf in phosphate phases.[32] For phosphate and silicate phases, elemental abundances obtained based on EPMA were used as an internal standard, either P or Ca, Si or Ca, Al or Si, and Si or Fe for phosphate, pyroxene, feldspar, and olivine phases, respectively. When the laser purely ablated the target mineral grain without any overlap with other phases, there was no resolvable difference in the abundances calculated between both internal standards. Thus, in this case, Ca, Al, and Fe were used as the internal standard for phosphate and pyroxene, feldspar, and olivine phases, respectively. However, the signals from these internal standards were in some subject spectrally overlapping with signals from major elements of other phases (*e.g.*, the ablation on the edge between two phases). In these cases, the other element was used as the internal standard for the corresponding phases if the effects of the overlap on the internal element and the trace elements were negligible. Specifically, the effects were considered negligible in case there was < 10% discrepancy with the data obtained upon ablation of the corresponding pure phases in which the major elemental abundances obtained are in good agreement with those obtained based on EPMA. Any data points showing a larger discrepancy were discarded. Consequently, the number of data points for some phases is limited, even though at least three grains per phase were analyzed for each sample. The precision and accuracy of each analysis were confirmed via analysis of the ATHO-G, GOR128-G, and GOR132-G reference materials using the same quantitative procedures.

Results and discussion

Assessment of quantification using LA-ICP-TOF-MS mapping and LA-ICP-SF-MS spot analysis

The elemental abundances in the reference materials determined using LA-ICP-TOF-MS mapping are listed in ESI Table 1,† together with their preferred or reference values and limits of detection (LODs) for each analysis point calculated using the IUPAC approximation formula.[33] Overall, elements contained in the material at more than 0.1 % m/m level are within ~10% relative uncertainty (RU) and those at μg/g level are within ~20% RU. Most elemental abundances obtained for BHVO-2G and GOR128-G and those in the Durango apatite agree within ~30% and ~20% of their preferred and reference values, respectively (Figure 1). In most cases in which the preferred or reference values were close to the LOD, the abundances obtained display a larger discrepancy from their comparison value (> 20%). For example, in the case of K in GOR128-G, the LOD is 0.01 % m/m, the preferred value is 0.030 % m/m, and the value obtained is 0.13 % m/m. Such a large discrepancy is also observed for Co in BHVO-2G and Ba, Ce,

Table 4 Experimental conditions of each mineral phase for LA-ICP-SF-MS spot analysis.

Mineral phase	Spot size (μm)	Monitored major elements	Monitored trace elements
Phosphate	10 - 100	Mg, Al, Si, P, Ca, Mn, and Fe	V, Rb, Sr, Y, Ba, REEs, Hf, Pb, Th, and U
Pyroxene	30 - 100	Mg, Al, Si, P, Ca, and Fe	Sc, Zn, Rb, Sr, Y, Ba, REEs, Hf, Pb, Th, and U
Feldspar and olivine	50 - 100	Na, Mg, Al, Si, P, K, Ca, Mn, and Fe	Zn, Rb, Sr, Y, Ba, REEs, Hf, Pb, Th, and U

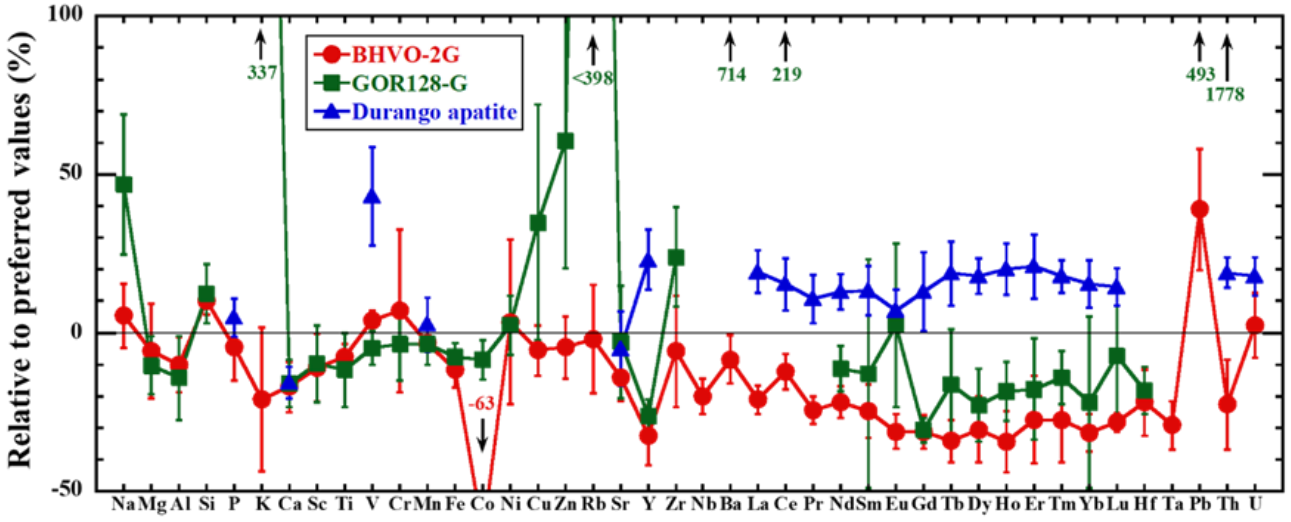

Figure 1 Bias (%) between the elemental abundances in reference materials obtained using LA-ICP-TOF-MS mapping and the corresponding preferred values (see Supplementary Table 1 for the details of the comparison values).[34-37] The error bars represent 1SD.

Pb, and Th in GOR128-G. Except for Co in BHVO-2G, all other values displaying such discrepancy are significantly higher than the preferred values and exhibit a large RU up to ~70%. Even though the signals of these elements monitored were above the LOD, the preferred values, *i.e.*, the actual values of these elements in GOR128-G are overall below the LOD and thus their abundances are considered unreliable, causing the observed discrepancy.

The trace element abundances in the reference materials obtained using LA-ICP-SF-MS spot analysis (hereafter LA-spot analysis) are listed in ESI Table 2,† together with their preferred values and LOD values (3SD). On average, the RU for each analysis is up to ~15% although Th and U in GOR128-G and GOR132-G, which are present at the level of less than tens of ng/g, display relatively high RUs (~20-85%). Compared with their preferred values, most elemental abundances determined overlap within uncertainty (Figure 2). A relatively large discrepancy between the obtained and preferred value is observed for Pb in ATHO-G and Th and U in GOR132-G determined using the

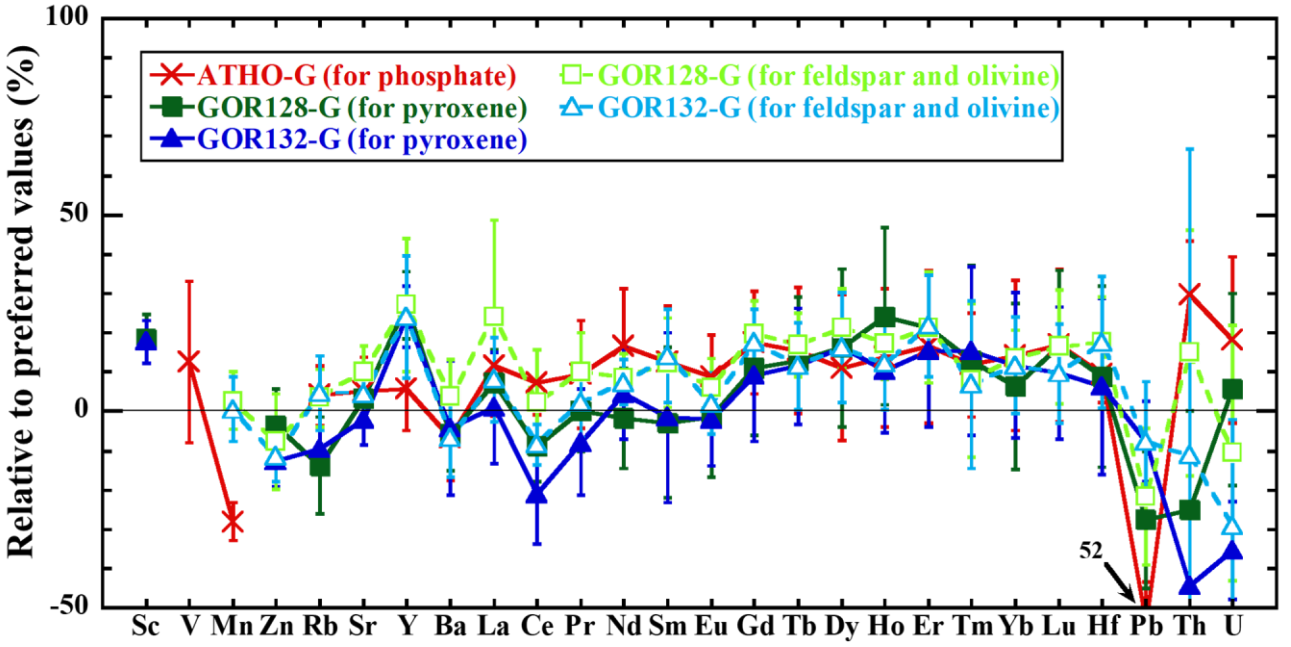

Figure 2 Bias (%) between the elemental abundances in reference materials obtained using LA-ICP-SF-MS spot analysis and the corresponding preferred values.[35] The error bars represent 1SD.

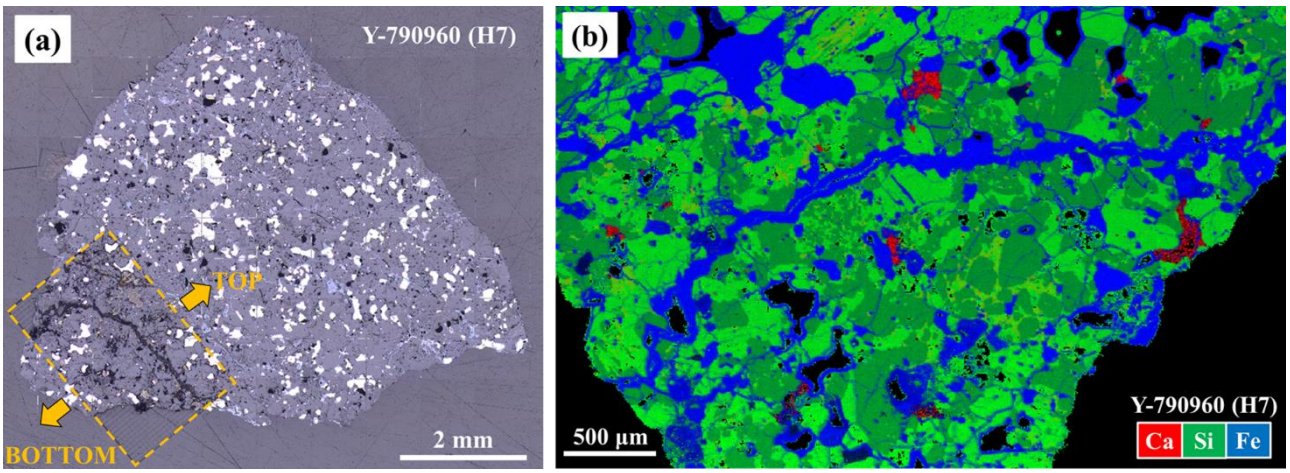

Figure 3 Optical image with the region analyzed using LA-ICP-TOF-MS mapping indicated by a broken orange rectangle (a) and a combined semi-quantitative element map obtained using LA-ICP-TOF-MS mapping (b) for meteorite Y-790960. The element map is shown in RGB (red: Ca, green: Si, and blue: Fe) and the color brightness in the RGB map indicates their abundance level as higher abundance is brighter.

pyroxene analysis condition (~50% differences from the preferred values). Especially in the case of Th in GOR132-G, the ratio of the LOD value to the preferred value is one of the largest values at ~5% while those of the other elements in all other analyses are less than 1%, which is similar to those obtained for LA-ICP-TOF-MS mapping in terms of those ratios. However, different from LA-ICP-TOF-MS mapping, all the values obtained with a large discrepancy are lower than the preferred values and none of the values obtained exceeding their preferred values display more than a 30% difference.

Based on the assessment of accuracy and precision of the quantitative procedure for LA-ICP-TOF-MS mapping and LA-spot analysis described above, the RU of elemental abundances in unknown samples obtained using LA-ICP-TOF-MS mapping identified as phosphate phases, all other phases, and LA-spot analysis can be estimated at 30%, 20%, and 15%, respectively. These RUs estimated are applied to the following results.

Quantitative elemental mapping of meteorites using LA-ICP-TOF-MS

Figure 3 shows an optical image for Y-790960 (H7) after being ablated for LA-ICP-TOF-MS mapping and a combined semi-quantitative element map for Y-790960 in RGB (Ca, Si, and Fe, respectively) obtained using LA-ICP-TOF-MS mapping. Metal and sulfide phases occur as bright (white) areas in Figure 3 (a). As such, the region ablated for LA-ICP-TOF-MS mapping obviously contains these metal and sulfide phases. However, the metal phase was not successfully ablated by the nanosecond laser pulses and thus some black regions are visible in Figure 3 (b), while the other phases including sulfide were ablated properly. Figure 4 shows combined RGB elemental maps and quantitative elemental maps for A 09618 (H5) together with the corresponding optical and BSE images and images identified for individual mineral phases using the automatic clustering approach. When comparing Figures 4 (a)-(d), all phases including the metal phase in the region of interest appear to have been ablated successfully. This successful ablation of the metal phase may be due to the metal phase in this sample being oxidized or hydrated by terrestrial weathering to some degree. Therefore, all elemental maps obtained with the experimental conditions selected for LA-ICP-TOF-MS mapping in this study do not contain metal phases unless these phases are oxidized or hydrated.

Figure 3 (a) shows that the region analyzed using LA-ICP-TOF-MS retains some traces of the ablation as the contrast of this region is different from that of the non-ablated area. However, no effects of this damage are observed upon BSE imaging (Figure 4 (b)). In addition, there are no resolvable differences in the elemental abundances within the minerals as obtained using EPMA and LA-spot analysis, following prior ablation. While the effects resulting from ablation of LA-ICP-TOF-MS mapping in this study appear limited based on BSE imaging, EPMA, and LA-spot analysis, optical and detailed petrographic observations using FE-SEM may indicate minor but discernible effects. In contrast, with the applied experimental condition for LA-ICP-TOF-MS mapping, pure metal was not ablated. As thermal diffusion in metal phases occurs more rapidly than in the other phases, the laser energy density was likely not sufficient to ablate metal. Although ablating the metal phase at higher laser energy density (7-8 J/cm^2) was attempted, the ablation of the metal phase remained ineffective. On the other hand, metal phases in iron meteorites were successfully ablated at a significantly higher laser energy density of 36 J/cm^2 using the Teledyne CETAC LSX-213 G2+ nanosecond LA-system at the NIPR.[38] However, this approach may result in total ion counts that exceed the detector's linear dynamic signal range of the icpTOF 2R (6 orders of magnitude), as the highest total ion count already reached 10^5-cps level with the experimental conditions used in this study. Furthermore, ablation with such a high energy density increases the degree of damage

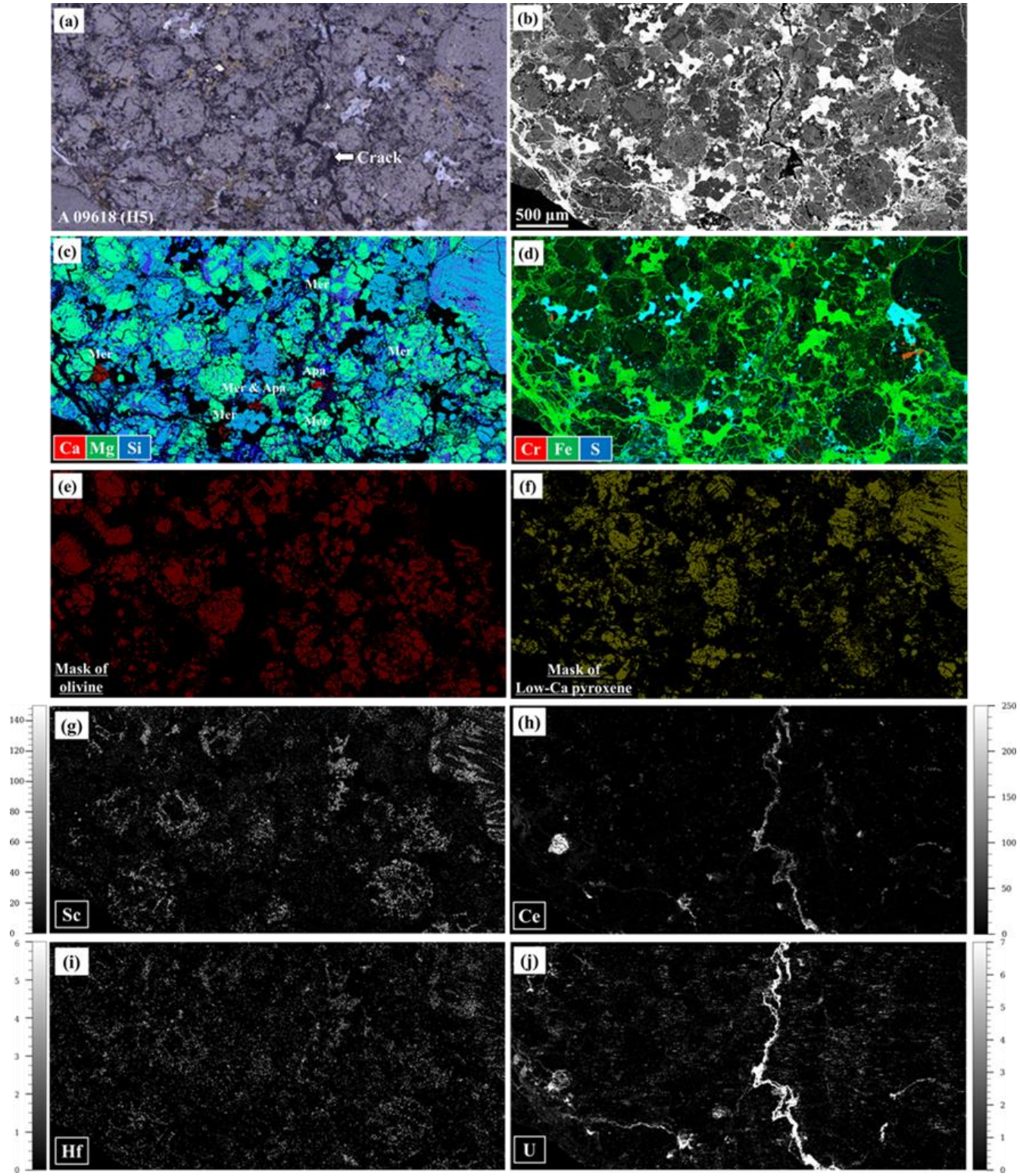

Figure 4. Optical and BSE images, individual mineral phase images after clustering, and (semi-)quantitative element maps for meteorite A 09618. (a) Optical image of the region analyzed using LA-ICP-TOF-MS. (b) BSE image of the region analyzed using mapping. (c) Combined RGB elemental map obtained using LA-ICP-TOF-MS mapping with red: Ca, green: Mg, and blue: Si. Based on the composition, the following mineralogy can be deduced red: Ca-phosphates (Mer: merrillite; Apa: chlorapatite), light green: olivine, light blue: low-Ca pyroxene, blue: feldspar, and violet: Ca-rich pyroxene. (d) Combined RGB elemental map with red: Cr, green: Fe, and blue: S. (e) Olivine phase identified using the automatic clustering. (f) Low-Ca pyroxene phase identified using the automatic clustering. (g) Scandium distribution map. (h) Cerium distribution map. (i) Hafnium distribution map. (j) Uranium distribution map. Scale bars for (g)-(j) in µg/g.

to the selected region of interest for LA-ICP-TOF-MS mapping, resulting in apparent effects for subsequent BSE imaging, EPMA, and LA-spot analysis.

Figure 5 shows combined elemental maps for Y-790960. Figures 4 (c) and 5 (a) exhibit their combined Ca, Mg, and Si maps, allowing identification of Ca-phosphates, Ca-rich

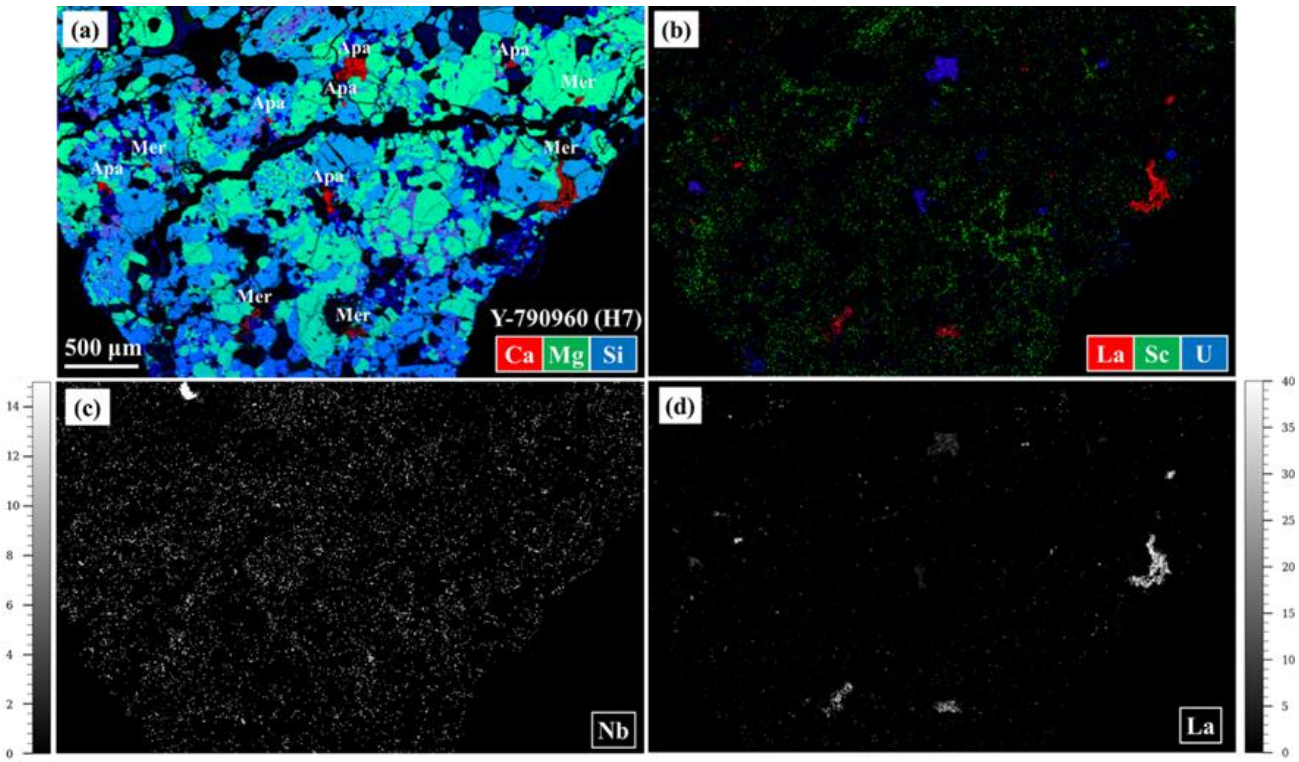

Figure 5. (Semi-)quantitative element maps for meteorite Y-790960. (a) Combined RGB elemental map with red: Ca, green: Mg, and blue: Si. Based on the composition, the following mineralogy can be deduced, red: Ca-phosphates (Mer: merrillite; Apa: chlorapatite), light green: olivine, light blue: low-Ca pyroxene, blue: feldspar, and violet: Ca-rich pyroxene. (b) Combined RGB elemental map with red: La, green: Sc, and blue: U. (c)Niobium distribution map. (d) Lanthanum distribution map. Scale bars for (c) and (d) in µg/g.

pyroxene, low-Ca pyroxene, feldspar, and olivine. Chromite, metal, and sulfide phases can be distinguished based on the Cr, Fe and S abundances in Figure 4 (d) as these appear in reddish orange, green, and bright blue, respectively. As such, the constituent minerals in the meteorite samples are readily identified using major element maps obtained based on LA-ICP-TOF-MS mapping. Figures 4 (e) and (f) display the results of the automatic clustering approach for individual mineral phases (*i.e.*, olivine and low-Ca pyroxene, respectively), as applied during the quantitative procedure. Based on Figures 4 (b) and (c), the automatic clustering zones are highly efficient at identifying the individual target silicate phases. This is a significant advantage of LA-ICP-TOF-MS mapping in terms of obtaining representative elemental abundances for the target phase, because the elemental abundances obtained using LA-ICP-TOF-MS mapping were averaged with as many grains as contained in the region analyzed, while conventional spot analysis usually provides those averaged based on a few grains only, especially in the case of trace element analysis. Combined, Figures 4 (c), (h), and (j) and Figures 5 (a), (b), and (d) demonstrate that REEs and U are concentrated in Ca-phosphate phases, with REEs mainly hosted in merrillite and U in apatite. Scandium and Hf are largely distributed in Ca-rich pyroxene according to Figures 4 (c), (g), and (i). Based on Figure 5 (c), Nb is highly concentrated in a phase identified as ilmenite. These observations are entirely consistent with previously determined elemental distributions and partition coefficients.[39-42] Therefore, LA-ICP-TOF-MS mapping provides adequate elemental distributions not only of major elements but also of trace elements, at least in their main host phase(s). Surprisingly, a significant fraction of the REEs and U reside in the crack displayed in Figure 4, almost at the same concentration levels as those observed in merrillite. A similar deposition was confirmed in other samples analyzed in this study (A 09436, A 09387, NWA 6771, Nuevo Mercurio, and A 09516). This distribution is also consistent with chemical leaching experiments,[43] in which REEs, Th, and U have been deduced to reside in cracks and along grain boundaries. These depositions in cracks likely result from terrestrial weathering because most meteorite samples displaying such depositions are heavily weathered (Table 1). The trace element mapping using LA-ICP-TOF-MS reported here represents the first instance in which such depositions are visually confirmed, and as such LA-ICP-TOF-MS mapping demonstrates the capability to determine elemental distributions in cracks and along grain boundaries where conventional spot analyses cannot be applied readily.

As demonstrated by Figures 4 (g)-(h) and Figures 5 (c) and (d), quantitative elemental maps were obtained using LA-ICP-TOF-MS. The elemental abundances for the whole area studied in A 09618 and Y-790960 as determined using LA-ICP-TOF-MS mapping are listed in ESI Table 3,† together with their bulk rock values and H chondrite mean values as a comparison.[24] In the following, only the results for A 09618 and Y-790960 are described and discussed in

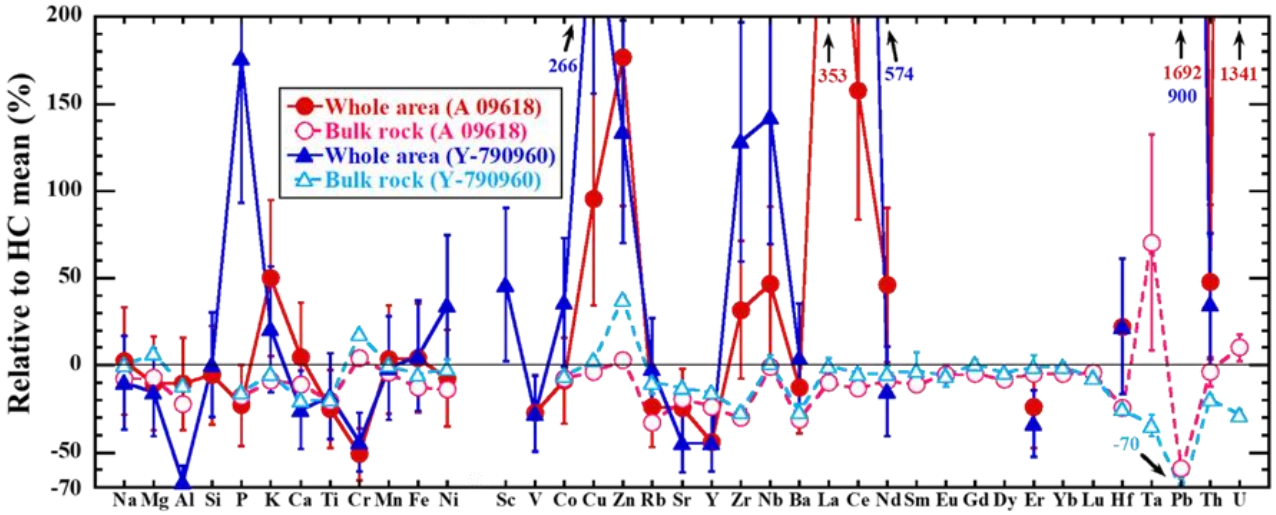

Figure 6 Bias (%) between the elemental abundances in the whole area of the meteorite samples as obtained using LA-ICP-TOF-MS mapping and the corresponding bulk rock values after compared to HC mean values. Bulk rock values and HC mean values are from Maeda *et al.* (2021).[24] The error bars for the whole areas represent 30% relative uncertainty.

detail as representative examples. The trends in all other obtained data sets are similar to those in the selected meteorites. In comparison with the corresponding bulk rock values and the H chondrite mean values (Figure 6), most elemental abundances obtained agree within uncertainty with them although REEs abundances were mostly below the corresponding LODs. A large discrepancy between the obtained and comparison values is systematically observed for Cr, Cu, Zn, Ce, Pb, and U in both samples. In addition, La in A 09618 and Al, P, Zr, and Nb in Y-790960 disagree with the comparison values. As meteorite samples, especially chondrites, are highly heterogeneous compared with the glass and apatite reference materials used for the data validation, heterogeneity at the scale of the whole areas analyzed likely causes these discrepancies. As such, the discrepancies for Al, P, and Cr observed may reflect a heterogeneous distribution of their corresponding host minerals in the samples studied because these elements are one of the major elements constituting feldspar, phosphate, and chromite, respectively. The lower abundance of Sr and the value below the LOD for Eu, largely accommodated in feldspar, in Y-790960 correspond to the lower Al abundance, while the abundances of V, largely partitioned in chromite, in both samples are depleted similar to the Cr abundances.[32,33] Thus, the discrepancies for Al in Y-790960 and Cr in both samples should be related to a heterogeneous distribution of feldspar and chromite, respectively. In the case of P, a region containing relatively abundant Ca-phosphates in the sample was selected for LA-ICP-TOF-MS mapping to see the effect on the REE distribution, likely leading to the high P abundance observed in Y-790960. Based on LA-ICP-TOF-MS mapping, Zr and Nb are highly concentrated in ilmenite (Figure 5 (c)), hence the discrepancies for these elements in Y-790960 may result from a heterogeneous distribution of this accessory phase. The discrepancy for La in A 09618 may be explained by the deposition in cracks as mentioned above, given that the U abundance in this sample is significantly higher than the comparison values. For the other elements displaying discrepancies (Cu, Zn, Ce, Pb, and U), similarly high abundances are obtained in the other meteorite samples analyzed in this study systematically. The too high results for Pb and U are attributed to their actual abundances being below the corresponding LODs. In the cases of Cu, Zn, and Ce, the signals obtained may have been elevated by matrix or memory effects. Incidentally, it is also possible that the anomalously high Zn and Pb abundances are caused by contamination on the surface of the PTSs.

Comparison of elemental abundances in constituent minerals

The elemental abundances in the Ca-phosphate, silicate, and oxide phases for A 09618 and Y-790960 determined using LA-ICP-TOF-MS mapping and spot analyses of EPMA and LA-ICP-SF-MS are summarized in ESI Tables 4-10,† together with literature values compiled from Ward *et al*. (2017) for Ca-phosphates and Mason and Graham (1970), Allen and Mason (1973), Curtis (1974), and Curtis and Schmitt (1979) for the other phases.[42,39,45,46,40] Here, the elemental abundances obtained for each phase and those compiled are shown in Figure 7, with the exception of the oxide phases, and compared for each phase one by one. Note that the clustering of mineral phases during the quantitative procedure on LA-ICP-TOF-MS mapping in some cases covers other phases than the target phase to a minor degree. This is attributed to ablation of tiny inclusions smaller than the laser spot size (5×5 μm) together with the target phase or to overlap with (an)other phase(s) during the ablation of the rim of the target phase. Moreover, particularly in the case of weathered samples, such samples may contain narrow Fe-rich veins within mineral grains (*e.g.*, Figure 4), which are also ablated together with the target phase. As such, each phase identified

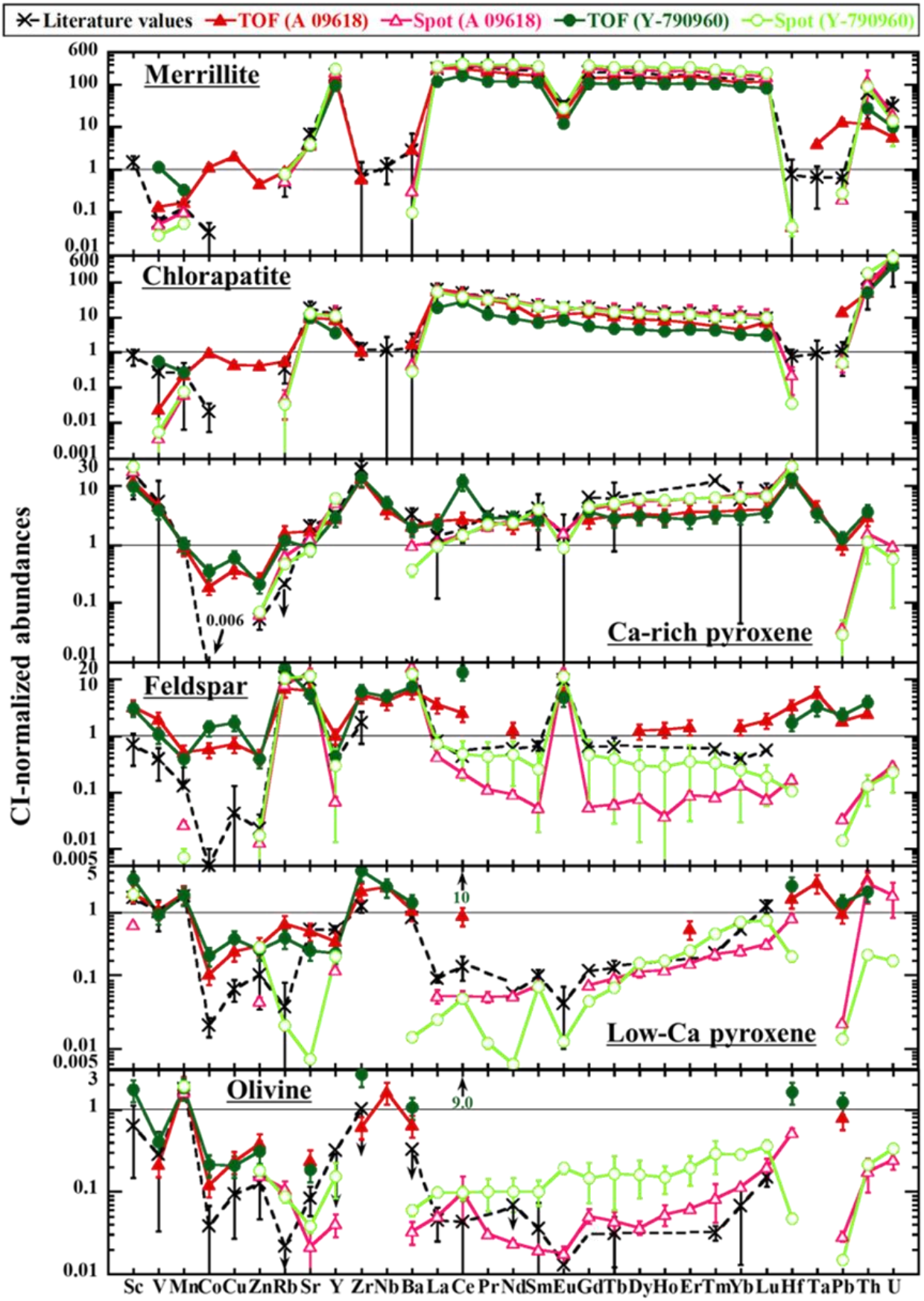

Figure 7 CI-normalized abundances of trace elements in constituent minerals as obtained using LA-ICP-TOF-MS mapping (TOF) and LA-ICP-SF-MS spot analysis (Spot) to the corresponding literature values.[39,40,42,45,46] See ESI Tables 4-9† for the details on the uncertainties. Error bars may be smaller than the symbol size. CI values are from Anders and Grevesse (1989).[47]

may contain analyzed points of non-target phases, affecting some of the elemental abundances in the phase as if contaminated by other phases. As an example, the Fe abundances in low-Fe phases such as Ca-phosphates and feldspar and the Co abundances in all phases determined are systematically elevated as the result of overlap with (oxidized or hydrated) metal phases (ESI Tables 4-10†). Especially the effects of metal phases on the Fe abundances in low-Fe phases can significantly modify the major element abundances following the applied 100% normalization, as all Fe is calculated as FeO. Similar effects may influence the values used for reference. For example, Ward *et al*. (2017) determined the major and trace element abundances in Ca-phosphates for several types of meteorites using EPMA, SIMS, and LA-spot analyses.[42] As they mostly focused on REE abundances, the abundances of other trace elements less concentrated in Ca-phosphates such as Ba and Hf may be affected by overlap with other phase(s), *e.g.*, resulting from ablating a phase underneath the target phase. The authors themselves note that the Pb abundances in some samples are possibly affected by contamination issues. In case of the elements systematically displaying a discrepancy for the whole areas mentioned above (Cu, Zn, Ce, Pb, and U), the abundances in constituent minerals determined using LA-ICP-TOF-MS mapping display a similar discrepancy from the comparison values overall. Because most of these elemental abundances obtained by LA-ICP-TOF-MS mapping show constant values (*e.g.*, ~100 µg/g for Cu and Zn), which are higher than the comparison values in all phases and their bulk rock values, these discrepancies should be attributed to matrix/memory effects or contamination affecting the entire area. Especially in the case of Pb, all abundances determined using LA-ICP-TOF-MS mapping appear to be affected by contamination. These effects must be considered during the following comparisons.

Merrillite. The major element abundances determined using EPMA are in excellent agreement with their literature values, while most of those determined using LA-ICP-TOF-MS mapping display slight discrepancies from the literature values (ESI Table 4†). In terms of trace elements (ESI Table 4† and Figure 7), the Ba, Hf, and Pb abundances determined using LA-spot analysis are significantly lower than the literature values, which suggests that the literature values of Ba and Hf suffer from simultaneously sampling other phases as noted above. The high literature value of Pb must result from terrestrial contamination.[41] The other trace element abundances determined using LA-spot analysis overlap within uncertainty with the literature values. The Th and U abundances determined using LA-ICP-TOF-MS mapping are remarkably lower than those obtained using LA-spot analysis, while the V and Ta abundances are higher than previously reported values. The Th and U discrepancies for the LA-ICP-TOF-MS values may occur because Th and U are more heterogeneously distributed in merrillite than the other elements as a result of their limited mobility. The high V and Ta abundances obtained using LA-ICP-TOF-MS mapping are either influenced by neighboring phases or caused by values too close to the corresponding LODs, especially in the case of Ta, as merrillite is one of the phases showing the lowest abundances of these elements. However, overall, the CI-normalized abundance patterns for LA-ICP-TOF-MS mapping, LA-spot analysis, and literature values overlap with each other. In particular, the REE abundance patterns are rich in light REEs (LREEs) relative to the heavy REEs (HREEs) and display a negative Eu anomaly. All Th/U ratios overlap within uncertainty, despite the discrepancies in their abundances observed between LA-ICP-TOF-MS mapping and LA-spot analysis.

Apatite. Based on the major element abundances determined using EPMA, apatite contains ~5 % m/m of Cl and ~0.5 % m/m of F, confirming it is chlorapatite. This is consistent with the literature values in ESI Table 5† and what is currently known about apatite in ordinary chondrites.[48] The major element abundances as determined using LA-ICP-TOF-MS mapping are affected by overlap with other phases (mostly metal phases) as the data obtained are slightly higher than the literature values (ESI Table 5†). In terms of trace elements, the V, Mn, Rb, and Ba abundances determined using LA-spot analysis are lower than the reported literature values (ESI Table 5† and Figure 7). Similar to merrillite, the literature values may be elevated due to overlap with neighboring phases. Although the REE abundances in Y-790960 as obtained using LA-ICP-TOF-MS mapping are lower than the literature values, the CI-normalized REE patterns for LA-ICP-TOF-MS mapping, LA-spot analysis, and literature values agree well with each other and display an enrichment in LREEs. As the main host phase for Th and U, their abundances obtained using LA-ICP-TOF-MS mapping, LA-spot analysis, and from literature values overlap with each other entirely.

Ca-rich pyroxene. The major element abundances determined using EPMA are in excellent agreement with literature values (ESI Table 6†). The average composition of Ca-rich pyroxene indicates the dominance of diopside ($En_{48}Wo_{46}$), which is also in excellent agreement with that observed for other H6 chondrites ($En_{49}Wo_{45}$).[48] In addition, the trace element abundances determined using LA-spot analysis overlap within uncertainty with the literature values (ESI Table 6† and Figure 7). Although the Fe abundances determined using LA-ICP-TOF-MS mapping are slightly affected by overlap with metal phases, most of the major element abundances for LA-ICP-TOF-MS mapping agree with the literature values. The trace element abundances for LA-ICP-TOF-MS mapping overall overlap both with those determined for LA-spot analysis and the literature values. Characterized by LREEs depletions and negative Eu anomalies, the CI-normalized REE patterns for LA-ICP-TOF-MS mapping, LA-spot analysis, and literature values are in good agreement as well, although negative Eu anomalies cannot be detected using LA-ICP-TOF-MS mapping due to the Eu abundances being below the LOD. However, the Ba and Th abundances based on LA-ICP-TOF-MS

mapping are ~2 to 5 times higher than those for LA-spot analysis. These discrepancies are likely the result of concentrations in Ca-rich pyroxene that are too close to the LODs. Remarkably, the Ce abundance in Y-790960 for LA-ICP-TOF-MS mapping is anomalously high and the CI-normalized REE pattern displays a strong positive Ce anomaly.

Feldspar. The major element abundances determined using EPMA are in excellent agreement with their literature values (ESI Table 7†). The average composition of feldspar indicates the presence of plagioclase, and albite ($Ab_{85}An_{10}$) more specifically. This is consistent with published values ($Ab_{82}An_{12}$).[48] The trace element abundances determined using LA-spot analysis overlap within uncertainty with the literature values, although those of HREEs in A 09618 are fairly low (ESI Table 7† and Figure 7). In contrast, the abundances of both major and trace elements determined using LA-ICP-TOF-MS mapping are inconsistent with those determined using spot analyses and the literature values, except for elements concentrated in feldspar (*e.g.*, Na, Si, and K for major elements and Rb, Ba, and Eu for trace elements). This suggests that the effect of overlap with other phases during LA-ICP-TOF-MS mapping of feldspar is larger than for the other phases, since most feldspar grains co-exist complicatedly with Ca-rich pyroxene grains based on the petrographic observation. This is illustrated by anomalously high Mg abundances (% m/m level), as this element should only be present at the trace level in feldspar.

Low-Ca pyroxene. The major element abundances as determined using LA-ICP-TOF-MS mapping and EPMA are in good agreement with the literature values (ESI Table 8†). Note that the literature values represent the mean values of major elements in low-Ca pyroxene for L6 and LL6 chondrites but not for H chondrites, resulting in slight differences in the MgO and FeO contents. The average composition of low-Ca pyroxene in H chondrites published is $En_{82}Fs_{17}$, in agreement with that obtained using EPMA ($En_{82}Fs_{17}$).[48] In terms of trace elements (ESI Table 8† and Figure 7), the values determined using LA-spot analysis approximately overlap within uncertainty with the literature values, except in the case of Sr and Ba where the literature values are apparently affected by contamination of feldspar. In addition, the CI-normalized REE patterns are mostly similar to those reported in the literature, all displaying increasing values from the LREEs to the HREEs with a negative Eu anomaly, except in the case of A 09618 where the Eu abundance was not determined. Overall, the LREE abundances as obtained using LA-spot analysis are lower than the literature values. On the other hand, the signals for REEs obtained using LA-ICP-TOF-MS are mostly below the LODs. In addition, the Rb abundances exhibit a large discrepancy with the values based on LA-spot analysis and the literature values. These high Rb abundances can be due to the overlap with other phases, especially feldspar, as the Sr and Ba abundances are also higher than those determined using LA-spot analysis.

Olivine. Similar to low-Ca pyroxene, the MgO and FeO contents reported in literature differ from those obtained in this study. Except for these elements, most other major element abundances determined using LA-ICP-TOF-MS mapping and EPMA analysis overlap within uncertainty with the literature values (ESI Table 9†). The average composition of olivine obtained using EPMA is magnesium-rich (Fo_{81}) and in good agreement with values observed in other H6 chondrites (Fo_{81}).[48] Although many trace elements cannot be quantified using LA-ICP-TOF-MS mapping due their signals being below the LODs, at least, the Mn, Cu, and Zn abundances overall agree within uncertainty with the literature values (ESI Table 9† and Figure 7). However, the abundances of the other elements quantified using LA-ICP-TOF-MS mapping appear to be elevated, likely as the result of overlap with other phases.

Oxides. Although the determinations of trace element abundances using LA-ICP-TOF-MS mapping and LA-spot analysis were focused primarily on Ca-phosphate and silicate phases, determination relying on LA-ICP-TOF-MS mapping was also applied to oxide phases. As such, LA-spot analysis was not conducted on oxide phases and the only abundances of trace elements available in literature or concentrated in the oxide phase are listed in ESI Table 10.† Overall, the major and trace element abundances determined in oxide phases agree within uncertainty with the literature values and those determined using EPMA, although no literature values for trace elements in ilmenite exist. Only a single grain of ilmenite, which is relatively large with ~100 μm for the major axis and ~50 μm for the minor axis, was found in the LA-ICP-TOF-MS maps (Figure 5 (c)) and analyzed, and hence the elemental abundances of ilmenite, particularly for the trace elements, may not reflect representative values.

In summary, the elemental abundances in each phase determined using fast high-resolution LA-ICP-TOF-MS mapping with a 5×5 μm spot size are mostly in agreement with the comparison values, although conventional EPMA and LA-spot analysis is generally more accurate and precise for major elements and trace elements, respectively, than LA-ICP-TOF-MS mapping. Especially for the elements in their main host phase(s), *i.e.*, REEs in Ca-phosphates, Th and U in apatite, Sc and Hf in Ca-rich pyroxene, etc., LA-ICP-TOF-MS mapping can be used to obtain quantitative data that are approaching the accuracy of those obtained by spot analyses. However, the lower the elemental abundances in the phases are, the larger the discrepancy between those values obtained using LA-ICP-TOF-MS mapping and the comparison values in general is. For example, it is challenging to quantify or even detect the REEs when the abundances of the REEs in the target phase are present at a concentration level similar to or lower than those of bulk chondrites. In general, elemental abundances in the target phase at least at the μg/g level are required for the quantification of LA-ICP-TOF-MS mapping to be at similar accuracy to those obtained by other, more conventional quantitative techniques, although levels at

hundreds of ng/g may be quantified in the case of heavy elements, from the HREEs onwards.

Conclusions

Fast elemental mapping using LA-ICP-TOF-MS was applied to H chondrites with the aim of obtaining element maps for a large collection of elements, including trace elements. The merits of quantification were assessed by comparison of the data obtained with those obtained using more conventional approaches, such as spot drilling analysis using LA-ICP-SF-MS, in an attempt to examine to what extent the accuracy and precision of the data obtained using this fast elemental mapping can approach those of more conventional analysis. A number of limitations for LA-ICP-TOF-MS mapping applying the experimental conditions used in this study (4.00 J/cm^2 laser energy density, 5×5 µm spot size, up to 200 pixel/s, etc.) are identified: pure metal phases which are not oxidized or hydrated due to terrestrial weathering cannot be ablated effectively, and the minimum abundances for trace elements required in terms of quantification are considerably higher than those for LA-spot analysis (*i.e.*, at the level of several of µg/g for LA-ICP-TOF-MS mapping vs. several ng/g level for LA-spot analysis). However, the trace element maps provide information on elemental distributions among the constituent minerals (semi-)quantitatively, especially for their primary host phase(s), and demonstrate the value of this technique to obtain high-resolution spatially resolved information without any stringent sample preparation, as is the case for more conventional techniques. Importantly, the approach applied in this study led to the identification of unexpected trace element carrier phases, on which almost no study focusing on trace elements has been conducted so far (*e.g.*, REEs in cracks, V and Zn in chromite, and Nb and Ta in ilmenite). Because no ablation effects in the regions studied using LA-ICP-TOF-MS mapping are observed based on the BSE imaging, EPMA, and LA-spot analysis, this fast LA-ICP-TOF-MS mapping can be used as a screening tool for particular geological samples and possibly also other types of samples (*e.g.*, archeological artefacts), providing (semi-)quantitative information of elemental distributions including trace elements on such samples.

Conflicts of interest

There are no conflicts to declare.

Acknowledgements

We would like to thank R. Kanemaru for his assistance during the EPMA and N. J. de Winter and S. M. Chernonozhkin for guidance with the µXRF and the HDIP software, respectively. We also thank the Royal Belgian Institute of Natural Sciences, Belgium, and the National Institute of Polar Research, Japan, for the loan of the Antarctic meteorites, meteorites collected from hot deserts, and the fall meteorites used in this study. RM thanks NIPR International Internship Program for Polar Science 2020 for financial and analytical support. RM, FV, VD, PhC, and SG acknowledge support from the Excellence of Science (EoS) project ‘‘ET-HoME”. TVA thanks the Special Research Fund of Ghent University (BOF PDO2020003501). FV thanks BOF-UGent for financial support under the form of a GOA grant and acknowledges Teledyne Photon Machines. for financial and logistic support. VD and SG thank the BRAIN-Be Belgian Science Policy (BELSPO) projects ‘‘BAMM” and “DESIRED”. VD thanks the ERC StG ISoSyC and FRS-FNRS for support. PhC and SG acknowledge support from the VUB Strategic Research Program. PhC also thanks the Research Foundation Flanders (FWO Hercules grant) for the purchase of the µXRF instrument. Finally, we gratefully acknowledge Derya Kara Fisher and Cara Sutton for the editorial work. We also thank two anonymous reviewers for their constructive reviews.

References

1 C.A. Heinrich, T. Pettke, W.E. Halter, M. Aigner-Torres, A. Audétat, D. Günther, B. Hattendorf, D. Bleiner, M. Guillong and I. Horn, *Geochim. Cosmochim. Acta*, 2003, **67**, 3473-3497.
2 K.P. Jochum, B. Stoll, K. Herwig and M. Willbold, *J. Anal. At. Spectrom.*, 2007, **22**, 112-121.
3 M. Humayun, F.A. Davis and M.M. Hirschmann, *J. Anal. At. Spectrom.*, 2010, **25**, 998–1005.
4 J.D. Woodhead, J. Hellstrom, J.M. Hergt, A. Greig and R. Maas, *Geostand. Geoanal. Res.*, 2007, **31**, 331-343.
5 T. Ulrich, B.S. Kamber, P.J. Jugo and D.K. Tinkham, *The Canadian Mineralogist*, 2009, **47**, 1001-1012.
6 S.J.M. Van Malderen, J.T. van Elteren and F. Vanhaecke, *J. Anal. At. Spectrom.*, 2015, **30**, 119–125.
7 S.J.M. Van Malderen, A.J. Managh, B.L. Sharp and F. Vanhaecke, *J. Anal. At. Spectrom.*, 2016, **31**, 423-439.
8 O.Borovinskaya, B. Hattendorf, M. Tanner, S. Gschwind and D. Günther, *J. Anal. At. Spectrom.*, 2013, **28**, 226-233.
9 L. Hendriks, A. Gundlach-Graham, B. Hattendorf and D. Günther, *J. Anal. At. Spectrom.*, 2017, **32**, 548–561.
10 A. Gundlach-Graham, P.S. Garofalo, G. Schwarz, D. Redi and D. Günther, *Geostand. Geoanal. Res.*, 2018, **42**, 559-574.
11 T. Stephan, *Planet. Space Sci.*, 2001, **49**, 859-906.
12 M. Morita, M. Miyamura, A. Yamaguchi and T. Sakamoto, *Anal. Sci.*, 2022, 1-8.
13 A.N. Krot, K. Keil, C.A. Goodrich, E.R.D. Scott and M.K. Weisberg, In *Meteorites, Comets, and Planets*, **1**, *Treatise on Geochemistry*, **341**, 2003, 83-128.
14 M. Burger, G. Schwarz, A. Gundlach-Graham, D. Käser, B. Hattendorf and D. Günther, *J. Anal. At. Spectrom.*, 2017, **32**, 1946–1959.
15 A. Gundlach-Graham, M. Burger, S. Allner, G. Schwarz, H.A.O. Wang, L. Gyr, D. Grolimund, B. Hattendorf and D. Günther, *Anal. Chem.*, 2015, **87**, 8250–8258.
16 Y. Bussweiler, O. Borovinskaya and M. Tanner, *Spectroscopy*, 2017, **32**, 14-20.

17 Krebs M.Y., Pearson D.G., Fagan A.J., Bussweiler Y. and Sarkar C., *Chem. Geol.*, 2019, **523**, 42-58.
18 Ubide T., Caulfield J., Brandt C., Bussweiler Y., Mollo S., Di Stefano F., Nazzari M. and Scarlato P., *Front. Earth Sci.*, 2019, **7**, 239.
19 Bussweiler Y., Gervasoni F., Rittner M., Berndt J. and Klemme S., *Lithos*, 2020, **352-353**, 105282.
20 Neff C., Keresztes Schmidt P., Garofalo P.S., Schwarz G. and Günther D., *J. Anal. At. Spectrom.*, 2020, **35**, 2255-2266.
21 Rubatto D., Burger M., Lanari P., Hattendorf B., Schwarz G., Neff C., Keresztes Schmidt P., Hermann J., Vho A. and Günther D., *Contrib. Mineral. Petrol.*, 2020, **175**, 1-19.
22 Förster M.W., Bussweiler Y., Prelević D., Daczko N.R., Buhre S., Mertz-Kraus R. and Foley S.F., *Geosci.*, 2021, **11**, 372.
23 Garofalo P.S., Scarsi M., Gundlach-Graham A., Schwarz G. and Günther D., *Mineralium Deposita.*, 2022, 1-20.
24 R. Maeda, S. Goderis, V. Debaille, H. Pourkhorsandi, G. Hublet and P. Claeys, *Geochim. Cosmochim. Acta*, 2021, **305**, 106-129.
25 K. Ninagawa, Y. Mieda, H. Ueda, N. Imae, H. Kojima and K. Yanai, *Antarct. Meteor. Res.*, 2005, **18**, 1-16.
26 S.J.M. Van Malderen, T. Van Acker and F. Vanhaecke, *Anal. Chem.*, 2020, **92**, 5756–5764.
27 F. Vanhaecke and S.J.M. Van Malderen, *European patent No.3195346B1.*, 2020, Munich, Germany. European Patent Office.
28 T. Van Acker, S.J.M. Van Malderen, T. Van Helden, C. Stremtan, M. Šala, J.T. van Elteren and F. Vanhaecke, *J. Anal. At. Spectrom.*, 2021, **36**, 1201–1209.
29 M. Burger, A. Gundlach-Graham, S. Allner, G. Schwarz, H.A. Wang, L. Gyr, S. Burgener, B. Hattendorf, D. Grolimund and D. Güther, *Anal. Chem.*, 2015, **87**, 8259-8267.
30 M.J. Cubison and J.L. Jimenez, *Atmos. Meas. Tech.*, 2015, **8**, 2333–2345.
31 J.T. van Elteren, N.H.Tennent and V.S. Šelih, *Anal. Chim. Acta*, 2009, **644**, 1-9.
32 M. Humayun, S.B. Simon and L. Grossman, *Geochim. Cosmochim. Acta*, 2007, **71**, 4609–4627.
33 M. Tanner, *J. Anal. At. Spectrom.*, 2010, **25**, 405–407.
34 K.P. Jochum, M. Willbold, I. Raczek, B. Stoll and K. Herwig, *Geostand. Geoanal. Res.*, 2005, **29**, 285–302.
35 K.P. Jochum, B. Stoll, K.P. Herwig, M. Willbold, A.W. Hofmann, M. Amini and 47 coauthors, *Geochem. Geophys. Geosyst.*, 2006, **7**, Q02008.
36 M.A.W. Marks, T. Wenzel, M.J. Whitehouse, M. Loose, T. Zack, M. Barth, L. Worgard, V. Krasz, G.N. Eby, H. Stosnach and G. Markl, *Chem. Geol.*, 2012, **291**, 241-255.
37 L.-K. Sha and W. Chappell, *Geochim. Cosmochim. Acta*, 1999, **63**, 3861-3881.
38 A. Yamaguchi, N. Shirai, M. Kimura, N. Imae, M. Haba, V. Debaille, R. Maeda, S. Goderis and P. Claeys, Meteorite Newsletter Vol 28, 2021.
39 B. Mason and A.L. Graham, *Earth Sci.*, 1970, **3**, 1-17.
40 D.B. Curtis and R.A. Schmitt, *Geochim. Cosmochim. Acta*, 1979, **43**, 1091-1103.
41 T.H. Green, *Chem. Geol.*, 1994, **117**, 1-36.
42 D. Ward, A. Bischoff, J. Roszjar and M.J. Whitehouse, *American Mineralogist*, 2017, **102**, 1856-1880.
43 M. Ebihara and M. Honda, *Meteoritics*, 1984, **19**, 69-77.
44 J.T. Wasson and G.W. Kallemeyn, *Philos. Trans. R. Soc. Lond.*, 1988, **A 325**, 535-544.
45 R.O. Allen Jr. and B. Mason, *Geochim. Cosmochim. Acta*, 1973, **37**, 1435-1456.
46 D.B. Curtis, Ph.D. Thesis, Oregon State University, Oregon, 1974.
47 E. Anders and N. Grevesse, *Geochim. Cosmochim. Acta*, 1989, **53**, 197-214.
48 W.R. Van Schmus, *Earth Sci. Rev.*, 1969, **5**, 145-184.

Chapter 4 "*Fluid mobilization of rare earth elements (REEs), Th, and U during the terrestrial alteration of chondrites*" (Accepted in MAPS 2023)

Chapter introduction

While the detailed mechanism of Antarctic alteration by fluids remained unanswered following the results from Chapter 2, the development of LA-ICP-TOF-MS mapping in Chapter 3 visualized a secondary deposition of REEs. These observations led us to investigate cracks in HCs in detail to address the question of fluid mobilization of elements in Antarctic alteration.

In this study, the degree of weathering of the sample was first evaluated quantitatively based on petrographic observations using optical microscopy, scanning electron microscopy, and μXRF, to examine if the REE deposition in cracks observed by LA-ICP-TOF-MS mapping (see Chapter 3) resulted from terrestrial alteration. Then, the chemical compositions in cracks for Antarctic, hot desert, and fall HCs were investigated by line scanning using LA-ICP-SF-MS. As observed based on LA-ICP-TOF-MS analysis, the results of LA-ICP-SF-MS line scanning on cracks confirm that they contain a considerable amount of REEs, Th, and U, but in some cases, only Ce resides there. These features are observed in weathered samples while not detected in less altered samples including falls with a single exception as discussed below. We, therefore, conclude that this elemental deposition results from terrestrial alteration where fluids pass through the meteorite interiors, triggered by melting of ice in Antarctica or rain/humidity in hot deserts and elsewhere on the Earth. On the other hand, we also found this process can proceed relatively fast as an altered "fall" sample in this study has been affected. As such, a first step towards unraveling the underlying mechanism of terrestrial alteration has been made in this work. The petrographic observations (except for μXRF) and LA-ICP-SF-MS analysis were conducted within the framework of the NIPR International Internship Programs for Polar Science 2020 and 2021.

Contributions to this paper

This study was led by RM and the AMGC, NIPR, A&MS, and G-Time teams. All *in-situ* measurements, interpretations, and writing were done by RM.

This chapter is accepted as:

Ryoga Maeda, Steven Goderis, Akira Yamaguchi, Thibaut Van Acker, Frank Vanhaecke, Vinciane Debaille and Phillippe Claeys (2023) Fluid mobilization of rare earth elements (REEs), Th, and U during the terrestrial alteration of chondrites. *Meteoritics & Planetary Science* (accepted).

Supporting information for this chapter can be found at:

https://vub-my.sharepoint.com/:f:/g/personal/ryoga_maeda_vub_be/EqwAm_k7CFZHp0BTrDKqaqABoSepq5xlSXgNU_W-Vx46Kw?e=uKB4jq (until 26 August 2023)

Password: phdthesis_rm

Otherwise, it can be requested digitally from the author.

Fluid mobilization of rare earth elements (REEs), Th, and U during the terrestrial alteration of chondrites

Ryoga Maeda[1,2,*], Steven Goderis[1], Akira Yamaguchi[3], Thibaut Van Acker[4], Frank Vanhaecke[4], Vinciane Debaille[2] and Phillippe Claeys[1]

[1]Analytical-, Environmental-, and Geo-Chemistry, Vrije Universiteit Brussel, Pleinlaan 2, 1050 Brussels, Belgium

[2]Laboratoire G-Time, Université libre de Bruxelles, CP 160/02, 50, Av. F.D. Roosevelt, 1050 Brussels, Belgium

[3]National Institute of Polar Research, 10-3 Midori-cho, Tachikawa-shi, Tokyo 190-8518, Japan

[4]Atomic & Mass Spectrometry (A&MS) research unit, Department of Chemistry, Ghent University, Campus Sterre, Krijgslaan, 281 – S12, 9000 Ghent, Belgium

* Corresponding author. *E-mail address*: Ryoga.Maeda@vub.be

Abstract

The chemical effects of terrestrial alteration, with a particular focus on lithophile trace elements, were studied for a set of H chondrites displaying various degrees of weathering from fresh falls to altered finds collected from hot deserts. According to their trace element distributions, a considerable fraction of rare earth elements (REEs), Th, and U resides within cracks observed in weathered meteorite specimens. These cracks appear to accumulate unbound REEs locally accompanied by Th and U relative to the major element abundances, especially P and Si. The deposition of Ce is observed in cracks in the case of most of the weathered samples. Trace element maps visually confirm the accumulation of these elements in such cracks, as previously inferred based on chemical leaching experiments. Because the positive Ce anomalies and unbound REE depositions in cracks occur in all weathered samples studied here while none of such features are observed in less altered samples including falls (except for altered fall sample Nuevo Mercurio), these features are interpreted to have been caused by terrestrial weathering following chemical leaching. However, the overall effects on the bulk chemical composition remain limited as the data for all Antarctic meteorites studied in this work (except for heavily weathered sample Asuka 09516), are in good agreement with published data for unaltered meteorites.

1. INTRODUCTION

Meteorites are divided into “falls” and “finds” depending on how they were recovered: falls are recovered after observed fall events, while finds cannot be associated with observed falls and include meteorites collected from cold and hot deserts. As falls are usually collected shortly after the fall events, they are in general significantly fresher than finds, as the latter have been subjected to weathering to various degrees during their terrestrial residence (roughly of the order of tens of kyr in most hot deserts and up to a few Myr in Antarctica and Atacama: *e.g.*, Nishiizumi *et al.*, 1989; Al-Kathiri *et al.*, 2005; Drouard *et al.*, 2019). Terrestrial weathering may change the original mineralogy and chemical compositions of meteorites due to oxidation or hydration, *i.e.*, the alteration to phases that are more stable at the Earth’s surface depending on environmental factors such

Table 1. Summary of the relationship between weathering scales and weathering effects.

Weathering degree	Minor							Severe
ABC index	A		B		C			
W0-6 scale	W0	W1	W2		W3	W4	W5	W6
Oxidation of metal and troilite	No visible oxidation	<7.5%	7.5%-20%	20%-35%	35%-60%	60%-95%	>95%	
Alteration of silicates	No alteration						Minor	Massive
Rustiness in veins	Limonitic staining is minor				Limonite veins are extensively found			

Based on Antarctic Meteorite Newsletter from NASA, Meteorite Newsletter from NIPR, Gooding (1989), Wlotzka (1993), and Bland *et al.* (2006).

as humidity and temperature *(e.g.*, Koeberl and Cassidy, 1991; Lee and Bland, 2004; Bland *et al.*, 2006; van Ginneken *et al.*, 2022). To evaluate the degree of weathering for finds, two classification systems are commonly applied: the ABC index for Antarctic meteorites and a scale with seven categories from W0 to W6 used mainly for ordinary chondrites (Antarctic Meteorite Newsletter, NASA; Meteorite Newsletter, NIPR; Gooding, 1989; Wlotzka, 1993; Bland *et al.*, 2006). Both scales are largely based on the effects of oxidation on metal and sulfide phases and the criteria applied are summarized in Table 1. Fundamentally, weathering affects the metal phases first, the sulfide phases later, and finally the silicates phases, especially in the case of olivine (Wlotzka, 1993). According to Wlotzka (1993), falls are usually of W0 grade and Antarctic meteorites are generally classified as W1 and up to W2 even when they are categorized C in the ABC index system as weathering in Antarctica proceeds more slowly. Although the ABC index is broadly used for various classes of Antarctic meteorites whereas the W0-W6 scale is applicable to meteorites containing metal phases only (Antarctic Meteorite Newsletter, NASA; Rubin and Huber, 2005), this system is largely subjective and significantly more qualitative than the W0-W6 scale (Gooding, 1989). As such, previous studies with regards to Antarctic alteration of meteorites pointed out discrepancies between more quantitative approaches and the ABC index (*e.g.*, Gooding 1989; Ikeda and Kojima, 1991; Miyamoto, 1991), demonstrating that such more quantitative examinations are preferable.

Rare earth elements (REEs) are universally used for understanding planetary processes, such as silicate differentiation, and are often considered to be relatively immobile (*e.g.*, Nakamura, 1974; DePaolo and Wasserburg, 1976; Middelburg *et al.*, 1988). Despite their limited degree of mobility, previous studies on the effects of weathering on REEs in meteorite samples have demonstrated that terrestrial weathering, including Antarctic alteration, can modify the original REE compositions both in terms of absolute concentrations and isotopic ratios (*e.g.*, Pourkhorsandi *et al.*, 2019, 2021). Maeda *et al.* (2021) assessed the effects of Antarctic alteration on the Sm-Nd and Lu-Hf systems in H chondrites (HCs) and demonstrated that Antarctic meteorites commonly preserve their original Sm-Nd and Lu-Hf isotopic compositions as much as chondrite falls. However, exceptions exist in that study. For

example, the Antarctic sample Asuka 09516 exhibited severe mineralogical and chemical alteration, with considerable losses of various elements even including the REEs disturbing the isotopic compositions. Based on these observations, Maeda *et al.* (2021) proposed that Antarctic alteration may be considerably more complex than previously acknowledged, and that the detailed mechanisms of the alteration remain relatively poorly understood.

In the last couple of years, the combination of laser ablation (LA) with time-of-flight (TOF) based inductively coupled plasma (ICP)-mass spectrometry (MS) is increasingly used for elemental mapping applications for a range of matrices (Burger *et al.*, 2015; Gundlach-Graham *et al.*, 2015, 2018; Bussweiler *et al.*, 2017). The use of ICP-TOF-MS allows for a nearly complete elemental mass spectrum to be obtained for every laser pulse fired by the LA-unit and interacting with the sample surface. Maeda *et al*. (2023) applied LA-ICP-TOF-MS for elemental mapping in HC samples and observed that REEs are concentrated in cracks of heavily weathered samples (weathering index C), suggesting that this REE deposition may result from terrestrial weathering. In this study, the details of cracks in HCs displaying various degrees of weathering from falls to finds recovered in hot deserts were investigated to reveal the underlying alteration mechanisms by combining several types of *in-situ* techniques including state-of-the-art technique LA-ICP-TOF-MS mapping.

2. EXPERIMENTAL

2.1. Samples

The same polished thick sections (PTSs) as those in Maeda *et al.* (2023) were used for the analyses described below. Petrographic information on the meteorite samples is summarized in Table 2 (A: Asuka; ALH: Allan Hills; northwest Africa: NWA; Y: Yamato). Note that the petrologic type of A-881258 has been recommended to be re-classified as H3.9 according to Ninagawa *et al.* (2005), and thus this sample will be regarded in this paper as H3.9, although it has been described as H3.0 in the Meteoritical Bulletin Database. This re-classification is consistent with the petrographic observations on the PTS in this work exhibiting relatively large secondary minerals such as plagioclase, Ca-phosphate, and chromite grains, as well as better crystallized mineral grains relative to those in the other unequilibrated HCs considered in this study.

2.2. Petrographic observations

All PTSs were first analyzed using a Bruker M4 Tornado μXRF scanner equipped with a Rh source and two XFlash 430 Silicon Drift detectors at the Vrije Universiteit Brussel (VUB), Belgium, to obtain major element maps. This analysis has been described in detail in Maeda *et al.* (2021). The PTSs were examined using optical microscopy at the VUB and the National Institute of Polar Research (NIPR), Japan, to evaluate their weathering degrees quantitatively by assessing the prevalence of limonite, the occurrence of cracks, and the appearance of rustiness. Next, back-scattered electron (BSE) images of all PTS were obtained using a JEOL JSM-7100F field emission-scanning electron microscope (FE-SEM) equipped with an Oxford energy dispersive spectrometer (EDS) at the NIPR. The modal abundance of limonite was determined using the ImageJ image analysis program based on the modal abundance of metals and an RGB map combining S, Si, and Fe X-ray maps. The nature of limonite was confirmed using optical microscopy and BSE images. Note that any limonite occurring near the

Table 2. List of H chondrites analyzed with the results of the petrographic observation and appearance of Ce anomaly in their cracks (n.d.: not determined).

Meteorite	Fall	Type	Weathering	Shock	Limonite/Metal	The state of cracks	Rustiness	Ce/Ce*
A-880941	No	H3.3	A/B	S1-2	4%	Only few observed	20-30%	1.0
Y-793574	No	H3.5	n.d.	n.d.	27%	Large cracks observed, filled up with Fe but not all	70-80%	1.1-1.3
Y-790461	No	H3.7	B	S3	18%	Several observed in the exterior, filled up with Fe but not all	~50%	1.0-1.4
ALH 78084	No	H3.9	B/Ce	n.d.	40%	Observed throughout the sample, filled up with Fe	80-90%	1.0-1.1
A-881258	No	H3.9[a]	B	n.d.	28%	Observed throughout the sample, filled up with Fe	60-70%	1.1-1.3
A 09436	No	H3	C	n.d.	9%	Large cracks observed in the exterior, filled up with Fe	80-90%	1.5-2.5
A 09387	No	H4	B/C	n.d.	10%	Large cracks observed, filled up with Fe	50-60%	1.1-1.6
NWA 6771	No	H4	W1	S1-2	43%	Observed throughout the sample, filled up with Fe	~90%	1.6-2.8
Jilin	Yes	H5	n.d.	S3	not detected	Highly limited	< 5%	1.0-1.1
Nuevo Mercurio	Yes	H5	n.d.	n.d.	2%	Only few observed	10-20%	1.3-2.8
Richardton	Yes	H5	n.d.	n.d.	not detected	Highly limited	< 5%	1.2-1.4
A 09618	No	H5	C	n.d.	36%	Large cracks observed, filled up with Fe	80-90%	0.74-1.7
Sahara 97035	No	H5	W2	S1-2	25%	Observed throughout the sample with large cracks, filled up with Fe	> 90%	0.39-2.0
Butsura	Yes	H6	n.d.	n.d.	not detected	Highly limited	< 5%	0.98-1.1
A 09516	No	H6	C	n.d.	48%	Observed throughout the sample, filled up with Fe	80-90%	1.1-5.8
Y-790960	No	H7	B	S3	26%	Several observed, filled up with Fe	70-80%	0.92-1.0

See Maeda *et al.* (2021) for the details of the type, weathering index, and shock stage. The Fe filling up cracks is in oxide or hydrate form. See Table 4 for the details of the Ce/Ce* values.

[a] Ninagawa *et al.* (2005).

exterior of the sample is excluded from the calculation of the modal abundance. The rustiness on the surface of a sample was semi-quantitatively determined using optical images based on the modal abundance of brown-stained crystalline material assuming the oxidation of mineral grain surface occurred during the terrestrial residence, although the use of a fresh PTS is preferred for the determination of the rustiness (Rubin and Huber, 2005).

2.3. LA-ICP-TOF-MS mapping

The PTSs of 12 samples (A-880941, A-881258, A 09436, A 09387, NWA 6771, Jilin, Nuevo Mercurio, Richardton, A 09618, Butsura, A 09516, and Y-790960) were analyzed using pulse-resolved multi-elemental LA-ICP-TOF-MS mapping at Ghent University, Belgium. Two different LA-units equipped with a 193 nm ArF* excimer-based nanosecond lasing system were used including a customized Teledyne Photon Machines Analyte G2 and a commercially available Iridia LA-unit equipped with a prototype and commercially available version of the Cobalt ablation chamber, respectively. Both systems were equipped with low-dispersion tube cell-type ablation cells (Van Malderen *et al.*, 2015, 2020; Vanhaecke and Van Malderen, 2020). The LA-units were coupled to a TOFWERK icpTOF 2R ICP-TOF-MS unit equipped with a 1 mm inner diameter torch injector via a low-dispersion aerosol transport system, named the aerosol rapid introduction system (ARIS), developed at Ghent University, and commercialized by Teledyne Photon Machines (Van Acker *et al.*, 2021). The regions where (a) crack(s) occur(s) in the samples were selected for LA-ICP-TOF-MS mapping, unless no cracks were observed. We refer the reader to Maeda *et al.* (2023) for more details on the analytical methodology.

2.4. LA-ICP-SF-MS analysis

After LA-ICP-TOF-MS elemental mapping, the PTSs ablated for mapping were slightly polished and the abundances of major and trace elements in cracks for all PTSs were determined in segmented line scan mode using LA- ICP-sector field (SF)-MS. This measurement was performed using a Teledyne CETAC LSX-213 G2+ laser system coupled to a Thermo Element XR ICP-SF-MS unit at the NIPR. The laser system provides an output wavelength of 213 nm and was operated at a laser spot size of 50 μm with a lateral scan speed of 10 μm/s, 20 Hz repetition rate, and a laser energy density of 36 J/cm^2. Parameters were tuned aiming at a low oxide formation level ($^{232}Th^{16}O^+/^{232}Th^+ < 0.5\%$) while ablating NIST SRM 612 glass reference material. All nuclide peaks were monitored at low mass resolution (M/ΔM = ~300) with triple mode detection and the following nuclides were monitored for the major elements: ^{23}Na, ^{24}Mg, ^{27}Al, ^{29}Si, ^{31}P, ^{39}K, ^{43}Ca, ^{44}Ca, ^{47}Ti, ^{53}Cr, ^{55}Mn, ^{57}Fe, and ^{60}Ni; and for the trace elements: ^{45}Sc, ^{51}V, ^{59}Co, ^{63}Cu, ^{66}Zn, ^{85}Rb, ^{88}Sr, ^{89}Y, ^{90}Zr, ^{93}Nb, ^{137}Ba, ^{139}La, ^{140}Ce, ^{141}Pr, ^{146}Nd, ^{147}Sm, ^{151}Eu, ^{157}Gd, ^{159}Tb, ^{161}Dy, ^{165}Ho, ^{166}Er, ^{169}Tm, ^{173}Yb, ^{175}Lu, ^{178}Hf, ^{181}Ta, ^{182}W, ^{208}Pb, ^{232}Th, and ^{238}U. All peaks were quantified via peak jumping between peak tops with 10% mass window (average of 5 acquisition points on the peak top) and 50–100 ms of acquisition time on the peak top. After LA-ICP-SF-MS analysis, BSE images of some PTSs focusing on the regions ablated were obtained using a JEOL JSM-IT300 SEM at the SURF research unit of the VUB.

Elemental abundances were calculated using average relative sensitivity factors (RSFs) obtained based on

analysis of BCR2-G, BHVO2-G, and ML3B-G (Jochum and Stoll, 2008). Background-subtracted intensity ratios were converted to elemental ratios with respect to SiO_2 by multiplying with the RSFs (Humayun *et al.*, 2007). The major elements were calculated from their oxide ratios, the sum of which was normalized to 100% while neglecting the effect from metal phases on Fe and Ni. The trace element abundances were then calculated from the elemental ratio multiplied by the SiO_2 content obtained from the major element procedure (Humayun *et al.*, 2010). The precision and accuracy of the applied procedure were evaluated using the GOR128-G and GOR132-G reference materials as QA/QC samples.

3. RESULTS

3.1. Weathering degrees

The modal abundances of limonite expressed in vol.% ratio of limonite to metal phases (*i.e.*, kamacite and taenite), the state of cracks (the number, width and length, presence of filling, *etc*.), and the rustiness on the surface expressed in vol.% for all samples are summarized in Table 2. The modal abundance of limonite may include that of iron oxides, such as magnetite, as limonite and iron oxides cannot be distinguished from each other based on the X-ray maps obtained using μXRF. However, according to Maeda *et al.* (2021), such iron oxides are not found in all samples and then only in trace abundances. This is consistent with mineralogical constraints based on the FE-SEM/EDS, which show that the effect of such phases on the modal abundance of limonite can be neglected.

No limonite and almost no cracks were observed in three of the four fall samples studied here (Jilin, Richardton, and Butsura), while these were found in all other samples, including H5 fall Nuevo Mercurio. Among the set of find samples, most cracks are filled with Fe. The exception to this general observation is A-880941, for which the cracks do not appear to be filled. Overall, the previously assigned weathering grades based on the classical ABC index system in the case of Antarctic meteorites and the W0-W6 scale for meteorites from hot deserts are mostly consistent with the petrographic observations in this study. For example, the metal phases in A 09516, categorized as weathering grade C, are replaced by limonite to the highest degree (48%), while Sahara 97035 categorized as grade W2 is the rustiest among the meteorites characterized in this study (> 90%). Moreover, A-880941, containing limited limonite and cracks, is categorized as A/B. However, exceptions exist, *e.g.*, the fragments of A 09436 and A 09387 studied here are categorized as C and B/C, respectively, but show that only ~10% of their metal has been limonitized, despite the requirement of a limonite/metal ratio of at least 35% or more for the categorization of B/C and C according to the index for Antarctic meteorites (Table 1). In terms of the fall samples, the weathering degrees of Jilin and Nuevo Mercurio were examined by Miyamoto (1991), who attempted to quantitatively determine weathering degrees by analyzing the infrared diffuse reflectance spectra of bulk meteorite samples (Jilin is described using its previous name Kirin in the paper). In the case of both fall meteorites, only limited weathering affected these samples. This is highly consistent with the observations in this study, as limonite is rarely found, and the overall appearance of these samples is not considered to be rusty. Note that Nuevo Mercurio is considered highly porous, which has been confirmed as an unusual feature of this meteorite (Fredriksson *et al.*, 1979).

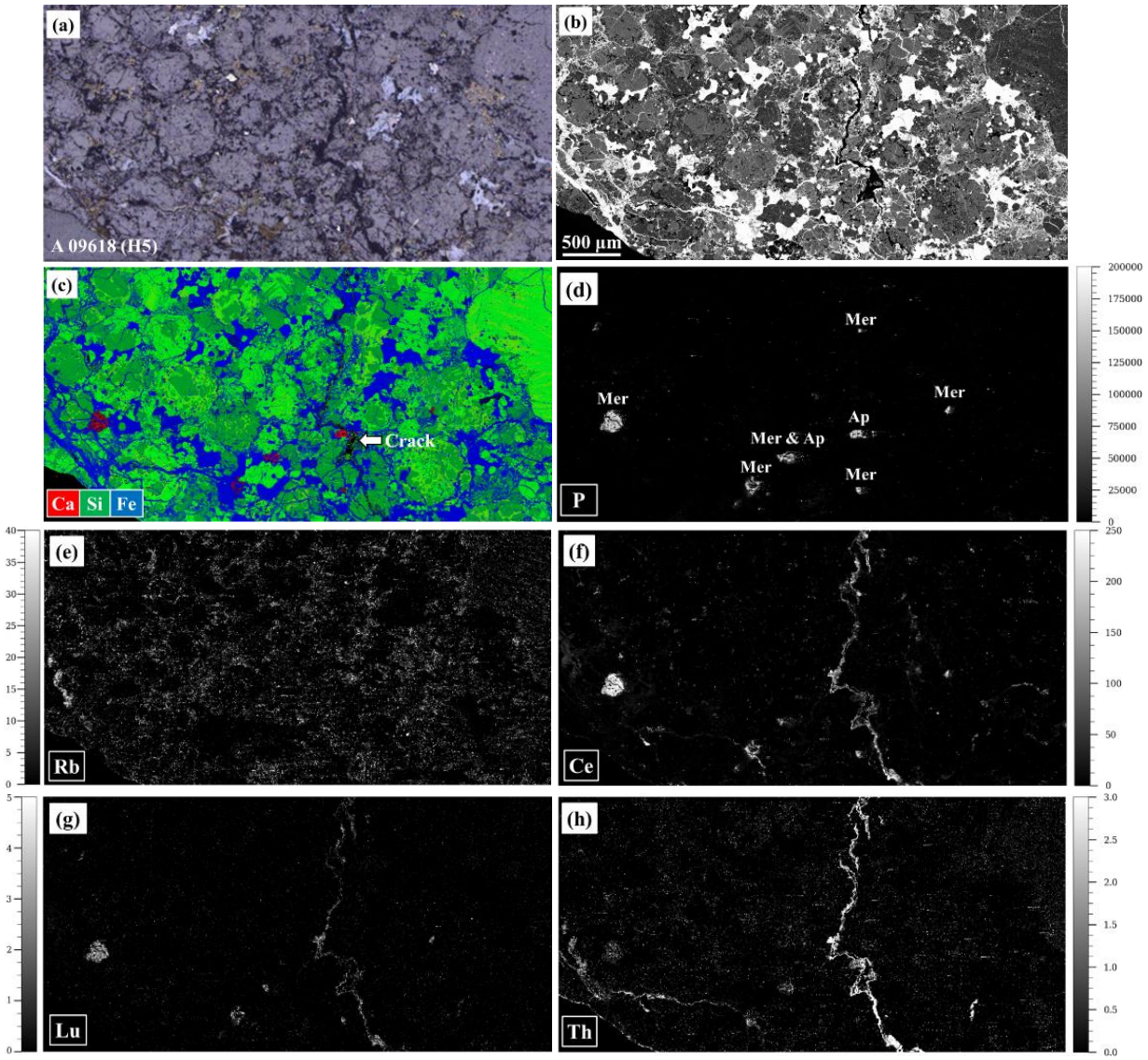

Fig. 1. Optical and BSE images and (semi-)quantitative element maps for A 09618. (a) Optical image of the region analyzed using LA-ICP-TOF-MS. (b) BSE image of the region analyzed for mapping. (c) Combined RGB elemental map obtained using LA-ICP-TOF-MS mapping with red: Ca, green: Si, and blue: Fe. Based on the composition, the following mineralogy can be deduced red: Ca-phosphates, orange: Ca-rich pyroxene, light green: low-Ca pyroxene and feldspar, dark green: olivine, and blue: metals, sulfides, and oxides. (d) Phosphorus distribution map. Mer: merrillite; Ap: chlorapatite. (e) Rubidium distribution map. (f) Cerium distribution map. (g) Lutetium distribution map. (h) Thorium distribution map. Scale bars for (d) to (h) in ppm.

3.2. Quantitative elemental maps

Figures 1 and 2 show (semi-)quantitative elemental maps obtained using LA-ICP-TOF-MS for A 09618 and A 09516 as examples, together with the corresponding optical and BSE images in the case of Fig. 1. Most of the metal phases shown in blue in the combined RGB maps (Fig. 1 (c) and 2 (a)) were limonitized. Figures 1 (d), (f), and (g) demonstrate that REEs are mostly distributed in Ca-phosphate phases, especially in merrillite. Surprisingly, REEs also reside in the crack displayed in Fig. 1, almost at the same concentration levels as those observed for merrillite. Mobile elements such as Rb are not enriched in the crack while relatively immobile elements, such as Th, are (Figs. 1 (e) and (h)). In the case of A 09516, Ce is the only REE that is enriched in

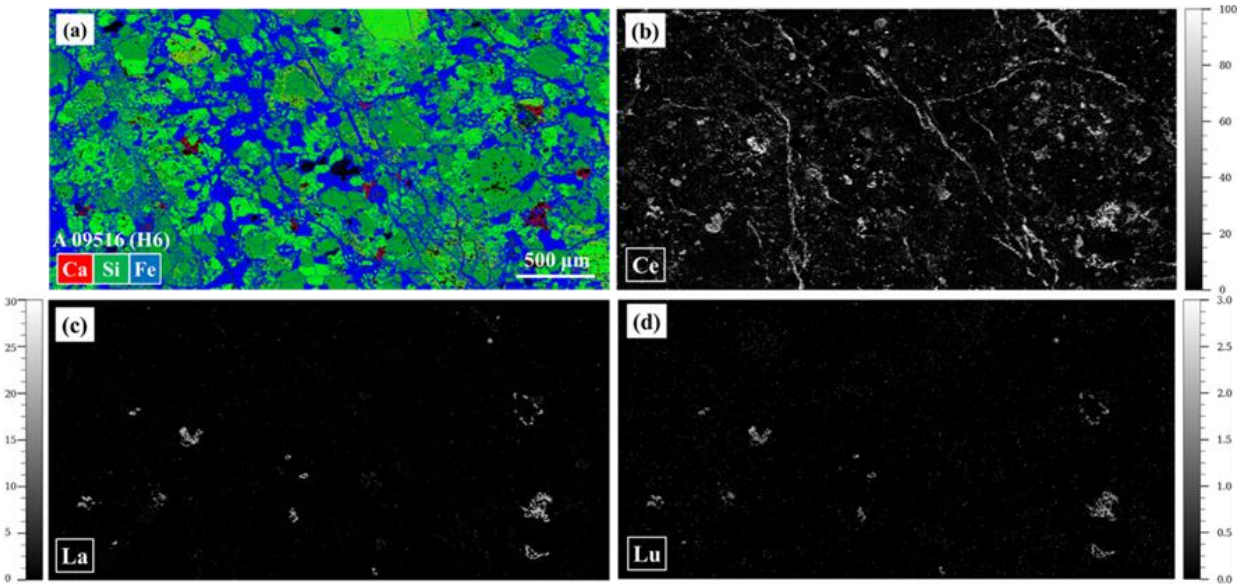

Fig. 2. (Semi-)quantitative element maps for A 09516. (a) Combined RGB elemental map with red: Ca, green: Si, and blue: Fe. Based on the composition, the following mineralogy can be deduced red: Ca-phosphates, orange: Ca-rich pyroxene, light green: feldspar and low-Ca pyroxene, dark green: olivine, and blue: metals, sulfides, and oxides. (b) Cerium distribution map. (c) Lanthanum distribution map. (d) Lutetium distribution map. Scale bars for (b) to (d) in ppm.

the cracks (Fig. 2). In the other samples analyzed in this study, such a Ce enrichment was observed in cracks of A 09436, A 09387, NWA 6771, and Nuevo Mercurio. As a result, at least three types of cracks are confirmed based on their REE abundances: cracks highly enriched in REEs, cracks highly enriched in Ce, and cracks exhibiting no REE enrichment.

3.3 Elemental abundances in cracks

The results of the reference materials analyzed using LA-ICP-SF-MS are listed in Table 3, including the detection limits (based on 3SD). Most of the major element abundances display up to ~10% relative standard deviation (RSD; 1SD) and these abundances are in excellent agreement within uncertainty with their preferred values. The trace element abundances are reproducible within ~15% RSD (1SD) on average. All trace element abundances overlap within uncertainty with their preferred values with a slight discrepancy for U in GOR132-G. Based on these results, the relative uncertainties accompanying the elemental abundances determined in the unknown samples using LA-ICP-SF-MS with the conditions applied in this study are estimated to be better than 10%.

The chemical compositions across the various cracks in all samples are summarized in Table 4, together with their ratios of Na_2O to SiO_2 and P_2O_5 to SiO_2 and ΣREEs, Ce/Ce*, and Eu/Eu* values. The Ce/Ce*and Eu/Eu* values are calculated using $\{Ce/(La^{0.48}\times Pr^{0.52})\}_N$ and $\{Eu/(Sm^{0.45}\times Gd^{0.55})\}_N$, respectively (Dauphas and Pourmand, 2015). The regions of the cracks in all samples are indicated in the corresponding optical and BSE images in supporting information. As the laser spot size was 50 µm in diameter and this spot size is larger than the width of most cracks analyzed in this study, neighboring minerals including those placed on the bottom of the crack were also ablated during the analysis of the cracks in most cases (Fig. 3 and supporting information),

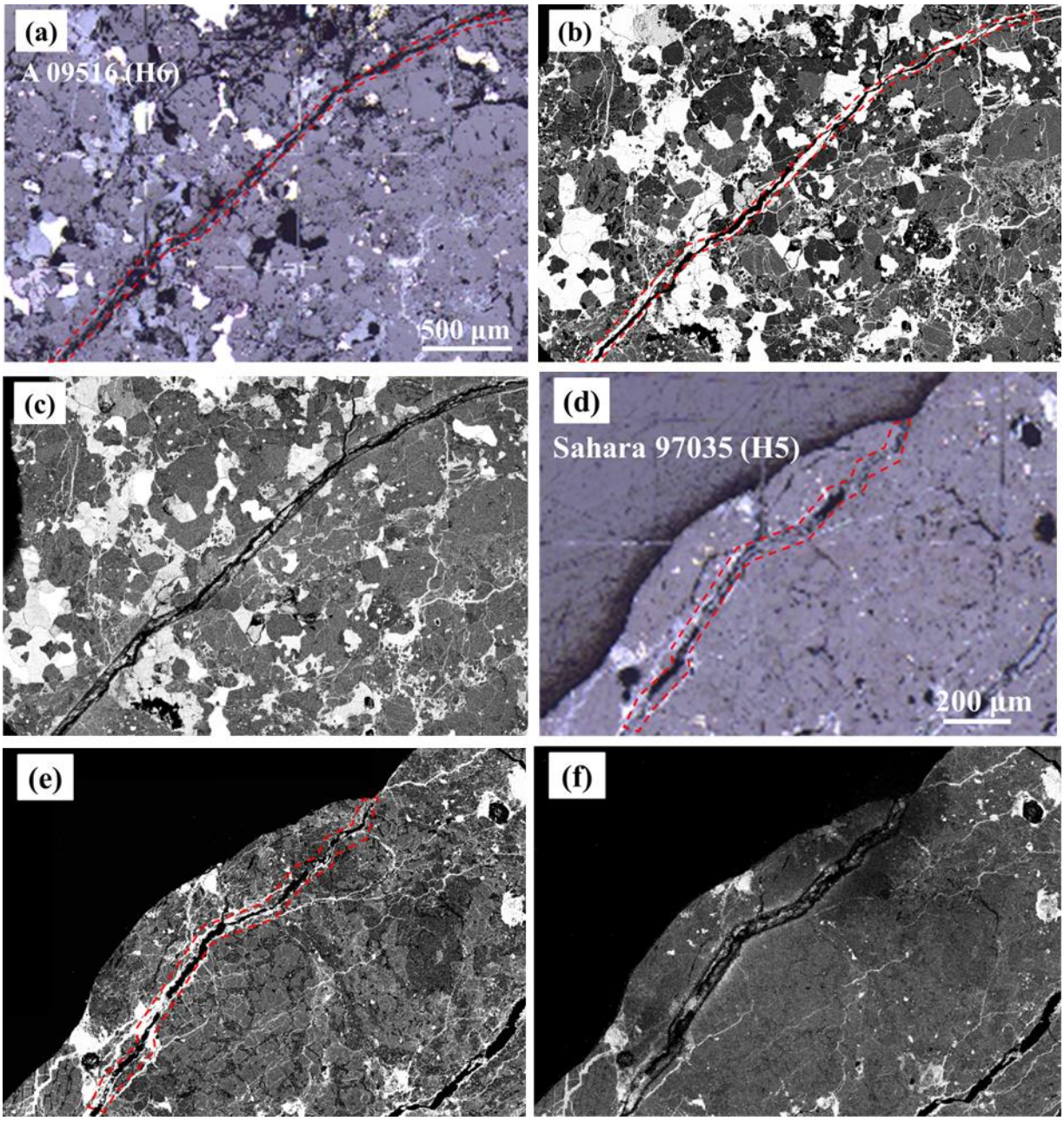

Fig. 3. Optical and BSE images of the regions before and after the ablation for LA-ICP-SF-MS indicated by a broken red line except for the BES images after the ablation. (a) Optical image of Crack-4 of A 09516 before the ablation. (b) BSE image of Crack-4 of A 09516 before the ablation. (c) BSE image of Crack-4 of A 09516 after the ablation. (d) Optical image of Crack-2 of Sahara 97035 before the ablation. (e) BSE image of Crack-2 of Sahara 97035 before the ablation. (f) BSE image of Crack-2 of Sahara 97035 after the ablation.

inducing the variety in their elemental abundances only due to a different proportion of the neighboring minerals ablated (*i.e.*, a different proportion of the constituent minerals in HCs, with limonite in the crack if it is applicable). Overall, some of the cracks analyzed display a similar feature to each other in their REE abundances and all cracks can be divided into some groups. As examples, the CI-normalized REE, Th, and U abundances and ratios of Na_2O to SiO_2 and P_2O_5 to SiO_2 in cracks of A 09618 and A 09516 are shown in Figs. 4 and 5, respectively. Crack-1, -2, and -3 of A 09618 and Crack-4 of A 09516 display elevated REE abundances relative to the bulk rock. These REE-enriched cracks also contain high Th and U abundances in most samples.

Table 3. Elemental abundances in reference materials (LOD: limit of detection).

	LOD	GOR128-G						GOR132-G					
		This work (n=5)			Preferred values			This work (n=5)			Preferred values		
(wt.%)													
Na_2O	0.005	0.53	±	0.04	0.574	±	0.026	0.84	±	0.06	0.830	±	0.040
MgO	0.0007	25	±	1	26.0	±	0.3	22	±	1	22.4	±	0.2
Al_2O_3	0.0003	10	±	1	9.91	±	0.17	11	±	1	11.0	±	0.2
SiO_2	0.02	47	±	0	46.1	±	0.4	46	±	1	45.5	±	0.4
P_2O_5	0.0006	0.024	±	0.006	0.025	±	0.005	0.031	±	0.000	0.036	±	0.012
K_2O	0.0005	0.032	±	0.002	0.036	±	0.005	0.033	±	0.004	0.031	±	0.003
CaO	0.02	6.5	±	0.2	6.24	±	0.12	8.8	±	0.3	8.45	±	0.12
TiO	0.003	0.30	±	0.02	0.288	±	0.012	0.33	±	0.03	0.306	±	0.013
Cr_2O_3	0.00005	0.36	±	0.01	0.332	±	0.025	0.41	±	0.02	0.369	±	0.027
MnO	0.00001	0.18	±	0.01	0.176	±	0.009	0.15	±	0.01	0.154	±	0.007
FeO	0.0009	10	±	0	9.81	±	0.12	10	±	0	10.1	±	0.1
NiO	0.00001	0.12	±	0.02	0.137	±	0.008	0.16	±	0.00	0.151	±	0.007
(ppm)													
Sc	0.3	33	±	3	32.1	±	1.4	40	±	3	36.5	±	1.2
V	0.03	180	±	10	189	±	13	220	±	10	214	±	17
Co	0.8	93	±	11	92.4	±	6.2	100	±	10	92.7	±	5.7
Cu	0.09	68	±	8	63.8	±	12.5	210	±	10	205	±	21
Zn	0.3	64	±	15	74.7	±	6.7	71	±	3	76.8	±	12.5
Rb	0.04	0.41	±	0.24	0.406	±	0.025	2.2	±	0.1	2.10	±	0.10
Sr	0.01	31	±	3	30.0	±	1.0	15	±	1	15.3	±	0.6
Y	0.005	13	±	2	11.8	±	0.5	14	±	1	12.9	±	0.5
Zr	0.006	10	±	2	10	±	0.5	10	±	1	9.9	±	0.3
Nb	0.006	0.080	±	0.043	0.099	±	0.007	0.063	±	0.004	0.073	±	0.013
Ba	0.02	1.1	±	0.1	1.06	±	0.03	0.78	±	0.05	0.815	±	0.062
La	0.002	0.12	±	0.01	0.121	±	0.004	0.085	±	0.008	0.0842	±	0.0029
Ce	0.002	0.45	±	0.04	0.450	±	0.016	0.36	±	0.03	0.393	±	0.018
Pr	0.001	0.11	±	0.02	0.100	±	0.004	0.088	±	0.008	0.089	±	0.004
Nd	0.005	0.81	±	0.10	0.784	±	0.047	0.71	±	0.07	0.689	±	0.017
Sm	0.02	0.50	±	0.14	0.525	±	0.02	0.53	±	0.05	0.508	±	0.015
Eu	0.003	0.28	±	0.03	0.264	±	0.008	0.26	±	0.02	0.255	±	0.007
Gd	0.02	1.2	±	0.2	1.17	±	0.04	1.2	±	0.1	1.19	±	0.04
Tb	0.004	0.26	±	0.06	0.248	±	0.012	0.28	±	0.03	0.269	±	0.011
Dy	0.004	2.1	±	0.3	1.98	±	0.07	2.2	±	0.2	2.15	±	0.06

(*continued on next page*)

Ho	0.001	0.49	±	0.08	0.443	±	0.019	0.51	±	0.06	0.507	±	0.019
Er	0.004	1.5	±	0.3	1.40	±	0.06	1.6	±	0.2	1.56	±	0.05
Tm	0.01	0.23	±	0.03	0.204	±	0.009	0.24	±	0.03	0.234	±	0.009
Yb	0.004	1.5	±	0.2	1.41	±	0.06	1.6	±	0.2	1.61	±	0.04
Lu	0.002	0.22	±	0.05	0.206	±	0.009	0.24	±	0.03	0.237	±	0.009
Hf	0.006	0.36	±	0.06	0.349	±	0.017	0.36	±	0.04	0.357	±	0.018
Ta	0.01	0.02	±	0.01	0.019	±	0.001	0.03	±	0.00	0.031	±	0.002
W	0.01	14	±	1	15.5	±	2.4	26	±	2	25.4	±	3.4
Pb	0.004	0.29	±	0.03	0.345	±	0.043	20	±	1	19.5	±	1.7
Th	0.001	0.013	±	0.010	0.008	±	0.001	0.004	±	0.002	0.009	±	0.003
U	0.0004	0.013	±	0.003	0.012	±	0.0012	0.062	±	0.008	0.048	±	0.005

The uncertainties reported represent 1SD. LOD values are calculated based on 3SD for the blank intensities characterized within the same analytical session. Preferred values are from Jochum *et al.* (2006).

The other cracks contain abundances of REEs, Th, and U, similar to or lower than those determined based on bulk rock analysis. The cracks enriched in REEs, Crack-1 and -2 of A 09618 and Crack-4 of A 09516, display a negative Eu anomaly (Eu/Eu* = 0.43, 0.57, and 0.22, respectively; Table 4) with higher ratios of P_2O_5 to SiO_2 than determined for the bulk rock, while the cracks with low REE abundances, Crack-4 of A 09618 and Crack-1, -2, and -3 of A 09516, display a positive Eu anomaly (Eu/Eu* = 2.3, 1.9, 2.1, and 2.3, respectively; Table 4) accompanied by ratios of P_2O_5 to SiO_2 lower than or similar to that of the bulk rock. In addition, these cracks with low REE abundances display a positive Ce anomaly (Ce/Ce* = 1.7, 1.3, 3.3, and 5.8, respectively; Table 4). Cracks of the other samples all display a flat CI-normalized REE pattern with abundances similar to the bulk rock or a positive Eu anomaly (Eu/Eu* is up to 7.1; Table 4) at lower REE abundances relative to the bulk rock but without a Ce anomaly (Table 4). Therefore, most of the cracks of the samples analyzed can be divided into the three main types of cracks, which is consistent with the observation from LA-ICP-TOF-MS mapping. However, even though Crack-3 of A 09618 displays REE, Th, and U abundances as high as those of Crack-1 and -2, the P_2O_5/SiO_2 is almost as low as that observed for Crack-4 (Fig. 4). A small negative Ce anomaly is also observed for this crack. Thus, Crack-3 of A 09618 can be assigned to a 4th type of crack, characterized by high REE abundances with a P_2O_5/SiO_2 as low as or even lower than that of the bulk rock and a slight negative Ce anomaly (Ce/Ce* = 0.74; Table 4).

4. DISCUSSION

4.1 Unbound REE deposition in cracks

LA-ICP-TOF-MS mapping clearly shows a deposition of all REEs or of Ce alone in cracks of HCs, which is confirmed using LA-ICP-SF-MS line scanning (Figs. 1, 2, 4, and 5 and Table 4). All the cracks analyzed in this study can be divided into four types based on their REE abundances and patterns: type I—cracks with elevated REE abundances with a high P_2O_5/SiO_2, type II—cracks with elevated REE abundances with a low P_2O_5/SiO_2 and a negative Ce anomaly, type III—cracks depleted in REE abundances and a positive Ce anomaly,

Table 4. Elemental abundances in cracks.

Meteorite	A-880941 (H3.3)			Y-793574 (H3.5)			Y-790461 (H3.7)			ALH-78084 (H3.9)		
Crack #	1	2	3	1	2	3	1	2	3	1	2	3
(wt.%)												
Na_2O	0.8	1.5	0.9	0.48	0.43	0.67	1.0	0.76	0.73	0.44	0.57	0.37
MgO	22	26	17	24	10	20	21	18	18	13	12	21
Al_2O_3	1.8	2.9	2.1	1.5	0.85	1.5	2.3	1.5	1.7	0.85	1.1	1.2
SiO2	35	44	33	33	17	33	40	35	30	24	20	34
P_2O_5	0.27	0.44	0.31	0.42	0.11	0.34	0.15	0.33	0.28	0.056	0.42	0.15
K_2O	0.10	0.14	0.12	0.054	0.043	0.11	0.14	0.10	0.11	0.052	0.067	0.024
CaO	1.2	2.3	1.2	1.2	0.81	1.2	2.3	1.9	1.0	0.96	1.2	0.94
TiO_2	0.098	0.14	0.12	0.084	0.054	0.070	0.12	0.096	0.086	0.051	0.035	0.079
Cr_2O_3	0.74	0.81	0.47	0.43	0.27	0.41	0.35	0.47	0.41	0.21	0.20	0.39
MnO	0.31	0.35	0.26	0.24	0.17	0.28	0.31	0.28	0.26	0.22	0.17	0.32
FeO	35	21	42	36	67	41	30	39	44	56	57	38
NiO	2.2	0.33	2.2	1.8	2.7	1.3	1.5	2.6	2.5	4.0	7.6	3.3
(ppm)												
Sc	7.8	13	8.1	6.7	5.1	9.0	14	10	6.5	5.8	5.3	5.5
V	71	89	60	48	30	52	59	59	44	31	27	43
Co	810	119	730	861	1464	854	448	1130	976	2560	3084	1170
Cu	152	49	153	48	29	81	196	108	51	134	33	205
Zn	86	75	59	79	40	79	60	68	64	28	33	57
Rb	1.2	2.1	1.7	1.5	1.0	3.2	3.0	2.6	3.1	1.1	1.5	0.94
Sr	11	17	15	14	4.1	10	12	11	12	3.7	6.3	7.3
Y	2.3	3.0	2.0	1.9	1.1	1.7	1.3	2.0	2.1	1.0	2.3	1.4
Zr	5.6	7.8	6.1	4.8	3.2	5.2	9.1	6.1	4.3	3.3	3.2	4.4
Nb	0.44	0.73	0.52	0.28	0.18	0.32	0.68	0.40	0.48	0.23	0.31	0.40
Ba	3.3	5.8	3.6	3.5	2.3	3.2	4.3	3.8	5.3	1.7	2.2	1.3
La	0.49	0.50	0.31	0.30	0.14	0.25	0.16	0.28	0.71	0.13	0.36	0.20
Ce	1.3	1.4	0.79	0.87	0.47	0.84	0.58	0.83	1.7	0.34	0.98	0.53
Pr	0.18	0.20	0.12	0.11	0.052	0.10	0.062	0.11	0.22	0.05	0.14	0.074
Nd	0.85	0.91	0.56	0.57	0.28	0.50	0.32	0.54	0.99	0.22	0.68	0.37
Sm	0.26	0.31	0.18	0.17	0.10	0.16	0.11	0.18	0.26	0.07	0.23	0.13
Eu	0.091	0.13	0.10	0.078	0.027	0.069	0.083	0.072	0.10	0.029	0.053	0.053
Gd	0.34	0.41	0.25	0.24	0.14	0.22	0.15	0.25	0.32	0.12	0.30	0.18
Tb	0.064	0.078	0.049	0.046	0.024	0.039	0.031	0.047	0.054	0.021	0.053	0.033
Dy	0.39	0.51	0.33	0.33	0.18	0.27	0.22	0.33	0.35	0.15	0.38	0.23

(*continued on next page*)

Ho	0.088	0.11	0.074	0.072	0.039	0.063	0.050	0.073	0.076	0.036	0.080	0.052
Er	0.26	0.34	0.23	0.22	0.12	0.19	0.16	0.22	0.23	0.11	0.25	0.16
Tm	0.04	0.06	0.04	0.03	0.02	0.03	0.03	0.03	0.03	0.01	0.04	0.03
Yb	0.26	0.35	0.25	0.21	0.11	0.20	0.19	0.24	0.24	0.13	0.24	0.17
Lu	0.040	0.056	0.041	0.033	0.018	0.031	0.031	0.037	0.036	0.021	0.034	0.027
Hf	0.18	0.23	0.19	0.15	0.074	0.15	0.27	0.18	0.12	0.086	0.092	0.12
Ta	0.03	0.04	0.02	0.02	0.01	0.01	0.03	0.02	0.03	0.01	0.01	0.02
W	0.21	0.070	0.34	0.42	0.40	0.75	0.40	0.20	0.16	0.15	0.31	0.31
Pb	0.20	0.23	0.35	1.4	0.96	2.53	0.67	0.94	1.43	0.16	0.21	0.12
Th	0.11	0.075	0.063	0.038	0.018	0.051	0.050	0.045	0.109	0.031	0.023	0.042
U	0.029	0.016	0.021	0.0090	0.0094	0.019	0.013	0.013	0.044	0.011	0.0073	0.011
P_2O_5/SiO_2	0.0075	0.0099	0.0095	0.012	0.0063	0.010	0.0037	0.0095	0.0093	0.0023	0.021	0.0042
Na_2O/SiO_2	0.024	0.034	0.029	0.014	0.025	0.020	0.025	0.022	0.024	0.018	0.029	0.011
ΣREEs	4.6	5.3	3.3	3.3	1.7	3.0	2.2	3.2	5.3	1.4	3.8	2.2
Ce/Ce*	1.0	1.0	1.0	1.1	1.3	1.2	1.4	1.1	1.0	1.0	1.0	1.1
Eu/Eu*	0.94	1.1	1.5	1.2	0.69	1.1	2.0	1.0	1.1	0.95	0.62	1.1

Table 4. (*continued*)

Meteorite	A-881258 (H3.9)			A 09436 (H3)			A 09387 (H4)			
Crack #	1	2	3	1	2	3	1	2	3	4
(wt.%)										
Na_2O	0.80	0.38	0.29	0.70	1.0	1.1	1.1	0.96	1.1	1.8
MgO	19	17	8.3	13	22	23	23	22	26	25
Al_2O_3	1.6	0.82	0.67	1.2	1.9	2.3	2.0	1.6	1.8	2.7
SiO2	31	29	15	21	37	42	40	38	39	45
P_2O_5	0.22	0.22	0.038	0.12	0.58	0.56	0.42	2.6	0.17	0.14
K_2O	0.096	0.054	0.036	0.24	0.15	0.11	0.11	0.12	0.11	0.10
CaO	2.1	1.2	0.43	0.82	1.8	2.8	2.3	3.8	1.6	2.1
TiO_2	0.070	0.075	0.032	0.053	0.098	0.12	0.47	0.11	0.15	0.30
Cr_2O_3	0.22	0.52	0.067	0.26	0.43	0.46	0.47	0.40	0.49	0.46
MnO	0.26	0.25	0.13	0.16	0.29	0.32	0.31	0.30	0.33	0.37
FeO	42	45	70	58	33	26	27	28	27	22
NiO	3.0	4.4	5.4	4.6	2.1	1.4	2.6	2.2	1.4	1.0
(ppm)										
Sc	11	5.0	2.1	5.0	8.3	12	10	9.2	8.9	10
V	44	52	11	34	57	68	64	57	61	60
Co	1124	1403	2146	1296	459	406	611	663	566	355
Cu	57	226	74	88	143	67	194	255	55	22

(*continued on next page*)

Zn	46	56	21	44	85	73	145	156	98	60
Rb	2.5	1.6	0.8	2.8	3.8	3.7	16	20	4.6	3.0
Sr	10	6.2	8.7	6.1	9.4	14	8.5	11	9.4	9.0
Y	1.5	0.81	0.51	0.78	3.4	2.0	1.9	11.3	0.99	2.0
Zr	5.7	1.9	0.83	5.6	11	8.2	6.8	4.8	6.6	6.0
Nb	0.37	0.26	0.10	0.25	0.40	0.50	0.45	0.42	0.44	0.47
Ba	3.4	1.6	1.7	2.5	3.4	4.3	2.9	3.2	3.4	3.4
La	0.24	0.12	0.23	0.11	0.52	0.32	0.30	1.9	0.12	0.26
Ce	0.75	0.37	0.60	0.72	2.7	1.2	0.89	6.1	0.53	0.77
Pr	0.091	0.043	0.071	0.044	0.22	0.12	0.12	0.76	0.05	0.10
Nd	0.46	0.21	0.30	0.22	1.0	0.57	0.55	3.6	0.26	0.54
Sm	0.15	0.07	0.07	0.08	0.33	0.20	0.20	1.1	0.11	0.22
Eu	0.067	0.033	0.040	0.043	0.074	0.092	0.062	0.11	0.066	0.062
Gd	0.20	0.09	0.07	0.10	0.44	0.25	0.24	1.4	0.11	0.24
Tb	0.038	0.016	0.014	0.019	0.081	0.047	0.049	0.25	0.026	0.047
Dy	0.26	0.12	0.085	0.13	0.56	0.33	0.31	1.8	0.16	0.32
Ho	0.054	0.026	0.017	0.029	0.12	0.071	0.067	0.371	0.036	0.068
Er	0.17	0.083	0.054	0.094	0.36	0.22	0.21	1.1	0.11	0.21
Tm	0.03	0.01	0.01	0.02	0.05	0.03	0.03	0.17	0.03	0.04
Yb	0.18	0.10	0.053	0.10	0.33	0.23	0.21	1.0	0.13	0.23
Lu	0.030	0.016	0.010	0.017	0.049	0.037	0.034	0.15	0.023	0.036
Hf	0.16	0.051	0.027	0.11	0.25	0.22	0.18	0.13	0.16	0.15
Ta	0.03	0.01	0.01	0.01	0.02	0.03	0.02	0.01	0.04	0.01
W	0.15	1.1	0.13	0.97	1.5	0.19	0.20	0.07	0.12	0.13
Pb	0.49	0.33	0.25	2.8	6.6	1.3	5.0	2.4	3.9	2.2
Th	0.038	0.018	0.011	0.016	0.040	0.052	0.046	0.090	0.032	0.041
U	0.012	0.0052	0.0081	0.015	0.034	0.022	0.017	0.016	0.010	0.012
P_2O_5/SiO_2	0.0072	0.0076	0.0026	0.0056	0.016	0.013	0.011	0.070	0.0044	0.0031
Na_2O/SiO_2	0.026	0.013	0.020	0.033	0.027	0.026	0.029	0.025	0.027	0.040
ΣREEs	2.7	1.3	1.6	1.7	6.9	3.7	3.3	20	1.8	3.1
Ce/Ce*	1.2	1.3	1.1	2.5	2.0	1.5	1.2	1.2	1.6	1.1
Eu/Eu*	1.2	1.3	1.7	1.5	0.59	1.3	0.87	0.28	1.9	0.84

Table 4. (*continued*)

Meteorite	NWA 6771 (H4)			Jilin (H5)			Nuevo Mercurio (H5)			Richardton (H5)		
Crack #	1	2	3	1	2	3	1	2	3	1	2	3
(wt.%)												
Na_2O	0.84	1.4	1.3	1.8	2.3	1.5	1.7	2.6	2.6	1.9	1.7	2.8

(*continued on next page*)

MgO	20	17	20	27	27	27	29	24	17	27	16	16
Al_2O_3	1.8	3.0	2.7	3.3	3.6	2.0	3.3	5.2	5.7	3.7	2.9	5.0
SiO2	38	35	37	45	51	51	45	50	41	47	40	38
P_2O_5	0.096	0.39	0.18	0.17	0.17	0.34	0.19	0.16	0.088	0.14	0.030	0.18
K_2O	0.062	0.17	0.096	0.20	0.18	0.096	0.19	0.28	0.33	0.16	0.47	0.23
CaO	1.2	1.4	1.2	1.4	3.9	3.1	1.7	1.9	2.7	1.8	0.97	1.5
TiO_2	0.083	0.11	0.13	0.079	0.16	0.15	0.17	0.11	0.17	0.14	0.13	0.082
Cr_2O_3	0.27	0.42	0.34	0.46	0.45	0.32	0.36	0.35	0.92	0.35	0.24	0.59
MnO	0.33	0.24	0.27	0.35	0.35	0.40	0.35	0.33	0.24	0.35	0.25	0.22
FeO	32	39	35	20	11	14	19	15	25	17	36	34
NiO	4.7	1.7	2.3	0.54	0.087	0.18	0.24	0.26	4.2	0.48	1.6	0.76
(ppm)												
Sc	7.3	7.7	7.9	8.9	21	17	7.9	8.6	12	11	6.0	6.4
V	44	56	51	59	90	78	45	50	97	58	38	60
Co	886	393	604	181	11	57	56	143	186	323	1051	482
Cu	134	216	181	129	13	21	68	370	509	132	219	118
Zn	75	68	80	56	49	49	70	76	93	103	88	93
Rb	1.2	2.6	1.8	6.6	4.1	2.5	3.4	5.1	6.8	4.3	16	5.6
Sr	10	17	13	20	27	11	19	22	26	14	14	21
Y	0.70	1.4	1.1	0.76	1.7	1.0	0.85	1.0	0.83	1.3	0.44	1.6
Zr	5.4	6.7	9.2	5.3	13	9.6	6.2	9.0	12	7.6	3.8	5.4
Nb	0.33	0.38	0.52	0.53	0.68	0.63	0.56	0.47	0.60	0.49	0.33	0.54
Ba	3.1	10	4.3	7.2	7.9	4.7	7.8	8.3	10	4.4	6.5	7.5
La	0.098	0.26	0.15	0.11	0.17	0.11	0.17	0.19	0.16	0.16	0.059	0.19
Ce	0.40	1.0	1.0	0.29	0.50	0.32	0.51	1.2	1.1	0.60	0.18	0.56
Pr	0.037	0.089	0.052	0.040	0.080	0.047	0.051	0.064	0.054	0.061	0.019	0.072
Nd	0.17	0.43	0.26	0.21	0.40	0.23	0.24	0.29	0.23	0.34	0.082	0.39
Sm	0.06	0.15	0.09	0.07	0.15	0.08	0.08	0.14	0.08	0.13	0.05	0.12
Eu	0.061	0.091	0.07	0.12	0.13	0.068	0.11	0.14	0.17	0.10	0.091	0.14
Gd	0.08	0.18	0.12	0.10	0.20	0.11	0.09	0.13	0.10	0.15	0.03	0.18
Tb	0.017	0.035	0.025	0.017	0.040	0.022	0.021	0.026	0.021	0.033	0.0084	0.028
Dy	0.11	0.23	0.17	0.12	0.30	0.17	0.13	0.16	0.14	0.20	0.061	0.24
Ho	0.025	0.052	0.039	0.027	0.064	0.039	0.029	0.037	0.032	0.045	0.016	0.052
Er	0.082	0.16	0.12	0.088	0.20	0.13	0.093	0.11	0.10	0.14	0.056	0.16
Tm	0.01	0.02	0.02	0.01	0.03	0.02	0.01	0.02	0.02	0.03	0.01	0.02
Yb	0.10	0.16	0.14	0.11	0.24	0.18	0.12	0.13	0.13	0.17	0.089	0.17
Lu	0.016	0.025	0.023	0.019	0.038	0.029	0.017	0.022	0.022	0.032	0.016	0.030
Hf	0.12	0.17	0.21	0.16	0.41	0.30	0.15	0.18	0.31	0.20	0.11	0.13
Ta	0.03	0.02	0.03	0.02	0.04	0.03	0.02	0.04	0.04	0.05	0.01	0.01

(*continued on next page*)

W	0.19	0.83	0.26	0.03	0.01	0.06	0.11	0.21	0.28	0.13	0.10	0.07
Pb	2.3	13	20	0.18	0.17	1.3	3.2	21	22	11	6.0	1.9
Th	0.032	0.030	0.074	0.026	0.059	0.069	0.053	0.047	0.063	0.036	0.047	0.037
U	0.010	0.047	0.027	0.0079	0.014	0.021	0.062	0.030	0.040	0.010	0.012	0.0081
P_2O_5/SiO_2	0.0025	0.011	0.0049	0.0037	0.0034	0.0066	0.0043	0.0032	0.0021	0.0030	0.00074	0.0047
Na_2O/SiO_2	0.022	0.039	0.034	0.040	0.045	0.029	0.039	0.051	0.062	0.040	0.041	0.073
ΣREEs	1.3	2.9	2.3	1.3	2.5	1.5	1.7	2.6	2.3	2.2	0.77	2.3
Ce/Ce*	1.6	1.6	2.8	1.0	1.0	1.1	1.3	2.5	2.8	1.4	1.3	1.2
Eu/Eu*	2.5	1.7	2.1	4.4	2.3	2.2	3.9	3.2	5.6	2.2	7.1	3.0

Table 4. (*continued*)

Meteorite	A 09618 (H5)				Sahara 97035 (H5)			Butsura (H6)		
Crack #	1	2	3	4	1	2	3	1	2	3
(wt.%)										
Na_2O	0.75	0.51	1.1	0.65	0.62	0.77	0.96	1.4	1.5	1.5
MgO	15	8.7	20	16	29	14	14	27	26	27
Al_2O_3	2.3	3.3	2.2	1.0	2.0	2.8	1.8	2.5	2.7	2.1
SiO2	22	21	38	24	43	31	25	50	45	51
P_2O_5	0.75	0.78	0.075	0.029	0.48	1.1	1.3	0.13	0.19	0.28
K_2O	0.097	0.47	0.15	0.069	0.055	0.29	0.33	0.13	0.24	0.098
CaO	0.89	1.1	2.1	0.60	3.1	1.8	1.2	2.5	1.8	3.1
TiO_2	0.083	0.36	0.12	0.063	0.14	0.10	0.052	0.15	0.11	0.15
Cr_2O_3	1.7	0.03	0.44	0.22	0.74	0.38	0.45	0.40	1.6	0.32
MnO	0.22	0.13	0.29	0.20	0.38	0.66	0.24	0.39	0.37	0.40
FeO	51	55	32	52	19	42	52	14	20	14
NiO	5.3	9.1	3.3	4.4	0.91	5.2	2.6	0.99	1.5	0.21
(ppm)										
Sc	2.7	5.5	12	3.8	15	7.1	4.6	15	10	17
V	135	34	64	27	120	93	57	68	142	77
Co	1407	1797	842	1175	282	2562	1052	125	54	64
Cu	149	104	145	114	183	389	585	45	153	23
Zn	131	62	65	46	71	83	71	56	132	48
Rb	2.1	32	2.9	1.4	0.93	8.5	3.8	3.3	7.6	2.5
Sr	8.1	24	11	5.0	37	412	1218	13	13	12
Y	6.2	10	4.6	0.42	2.8	55	10	1.4	0.99	1.0
Zr	4.9	29	7.0	4.0	8.4	10	5.6	7.7	5.7	9.5
Nb	0.57	3.1	0.41	0.24	0.27	0.64	0.31	0.52	0.51	0.63
Ba	27	87	3.7	2.1	1.9	473	390	4.4	5.1	4.8

(*continued on next page*)

La	5.51	9.8	4.6	0.19	0.37	33	4.0	0.17	0.14	0.11
Ce	9.5	16	6.8	0.62	1.9	25	7.2	0.47	0.40	0.32
Pr	1.3	2.5	1.1	0.041	0.13	7.5	1.2	0.077	0.060	0.047
Nd	4.5	9.4	3.9	0.17	0.70	33	5.5	0.38	0.28	0.23
Sm	0.87	1.9	0.74	0.04	0.24	7.1	1.4	0.12	0.10	0.08
Eu	0.12	0.34	0.13	0.034	0.060	1.6	0.25	0.093	0.090	0.071
Gd	0.91	1.8	0.72	0.05	0.36	8.7	1.7	0.17	0.13	0.11
Tb	0.15	0.27	0.12	0.0099	0.067	1.2	0.27	0.033	0.024	0.022
Dy	0.97	1.7	0.76	0.063	0.48	7.3	1.7	0.23	0.17	0.17
Ho	0.21	0.34	0.16	0.014	0.10	1.5	0.36	0.049	0.037	0.039
Er	0.66	1.0	0.49	0.047	0.31	4.3	1.0	0.17	0.12	0.13
Tm	0.10	0.15	0.07	0.01	0.04	0.56	0.14	0.03	0.02	0.02
Yb	0.71	1.0	0.53	0.058	0.32	3.4	0.85	0.20	0.14	0.18
Lu	0.11	0.16	0.084	0.011	0.048	0.51	0.12	0.030	0.022	0.030
Hf	0.077	0.77	0.19	0.085	0.22	0.30	0.15	0.22	0.18	0.30
Ta	0.02	0.20	0.02	0.02	0.01	0.04	0.01	0.03	0.02	0.03
W	0.52	0.32	0.10	1.2	0.27	0.76	0.83	0.12	0.03	0.06
Pb	401	4.1	0.72	2.0	10	8.6	33	0.20	0.33	1.3
Th	0.92	1.7	0.51	0.017	0.040	1.0	0.23	0.045	0.029	0.069
U	2.7	1.4	1.2	0.036	0.027	5.8	1.8	0.015	0.011	0.021
P_2O_5/SiO_2	0.033	0.037	0.0020	0.0012	0.011	0.037	0.052	0.0027	0.0044	0.0055
Na_2O/SiO_2	0.034	0.025	0.028	0.027	0.014	0.025	0.038	0.028	0.035	0.030
ΣREEs	26	47	20	1.3	5.1	136	26	2.2	1.7	1.5
Ce/Ce*	0.88	0.79	0.74	1.7	2.0	0.39	0.79	0.98	1.0	1.1
Eu/Eu*	0.43	0.57	0.56	2.3	0.61	0.60	0.49	2.0	2.4	2.3

Table 4. (*continued*)

Meteorite	A 09516 (H6)				Y-790960 (H7)		
Crack #	1	2	3	4	1	2	3
(wt.%)							
Na_2O	0.82	0.44	0.59	0.51	1.0	1.0	0.71
MgO	12	12	12	6.2	20	24	23
Al_2O_3	1.4	0.79	1.2	0.93	2.0	1.9	1.1
SiO2	22	19	21	12	31	41	31
P_2O_5	0.16	0.059	0.071	1.4	0.039	0.061	2.1
K_2O	0.10	0.051	0.085	0.058	0.13	0.12	0.084
CaO	1.7	0.66	0.90	2.3	1.7	3.2	2.4
TiO_2	0.063	0.16	0.10	0.097	0.063	0.11	0.039
Cr_2O_3	0.12	0.11	0.12	1.0	0.11	0.14	0.10

(*continued on next page*)

MnO	0.15	0.15	0.15	0.088	0.25	0.33	0.29
FeO	57	62	59	69	41	25	37
NiO	3.5	4.5	4.6	6.3	2.9	3.5	1.8
(ppm)							
Sc	8.7	3.9	4.9	7.0	11	19	4.8
V	31	19	22	83	32	55	18
Co	1348	1712	1698	2201	1392	470	996
Cu	64	120	91	75	278	150	38
Zn	27	33	58	60	29	42	41
Rb	1.4	0.70	1.5	0.82	3.9	3.7	2.3
Sr	7.7	4.2	6.4	5.5	11	9.7	8.0
Y	0.80	0.37	0.44	6.8	0.75	1.3	13
Zr	6.0	3.4	6.0	4.8	7.5	13	2.6
Nb	0.36	0.21	0.34	0.19	0.40	0.54	0.40
Ba	2.9	1.5	2.6	1.9	3.8	3.4	2.3
La	0.11	0.050	0.068	1.1	0.052	0.075	2.0
Ce	0.35	0.42	1.0	3.3	0.13	0.22	5.5
Pr	0.039	0.018	0.023	0.45	0.022	0.040	0.84
Nd	0.20	0.083	0.11	2.2	0.13	0.23	4.0
Sm	0.08	0.04	0.04	0.79	0.05	0.09	1.2
Eu	0.053	0.027	0.034	0.062	0.084	0.071	0.095
Gd	0.09	0.04	0.05	0.92	0.08	0.14	1.7
Tb	0.021	0.012	0.010	0.17	0.016	0.029	0.31
Dy	0.13	0.056	0.072	1.1	0.12	0.22	2.1
Ho	0.030	0.013	0.016	0.24	0.029	0.049	0.46
Er	0.098	0.041	0.050	0.73	0.092	0.15	1.4
Tm	0.02	0.01	0.01	0.11	0.01	0.03	0.19
Yb	0.10	0.050	0.060	0.65	0.12	0.20	1.2
Lu	0.018	0.0064	0.010	0.095	0.020	0.032	0.17
Hf	0.16	0.071	0.14	0.14	0.21	0.38	0.067
Ta	0.03	0.02	0.03	0.02	0.02	0.03	0.02
W	0.18	0.38	0.98	0.35	0.11	0.08	0.04
Pb	0.69	2.3	7.4	1.0	0.056	0.061	0.10
Th	0.034	0.017	0.021	0.039	0.019	0.036	0.10
U	0.011	0.0073	0.016	0.019	0.0018	0.0050	0.026
P_2O_5/SiO_2	0.0070	0.0031	0.0033	0.12	0.0013	0.0015	0.066
Na_2O/SiO_2	0.036	0.023	0.028	0.042	0.033	0.026	0.023
ΣREEs	1.3	0.9	1.5	12	0.96	1.6	21
Ce/Ce*	1.3	3.3	5.8	1.1	0.92	0.96	1.0

(*continued on next page*)

Eu/Eu*	1.9	2.1	2.3	0.22	4.0	1.9	0.20

The uncertainties for the elemental abundances determined in each crack are estimated to be ~10% relative. ΣREEs is the total concentration of REEs from La to Lu in ppm. Ce/Ce* = $\{Ce/(La^{0.48}\times Pr^{0.52})\}_N$ and Eu/Eu* = $\{Eu/(Sm^{0.45}\times Gd^{0.55})\}_N$ (Dauphas and Pourmand, 2015; Anders and Grevesse, 1989 for CI values).

and type IV—cracks with REE abundances similar to or lower than CI values without a Ce anomaly (Fig. 6). Considering the P_2O_5/SiO_2 in cracks, the type I cracks must be explained by the heterogeneous distribution of Ca-phosphate phases neighboring to the crack (the "nugget effect"), as the ratios of P_2O_5 to SiO_2 are higher in the type I cracks (*e.g.*, Crack-1 and -2 of A 09618 and in Crack-4 of A 09516) than in the bulk rock. In contrast, the type IV cracks (*e.g.*, Crack-4 of A 09618 and Crack-1, -2, and -3 of A 09516) display ratios lower than or similar to the bulk rock ratios. This is supported by negative Eu anomalies in the type I cracks and positive Eu anomalies in the type IV cracks, because Ca-phosphates of ordinary chondrites display a negative Eu anomaly and feldspar exhibiting a positive Eu anomaly is homogeneously distributed in cracks as expressed by their constant Na_2O/SiO_2 (*e.g.*, Curtis and Schmitt, 1979; Ward *et al.*, 2017). Thus, these two types of cracks likely reflect a nugget effect of Ca-phosphates. A similar effect of ilmenite, highly concentrating in Zr, Nb, Hf, and Ta (Maeda *et al.* 2023), explains their highest abundances in Crack-2 of A 09618 displaying the highest TiO_2/SiO_2 in this study (0.17; Table 4). However, the type II cracks as observed in Crack-3 of A 09618, shown in Fig. 4, cannot be explained by such effect due to their low P_2O_5/SiO_2, indicating that cracks appear to accumulate unbound REEs locally as visible on the trace element maps. Similarly, Th and U are deposited in these cracks as well. This is consistent with chemical leaching experiments (*e.g.*, Ebihara and Honda, 1984), in which REEs, Th, and U are observed to be deposited in cracks and along grain boundaries.

A crack having similar features to the type II cracks such as Crack-3 of A 09618 is observed for Sahara 97035 but for none of the other samples. The CI-normalized REE, Th, and U abundances and ratios of Na_2O to SiO_2 and P_2O_5 to SiO_2 in these cracks are shown in Fig. 7. Crack-2 of Sahara 97035 displays a P_2O_5/SiO_2 as

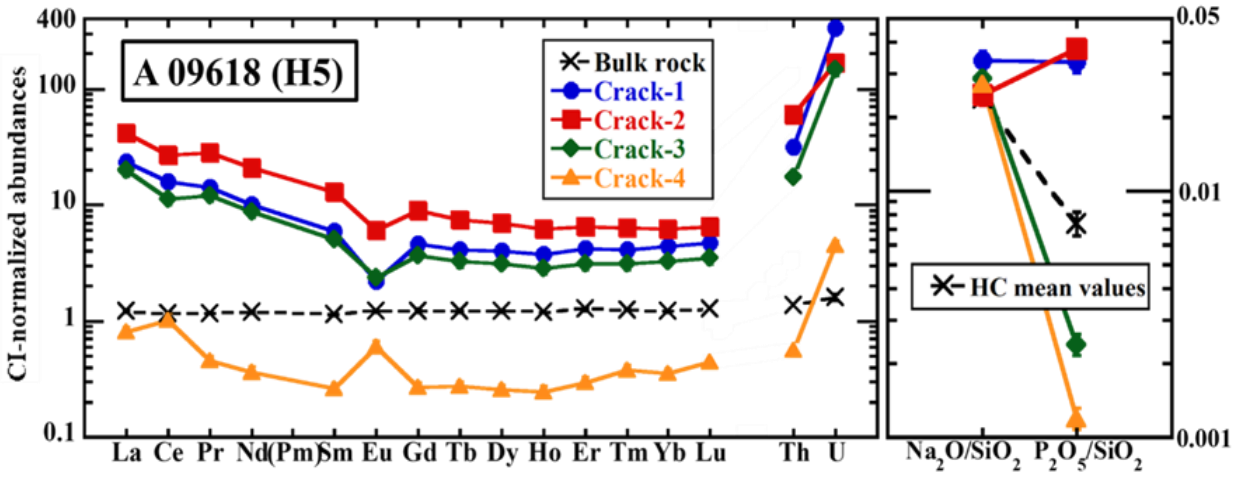

Fig. 4. CI-normalized REE, Th, and U abundances together with the Na_2O to SiO_2 and P_2O_5 to SiO_2 ratios in cracks of A 09618. The error bars represent 10% relative uncertainty (Table 4). Error bars may be smaller than the symbol size. The bulk rock and HC mean values are also shown for comparison (Maeda *et al.*, 2021; Jarosewich, 1990, respectively). CI values are from Anders and Grevesse (1989).

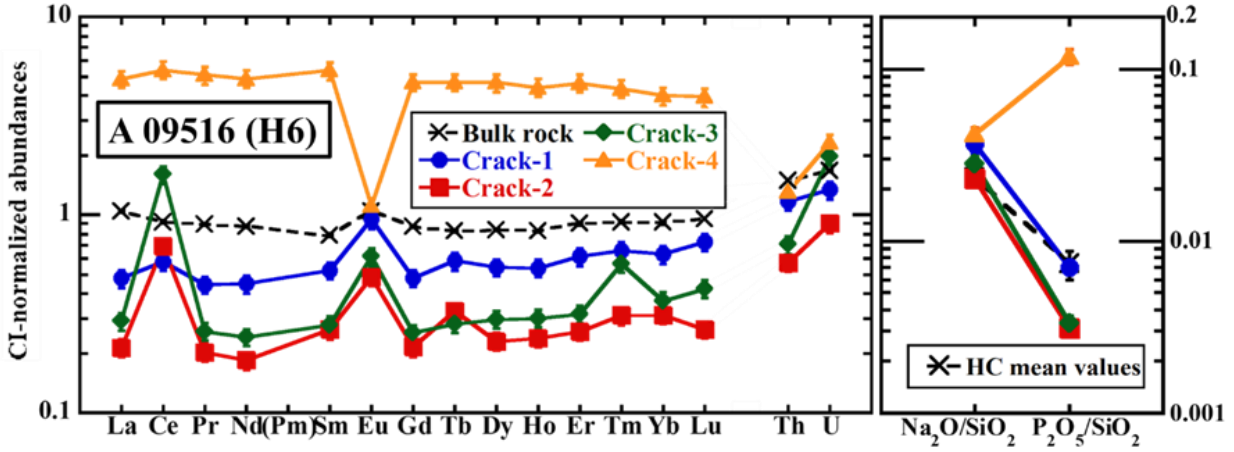

Fig. 5. CI-normalized REE, Th, and U abundances together with the Na_2O to SiO_2 and P_2O_5 to SiO_2 ratios in cracks of A 09516. The error bars represent 10% relative uncertainty (Table 4). Error bars may be smaller than the symbol size. The bulk rock and HC mean values are also shown for comparison (Maeda *et al.*, 2021; Jarosewich, 1990, respectively). CI values are from Anders and Grevesse (1989).

high as those in Crack-1 and -2 of A 09618 (Fig. 4), which is higher than the bulk rock ratio. Nevertheless, the REE and U abundances in Crack-2 of Sahara 97035 are more than twice higher than those in Crack-1 and -2 of A 09618. Even if the nugget effect of Ca-phosphates is considered, the REE and U abundances in this crack are still too high. Thus, it seems that the two cracks shown in Fig. 7 represent unbound REE deposition with a negative Ce anomaly. Alternatively, the high REE and U abundances in Crack-2 of Sahara 97035 may reflect terrestrial soil grains residing in the crack as contaminants because this crack contains the highest Ba and the second highest Sr abundances of all cracks analyzed in this study (Table 4). However, this is highly unlikely because the large negative Ce anomaly in the crack (Ce/Ce* = 0.39; Table 3) should not be observed if the high REE and U content was caused by mixing with such terrestrial material, as terrestrial soils hardly display a Ce anomaly, especially negative one, and the admixture of these soils strongly affects a LREE abundance but does not create a Ce anomaly without the following chemical leaching described later (Fig. 7; Al-Kathiri *et al.*, 2005; Pourkhorsandi *et al.*, 2017; Maeda *et al.*, 2021).

4.2 Fluid mobilization on REEs, Th, and U due to terrestrial alteration

Both the positive and negative Ce anomalies observed in the cracks, shown in Figs. 4-7 and Table 4, are summarized in Table 2 together with the petrographic observations. Overall, cracks of most weathered samples, previously categorized as B/C, C, W1, or W2 with validated weathering degrees by the petrographic observations in this study, display strong positive Ce anomalies (Ce/Ce* = 1.5-5.8) and are all filled up with Fe oxides or hydrates, although cracks of A 09436 and A 09387 show a Ce anomaly despite their low limonite/metal. However, no Ce anomalies are observed in cracks of the fresh fall samples and samples that were validated to have low weathering degrees and previously categorized as A/B or B, except for Nuevo Mercurio. In addition, the cracks observed in the samples used in this study were more likely created, at least widening of the cracks occurred due to thermal effects on the Earth such as daily temperature fluctuations but not due to a shock event on the parent body (Al-Kathiri *et al.*, 2005; McFadden *et al.*, 2005), because Jilin, which is a fresh fall and

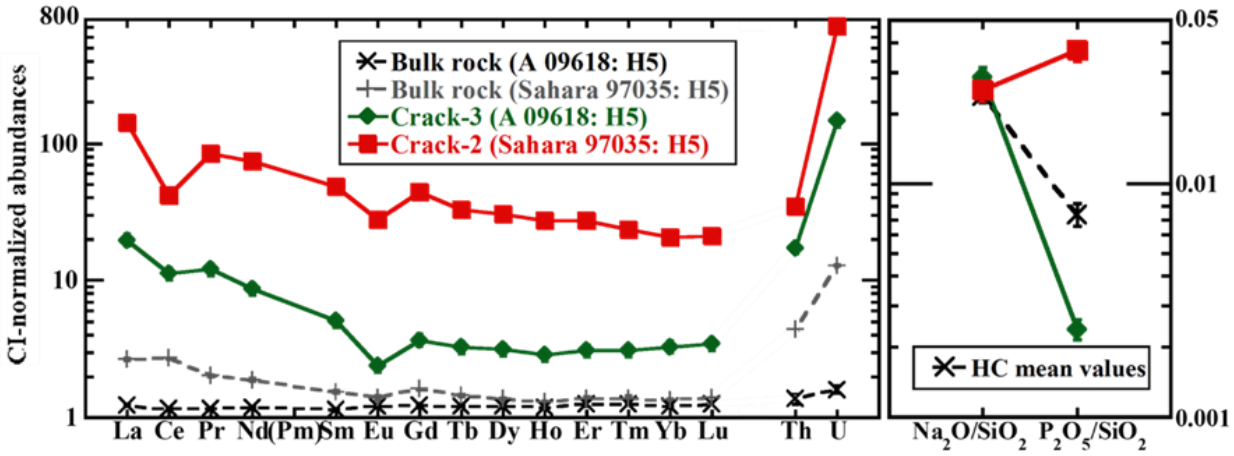

Fig. 7. CI-normalized REE, Th, and U abundances together with the Na_2O to SiO_2 and P_2O_5 to SiO_2 ratios in Crack-3 of A 09618 and in Crack-2 of Sahara 97035. The error bars represent 10% relative uncertainty (Table 4). Error bars may be smaller than the symbol size. The bulk rock and HC mean values are also shown for comparison (Maeda *et al.*, 2021; Jarosewich, 1990, respectively). CI values are from Anders and Grevesse (1989).

displays one of the highest shock stage in this study (S3; Table 2), contains almost no cracks while weathered samples that underwent a low degree of a shock event such as NWA 6771 and Sahara 97035 display an extensive fracturing (Table 2). Yet, the information on the shock stages in the samples is limited. Therefore, the positive Ce anomalies and unbound REE depositions with a negative Ce anomaly observed in cracks, *i.e.*, type II and III cracks likely result from terrestrial weathering. In the case of Nuevo Mercurio, this meteorite fell as a shower on December 15, 1978, and more than 300 pieces had been recovered when it was officially reported (Fredriksson *et al.*, 1979). In addition, many more pieces have been collected in the following years. In these contexts, some pieces had ample time to be exposed to the terrestrial environment before the recovery. Thus, the fragment of Nuevo Mercurio used in this study was probably already weathered, resulting in the positive Ce anomaly observed in its cracks. Moreover, the high porosity observed in Nuevo Mercurio, as mentioned in subsection 3.1, can promote alteration and weathering.

According to Mittlefehldt and Lindstrom (1991), melting of ice in Antarctica can trigger sample alteration following chemical leaching as demonstrated by the loss of Ca-phosphates in eucrites from Antarctic samples, in line with our observations for cracks in Antarctic chondrites. Rain or humidity is known to trigger a similar

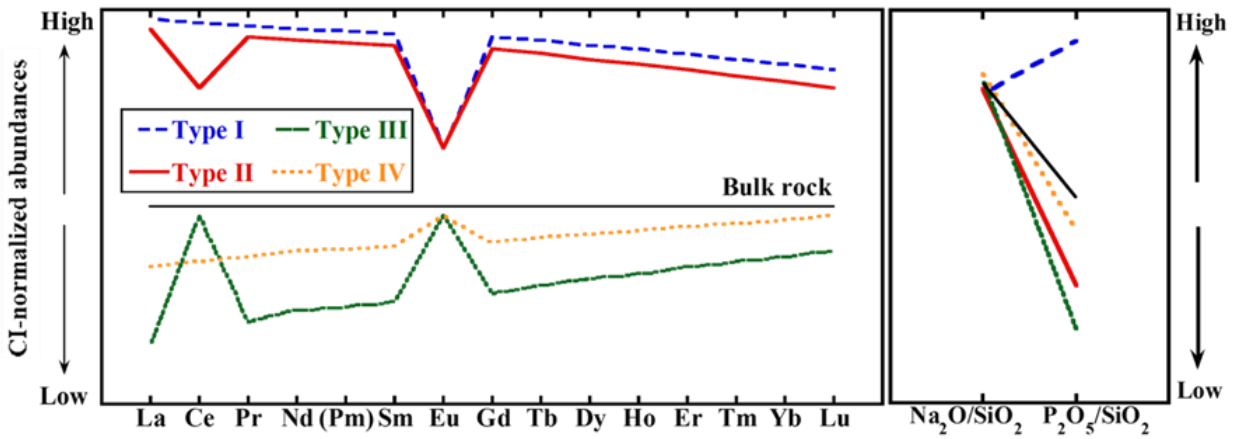

Fig. 6. Approximations of CI-normalized REE patterns together with the Na_2O to SiO_2 and P_2O_5 to SiO_2 ratios for type I-IV cracks.

mechanism in hot deserts (*e.g.*, Al-Kathiri *et al.*, 2005; van Ginneken *et al.*, 2022). During the residence of meteorites in Antarctica, hot deserts, or anywhere else on the Earth, fluids such as melting ice or rain pass through the interior of a meteorite following any physical weaknesses, cracks, or grain boundaries. These fluids turn to a dilute carbonic acid solution in equilibrium with CO_2, *i.e.*, the atmosphere, and then also a sulfuric acid solution as a result of oxidation and hydration of metal and sulfide phases (Mittlefehldt and Lindstrom, 1991). Finally, a fraction of the Ca-phosphate minerals located near cracks is dissolved during the passing of such acidic fluids. As for the dissolution of Ca-phosphate phases, both a complete dissolution and a partial dissolution can be considered. Note that HCs generally contain chlorapatite and merrillite as Ca-phosphate phases and they have different abundances of REEs, Th, and U (*e.g.*, Crozaz, 1979; Ward *et al.*, 2017), which may vary their abundances in the crack depending on the proportion of chlorapatite and merrillite dissolved. Because the solubilities of these Ca-phosphates are comparable under acidic conditions (Adcock *et al.*, 2013), however, it is assumed in the following discussion that chlorapatite and merrillite were affected by the following alterations to the same extent.

(i) In the case of a complete dissolution

Once dissolved, all elements in the Ca-phosphate phases are transferred to a crack by the fluid. Subsequently, more mobile major elements such as P and Ca completely pass through the meteorite, while REEs largely remain in the crack because REEs are significantly less mobile than P and Ca (Middelburg *et al.*, 1988; Bland *et al.*, 2006). During a later stage of this alteration sequence, only Ce remains within the cracks, while the other REEs are removed because Ce is considerably less mobile than the other REEs following oxidation from Ce^{3+} to Ce^{4+} (Mittlefehldt and Lindstrom, 1991). As a result, a crack may display a positive Ce anomaly with a depletion in all other REEs while another crack can still contain a considerable amount of REEs with a negative Ce anomaly, which is supported by the observation that unbound REEs deposited in type II cracks show a negative Ce anomaly (Figs. 6 and 7).

(ii) In the case of a partial dissolution

In this scenario, only trace elements such as REEs are extracted from Ca-phosphates as a result of an interruption in the ionic bonding between cations, particularly impurity cations, and $(PO4)^{2-}$ in the Ca-phosphates (Maeda *et al.*, 2021). As such, only trace elements, *i.e.*, REEs are transferred to a crack by the fluids. Then, in a manner similar to that described above, the REEs are mobilized from the cracks while only Ce remains there during the later stages.

In hot deserts, such a natural chemical leaching may extract trace elements including REEs in both secondary carbonates and terrestrial soil grains residing within or surrounding a meteorite as well as Ca-phosphates, reinforcing the alteration scenarios by Crozaz *et al.* (2003) and Pourkhorsandi *et al.* (2017). In the case of unequilibrated chondrites, glass mesostasis in chondrules may be affected as well, although it can be expected that the solubility of chondrule glass in an acidic solution is lower than that of Ca-phosphates according to Shinotsuka and Ebihara (1997). Considering similar modal abundances of total Ca-phosphates between the weathered samples in this study and published values for fall HCs (Maeda *et al.*, 2021), the alteration scenario (ii) seems more likely and the scenario (i) can follow the scenario (ii). Moreover, in this case, the grain size of Ca-phosphates

should not be a large factor in the extent of alteration because it is a partial dissolution, indicating a partial dissolution can occur at the same extent regardless of the metamorphic grade even though the Ca-phosphates grains grew during thermal metamorphism on the parent body (Huss *et al.*, 2006; Maeda *et al.*, 2021). Even for the alteration scenario (i), however, the difference in the modal abundance may not be resolvable because the complete dissolution of Ca-phosphates may only have involved a small proportion, *i.e.*, small grains of the Ca-phosphates only. Because Th and U are concentrated in Ca-phosphates (Pellas and Störzer, 1975; Crozaz, 1979; Ward *et al.*, 2017), they would behave similarly to REEs during the dissolution, accumulating in cracks as observed in this study (Fig. 7). Based on Jones and Burnett (1979), it can also be considered that a substantial amount of these actinoids originally residing in cracks was detected by chance or those residing in cracks and on grain boundaries were transferred to specific cracks by the fluid. Alternatively, Th and U may be deposited in cracks in a more complicated manner, by combining the considerations mentioned above. However, the first hypothesis that these elements accumulated in cracks together with REEs is preferable given that the high Th and U abundances in cracks analyzed are accompanied by high REE abundances in most cases (Table 4).

Both alteration scenarios can explain a deposition of unbound REEs with a small negative Ce anomaly and a depleted REE pattern with a positive Ce anomaly in cracks, which also supports the observation that cracks of Nuevo Mercurio display a positive Ce anomaly due to weathering, as its high porosity promotes the infiltration of the fluids. In addition, the REEs extracted from Ca-phosphates can accumulate in cracks even without being filled up with Fe-rich phases, as cracks of Nuevo Mercurio are not filled up with such phases because Ca-phosphates can more readily be dissolved in acid than metals (*e.g.*, Shima and Honda, 1967). Based on the alteration scenarios, the deposition of unbound REEs likely represents a transitional stage in the alteration, while the positive Ce anomalies represent a later stage, and as such, positive Ce anomalies may be a more common feature in cracks than the deposition of unbound REEs (Fig. 8). This is indeed consistent with the observation that only two cracks show a deposition of unbound REEs, while 13 out of the 51 cracks studied here exhibit a positive Ce anomaly (Ce/Ce* > 1.5; Table 4). Therefore, the deposition of unbound REEs and positive Ce anomalies in cracks are both caused by terrestrial alteration following chemical leaching. However, it is hard to judge systematically whether or not such elemental mobilizations by terrestrial fluids occurred in a sample based on the petrological observations. Such evaluation must in contrast be based on an evaluation of several of the factors described in Table 2, including the limonite/metal ratio, the state of cracks, the rustiness, and the petrological features such as porosity, because no obvious correlation between the appearance of a Ce anomaly and these factors is observed. For example, A 09436 and A 09387 having limonite/metal ratio of ~10% only display a positive Ce anomaly in their cracks (Ce/Ce* = 1.6-2.5) while ALH 78084 with a limonite/metal ratio of 40% does not (Ce/Ce* = 1.0-1.1), even though the state of the cracks and the overall rustiness are comparable between the three samples (Table 2). Overall, the elemental mobilization by terrestrial fluids appears to have occurred if the sample is categorized as B/C, W1, or higher. This mobilization can occur rapidly as Nuevo Mercurio, a possibly altered fall sample, displays a positive Ce anomaly in the cracks surely, even if this sample has specific features mentioned above, which is consistent with the observations that this kind of alteration can occur on a meteorite sample over timescales of decades to less than a year (Velbel, 2014). In addition, a similar alteration scenario may be generally applied to other classes of weathered chondrites because REEs are concentrated in Ca-phosphates for ordinary, CK, CV, and Rumuruti chondrites and in

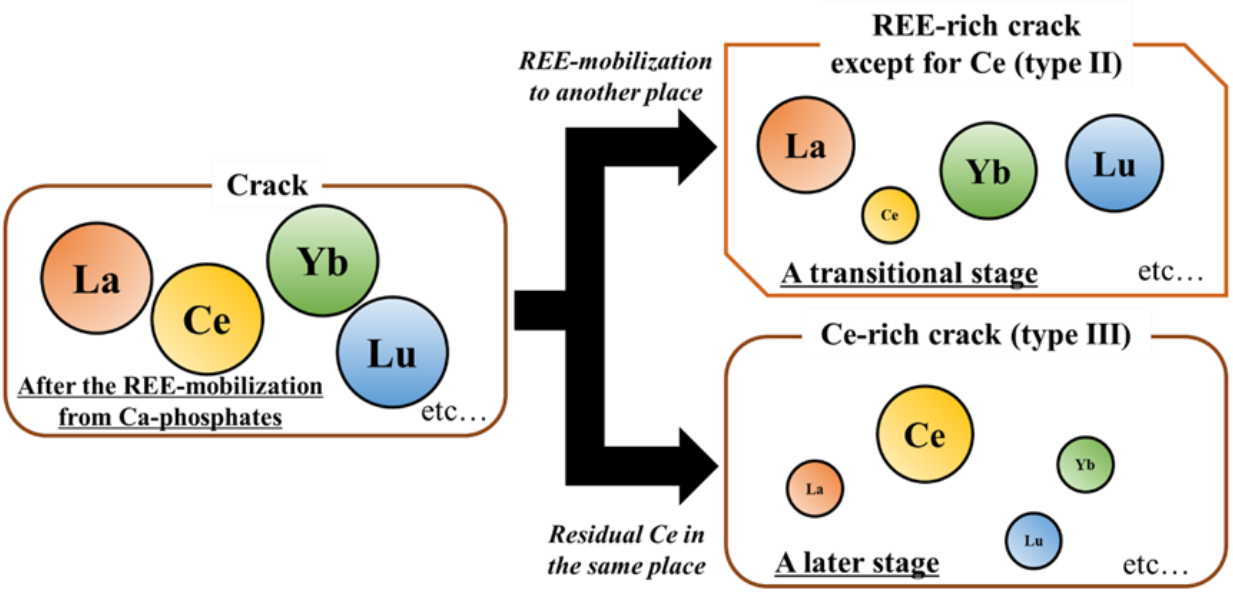

Fig. 8. REE mobilization upon the dissolution of Ca-phosphates within the crack resulting from chemical alteration.

oldhamite, which is readily dissolved even in water (Shima and Honda, 1967), for enstatite chondrites (*e.g.*, Ebihara and Honda, 1987; Maeda *et al.*, 2021) , which at least has been observed in L and LL chondrites (Pourkhorsandi *et al.*, 2017).

In any case, bulk elemental abundances including REEs in all the weathered Antarctic samples in this study, except for A 09516, are in good agreement with non-Antarctic HC mean values (Maeda *et al.*, 2021). Moreover, the elemental abundances in the constituent minerals of A 09618 displaying both a positive and negative Ce anomaly in its cracks also overlap with their literature values and do not exhibit any Ce anomaly in the phases (Maeda *et al.*, 2023). Thus, the effect of this alteration on the elemental abundance s in bulk rock and in the constituent minerals is generally limited. However, as mentioned above, ~61% of the bulk Antarctic eucrites measured by Mittlefehldt and Lindstrom (1991) displayed a Ce anomaly (both positive and negative) while none of non-Antarctic eucrites displayed such an anomaly. Furthermore, Crozaz *et al.* (2003) observed such Ce anomalies in silicates of Antarctic eucrites and some other classes of achondrites, mainly pyroxene. They have interpreted that these Ce anomalies are caused by a similar alteration scenario to ours and can be promoted by the large presence of fractures and microcracks resulted by the shock events. Given that the grain sizes of Ca-phosphates in eucrites and HCs are relatively similar to each other (submicron up to 50 μm vs. < 5 μm up to tens of μm: Delaney *et al.*, 1984; Huss *et al.*, 2006) while Antarctic eucrites were more extensively affected by alteration, the networks of fractures and cracks would enhance the extent of the alteration rather than the grain size of Ca-phosphates in the case of Antarctic samples. Therefore, once the elemental mobilization by terrestrial fluids extensively affected a sample through its physical weaknesses, the elemental contents, including elements generally considered relatively immobile such as REEs, in bulk rock and some mineral phases can be modified to release them to a sufficiently high degree to disturb their original isotopic compositions, as observed in the cases of Antarctic eucrite and even an Antarctic HC A 09516 (Mittlefehldt and Lindstrom, 1991; Crozaz *et al.*, 2003; Maeda *et al.*, 2021).

5. CONCLUSIONS

Cracks of HCs were investigated in detail using LA-ICP-TOF-MS and LA-ICP-SF-MS through an elemental mapping and a line-scanning approach, respectively. According to the results of the trace element maps and line-scanning analysis, a considerable amount of REEs, Th, and U, and in some cases only Ce (Ce/Ce* = 1.5-5.8), resides in cracks. Considering the P_2O_5/SiO_2 in cracks, the heterogeneous distribution of Ca-phosphate phases neighboring to the crack likely explains the enrichments in REEs, Th, and U in most of the cracks although some may accumulate unbound REEs as well as Th and U. As these remarkable features are observed mostly in highly weathered samples but not in less altered samples including falls (except for an altered fall sample), the elemental mobilization is interpreted to result from the dissolution of Ca-phosphate phases taking place when fluids pass through the meteorite interiors during terrestrial weathering. This process can proceed relatively fast (at slowest on a scale of tens of years) as one of the fall samples has been affected. Furthermore, this alteration scenario can be applied to other classes of weathered chondrites in a similar manner as long as its chondrite contains a REE-rich mineral less resistant to acids such as Ca-phosphates or oldhamite. However, the effects on the bulk composition are generally limited and this alteration occurs at micro-scale only because the bulk elemental abundances in the weathered Antarctic samples studied in this work, except for A 09516, are in good agreement with published data for falls and other unaltered meteorites.

SUPPORTING INFORMATION

Additional supporting information can be found online at https://vub-my.sharepoint.com/:f:/g/personal/ryoga_maeda_vub_be/EqwAm_k7CFZHp0BTrDKqaqABoSepq5xlSXgNU_W-Vx46Kw?e=uKB4jq until 26 August 2023 (Password: phdthesis_rm). Otherwise, it can be requested digitally from the author.

ACKNOWLEDGMENT

We would like to thank N. J. de Winter, S. M. Chernonozhkin, and F. Van Maldeghem for guidance with the μXRF instrumentation and with the HDIP software, and for assistance during the SEM, respectively. We also thank the Royal Belgian Institute of Natural Sciences, Belgium, and the National Institute of Polar Research, Japan, for the loan of the Antarctic meteorites, meteorites collected from hot deserts, and the fall meteorites used in this study. RM thanks NIPR International Internship Programs for Polar Science 2020 and 2021 for financial and analytical supports. RM, SG, FV, VD, and PhC acknowledge support from the Excellence of Science (EoS) project ‘‘ET-HoME”. SG and VD thank the BRAIN-Be Belgian Science Policy (BELSPO) projects ‘‘BAMM” and “DESIRED”. SG and PhC acknowledge support from the VUB Strategic Research Program. TVA thanks Research Foundation – Flanders (FWO) for his junior postdoctoral fellowship grant (FWO.3E0.2022.0048.01). FV thanks BOF-UGent for financial support under the form of a GOA grant and acknowledges Teledyne Photon Machines for logistic support. VD thanks the ERC StG ISoSyC and FRS-FNRS for support. PhC also thanks the Research Foundation Flanders (FWO Hercules grant) for the purchase of the μXRF instrument. We specifically would like to thank Makoto Kimura, Naoya Imae, Conel M. O’D Alexandar, and Martin R. Lee for discussions on the content of this manuscript. Finally, we grateful acknowledge John

Spray for the editorial work. We also thank Julia Roszgar and an anonymous reviewer for their constructive reviews.

REFERENCES

Adcock C. T., Hausrath E. M. and Forster P. M. (2013) Readily available phosphate from minerals in early aqueous environments on Mars. *Nat. Geosci.* **6**, 824-827.

Al-Kathiri A., Hofmann B. A., Jull J. T., and Gnos E. (2005) Weathering of meteorites from Oman: Correlation of chemical and mineralogical weathering proxies with 14C terrestrial ages and the influence of soil chemistry. *Meteorit. Planet. Sci.* **40**, 1215-1239.

Anders E. and Grevesse N. (1989) Abundances of the elements: Meteoritic and solar. *Geochim. Cosmochim. Acta* **53**, 197-214.

Bland P. A., Zolensky M. E., Benedix G. K., and Sephton M. A. (2006) Weathering of chondritic meteorites. In *Meteorites and the Early Solar System II* (eds. Lauretta D. S. and McSween Jr. H. Y.). The University of Arizona Press, Tucson, pp. 853-867. in collaboration with Lunar and Planetary Institute, Houston.

Burger M., Gundlach-Graham A., Allner S., Schwarz G., Wang H. A., Gyr L., Burgener S., Hattendorf B., Grolimund D., and Güther D. (2015) High-speed, high-resolution, multielemental LA-ICP-TOFMS imaging: Part II. Critical evaluation of quantitative three-dimensional imaging of major, minor, and trace elements in geological samples. *Anal. Chem*. **87**, 8259-8267.

Bussweiler Y., Borovinskaya O., and Tanner M. (2017) Laser Ablation and inductively coupled plasma-time-of-flight mass spectrometry—A powerful combination for high-speed multielemental imaging on the micrometer scale. *Spectroscopy* **32**, 14-20.

Crozaz G. (1979) Uranium and thorium microdistributions in stony meteorites. *Geochim. Cosmochim. Acta* **43**, 127-136.

Crozaz G., Floss C. and Wadhwa M. (2003) Chemical alteration and REE mobilization in meteorites from hot and cold deserts. *Geochim. Cosmochim. Acta* **67**, 4727-4741.

Curtis D. B. and Schmitt R. A. (1979) The petrogenesis of L-6 chondrites: insights from the chemistry of minerals. *Geochim. Cosmochim. Acta* **43**, 1091-1103.

Dauphas N. and Pourmand A. (2015) Thulium anomalies and rare earth element patterns in meteorites and Earth: Nebular fractionation and the nugget effect. *Geochim. Cosmochim. Acta* **163**, 234-261.

Delaney J. S., O'Neill C. and Prinz M. (1984) Phosphate minerals in eucrites. In *Lunar Planet. Sci.* **XV**, 208-209. The Lunar and Planetary Institute, Houston (abstract).

DePaolo D. J. and Wasserburg G. J. (1976) Nd isotopic variations and petrogenetic models. *Geophys. Res. Lett.* **3**, 249-252.

Drouard A., Gattacceca J., Hutzler A., Rochette P., Braucher R., Bourlès D., ASTER Team, Gounelle M., Morbidell A., Debaille V., van Ginneken M., Valenzuela M., Quesnel Y. and Martinez R. (2019) The meteorite flux of the past 2 my recorded in the Atacama Desert. *Geology* **47**, 673-676.

Ebihara M. and Honda M. (1984) Distribution of rare earth elements and uranium in various components of ordinary chondrites. *Meteoritics* **19**, 69-77.

Ebihara M. and Honda M. (1987) Rare earth elements in Ca-phosphates of Allende carbonaceous chondrite. *Meteoritics* **3**, 179-190.

Fredriksson K., Treviño R., Montemayor F., King E. A., and Sánchez-Rubio G. (1979) The Nuevo Mercurio, México, Chondrite. *Meteoritics* **14**, 400 (abstract).

Gooding J. L. (1989) Significance of terrestrial weathering effects in Antarctic meteorites. *Smithson. Contrib. Earth Sci.* **28**, 93-98.

Gundlach-Graham A., Burger M., Allner S., Schwarz G., Wang H. A. O., Gyr L., Grolimund D., Hattendorf B., and Günther D. (2015) High-speed, high-resolution, multielemental laser ablation-inductively coupled plasma-time-of-flight mass spectrometry imaging: Part I. Instrumentation and two-dimensional imaging of geological samples. *Anal. Chem.* **87**, 8250-8258.

Gundlach-Graham A., Garofalo P. S., Schwarz G., Redi D., and Günther D. (2018) High-resolution, Quantitative Element Imaging of an Upper Crust, Low-angle Cataclasite (Zuccale Fault, Northern Apennines) by Laser Ablation ICP Time-of-Flight Mass Spectrometry. *Geostand. Geoanal. Res.* **42**, 559-574.

Humayun M., Simon S. B., and Grossman L. (2007) Tungsten and hafnium distribution in calcium-aluminum inclusions (CAIs) from Allende and Efremovka. *Geochim. Cosmochim. Acta* **71**, 4609-4627.

Humayun M., Davis F. A., and Hirschmann M. M. (2010) Major element analysis of natural silicates by laser ablation ICP-MS. *J. Anal. At. Spectrom.* **25**, 998-1005.

Huss G. R., Rubin A. E. and Grossman J. N. (2006) Thermal metamorphism in chondrites. In *Meteorites and the Early Solar System II* (eds. Lauretta D. S. and McSween Jr. H. Y.). The University of Arizona Press, Tucson, pp. 567-586. in collaboration with Lunar and Planetary Institute, Houston.

Ikeda Y. and Kojima H. (1991) Terrestrial alteration of Fe-Ni metals in Antarctic ordinary chondrites and the relationship to their terrestrial ages. *Proc. NIPR Symp. Antract. Meteorites* **4**, 307-318.

Jarosewich E. (1990) Chemical analyses of meteorites: A compilation of stony and iron meteorite analyses. *Meteoritics* **25**, 323-337.

Jochum K. P. and Stoll B. (2008) Reference materials for elemental and isotopic analyses by LA-(MC)-ICP-MS: successes and outstanding needs. In *Laser Ablation-ICP-MS in The Earth Sciences: Current practices and outstanding issues* (ed. Sylvester P.). Mineralogical Association of Canada Short Course **40**, pp. 147–168.

Jochum K. P., Stoll B., Herwig K. P., Willbold M., Hofmann A. W., Amini M., and 47 coauthors (2006) MPI-DING reference glasses for in situ microanalysis: New reference values for element concentrations and isotope ratios. *Geochem. Geophys. Geosyst.* **7**, Q02008.

Jones J. H. and Burnett D. S. (1979) The distribution of U and Pu in the St. Severin chondrite. *Geochim. Cosmochim. Acta* **43**, 1895-1905.

Koeberl C. and Cassidy W. A. (1991) Differences between Antarctic and non-Antarctic meteorites: An assessment. *Geochim. Cosmochim. Acta* **55**, 3-18.

Lee M. R. and Bland P. A. (2004) Mechanism of weathering of meteorites recovered from hot and cold deserts and the formation of phyllosilicates. *Geochim. Cosmochim. Acta* **68**, 893-916.

Maeda R., Goderis S., Debaille V., Pourkhorsandi H., Hublet G., and Claeys P. (2021) The effects of Antarctic alteration and sample heterogeneity on Sm-Nd and Lu-Hf systematics in H chondrites. *Geochim. Cosmochim. Acta* **305**, 106-129.

Maeda R., Van Acker T., Vanhaecke F., Yamaguchi A., Debaille V., Claeys P., and Goderis S. (2023) Quantitative elemental maps of chondritic meteorite samples using Laser Ablation-Inductively Coupled Plasma-Time of Flight-Mass Spectrometry (LA-ICP-TOF-MS). *J. Anal. At. Spectrom.* **38**, 369-381.

McFadden L. D., Eppes M. C., Gillespie A. R. and Hallet B. (2005) Physical weathering in arid landscapes due to diurnal variation in the direction of solar heating. *Geol. Soc. of Am. Bull.* **117**,161–173.

Middelburg J. J., van der Weijden C. H., and Woittiez J. R. W. (1988) Chemical processes affecting the mobility of major, minor and trace elements during weathering of granitic rocks. *Chem. Geol.* **68**, 253-273.

Mittlefehldt D. W. and Lindstrom M. M. (1991) Generation of abnormal trace element abundances in Antarctic eucrites by weathering processes. *Geochim. Cosmochim. Acta* **55**, 77-87.

Miyamoto M. (1991) Differences in the degree of weathering between Antarctic and non-Antarctic meteorites inferred from infrared diffuse reflectance spectra. *Geochim. Cosmochim. Acta* **55**, 89-98.

Nakamura N. (1974) Determination of REE, Ba, Fe, Mg, Na and K in carbonaceous and ordinary chondrites. *Geochim. Cosmochim. Acta* **38**, 757-775.

Ninagawa K., Mieda Y., Ueda H., Imae N., Kojima H., and Yanai K. (2005) Thermoluminescence studies of ordinary chondrites in the Japanese Antarctic meteorite collection IV: Asuka ordinary chondrites. *Antarct. Meteor. Res.* **18**, 1-16.

Nishiizumi K., Elmore D. and Kubik P. W. (1989) Update on terrestrial ages of Antarctic meteorites. *Earth Planet. Sci. Lett.* **93**, 299-313.

Pellas P. and Störzer D. (1975) Uranium and plutonium in chondritic phosphates. *Meteoritics* **10**, 471 (abstract).

Pourkhorsandi H., D'Orazio M., Rochette P., Valenzuela M., Gattacceca J., Mirnejad H., Sutter B., Hutzler A. and Aboulahris M. (2017) Modification of REE distribution of ordinary chondrites from Atacama (Chile) and Lut (Iran) hot deserts: Insights into the chemical weathering of meteorites. *Meteorit. Planet. Sci.* **52**, 1843-1858.

Pourkhorsandi H., Gattacceca J., Rochette P., D'Orazio M., Kamali H., de Avillez R., Letichevsky S., Djamali M., Mirnejad H., Debaille V., and Jull A. J. T. (2019) Meteorites from the Lut Desert (Iran). *Meteorit. Planet. Sci.* **54**, 1737-1763.

Pourkhorsandi H., Debaille V., Armytage R. M. G., van Ginneken M., Rochette P., and Gattacceca J. (2021) The effects of terrestrial weathering on samarium-neodymium isotopic composition of ordinary chondrites. *Chem. Geol.* **562**, 120056.

Rubin A. E. and Huber H. (2005) A weathering index for CK and R chondrites. *Meteorit. Planet. Sci.* **40**, 1123-1130.

Shima M. and Honda M. (1967) Distributions of alkali, alkaline earth and rare earth elements in component minerals of chondrites. *Geochim. Cosmochim. Acta* **31**, 1995-2006.

Shinotsuka K. and Ebihara M. (1997) Migrational behaviors of rare-earth elements and actinoides during thermal metamorphism of ordinary chondrites. *Meteorit. Planet. Sci.* **32**, A119-120.

Van Acker T., Van Malderen S. J. M., Van Helden T., Stremtan C., Šala M., van Elteren J. T., and Vanhaecke F. (2021) Analytical figures of merit of a low-dispersion aerosol transport system for high-throughput LA-ICP-MS analysis. *J. Anal. At. Spectrom.* **36**, 1201-1209.

van Ginneken M., Debaille V., Decrée S., Goderis S., Woodland A. B., Wozniakiewicz P., De Ceukelaire M., Leduc T., and Claeys P. (2022) Artificial weathering of an ordinary chondrite: Recommendations for the curation of Antarctic meteorites. *Meteorit. Planet. Sci.* **57**, 1247-1266.

Van Malderen S. J. M., Van Acker T., and Vanhaecke F. (2020) Sub-micrometer nanosecond LA-ICP-MS imaging at pixel acquisition rates above 250 Hz via a low-dispersion setup. *Anal. Chem.* **92**, 5756-5764.

Van Malderen S. J. M., van Elteren J. T., and Vanhaecke F. (2015) Development of a fast laser ablation-inductively coupled plasma-mass spectrometry cell for sub-μm scanning of layered materials. *J. Anal. At. Spectrom.* **30**, 119-125.

Vanhaecke F. and Van Malderen S. J. M. (2020) Laser ablation probe. *European patent No.3195346B1*. Munich, Germany. European Patent Office.

Velbel M. A. (2014) Terrestrial weathering of ordinary chondrites in nature and continuing during laboratory storage and processing: Review and implications for Hayabusa sample integrity. *Meteorit. Planet. Sci.* **49**, 154-171.

Ward D., Bischoff A., Roszjar J., and Whitehouse M. J. (2017) Trace element inventory of meteoritic Ca-phosphates. *American Mineralogist* **102**, 1856-1880.

Wlotzka F. (1993) A weathering scale for the ordinary chondrites. *Meteoritics* **28**, 460 (abstract).

Chapter 5 "*The distributions of lithophile elements and their re-mobilization during thermal metamorphism in the H chondrite parent body(ies)*" (Submitted in GCA in 2023)

Chapter introduction

After the determination of the chemical, isotopic, and petrographic features of HCs collected from cold and hot deserts and the examination of the effects of terrestrial weathering including Antarctic alteration, which are generally to be limited at the bulk scale, we can now focus on the elemental distributions in HCs to unravel the effects of thermal metamorphism in the parent body(ies) of HCs.

In this chapter, the distribution of lithophile elements among the constituent minerals in HCs of various metamorphic grades was investigated in a systematic manner. Combined with the data for the bulk samples obtained in chapter 2, the elemental budgets in individual phases were quantitatively estimated to compare their distributions between unequilibrated HCs (UHCs) and equilibrated HCs (EHCs). The distributions obtained in this study are overall consistent with previous studies. For example, REEs are mainly distributed in Ca-phosphates with the exception of Eu which is hosted in feldspar mostly, in the case of EHCs. However, several remarkable observations are made as well, especially in the case of the UHCs: refractory lithophile elements are distributed not only in the phases analyzed in this study but also in (an) unidentified phase(s) according to the mass balance calculation. As such, in this chapter, we address the effects of thermal processing on the elemental distributions in the parent bodies. The spot analyses used in this study were conducted within the framework of the NIPR International Internship Programs for Polar Science 2020 and 2021.

Contributions to this paper

This study was led by RM and the AMGC, NIPR, A&MS, and G-Time teams. all *in-situ* measurements, bulk elemental analysis, interpretations, and writing were done by RM.

This chapter is submitted as:

Ryoga Maeda, Steven Goderis, Akira Yamaguchi, Thibaut Van Acker, Frank Vanhaecke, Vinciane Debaille and Phillippe Claeys (2023) The distributions of lithophile elements and their migrations during thermal metamorphism in H chondrites. *Geochimica et Cosmochimica Acta* (submitted).

Supplementary data for this chapter can be found at:

https://vub-my.sharepoint.com/:f:/g/personal/ryoga_maeda_vub_be/EqwAm_k7CFZHp0BTrDKqaqABoSepq5xlSXgNU_W-Vx46Kw?e=uKB4jq (until 26 August 2023)

Password: phdthesis_rm

Otherwise, it can be requested digitally from the author.

The distributions of lithophile elements and their re-mobilization during thermal metamorphism in the H chondrite parent body(ies)

Ryoga Maeda[a,b,*], Steven Goderis[a], Akira Yamaguchi[c], Thibaut Van Acker[d], Frank Vanhaecke[d], Vinciane Debaille[b] and Philippe Claeys[a]

[a] *Analytical-, Environmental-, and Geo-Chemistry, Vrije Universiteit Brussel, Pleinlaan 2, 1050 Brussels, Belgium.*

[b] *Laboratoire G-Time, Université libre de Bruxelles, CP 160/02, 50, Av. F.D. Roosevelt, 1050, Brussels, Belgium.*

[c] *National Institute of Polar Research, 10-3 Midori-cho, Tachikawa-shi, Tokyo 190-8518, Japan*

[d] *Atomic & Mass Spectrometry (A&MS) research unit, Department of Chemistry, Ghent University, Campus Sterre, Krijgslaan, 281 – S12, 9000 Ghent, Belgium*

* Corresponding author. *E-mail address*: Ryoga.Maeda@vub.be (R. Maeda)

Abstract

The distributions of lithophile elements among the constituent minerals in H chondrites were investigated in a systematic manner using samples from metamorphic grades 3.3 to 7. The distributions obtained in this study are generally consistent with previous studies focusing on such elemental distributions in ordinary chondrites: Sc, Zr, and Hf are mainly distributed in Ca-rich pyroxene; Rb, Sr, Ba, and Eu in feldspar; and Y and rare earth elements (REEs) except for Eu in Ca-phosphates while Y and the heavy REEs are also partly hosted in Ca-rich pyroxene. The distributions of V, Mn, Zn, Nb, Ta, Pb, Th, and U are more complicated: V and Zn reside in chromite and silicates; Mn in olivine and low-Ca pyroxene; Nb and Ta possibly in silicates; Pb in metals, sulfides, and silicates; and Th and U in Ca-phosphates, cracks, and grain boundaries. However, refractory lithophile elements are also considerably distributed in (a) phase(s) other than the minerals analyzed in this study, especially in the case of less metamorphosed samples. This reaffirms the importance of glass mesostasis in chondrules on their bulk elemental budgets, and the re-distributions of these elements during thermal metamorphism. Therefore, this study demonstrates that the re-distribution of refractory lithophile elements (Sc, Zr, Y, REEs except for Eu, Hf, Th, and U) from glass mesostasis to specific phases occurred in a largely closed system during thermal metamorphism in the parent body(ies) and was accompanied by the recrystallization of glass mesostasis. This re-distribution scenario is applicable to all ordinary chondrite groups and supports an onion shell-type internal structure of their parent bodies.

1 INTRODUCTION

Elemental abundances are fractionated among the constituent minerals in a meteorite, even for rare earth elements (REEs) that share strongly comparable chemical properties. For example, REEs are concentrated in Ca-phosphates and are only distributed in olivine for a small fraction in the case of ordinary chondrites (OCs; *e.g.*, Curtis and Schmitt, 1979). The main host of REEs differs among the classes of chondrites: oldhamite

(CaS) and Ca, Al-rich inclusions (CAIs) dominate the REE budgets of enstatite chondrites (ECs) and CV chondrites, respectively (*e.g.*, Laimer and Ganapathy, 1987; Ebihara and Honda, 1987). As such, the elemental fractionation and its extent depend on many factors such as nebular and parent body processes, chemical affinities, mineralogy, ionic radii, *etc*. So far, studies focusing on such an elemental distribution have applied physical mineral separation, *in-situ* measurement, and chemical leaching techniques for various classes of chondrites (*e.g.*, Mason and Graham, 1970; Martin *et al.*, 2013; Barrat *et al.*, 2014), significantly improving our understanding of the conditions of equilibration induced by thermal metamorphism in their parent bodies and the subsequent variations of isotopic compositions and elemental abundances in bulk samples (*e.g.*, McIntire, 1963; Bouvier *et al.*, 2008; Dauphas and Pourmand, 2015). Based on these studies, it has been demonstrated that REEs were transferred from glass mesostasis in chondrules to Ca-phosphates during thermal metamorphism in the parent bodies in the case of OCs (Shinotsuka and Ebihara, 1997). Such a re-distribution scenario based on thermal processing has also been suggested for CK chondrites and ECs by Martin *et al.* (2013) and Barrat *et al.* (2014), respectively. This implies that also other elements were re-distributed during thermal metamorphism and the elemental distributions in unequilibrated ordinary chondrites (UOCs) and equilibrated ordinary chondrites (EOCs) are thus distinct from each other. Nevertheless, in most cases of OCs, only EOCs were investigated in the previous studies. Moreover, the measurements for most of their studies were performed in the 1970s and 1980s when elemental abundances at ppb levels were challenging to determine due to instrumental limitations, even though such elements include Hf and U, which are important in the context of radiometric dating systems such as Lu-Hf and U-Pb (*e.g.*, Mason and Graham, 1970; Allen and Mason, 1973; Curtis and Schmitt, 1979).

As such, the available information on the elemental distributions in UOCs and elements at very low concentrations remains limited, and hence the thermal effects on the elemental distributions, especially in OCs, remain poorly constrained. In this study, we have therefore investigated the elemental budgets, with a particular focus on the lithophile elements (Na, Mg, Al, Si, P, K, Ca, Sc, Ti, V, Cr, Mn, Fe, Ni, Zn, Rb, Sr, Y, Zr, Nb, Ba, REEs, Hf, Ta, Pb, Th, and U; a few siderophile/chalcophile elements included), of the constituent minerals in both unequilibrated H chondrites (UHCs) and equilibrated H chondrites (EHCs).

2 EXPERIMENTAL

2.1 Qualitative mapping using µXRF

The same polished thick sections (PTSs) as those studied in Maeda *et al.* (2021, 2023a, 2023b) were used for the analyses described below. Petrographic information on the meteorite samples is listed in Table 1. All PTSs were first analyzed using a Bruker M4 Tornado micro-X-ray fluorescence (µXRF) scanner equipped with a Rh source and two XFlash 430 Silicon Drift detectors at the Vrije Universiteit Brussel (VUB), Belgium, to obtain major element maps. Constituent minerals in the fall samples, Jilin (H5), Nuevo Mercurio (H5), Richardton (H5), and Butsura (H6), were identified from the elemental maps and their modal abundances were determined using the ImageJ image analysis program. This analysis has been described in detail in Maeda *et al.* (2021).

2.2 Quantitative mapping using LA-ICP-TOF-MS

The PTSs of 12 samples (A-880941, A-881258, A 09436, A 09387, NWA 6771, Jilin, Nuevo Mercurio, Richardton, A 09618, Butsura, A 09516, and Y-790960) were analyzed using pulse-resolved multi-elemental laser ablation-inductively coupled plasma-time of flight-mass spectrometry (LA-ICP-TOF-MS) mapping at Ghent University, Belgium. The LA-ICP-TOF-MS instrumentation is comprised of an Iridia LA unit (Teledyne Photon Machines, U.S.) equipped with a nanosecond 193 nm ArF* excimer-based laser and coupled to an icpTOF 2R instrument (TOFWERK, Switzerland) via a low-dispersion aerosol transport system named the ARIS (Van Acker *et al.*, 2021). The regions of interest for LA-ICP-TOF-MS mapping were selected based on the major element X-ray maps. Once the quantitative elemental maps were obtained, each constituent mineral in a sample was systematically identified using automatic clustering zones in the HDIP software (Teledyne Photon Machines, U.S.). The elemental abundances in the identified minerals were determined by taking an average of the elemental abundances in the corresponding regions. See Maeda *et al.* (2023a) for more details on these analyses.

Table 1. List of H chondrites analyzed in this study.

Meteorite	Fall/Find	Type	Weathering
A-880941	Find	H3.3	A/B
Y-793574	Find	H3.5	n.d.
Y-790461	Find	H3.7	B
ALH 78084	Find	H3.9	B/Ce
A-881258	Find	H3.9	B
A 09436	Find	H3	C
A 09387	Find	H4	B/C
NWA 6771	Find	H4	W1
Jilin	Fall	H5	n.d.
Nuevo Mercurio	Fall	H5	n.d.
Richardton	Fall	H5	n.d.
A 09618	Find	H5	C
Sahara 97035	Find	H5	W2
Butsura	Fall	H6	n.d.
A 09516	Find	H6	C
Y-790960	Find	H7	B

See Maeda *et al.* (2021, 2023b) for more details.

2.3 Determination of major element abundances using electron probe microanalysis

After LA-ICP-TOF-MS mapping, all the samples analyzed using LA-ICP-TOF-MS were slightly polished and subjected to the following analyses. Back-scattered electron (BSE) images of all PTSs were generated using a JEOL JSM-7100F field emission-scanning electron microscope (FE-SEM) equipped with an Oxford energy-dispersive spectrometer (EDS) at the National Institute of Polar Research (NIPR), Japan. Based on the constituent minerals identified using the BSE images and the X-ray maps, the major and minor element abundances of the constituent minerals in the PTSs were determined using a JEOL JXA-8200 electron micro probe analyzer (EPMA) at the NIPR. See Maeda *et al.* (2023a) for more details of these analyses. In addition to the phases analyzed in Maeda *et al.* (2023a), metal and sulfide phases were also analyzed using a 15 kV accelerating voltage, a 30 nA beam current, and a focused beam with a diameter of less than 1 μm. The following elements were monitored: Mg, Si, P, S, Cr, Fe, Co, Ni, and Cu. Correction procedures are based on the ZAF method. As a result of the occurrence of overlapping signals, the intensities of Co and Cu were mathematically corrected for those of Fe and Ni, respectively. Natural and synthetic silicate, phosphide, sulfide, and metals with well-known chemical compositions were used as standards for the metal and sulfide phases.

2.4 Determination of trace element abundances using LA-ICP-SF-MS spot analysis

The trace element abundances in Ca-phosphates and silicates were determined using LA-ICP-SF-MS in

single-point drilling mode. These measurements were performed using a Teledyne CETAC LSX-213 G2+ LA-system coupled to a Thermo Element XR ICP-sector field (SF)-MS unit at the NIPR. The laser system provides an output wavelength of 213 nm and 100 shots were fired per spot analysis at a laser repetition frequency of 10 Hz and a laser energy density of 36 J/cm^2. All nuclide peaks were collected at low mass resolution (M/ΔM = 300) with triple mode detection and the following nuclides were monitored for the major elements: ^{23}Na, ^{24}Mg, ^{27}Al, ^{29}Si, ^{31}P, ^{39}K, ^{43}Ca, ^{44}Ca, and ^{57}Fe; and for the trace elements: ^{45}Sc, ^{51}V, ^{55}Mn, ^{66}Zn, ^{85}Rb, ^{88}Sr, ^{89}Y, ^{137}Ba, ^{139}La, ^{140}Ce, ^{141}Pr, ^{146}Nd, ^{147}Sm, ^{151}Eu, ^{157}Gd, ^{159}Tb, ^{161}Dy, ^{165}Ho, ^{166}Er, ^{169}Tm, ^{173}Yb, ^{175}Lu, ^{178}Hf, ^{208}Pb, ^{232}Th, and ^{238}U. All peaks were acquired by "peak jumping" between peak tops with a 10% mass window (resulting in an average of 5 peaks on the peak top) and 50–100 ms of acquisition time on the peak top. This analysis is described in more detail in Maeda *et al.* (2023a).

2.5 Mass balance calculations

Based on the elemental abundances in the constituent minerals obtained, the whole rock (WR) values for each element were calculated for all samples. Two ways were compared to calculate the mass balance: by using the "observed" modal abundances obtained using μXRF or alternatively employing "ideal" modal abundances. In the latter case, the estimated WR (EWR) values using the observed modal abundance were modified to obtain a better mass balance by adjusting the observed modal abundance when significant discrepancies (*e.g.*, more than twice higher or lower than the bulk rock values) were established between the EWR values and the bulk rock values, which are obtained from the corresponding powdered samples as described in Maeda *et al.* (2021, 2023a). To do this, the EWR values of the major elements (Na, Mg, Al, Si, P, K, Ca, Ti, Cr, Mn, Fe, and Ni) were first matched to 100% of the bulk rock values by adjusting the observed modal abundances. Secondly, the EWR values of the REEs were matched to the bulk rock values by the adjustment while the EWR values of the major elements were monitored. Finally, the EWR values calculated using the adjusted modal abundance were further fine-tuned by matching the EWR values of Th, U, Hf, and the other elements to the bulk rock values. This final modal abundance adjusted based on the observed modal abundance to obtain the optimal mass balance is defined as the "ideal" modal abundance in this paper and the EWR values based on the ideal modal abundances are used as the primary basis for most of the discussion in this work.

For elements or samples not determined in Maeda *et al.* (2021, 2023a), *i.e.*, the Si, V, and Sc abundances in all find samples and the elemental abundances in the four fall samples, literature values were used for their bulk rock values (Wasson and Kallemeyn, 1988; Kallemeyn *et al.*, 1989; Jarosewich, 1990; Shinotsuka, 1997; Schaefer and Fegley Jr., 2010). Overall, the uncertainties for the EWR values using the ideal and observed modal abundances are estimated to be better than 10% relative.

3 RESULTS

3.1 Modal abundances

The modal abundances in the fall samples obtained using μXRF are summarized in Supplementary Table 1, together with those in the other samples reported in Maeda *et al.* (2021) and the published modal abundances of EHCs (Van Schmus, 1969; McSween *et al.*, 1991). Note that the kamacite abundance in Richardton is

anomalously high compared with those in the other samples (23.1 vol.% vs. ~6 vol.%). As the surface area on the PTS is the smallest in this study (~9 mm^2), this high kamacite abundance must result from the heterogeneous distribution of kamacite but not the nature of this sample. As such, the modal abundance of the Richardton was excluded from the EHC mean values in Supplementary Table 1. Except for Richardton, the modal abundances of all fall samples are overall in good agreement with those in the other EHC samples, including the published values.

3.2 Quantitative elemental maps

Figure 1 shows (semi-)quantitative elemental maps obtained using LA-ICP-TOF-MS for A 09618 together with the corresponding BSE image, as an example of the approach applied. Figure 1 (b) exhibits the combined Ca, Mg, and Si map, allowing identification of Ca-phosphates, olivine, low-Ca pyroxene, feldspar, and Ca-rich pyroxene as these appear in red, light green, light blue, blue, and purple, respectively. The identification in combination with Figs. 1 (c) and (d) demonstrates that Sc is mainly distributed in Ca-rich pyroxene and Sr is concentrated in feldspar and Ca-phosphates. The elements La and U are concentrated in Ca-phosphates, with

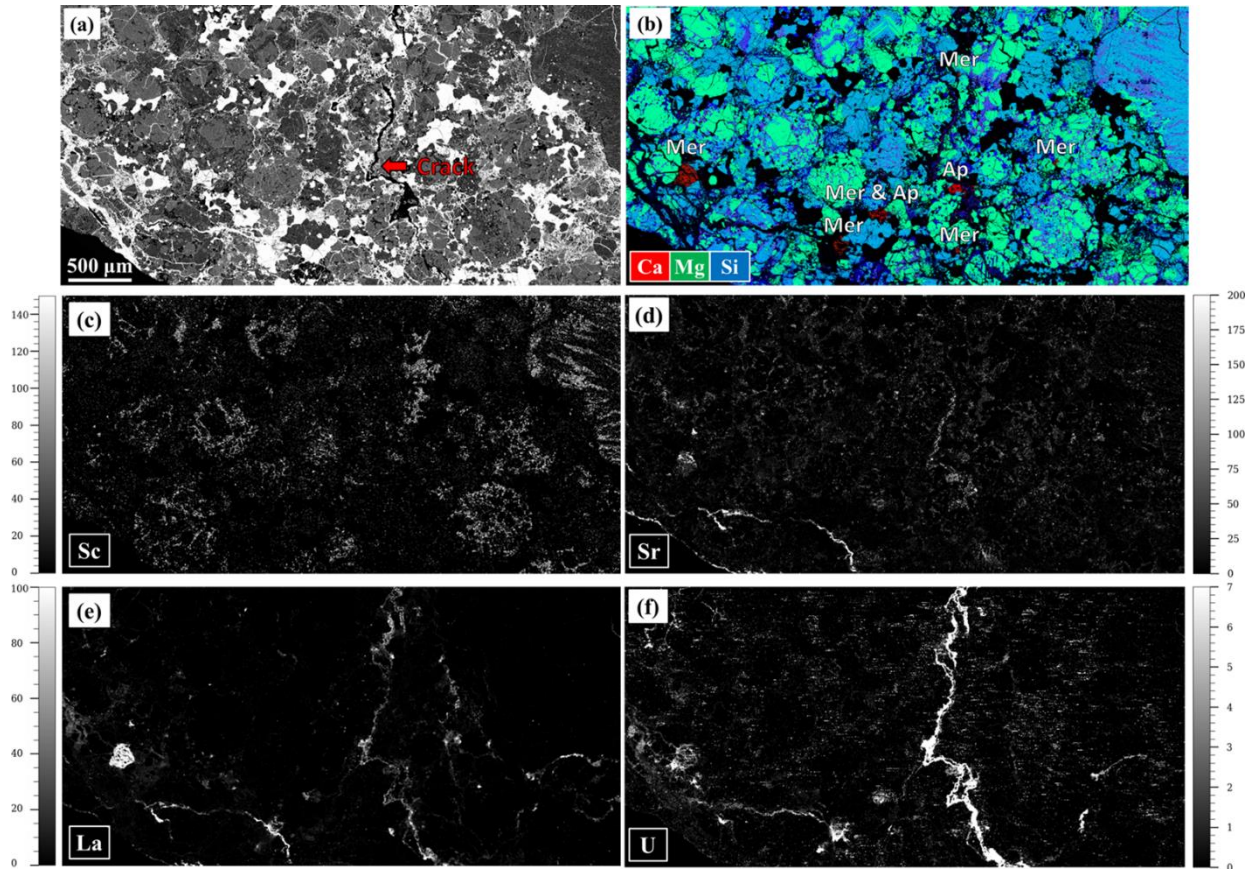

Fig. 1. BSE image and (semi-)quantitative element maps for A 09618 (H5). (a) BSE image for the region analyzed using LA-ICP-TOF-MS. (b) Combined RGB elemental map obtained using LA-ICP-TOF-MS mapping with red: Ca, green: Mg, and blue: Si. Based on the composition, the following mineralogy can be deduced red: Ca-phosphates, light green: olivine, light blue: low-Ca pyroxene, blue: feldspar, and purple: Ca-rich pyroxene. Mer: merrillite; Ap: chlorapatite. (c) Scandium distribution map. (d) Strontium distribution map. (e) Lanthanum distribution map. (f) Uranium distribution map. Concentration scale bars for (c) to (f) are expressed in ppm.

La mainly hosted in merrillite and U in apatite according to Figs. 1 (e) and (f). In addition, Sr, La, and U reside also in the crack displayed in Fig. 1, especially in the case of U. The quantitative elemental maps obtained in this study provide a visual validation of the elemental abundances and distributions discussed in the following sections. Additional maps for the other samples can be found in Supplementary data-2.

3.3 Elemental abundances in the constituent minerals

The major and trace element abundances in the constituent minerals for each sample measured using EPMA, LA-ICP-TOF-MS, and LA-ICP-SF-MS are summarized in Supplementary Tables 2-12 (merrillite, apatite, Ca-rich pyroxene, feldspar, low-Ca pyroxene, olivine, kamacite, taenite, troilite, chromite, and ilmenite, respectively), together with their mean values for each metamorphic grade, including HCs collected from hot deserts. Note that only major element abundances were determined for kamacite, taenite, and troilite phases. Some values in minerals for NWA 6771 (H4) and Sahara 97035 (H5) are excluded from the mean values for H4 and H5, respectively, when the value is obviously affected by terrestrial contamination (see the following subsubsections for the details). Although most of the trace element abundances were determined using LA-ICP-SF-MS, those in chromite and ilmenite and the V, Zr, Nb, and Ta abundances in all silicates were determined using LA-ICP-TOF-MS. The trace element abundances obtained using LA-ICP-TOF-MS are predominantly considered upper limits as most of these abundances, especially Nb and Ta, are close to their LOD values. The CI-normalized abundances of trace elements in the constituent minerals for each metamorphic grade including HCs collected from hot deserts are shown in Figs. 2-4. Overall, the elemental abundances in the constituent minerals obtained in this study are in good agreement with the literature values compiled in Maeda *et al*. (2023a). However, note that the elemental abundances obtained in those cases for which the number of analyses available is only one or two may not reflect representative values, especially in the case of UHCs due to the absence of equilibration of elemental distributions among mineral grains. In addition, some elemental abundances less concentrated in the phase are possibly affected by overlap with other phases during the ablation, due to too small grains in UHCs or the presence of inclusions in the targeted mineral, even though the sampling of pure target phases was monitored based on the major element abundances obtained.

3.3.1 Merrillite and apatite

Merrillite was found in all samples, while apatite was not found or available for analysis in all samples (not in A-880941, Y-793574, A 09387, or Sahara 97035). Based on the major element abundances in apatite, their substituents are dominated by Cl at more than 70% and F at up to ~20% (Supplementary Table 3), confirming that the predominant form is chlorapatite. According to the CI-normalized abundances of trace elements in merrillite and chlorapatite shown in Figs. 2 (a) and (b), respectively, Sr, Y, REEs, Th, and U are concentrated in both merrillite and chlorapatite regardless of the metamorphic grades but to different extents. While Y and REEs are more concentrated in merrillite up to ~300 × CI as the highest abundances among the constituent minerals, Th and U are highly concentrated in chlorapatite up to ~500 × CI as the highest abundances among the minerals studied. The Sr abundance in chlorapatite is also one of the highest among the minerals, being comparable with that in feldspar (~15 × CI).

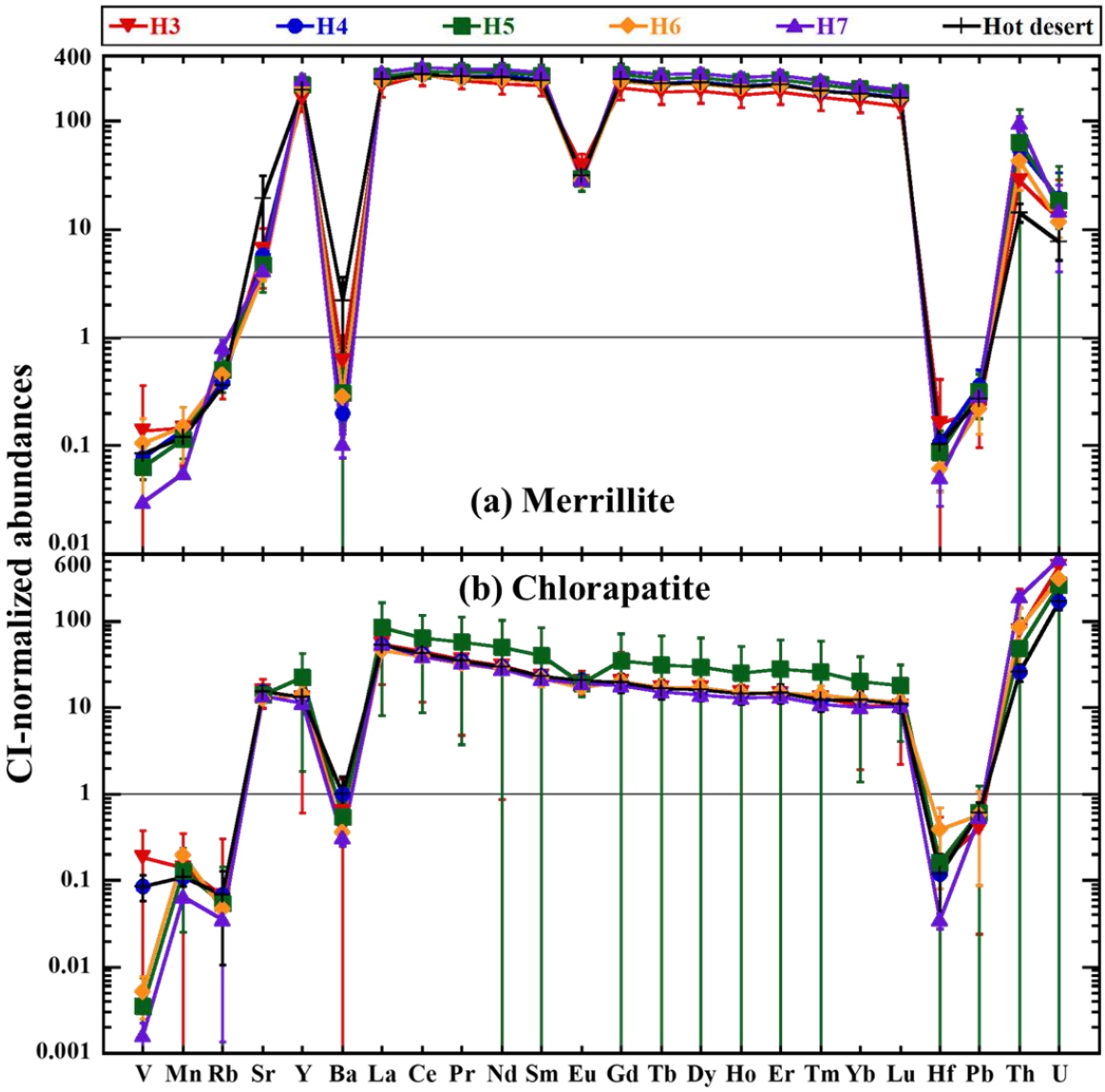

Fig. 2. CI-normalized abundances of trace elements in merrillite (a) and chlorapatite (b) for each metamorphic grade including HCs from hot deserts. The error bars represent the 95% confidence interval (see Supplementary Tables 2 and 3 for the details). Error bars may be smaller than the symbol size. CI values are from Anders and Grevesse (1989).

In the case of merrillite, only the hot desert mean displays relatively high Sr and Ba abundances compared with the other metamorphic grades (150 ± 96 ppm and 5.1 ± 3.5 ppm, respectively; Supplementary Table 2). Compared to the major element abundances in merrillite based on the metamorphic grades, the Cl and FeO contents seem to decrease with increasing metamorphic grade although the FeO contents for H3 and H7 overlap within uncertainty with each other (Cl: 0.03 ± 0.01 wt.%, <LOD, and <LOD; FeO: 1.43 ± 0.75 wt.%, 0.46 ± 0.01 wt.%, and 0.52 ± 0.21 wt.%; for H3, H6, and H7, respectively). In terms of their trace elements, there are resolvable differences in Y and REE abundances except for Eu between H3 and H7 (Y: 257 ± 65 ppm vs. 378 ± 32 ppm, respectively), implying that their abundances increase with increasing metamorphic grade. However, the values for H4-H6 overlap within uncertainty with those of H3. In the case of chlorapatite, on the other hand, there is no resolvable difference in the elemental abundances among the metamorphic grades, including the hot desert HCs.

3.3.2 Ca-rich pyroxene and feldspar

The major element abundances in Ca-rich pyroxene indicate the dominance of diopside based on their average compositions ($En_{48-53}Wo_{39-46}$; Supplementary Table 4). In the case of feldspar, the average composition indicates the presence of plagioclase, more specifically albite (~$Ab_{85}An_{10}$; Supplementary Table 5), except for K-feldspar in Y-793574 (H3.5) and Ca-rich feldspar in NWA 6771 (H4). Based on the elemental abundances in each metamorphic grade, the major element abundances in H3 minerals vary more than those for H4-H7. Figures 3 (a) and (b) demonstrate that Sc, V, Y, REEs (especially HREEs), and Hf are concentrated in Ca-rich pyroxene and Rb, Sr, Ba, and Eu are concentrated in plagioclase, respectively, regardless of the metamorphic grade. In addition, Zr, Nb, and Ta are also concentrated in both minerals to almost the same extent. Both minerals contain among the highest Nb and Ta abundances of all constituent minerals, with the exception of oxide phases.

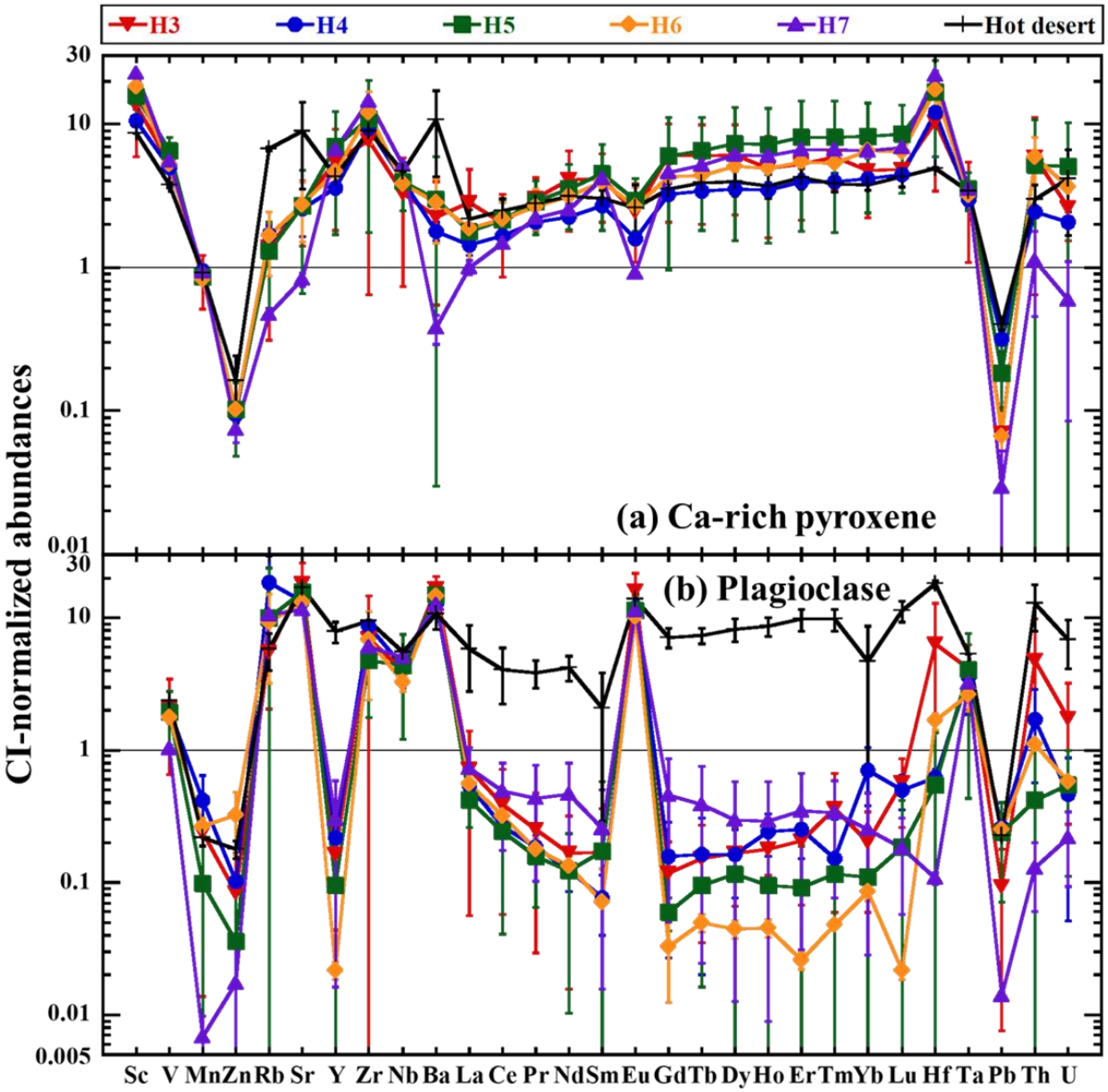

Fig. 3. CI-normalized abundances of trace elements in Ca-rich pyroxene (a) and plagioclase (b) for each metamorphic grade including HCs from hot deserts. The error bars represent mostly the 95% confidence interval (see Supplementary Tables 4 and 5 for the details). Error bars may be smaller than the symbol size. CI values are from Anders and Grevesse (1989).

In the case of Ca-rich pyroxene, the Sc, Zr, and Hf abundances display more than ~10 × CI values and are the highest among the constituent minerals. In addition, except for oxide phases, the V abundance is also the highest among the mineral phases studied. Remarkably, Sc and Hf abundances of H7 Ca-rich pyroxene grains are resolvably higher than those of H3 (Sc: 132 ± 5 ppm vs. 79 ± 45 ppm; Hf: 2.3 ± 0.1 ppm vs. 1.1 ± 0.7 ppm, respectively; Supplementary Table 4). The hot desert mean displays relatively high Rb, Sr, Ba, and Pb abundances compared with the other metamorphic grades (16 ± 0 ppm, 69 ± 42 ppm, 25 ± 15 ppm, and 0.99 ± 0.08 ppm, respectively; Supplementary Table 4).

In the case of feldspar, the Rb and Ba abundances in plagioclase are the highest among the constituent minerals (~10 × CI for both) and the Eu abundance is nearly as high as that in chlorapatite (~0.7 ppm vs. 1.1 ppm, respectively; Supplementary Table 5). As mentioned in subsubsection 3.3.1 for chlorapatite, the Sr abundance in plagioclase is also one of the highest among the HC minerals. Apparently, K-feldspar contains more Rb and less Ba than plagioclase (Rb: 103 ± 15 ppm vs. ~20 ppm; Ba: 10 ± 2 ppm vs. ~30 ppm, respectively; Supplementary Table 5). According to Fig. 3 (b), the hot desert mean displays distinct concentrations of Y, REEs, except for Eu, Hf, Th, and U. In terms of the trace element abundances among the metamorphic grades, the Rb abundance of H7 is higher than that of H3 (24 ± 1 ppm vs. 13 ± 8 ppm, respectively; Supplementary Table 5). In addition, Hf, Th, and U seem progressively depleted with increasing metamorphic grade as UHCs display higher abundances of these elements than most of the EHCs, especially when comparing H3.3, H3.5, and H7 (Supplementary Table 5).

3.3.3 Low-Ca pyroxene and olivine

The average compositions of low-Ca pyroxene and olivine are both Mg-rich ($En_{81-90}Fs_{10-17}$ and Fo_{81-83}; Supplementary Tables 6 and 7). According to Figs. 4 (a) and (b), most of the trace elements are depleted in both minerals. Only Mn is somewhat concentrated in both minerals, especially in the case of olivine which contains the highest Mn abundance among the minerals except for the oxides (~2 × CI). The REE abundances in low-Ca pyroxene for the mean H3 seem higher than those for EHCs, while there is no correlation between the elemental abundances in olivine in terms of the metamorphic grades. The Sr abundance in olivine for the hot desert mean is higher than for the falls and Antarctic finds (Fig. 4 (b)). Note that the Cr content in olivine of A-880941 (H3.3) is higher than those of the other samples (0.15 ± 0.06 wt.% vs. ~0.04 wt.%; Supplementary Table 7).

3.3.4 Kamacite, taenite, and troilite

Among the metamorphic grades, overall, there are no resolvable differences in the major and minor element abundances in metal and sulfide phases (Supplementary Tables 8-10). However, the metal and sulfide of the least metamorphic sample in this study, A-880941 (H3.3), display differences from those of the other samples as both kamacite and taenite and troilite contain remarkably higher P and Cr contents (P: ~0.35 wt.% vs. < 0.01 wt.%; Cr: 0.354 ± 0.136 wt.% vs. < 0.04 wt.%), respectively. The metal and sulfide phases of NWA 6771 (H4) are fairly oxidized as the abundances total ~90%. In addition, the Ni abundance in the troilite of NWA 6771 is significantly higher than those for the other samples (0.76 ± 0.54 wt.% vs. < 0.16 wt.%).

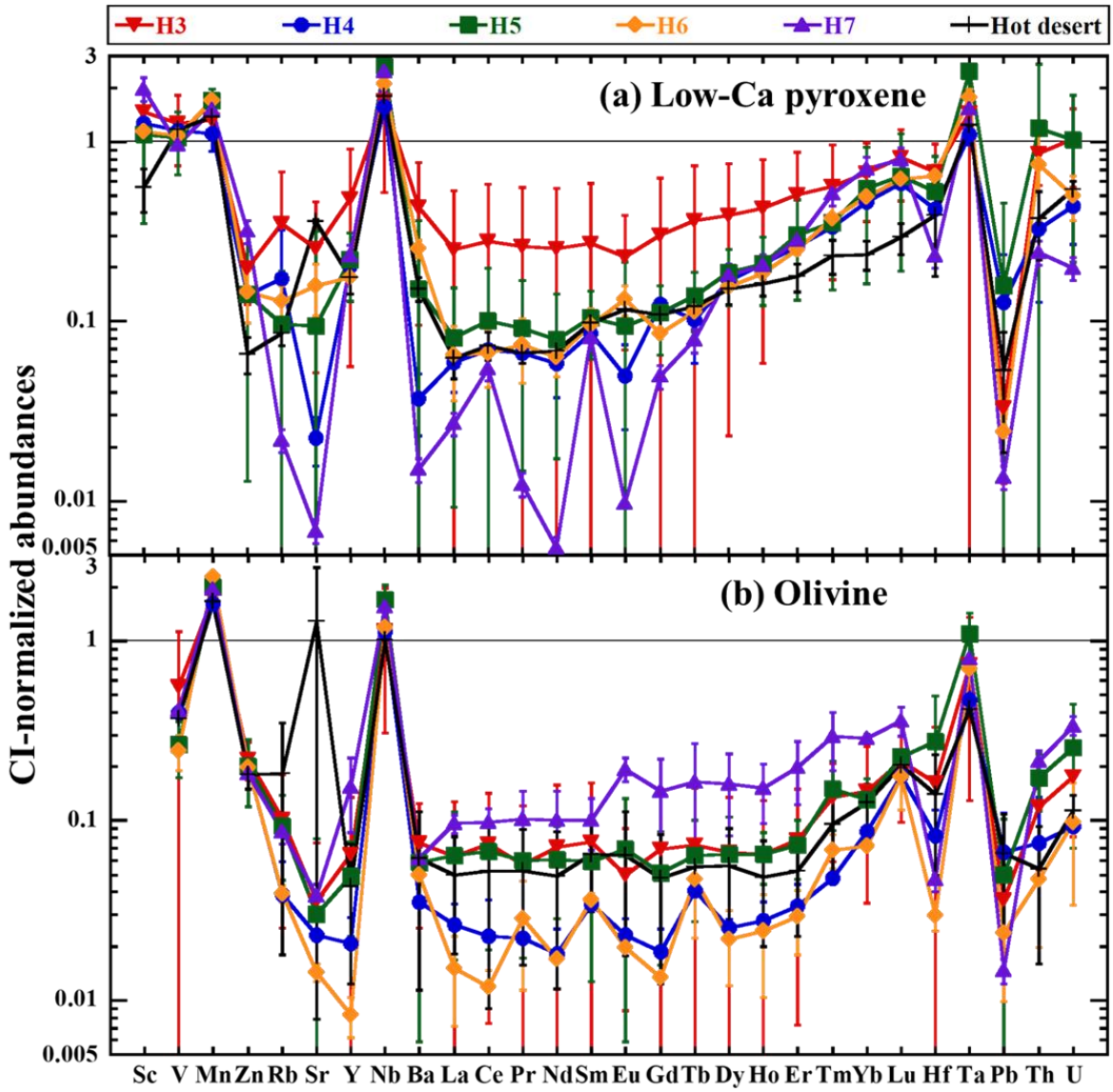

Fig. 4. CI-normalized abundances of trace elements in low-Ca pyroxene (a) and olivine (b) for each metamorphic grade including HCs from hot deserts. The error bars represent mostly the 95% confidence interval (see Supplementary Tables 6 and 7 for the details). Error bars may be smaller than the symbol size. CI values are from Anders and Grevesse (1989).

3.3.5 Chromite and ilmenite

Similar to apatite, chromite was not found or available to analyze in Y-793574 and ALH 78084, while ilmenite was found in four samples only (Jilin, Nuevo Mercurio, A 09516, and Y-790960). Furthermore, the chromite of A-880941 and the ilmenite of Nuevo Mercurio and A 09516 were analyzed using LA-ICP-TOF-MS including their major element abundances. Because their elemental abundances must be affected by overlap with silicate and metal phases judging from the major element abundances (Supplementary Tables 11 and 12), the trace elemental abundances may display their lower limit values, especially in the case of V, Mn, and Zn for chromite and Mn, Nb, and Ta for ilmenite. Due to this overlap, their major element abundances were excluded from the mean values.

The elements V, Mn, and Zn are highly concentrated in chromite (Supplementary Table 11). Chromite is the

most enriched in V and Zn among the constituent minerals. In addition, Zr, Nb, Hf, and Ta are also relatively concentrated in this phase. The Zn abundance for H7 is higher than those for all H3 samples (3400 ± 1000 ppm vs. < 2200 ppm). Note that the chromite phase of NWA 6771 is oxidized as is the case for its metal and sulfide phases.

The elements Mn, Zr, Nb, Hf, and Ta are concentrated in ilmenite (Supplementary Table 12). Ilmenite is the mineral containing the highest Mn, Nb, and Ta abundances among the constituent minerals. In particular, Mn is one of the major elements in this phase. Ilmenite contains Zr and Hf at nearly the same concentration level as Ca-rich pyroxene (~35 ppm and ~1 ppm, respectively). Because only a couple of ilmenite grains were available to analyze in all the samples studied, the elemental abundances in ilmenite obtained may not reflect their representative values, particularly in the case of the trace elements.

3.4 Elemental budgets in the constituent minerals

The EWR values for all samples were obtained using the ideal and observed modal abundances based on the elemental abundances in the constituent minerals. The comparison between the EWR values based on the two modal abundances demonstrates that the EWR values based on the ideal modal abundances are more consistent with the bulk rock values, despite good agreement of the observed modal abundances with published values (Maeda *et al*., 2021). For example, in the case of Y-790960 (H7), which is the most equilibrated sample in this study, the EWR values relative to the bulk rock values expressed in % are the following (ideal vs. observed, respectively): Mg: 96 vs. 101; P: 103 vs. 137; Ca: 110 vs. 127; Cr 95 vs. 44; Ni: 106 vs. 145; La: 86 vs. 102; Eu: 103 vs. 115; Lu: 103 vs. 114; and U: 100 vs. 175. The less equilibrated samples are, the more noticeable such differences in the EWR values are, especially in the case of trace elements. Thus, only the EWR values based on the ideal modal abundances are considered in the following results and discussion.

The relative EWR values in individual minerals for A-880941 (H3.3), A 09618 (H5), and Y-790960 (H7) are shown in Fig. 5 as an example. Overall, the EWR values of the major elements (*e.g.*, Mg, Al, P, Ca, and Fe

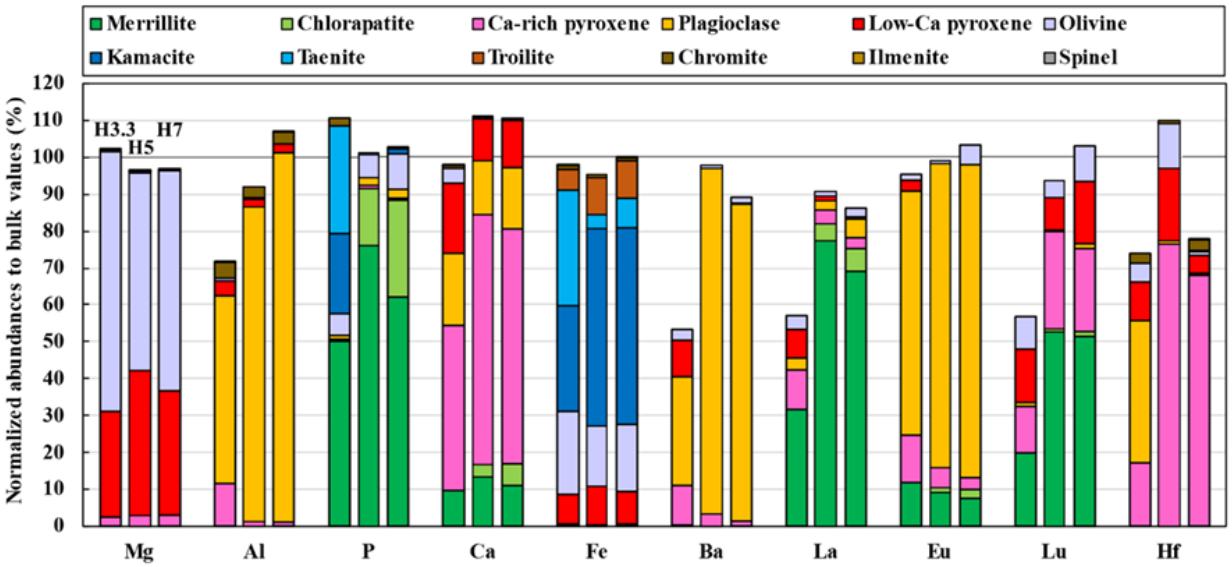

Fig. 5. Estimated whole-rock values with bulk rock-normalized abundances in individual minerals for A-880941 (H3.3; at the left), A 09618 (H5; in the middle), and Y-79060 (H7; at the right) in %. The bulk rock values are from Maeda *et al.* (2021).

in Fig. 5) for both unequilibrated and equilibrated samples are in good agreement with the bulk rock values, although some discrepancies are observed, especially in the case of the unequilibrated samples (*e.g.*, Al for A-880941; Fig. 5). Even in the case of the trace elements (*e.g.*, Ba, La, Eu, Lu, and Hf in Fig. 5), the EWR values for equilibrated samples are fairly consistent with the bulk rock values (~80-110%; Fig. 5). In addition, the ideal modal abundances for A 09618 (H5) and Y-790960 (H7) are compared with published values in Table 2 (Van Schmus, 1969; McSween *et al*., 1991), and their ideal modal abundances overlap with the published values. However, the largest discrepancies between the EWR values of the trace elements and the bulk rock values are observed for A-880941 (< 80%; Fig. 5), while the ideal modal abundance also differs from the published values (Table 2). Similar to the comparison between the EWR values based on the ideal and observed modal abundances, the less equilibrated samples are, the larger the overall discrepancies are between the EWR values of the trace elements and the bulk rock values, and between the ideal modal abundances and the published modal abundance, even though their EWR values of the major elements are in agreement with the bulk rock values. Moreover, in most of the cases, their EWR values and ideal modal abundances are lower than the comparison values, indicating that there are phases missing from the samples. Consequently, in order to compare elemental budgets in the constituent minerals for all samples, it is therefore assumed that there is (an) unidentified phase(s) in the sample to increase the low EWR values to 100%, while the EWR values displaying over 100% are normalized to 100%.

After this assumption and normalization, the Nd budgets in the constituent minerals for each sample studied are shown in Fig. 6, as an example of the approach applied. Neodymium is strongly partitioned to Ca-phosphates,

Table 2. Ideal modal abundances used for calculating the mass balance (Ideal) and observed modal abundances obtained using μXRF (Observed) in wt.%.

Name	A-880941 (H3.3)		A 09618 (H5)		Y-790960 (H7)		Equilibrated H chondrite mean			
	Ideal	Observed	Ideal	Observed	Ideal	Observed	Van Schmus (1969)	McSween *et al*. (1991)		
Olivine	35	33.4	30	35.6	33	36.0	33-37	35.7	±	1.5
Low-Ca pyroxene	20	20	30	26	26	25	23-27	26.3	±	1.2
Ca-rich pyroxene	3.5	5.6	4.2	2.1	4.0	4.6	4-5	4.1	±	0.2
Feldspar	3.5	9.91	7.5	9.58	9.0	9.77	9-10	9.6	±	0.2
Kamacite	7.0	7.2	15	15	15	14	15-17	18.2	±	0.6
Taenite	8.0	18.5	1.5	4.45	3.0	5.54	2-3			
Troilite	2.0	3.75	4.3	4.94	4.3	4.67	5-6	5.5	±	0.2
Chlorapatite	0	0.07	0.09	0.26	0.15	0.30	0.6	0.65	±	0.03
Merrillite	0.27	0.30	0.39	0.28	0.32	0.36				
Chromite	1.0	1.2	0.80	0.98	0.90	0.35	0.5	0.76	±	0.02
Ilmenite	-		0	trace	0.01	trace	-	0.23	±	0.01
(Mg, Fe)-spinel	0.01	trace	-		-		-	-		
Total	80	100	94	100	96	100				

The uncertainties for McSween *et al.* (1991) are 2SE calculated from their data (n = 25).

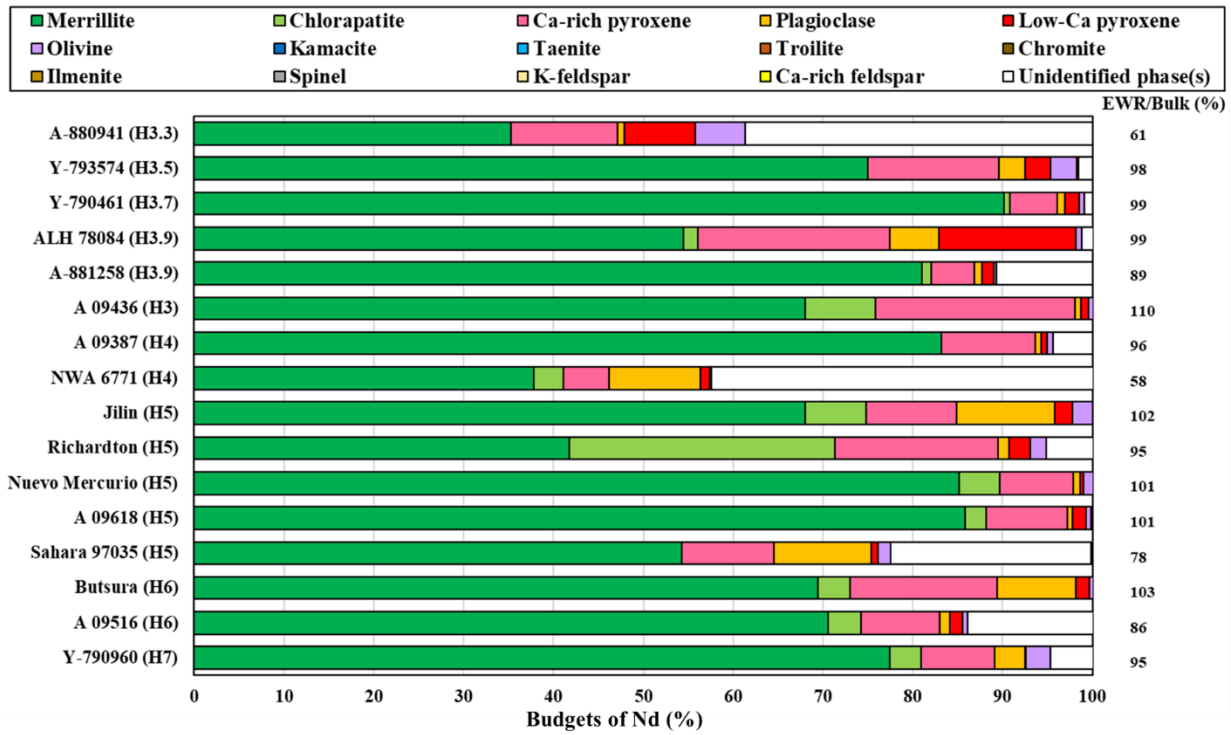

Fig. 6. Neodymium budgets normalized to 100% in the constituent minerals for each sample, summarizing the ratios of the estimated whole-rock (EWR) value to the bulk rock (Bulk) value in %. The bulk rock values are from Shinotsuka (1997) and Maeda *et al.* (2021).

especially merrillite (40-90%). Ca-rich pyroxene contributes 5-20% to the WR budget of Nd. The contributions of (an) unidentified phase(s) to the WR budget of Nd are negligible for most of the samples as their EWR values are in agreement with the bulk rock values within ~10%, but this is not the case for the most unequilibrated sample A-880941 (H3.3) and the hot desert samples NWA 6771 (H4) and Sahara 97035 (H5) studied here. The unidentified phase(s) contribute(s) up to 40% in these cases.

Figures 7 and 8 exhibit the mean elemental budgets for each metamorphic grade and samples from hot deserts. The mean budgets of light REEs (LREEs) and heavy REEs (HREEs) are calculated by taking an average from the budgets of La-Nd and Ho-Lu, respectively. According to Figs. 7 and 8, the distribution of an element among the constituent minerals is overall consistent regardless of the metamorphic grades. For example, REEs, except for Eu, are mostly distributed in Ca-phosphates, especially in the case of merrillite (40-85%; Fig. 7) and Sr is mainly distributed in plagioclase (80-95% except in the case of hot desert meteorites; Fig. 8). However, there are some remarkable differences between UHCs and EHCs: *e.g.*, the U budgets in Ca-phosphates, especially chlorapatite, and the Sc budgets in Ca-rich pyroxene increase with increasing metamorphic grade (H3: 16% and 40%; H7: 80% and 65%, respectively). In addition, the hot desert mean displays higher contributions of the unidentified phase(s) to the WR budgets for most of the elements, *i.e.*, their EWR values are significantly lower than the bulk rock values. More information on the budgets of each element based on both ideal modal and observed modal abundances and their EWR values for individual samples and the mean budgets of each element can be found in Supplementary data-3.

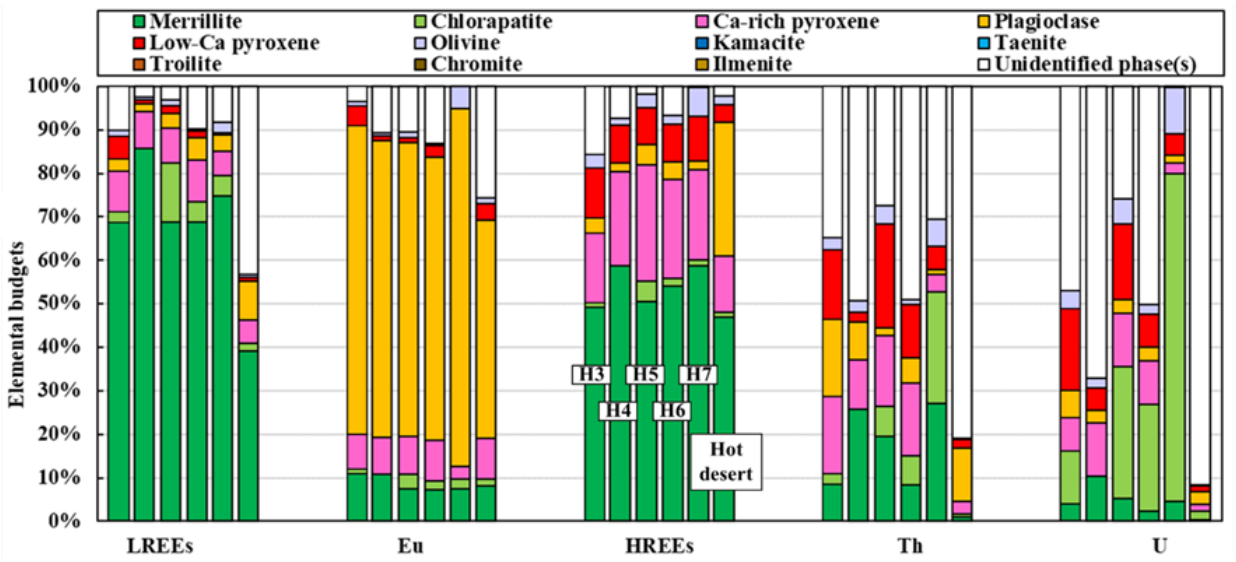

Fig. 7. Mean budgets for LREEs, Eu, HREEs, Th, and U in the constituent minerals for each metamorphic grade, including HCs from hot deserts, in %. The order of the bars is H3, H4, H5, H6, H7, and Hot desert HCs from left to right.

4 DISCUSSION

4.1 Unidentified phase(s) in UHCs and hot desert HCs

As a result of the comparisons between the EWR values based on the ideal modal abundances and the bulk rock values and between the ideal modal abundances and the published modal abundances, the assumption of (an) unidentified phase(s) in the sample was applied to the elemental budgets for each sample (subsection 3.4). Although the contributions of the unidentified phase(s) to the elemental budgets are in some cases negligible considering the associated uncertainty, a significant contribution of the unidentified phase(s) is required to explain the budgets of some samples (*e.g.*, A-880941 and NWA 6771; Figs. 5 and 6 and Supplementary data-3). Including the EWR values displaying over 100% relative to the bulk rock values, it cannot be excluded that the difference between the EWR and the bulk rock values observed reflects non-representative abundances obtained for some minerals due to heterogeneity in terms of the elemental abundances in these minerals, as only a single grain (or a few) was available for the determination of the trace element abundances in some samples (Supplementary Tables 2-12). However, other factors should be also considered to explain the unidentified phase(s), especially in UHCs and HCs from hot deserts, as overall these display larger contributions of the unidentified phase(s) (Figs. 7 and 8 and Supplementary data-3).

4.1.1 Mineralogical heterogeneity in UHCs

As the name suggests, equilibration between the silicate phases in UHCs is not completed. As such, the chemical compositions of the phases for UHCs including trace elements are in general more variable than those for EHCs (Huss *et al.*, 2006). Unequilibrated silicate phases were indeed observed in UHCs and H4 (Maeda *et al.*, 2021): forsterite in Y-793574 (H3.5), Y-790461 (H3.7), A-881258 (H3.9), and A 09387 (H4); K-rich feldspar in Y-793574, ALH 78084 (H3.9), and A-881258; Ca-rich feldspar in A-880941 (H3.3), A-881258, and NWA 6771 (H4). In addition, Wo compositions in Ca-rich pyroxene for H3 and H4 are more variable than those

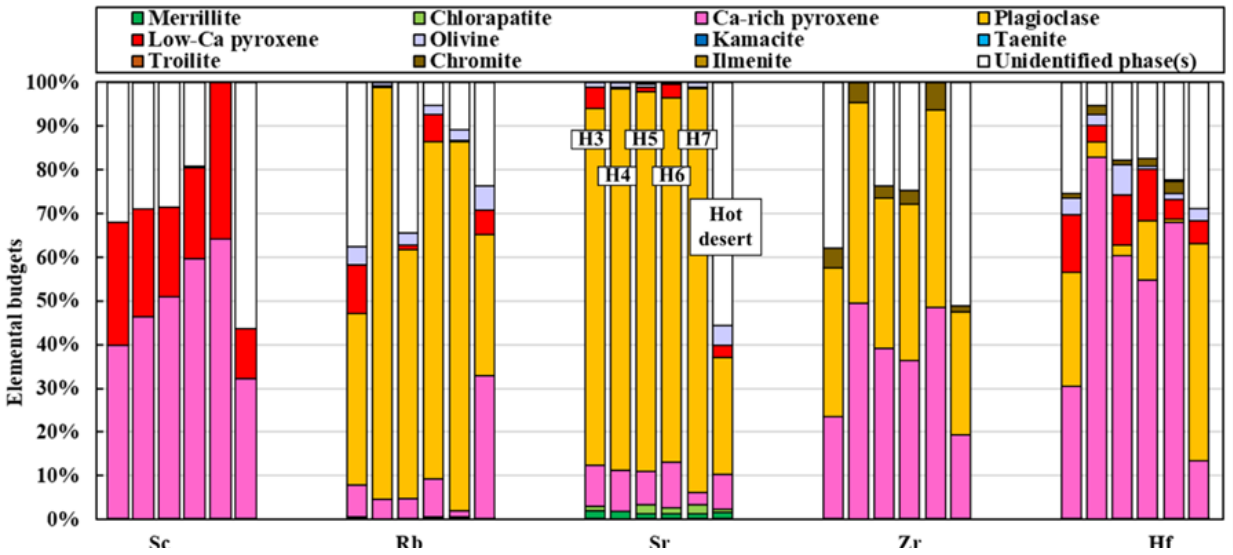

Fig. 8. Mean budgets for Sc, Rb, Sr, Zr, and Hf in the constituent minerals for each metamorphic grade, including HCs from hot deserts, in %. The order of the bars is H3, H4, H5, H6, H7, and Hot desert HCs from left to right.

for H5-H7 and some of their Ca-rich pyroxenes indicate the presence of augite and pigeonite instead of diopside (Supplementary Table 4). These unequilibrated phases were not analyzed using LA-ICP-SF-MS due to their relatively small grain sizes or inclusions in the grains, and thus are not included in the calculation of the elemental budgets. According to Dunn *et al.* (2010), however, the amounts of these phases, especially in the case of augite and pigeonite, are non-negligible for UOCs although their exact modal abundances are difficult to determine. Augite and pigeonite have chemical compositions between diopside and low-Ca pyroxene in terms of trace lithophile elements, as the higher Ca content is, the higher the abundances of the trace lithophile elements are (Jones and Layne, 1997), which can largely contribute to the elemental budgets. Thus, the non-negligible contributions of the unidentified phase(s) to the WR elemental budgets for UHCs may reflect the presence of these unequilibrated silicate phases not analyzed in this study. This is supported by the larger differences between the ideal and observed modal abundances for UHCs than those for EHCs mentioned in subsection 3.4 (Table 2), as such unequilibrated phases are not taken into account for the ideal modal abundances.

Nevertheless, the budgets of trace elements in A-880941 (H3.3), the least metamorphosed sample in this study, are still significantly lower than the bulk rock value (35-65%; Fig. 5). This sample exhibits mineralogical and chemical features of samples that underwent a low degree of thermal metamorphism (Huss *et al.*, 2006), as secondary minerals such as Ca-phosphates and chromite were only found in rare instances, the grains of secondary feldspar are much smaller than those of the other UHCs, olivine contains the highest Cr content (subsubsection 3.3.3; Supplementary Table 7), and metals contain high P contents (subsubsection 3.3.4; Supplementary Tables 8 and 9). In the case of such low metamorphic samples, primary phases should be considered as the unidentified phase(s). In terms of the abundance of overall lithophile elements, CAIs and glass mesostasis in chondrules are viable candidates as bulk CAIs and mesostasis contain refractory lithophile elements at ~20 × CI and ~10 × CI, respectively (Alexander, 1994; Jones and Layne, 1997; El Goresy *et al.*, 2002; Ruzicak *et al.*, 2008; Jacquet *et al.*, 2015). Both type I and II chondrules, composing the majority of chondrules (Hewins *et al.*, 2005), are considered here for chondrules that contain such glass mesostasis. However, the modal abundance of CAIs in HCs is only 0.01-0.2 vol.% (Krot *et al.*, 2003; Hezel *et al.*, 2008), and thus CAIs contribute

only up to 5% of the WR budgets for lithophile elements of A-880941. On the other hand, glass mesostasis is more commonly distributed in samples as such mesostasis is used as an indicator of the metamorphic degree classification (Huss *et al*., 2006; Jacquet *et al*., 2015), although the exact modal abundances remain poorly constrained. If the modal abundance of mesostasis is the same as the ideal abundance of feldspar for A-880941, or is similar to that of the ideal modal abundance of feldspar subtracted from the observed modal abundance assuming that the observed modal abundance of feldspar includes that of mesostasis for A-880941 (3.5 wt.% and ~5 wt.%; Table 2), the contribution of mesostasis to the WR budgets of lithophile elements is estimated to be ~25% or ~40%, respectively. In such case, glass mesostasis can contribute to the lithophile element budgets in an important manner, especially for samples that underwent a low degree of thermal metamorphism such as A-880941.

4.1.2 Effects of terrestrial weathering and contamination on hot desert HCs

Following the comparison of the elemental abundances in the constituent minerals between hot desert HCs and the other HCs (subsection 3.3), some elements display enrichments in mineral phases identified in hot desert HCs: Rb, Sr, Ba, and Pb in Ca-rich pyroxene; Y, REEs except for Eu, Hf, Th, and U in plagioclase; and Sr in olivine. However, most of the mean elemental budgets display large contributions of the unidentified phase(s) despite these enrichments (Na, K, Ca, Sc, Sr, Zr, Nb, Ba, LREEs, Hf, Ta, Th, and U; Figs. 7 and 8), *i.e.*, the EWR values are significantly lower than the bulk rock values. Consequently, these differences should be explained by terrestrial weathering and contamination because the bulk rock values are enriched in K, Ca, Sr, Zr, Nb, Ba, REEs especially LREEs, Hf, Th, and U (Maeda *et al.*, 2021). Thus, some minerals appear affected by terrestrial weathering based on the enrichments observed while terrestrial contamination through the admixture of terrestrial material dominates the elemental enrichments observed at the bulk rock scale (Maeda *et al.*, 2021).

In the case of chemical alteration on Ca-rich pyroxene and olivine, the low-valent elements displaying enrichments may have been transferred from terrestrial soils via fluid (Al-Kathiri *et al.*, 2005). Once these elements are extracted from the soils by interacting with fluids, cations in Ca-rich pyroxene and olivine are presumably replaced by them. The way in which chemical alteration takes place for plagioclase should be distinct from that for Ca-rich pyroxene and olivine because the elements becoming enriched in plagioclase display higher valence states. Maeda *et al.* (2023b) demonstrated that such high-valent elements, more specifically REEs, Th, and U, can accumulate in cracks and limonite veins, through terrestrial alteration as acidic fluids extract the trace elements from Ca-phosphates. Because the grains of plagioclase analyzed in the hot desert HCs in this study contain limonite veins, their elemental abundances may be elevated by such a REE-rich vein. Alternatively, the grains of plagioclase of the hot desert HCs contain terrestrial soil grains as embedded or inclusions, and thus such soil grains were ablated together with plagioclase. Nevertheless, this is unlikely because no trace of this terrestrial contaminant is observed in the signatures of the other elements (*e.g.*, Sr, Ba, and Zr; Supplementary Table 5). In any case, because of the high REE abundances in plagioclase of the hot desert HCs, the contributions of plagioclase to the hot desert mean WR budgets in terms of middle REEs (MREEs) and HREEs are significantly larger than those for the other samples (20-30% vs. < 5%; Fig. 7 and Supplementary data-3). Related to this, the EWR values of Na for the hot desert HCs are lower than the bulk

rock values despite the absence of Na contamination in the bulk rock because the EWR values of REEs would largely exceed the bulk rock values if the ideal modal abundances were modified to match Na.

4.2 Distributions of lithophile elements among the constituent minerals in HCs

4.2.1 Major elements (Na, Mg, Al, Si, P, K, Ca, Ti, Cr, Fe, and Ni)

Fundamentally, the distribution of major elements is largely determined by the occurrence of the minerals that are predominantly composed of these elements. The elements Na, Al, and K are largely hosted by plagioclase contributing 35-95%, 50-95%, and 25-100%, respectively, to the WR budgets of these elements. To a lesser extent, Na and Al are also distributed in Ca-rich pyroxene at 5-10%. Although the data for K-feldspar were limited and the ideal modal abundance of K-feldspar for Y-793574 (H3.5) was only 0.6 wt.%, K-feldspar contributes ~35% of K. The budgets of these elements in the unidentified phase(s) are significant in the case of UHCs (Na: 25-60%, Al: 5-35%, K: 20-90%), implying the existences of glass mesostasis and K-feldspar in the samples. These budgets in plagioclase increase while those in the unidentified phase(s) decrease with increasing metamorphic grade.

The elements Mg and Si are mainly carried by low-Ca pyroxene and olivine (Mg: 25-40% and 55-70%, Si: 30-50% and 30-40%, respectively). Ca-rich pyroxene contributes ~5% of these elements. Silicon is also hosted by plagioclase at 5-15%.

Ca-phosphates are the major host phases of P (45-100%), especially merrillite (45-80%). Olivine contributes up to ~5% of the WR P budgets. Importantly, in the case of A-880941 (H3.3), characterized by the lowest metamorphic degree, P is in large part also distributed in metal phases (~20% in kamacite and ~25% in taenite).

Calcium is mainly distributed in Ca-rich pyroxene at 45-75% and also in Ca-phosphates, plagioclase, and low-Ca pyroxene at 10-20%, 5-25%, and 5-20%, respectively. The budgets in the unidentified phase(s) for the hot desert HCs are seemingly larger than those for the other HCs, but this is because the bulk rock values are elevated by terrestrial contamination as mentioned in subsubsection 4.1.2. Ca-rich pyroxene also accommodates 15-65% of Ti. However, the distribution of Ti is more complicated; Ti is distributed in low-Ca pyroxene at 15-50% and to some degree in plagioclase, olivine, and chromite at 5-30%, < 20%, and 5-20%, respectively. With increasing metamorphic grade, the budgets in low-Ca pyroxene increase, while those in Ca-rich pyroxene, plagioclase, and olivine decrease. Although ilmenite consists of Ti mainly, the budgets in ilmenite are moderate (5-25%).

Chromium is mainly distributed in chromite at 60-85% and to a lesser degree in Ca-rich pyroxene and low-Ca pyroxene at 5-10% and 5-20%, respectively. The budgets in low-Ca pyroxene decrease with increasing metamorphic grade. The large contributions of the unidentified phase(s) for Y-793574 and ALH 78084 are simply due to the lack of data for chromite in these samples.

Although Fe and Ni are rather siderophile/chalcophile than lithophile elements, their distributions are described here as they are major elements. These elements are mainly distributed in metals (55-65% for Fe and < 95% for Ni). Low-Ca pyroxene and olivine account for 5-10% and 15-20%, respectively, of the Fe. These budgets in low-Ca pyroxene and olivine are similar to or larger than those in taenite while kamacite is always the major host phase of Fe, except in the case of A-880941 (H3.3). Iron is also distributed in troilite at 5-15%.

Nickel is distributed almost equally in kamacite and taenite. The contributions of non-metal phases to the WR budgets of Ni are overall negligible (< 3%).

4.2.2 Minor elements (Sc, V, Mn, and Zn)

Scandium is mainly distributed in Ca-rich pyroxene and low-Ca pyroxene at 15-65% and 10-40%, respectively (Fig. 8). The budgets in Ca-rich pyroxene systematically increase while those in the unidentified phase(s) decrease with increasing metamorphic grade, indicating the equilibration of pyroxene converting the mineral either in low-Ca pyroxene or diopside. Especially in the case of A-880941 (H3.3), the contribution of glass mesostasis should be also considered for 67% of the unidentified phase(s).

Vanadium is distributed among multiple constituent minerals. Chromite is a major host phase for V at 15-45%, as V is most concentrated in this phase among all minerals studied. The silicate phases accommodate 5-30% of the V budget. In most of the cases, the budgets in Ca-rich pyroxene and low-Ca pyroxene are larger than those in plagioclase and olivine (~20% vs. ~10%, respectively).

Olivine and low-Ca pyroxene host Mn at 40-70% and 20-40%, respectively. Manganese is also distributed in Ca-rich pyroxene and chromite at < 5%. The contribution of ilmenite to the WR budget is negligible with less than 0.5%, although Mn is most concentrated in ilmenite among the constituent minerals (~2.5 wt.%; Supplementary Table 12).

Zinc is hosted in three main phases: low-Ca pyroxene, olivine, and chromite at 10-50%, 25-65%, and 15-40%. Although chromite is most enriched in Zn among the constituent minerals, the budgets in olivine are larger than those in chromite in most cases.

4.2.3 Alkali metals and alkaline earth metals (Rb, Sr, and Ba)

As Rb, Sr, and Ba are highly concentrated in plagioclase regardless of the metamorphic grade, plagioclase is the major host phase of these elements at 25-95%, 70-95%, and 30-95%, respectively (Fig. 8). Ca-rich pyroxene also accommodates these elements to a lesser degree (5-10%). Although both Ca-phosphates merrillite and chlorapatite are enriched in Sr, their contributions to the Sr budgets represent less than 4% only. Because of terrestrial weathering and contamination, the Rb budgets in Ca-rich pyroxene and the Sr and Ba budgets in the unidentified phase(s) for the hot desert HCs are larger than those for the other HCs.

The Rb budgets in the unidentified phase(s) are mostly larger than those of Sr and Ba (10-60% vs. < 10%). This is attributed to the existence of K-feldspar because K-feldspar contributes 27% to the Rb budget of Y-793574 (H3.5) while it only adds 6% and 2% of the Sr and Ba budgets, respectively. Thus, K-feldspar is a major host phase of Rb next to plagioclase, while this is not the case for Sr and Ba. In the case of A-880941 (H3.3), Rb and Ba may be accommodated in glass mesostasis as well as K-feldspar because the unidentified phase(s) display(s) large contributions to the WR budgets at 58% and 47%, respectively, and it has been observed that Rb is concentrated in glass mesostasis together with refractory lithophile elements (Alexander, 1994; Ruzicak *et al*., 2008). In addition, it seems that these elemental budgets increase with increasing metamorphic grade.

4.2.4 Rare earth elements (Y and REEs)

Yttrium and the REEs are mainly distributed in Ca-phosphates at 20-90%, except in the case of Eu (Fig. 7). The abundances of these elements in merrillite are significantly higher than those in chlorapatite, and as a result the budgets of these elements in merrillite are significantly larger than those in chlorapatite (Y: 20-75% vs. < 1-10%; LREEs: 30-85% vs. 1-35%, respectively). While the LREEs are mostly distributed in merrillite, a considerable amount of Y, the MREEs, and the HREEs is distributed in Ca-rich pyroxene at 10-45%, 10-35%, and 10-45%, respectively. The distribution of Y among the constituent minerals is most comparable to those of the HREEs among the REEs, which is consistent with their ionic radii (Shannon, 1976). On the other hand, the distribution of Eu is completely different from those of the other REEs and Y as Eu is mainly distributed in plagioclase instead of Ca-phosphates at 50-85% although merrillite still contains ~2.5-fold higher Eu abundances than plagioclase (Supplementary Tables 2 and 5). Both Ca-phosphates and Ca-rich pyroxene accommodate Eu at ~10%.

As mentioned in subsubsection 4.1.2, the large contributions of the unidentified phase(s) and of plagioclase for the hot desert HCs to the WR budgets of the LREEs, Y, and the HREEs are due to terrestrial contamination affecting the bulk rock values and terrestrial weathering on plagioclase, respectively. Glass mesostasis may significantly contribute to the large budgets of Y and the REEs, except in the case of Eu in the unidentified phase(s) for A-880941 (H3.3). Apparently, the budgets of Y and the REEs (except for Eu) in Ca-phosphates, and especially merrillite, increase, while the budgets of Y, LREEs, and MREEs in low-Ca pyroxene decrease with increasing metamorphic grade, although the large budgets of Y, the LREEs, and the MREEs in low-Ca pyroxene for H3 may reflect that the pure phases were not successfully ablated due to inclusions in the grains, resulting in unrepresentative high abundances (Fig. 4 and Supplementary Table 6).

4.2.5 High field strength elements (Zr, Nb, Hf, and Ta)

Hafnium is mainly distributed in Ca-rich pyroxene and plagioclase at 5-85% and up to 60%, respectively. Low-Ca pyroxene contributes to the WR budgets of Hf to a minor degree at 5-25%. Chromite and ilmenite also concentrate Hf as well as Ca-rich pyroxene (Supplementary Tables 11 and 12), which is consistent with their partition coefficients (Green, 1994). However, the Hf budgets in chromite and ilmenite make up < 3% and < 0.3% only, respectively. The budgets in the unidentified phase(s) are overall larger than those of the other elements discussed above regardless of the metamorphic grade (~20% on average), implying that the heterogeneity of Hf abundances in the minerals is significantly more outspoken than for the other elements. This likely results from Hf being tetravalent and more immobile than these other elements, *i.e.*, due to the high valence and relatively small ionic radius as one of high field strength elements (HFSEs). Yet, glass mesostasis contributes considerably to the large budgets in the unidentified phase(s) for UHCs, *e.g.*, ~40% for Y-790461 (H3.7) and A-881258 (H3.9). On the other hand, the large budgets in plagioclase for the hot desert HCs must be explained by terrestrial weathering leading to high Hf abundances in plagioclase. There are obvious differences in the Hf budgets in Ca-rich pyroxene and plagioclase between UHCs and EHCs; the Hf budgets in Ca-rich pyroxene for UHCs are smaller than those for EHCs, while this is the opposite for plagioclase (~30% vs. ~65% and ~25% vs. ~5%, respectively).

The abundances of other HFSEs, Zr, Nb, and Ta, in the minerals were determined using LA-ICP-TOF-MS in a semi-quantitative manner. Although these elements including Hf are classified as HFSEs showing similar behaviors due to their comparable chemical features, Zr-Hf and Nb-Ta fractionate mostly between the pairs and even within the pairs in some cases during geochemical processes (*e.g.*, Chakhmouradian, 2006). As such, the Zr distribution is similar to that of Hf and it is mainly distributed in Ca-rich pyroxene and plagioclase with a minor contribution from chromite at 10-50%, 15-60%, and 1-6%, respectively. In addition, the large budgets in the unidentified phase(s) for UHCs and the hot desert HCs can be explained in an analogous manner by the contributions of glass mesostasis and terrestrial contamination to the bulk rock values. However, a difference in the distributions between Zr and Hf is observed, in which Zr is distributed almost equally in both Ca-rich pyroxene and plagioclase while Hf is fundamentally distributed in one or the other. Even though the Zr abundance in plagioclase can be expected to be almost as high as that in Ca-rich pyroxene according to their partition coefficients (Green, 1994; Bindeman and Davis, 2000; Bédard, 2006; Nielsen *et al.*, 2017), and such abundances were indeed obtained in this study, the high Zr abundances measured in plagioclase are probably also influenced by the overlap with Ca-rich pyroxene grains during the ablation of LA-ICP-TOF-MS because most plagioclase grains co-exist with Ca-rich pyroxene grains in a complicated manner (Maeda *et al.*, 2023a). This is supported by the quantitative maps as Zr is distributed more in Ca-rich pyroxene than in plagioclase based on the distribution maps of Na, Ca, Sc, and Zr (Fig. 9). Therefore, Ca-rich pyroxene is the major host phase of Zr, at least for EHCs. In a similar manner to Hf, the Zr budgets in Ca-rich pyroxene for UHCs are smaller than those for EHCs.

The distributions of Nb and Ta differ from those of Zr and Hf, with a more complicated dispersal among the silicate phases. However, the exact Nb and Ta budgets among the constituent minerals are poorly determined because the Nb abundances in low-Ca pyroxene and olivine and those of Ta in all silicates obtained principally represent their upper limits. Overall, it appears that the large budgets of Nb and Ta in the unidentified phase(s)

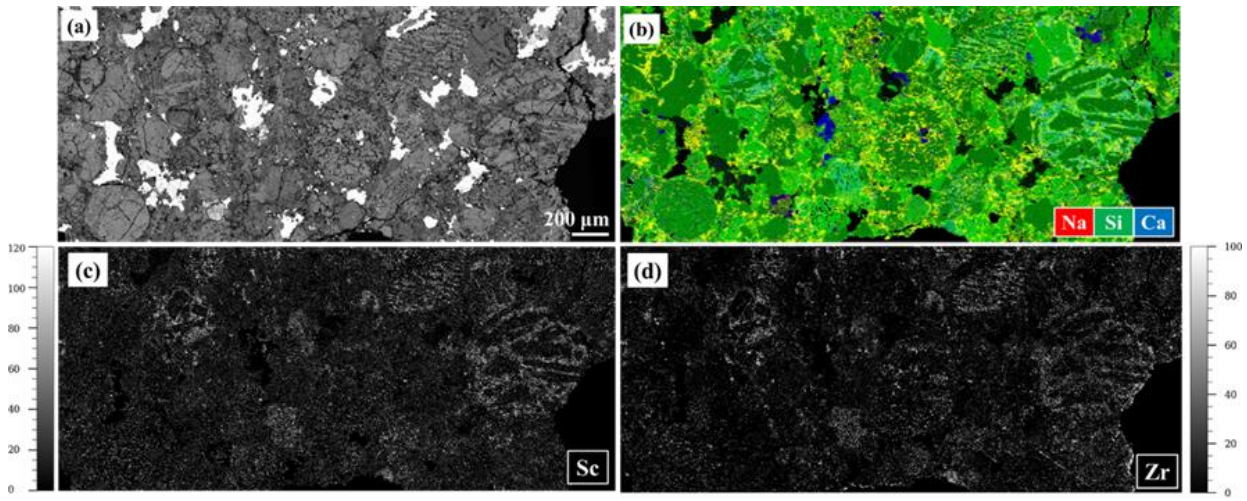

Fig. 9. BSE image and (semi-)quantitative element maps for Butsura (H6). (a) BSE image for the region analyzed using LA-ICP-TOF-MS. (b) Combined RGB elemental map obtained using LA-ICP-TOF-MS mapping with red: Na, green: Si, and blue: Ca. Based on the composition, the following mineralogy can be deduced yellow: plagioclase, light green: low-Ca pyroxene, green: olivine, light blue: Ca-rich pyroxene, and blue: Ca-phosphates. (c) Scandium distribution map. (d) Zirconium distribution map. Concentration scale bars for (c) and (d) are expressed in ppm.

for A-880941 (H3.3) may relate to the existence of glass mesostasis, while the contribution of ilmenite is limited to maximum 10% even though ilmenite contains high Nb and Ta concentrations (Supplementary Table 12).

4.2.6 Pb, Th, and U

In the case of Pb, the EWR values are systematically lower than the bulk rock values for all samples except for Richardton which displays an EWR value that is too high relative to the bulk rock value, indicating that Pb is also hosted by troilite and metal phases, as Pb is regarded to be chalcophile rather than lithophile (Davis, 2006). However, the contributions of the silicate phases to the WR budgets of Pb are not negligible as plagioclase, low-Ca pyroxene, and olivine contribute up to 45%, 35%, and 35%, respectively, of these elements to the WR budgets, except for Richardton. Thus, the distribution of Pb suggests that the affinity of Pb in HCs is in between chalcophile/siderophile and lithophile.

The elements Th and U are also distributed intricately among the constituent minerals: Ca-phosphates often largely contribute to the WR budgets of Th and U by up to 55% and 80%, respectively, but the contributions of silicate phases are not negligible as the Th and U budgets in Ca-rich pyroxene, plagioclase, and low-Ca pyroxene are up to 45% and 30%, 40% and 15%, and 55% and 35%, respectively. The distributions of Th and U are fractionated even within Ca-phosphates: Th is distributed in merrillite more than or similar to chlorapatite while chlorapatite dominates the U budget. In addition, the Th and U budgets in the unidentified phase(s) are larger than those of the Ca-phosphates in most of the cases (15-60% and up to 65%, respectively, except for the hot desert HCs). The large contributions of the unidentified phase(s) in the case of the hot desert HCs is attributed to terrestrial contamination on the bulk rock values as discussed above (subsubsection 4.1.1). In the case of UHCs, their budgets in the unidentified phase(s) are due to the contributions of glass mesostasis in a manner similar to that for other elements as previously discussed. The heterogeneity of Th and U abundances in minerals needs to be considered as well as that of Hf because Th and U also have high valence states similar to the HFSEs, occurring in tetravalent form and either tetravalent or hexavalent form, respectively. In addition, the quantitative maps indicate that a considerable amount of these elements accumulates in cracks (Fig. 1). Because Maeda *et al*. (2023b) suggest that the accumulation of Th and U is not only due to terrestrial alteration but also results from their original depositions in cracks and on grain boundaries based on previous studies (Jones and Burnett, 1979; Ebihara and Honda, 1984), such depositions should also be considered for the large contribution in the unidentified phase(s). In any case, the Th and U budgets in Ca-phosphates increase while those in plagioclase decrease with increasing metamorphic grade.

4.3 Thermal effects on the distribution of lithophile elements

According to the elemental budgets among the constituent minerals in HCs obtained in this study, the major hosts of specific elements are overall the same between UHCs and EHCs (*e.g.*, merrillite for LREEs and plagioclase for Sr; Figs. 7 and 8). However, the contributions of the unidentified phase(s) to the WR budgets are large for most of the refractory lithophile elements, especially in the case of A-880941 (H3.3), where this/these phase(s) host(s) 30-65% (Fig. 5; Al, Sc, Ba, Y, REEs, HFSEs, Th, and U). These large contributions likely relate to the occurrence of glass mesostasis, enriched in such refractory lithophile elements, as discussed in subsubsection 4.1.1 (Alexander, 1994; Jones and Layne, 1997; Ruzicak *et al*., 2008; Jacquet *et al*., 2015). In addition,

the budgets of the refractory lithophile elements in minerals and the metamorphic grades appear to correlate with each other. For example, the budgets of Sc in Ca-rich pyroxene and those of REEs, except for Eu, in Ca-phosphates increase with increasing metamorphic grade, while those of Hf in plagioclase decrease. These differences in the budgets are in particular remarkable between UHCs and EHCs. In terms of mineralogy, the equilibration of minerals proceeds with increasing metamorphic grade and some minerals, especially secondary minerals such as Ca-phosphates, grow in a closed system during thermal metamorphism in the parent body or bodies (Huss *et al.*, 2006; Maeda e*t al.*, 2021). As such, the minerals are refined during thermal metamorphism, resulting in the release of incompatible elements from specific primary minerals and the absorption of compatible elements into other minerals depending on the partition coefficients. Based on the thermal effects on minerals and the results from a chemical leaching technique applied to UOCs and EOCs by Ebihara (1989) and Shinotsuka and Ebihara (1995), it has been demonstrated that REEs are re-distributed mainly from glass mesostasis to Ca-phosphates in a closed system during thermal metamorphism (Shinotsuka, 1997; Shinotsuka and Ebihara, 1997; Maeda *et al.*, 2021). This re-distribution scenario is entirely consistent with the observations here: A-880941 (H3.3), the least metamorphic sample in this study containing P-rich metals and rare Ca-phosphates (< 0.4 wt.%; Maeda *et al.*, 2021), hosts only ~45% and ~20% of the bulk LREE and HREE budgets in Ca-phosphates and ~30% and 45% of those elements in the unidentified phase(s), *i.e.*, glass mesostasis, respectively. In contrast, EHCs host 80 ± 5% and 55 ± 6% of the LREE and HREE in Ca-phosphates and negligible amounts equivalent to 3.2 ± 2.6% and 3.4 ± 3.2% on average at the 95% confidence interval in the unidentified phase(s). Note that the budgets for the hot desert HCs and A 09516 are excluded from the mean values due to their altered bulk rock values resulting in relatively large budgets for the unidentified phase or phases (Maeda *et al.*, 2021). The re-distribution of REEs from glass mesostasis to Ca-phosphates, especially to merrillite, may also result in higher abundances of Y and REEs, except for Eu, in merrillite of EHCs relative to those of A-880941 (*e.g.*, Y: 292-378 ppm vs. 160 ± 24 ppm, respectively; Supplementary Table 2).

A similar re-distribution scenario should be applied to the other refractory lithophile elements displaying differences in their elemental budgets for minerals between UHCs and EHCs as glass mesostasis concentrates not only REEs but also other refractory lithophile elements. According to the thermal effects on glass mesostasis (Huss *et al.*, 2006), small grains of Ca-rich pyroxene are found in mesostasis and the size of these grains becomes larger during thermal metamorphism. In addition, the crystallization of glass mesostasis proceeds during the thermal metamorphism and glass mesostasis recrystallizes predominantly to plagioclase (Kovach and Jones, 2010). Thus, both Ca-rich pyroxene and plagioclase grow through the recrystallization of glass mesostasis during thermal metamorphism. With growing Ca-rich pyroxene and plagioclase, Sc is re-distributed from glass mesostasis to Ca-rich pyroxene and the budgets of Sr and Ba in plagioclase increase due to the recrystallization of glass mesostasis to plagioclase, which resulted in the increase of the modal abundance of plagioclase instead of glass mesostasis. Although Rb may remain in plagioclase similar to Sr and Ba, its behavior is more complicated because of the existence of K-feldspar hosting Rb next to plagioclase (subsubsection 4.2.3). According to Lewis *et al.* (2022) and Lewis and Jones (2022), K-feldspar in OCs is found most for metamorphic grade 4 specimens, as an exsolution in albite. With increasing metamorphic grade, however, such K-feldspar is less commonly found. Based on such observations, previous studies demonstrated that plagioclase, especially albite, absorbs more K with increasing metamorphic grade due to increased time for Na-K equilibration. Because Rb

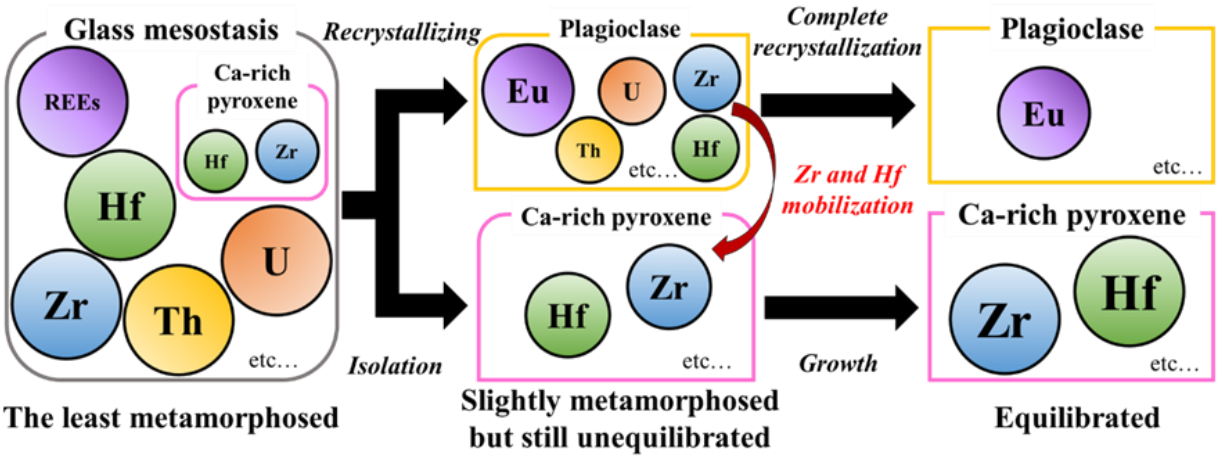

Fig. 10. Re-distribution scenario focusing on HFSEs including Th and U from glass mesostasis to Ca-rich pyroxene via plagioclase.

behaves more similarly to K than Na, therefore, Rb is re-distributed in K-feldspar while remaining in plagioclase to some extent in the case of H3-H5 and most Rb remains in plagioclase in the case of H6 and H7.

In the case of the HFSEs, together with Th and U, their re-distributions are also more convoluted than those of the REEs, as simply illustrated in Fig. 10. In the less metamorphosed samples, these high-valent elements are concentrated in glass mesostasis, with Zr and Hf also in part hosted in small Ca-rich pyroxene grains. As thermal metamorphism proceeds, the glass mesostasis recrystallizes to plagioclase and Ca-rich pyroxene isolates from glass mesostasis. During the early stages of this recrystallization, some lithophile elements concentrated in glass mesostasis, *i.e.*, Sc, Y, and the REEs except for Eu, are re-distributed to their major hosts relatively rapidly. Although the HFSEs, together with Th and U, might also be released from glass mesostasis, a considerable amount of these elements remains in plagioclase following recrystallization, as these high-valent elements are relatively immobile compared with the other elements already re-distributed. This is supported by the observation that the UHC samples display high Hf abundances and large budgets in plagioclase, accompanied by high contributions of Th and U in plagioclase as well (A-880941, Y-793574, and A 09436 except for U). During the recrystallization of plagioclase, Zr and Hf are removed from plagioclase and transferred to Ca-rich pyroxene according to their partition coefficients. The elements Th and U are also removed and transferred to Ca-phosphates but also to cracks and grain boundaries (Shinotsuka and Ebihara, 1997). Once the recrystallization is completed, finally, the high-valent elements that are incompatible in plagioclase have been removed from plagioclase and Ca-rich pyroxene becomes the major host of Zr and Hf in EHCs. As this study demonstrates a continuum in the re-mobilization of refractory lithophile elements during thermal metamorphism, our re-distribution scenario supports a layered shell structure for the OC parent bodies in which internal heating is generated in a closed system (*e.g.*, Miyamoto, 1981).

Note that such elemental re-distributions including the REEs from glass mesostasis are probably not completed yet even in the case of type 4 OCs, which are classified as EOCs, because glass mesostasis is still commonly found in type 4 OCs (*e.g.*, Kovach and Jones, 2010). This is consistent with the interpretation that type 4 OCs represent a transitional stage in the re-distribution of REEs (Shinotsuka and Ebihara, 1997). In the case of Th and U, the re-mobilization of Th and U to cracks and grain boundaries dominates over the re-distribution to Ca-phosphates, as most of the samples display larger budgets in the unidentified phase(s), which may indicate

the involvement of cracks and grain boundaries (Supplementary data-3). In addition, these re-distributions may still reflect a transitional stage in the case of type 5 or even type 6 because the Th and U abundances in chlorapatite of H7 are even higher than those of H6 (5.7 ± 0.1 ppm and 4.3 ± 0.1 ppm vs. 2.5 ± 1.8 ppm and 2.5 ± 1.2 ppm, respectively; Supplementary Table 3) and their budgets in Ca-phosphates of H7 are the largest recorded in this study (Fig. 7 and Supplementary data-3). Therefore, once Th and U are released from plagioclase during the recrystallization, they are re-distributed mainly in cracks and grain boundaries and partly in Ca-phosphates, especially chlorapatite. Subsequently, Th and U are gradually transferred from cracks and grain boundaries to chlorapatite for type 7. Because the EWR value of U in H7 is in excellent agreement with the bulk rock value while that of Th is significantly lower than the bulk rock value, U is more rapidly re-distributed than Th, which is consistent with its higher mobility (*e.g.*, Middelburg *et al.*, 1988). This re-distribution model also implies that Th cannot be equilibrated among the constituent minerals with the conditions of thermal metamorphism in parent bodies of chondrites.

5 CONCLUSIONS

We investigated the distributions of lithophile elements among the constituent minerals in both unequilibrated and equilibrated HCs in a systematic manner. The elemental abundances in and distributions among the constituent minerals in EHCs obtained in this study are overall consistent with previous studies: Sc, Zr, and Hf are concentrated and mainly distributed in Ca-rich pyroxene; Rb, Sr, Ba, and Eu in feldspar; and Y and REEs, except for Eu, in Ca-phosphates, especially in merrillite. Ca-rich pyroxene also accommodates considerable concentrations of Y and HREEs. Although V, Mn, Zn, Nb, and Ta are most concentrated in oxides, more specifically in chromite in the case of V and Zn and in ilmenite in the case of the other elements, V and Zn are mainly distributed in chromite and silicates; Mn in olivine and low-Ca pyroxene; and Nb and Ta possibly in silicates. The distribution of Pb, Th, and U is more complicated: Pb is hosted more in metal and sulfide phases than in the other phases, but the contributions in silicates are not negligible. A considerable amount of Th and U also resides in cracks and grain boundaries although they are concentrated and fairly distributed in Ca-phosphates. However, a remarkable difference in the elemental distributions between UHCs and EHCs is observed due to the incomplete equilibration of minerals and the existence of glass mesostasis in chondrules. The contribution of glass mesostasis to the WR budgets of lithophile elements is large in particular in the case of less metamorphosed samples. The re-distributions of lithophile elements must thus have occurred in a closed system during thermal metamorphism in the parent body(ies) accompanied by the recrystallization of glass mesostasis. As such, Sc and REEs including Y, but not Eu, were re-distributed from glass mesostasis to Ca-rich pyroxene and Ca-phosphates, respectively, while Rb, Sr, Ba, and Eu fundamentally remained in plagioclase during the recrystallization of glass mesostasis. The elements Zr, Hf, Th, and U were also re-distributed from glass mesostasis, but more gradually than Sc and REEs because of their limited mobility. Therefore, a considerable amount of these elements remained in plagioclase during the recrystallization while a large portion of Sc and the REEs was already re-distributed. The elements Zr and Hf were completely re-distributed to Ca-rich pyroxene and Th and U migrated to Ca-phosphates, cracks, and grain boundaries. As L and LL chondrites share similarities with HCs in terms of chemistry, petrology, and mineralogy, this re-distribution scenario can be

applied to all groups of OCs and supports an onion shell-type internal structure for the OC parent bodies. However, the extent of the distributions among the constituent minerals, *i.e.*, the exact budgets in the constituent minerals should be distinct for H, L, and LL chondrites.

SUPPLEMENTARY MATERIAL

Supplementary data to this article can be found online at https://vub-my.sharepoint.com/:f:/g/personal/ryoga_maeda_vub_be/EqwAm_k7CFZHp0BTrDKqaqABoSepq5xlSXgNU_W-Vx46Kw?e=uKB4jq until 26 August 2023 (Password: phdthesis_rm). Otherwise, these can be requested digitally from the author.

Acknowledgments

We would like to thank the Royal Belgian Institute of Natural Sciences, Belgium, and the National Institute of Polar Research, Japan, for the loan of the Antarctic meteorites, meteorites collected from hot deserts, and the fall meteorites used in this study. RM thanks NIPR International Internship Programs for Polar Science 2020 and 2021 for financial and analytical support. RM, SG, FV, VD, and PhC acknowledge support from the Excellence of Science (EoS) project "ET-HoME". SG and VD thank the BRAIN-Be Belgian Science Policy (BELSPO) projects "BAMM" and "DESIRED". SG and PhC acknowledge support from the VUB Strategic Research Program. TVA thanks Research Foundation – Flanders (FWO) for his junior postdoctoral fellowship grant (FWO.3E0.2022.0048.01). FV thanks BOF-UGent for financial support under the form of a GOA grant and acknowledges Teledyne Photon Machines for logistic support. VD thanks the ERC StG ISoSyC and FRS-FNRS for support. PhC thanks the Research Foundation Flanders (FWO Hercules grant) for the purchase of the μXRF instrument. We specifically would like to thank C. M.O'D. Alexander and M. R. Lee for their constructive comments on an earlier version of this manuscript.

REFERENCES

Alexander C.M.O'D. (1994) Trace element distributions within ordinary chondrite chondrules: Implications for chondrule formation conditions and precursors. *Geochim. Cosmochim. Acta* **58**, 3451-3467.

Al-Kathiri A., Hofmann B.A., Jull J.T. and Gnos E. (2005) Weathering of meteorites from Oman: Correlation of chemical and mineralogical weathering proxies with ^{14}C terrestrial ages and the influence of soil chemistry. *Meteorit. Planet. Sci.* **40**, 1215-1239.

Allen Jr. R.O. and Mason B. (1973) Minor and trace elements in some meteoritic minerals. *Geochim. Cosmochim. Acta* **37**, 1435-1456.

Anders E. and Grevesse N. (1989) Abundances of the elements: Meteoritic and solar. *Geochim. Cosmochim. Acta* **53**, 197-214.

Barrat J.A., Zanda B., Jambon A. and Bollinger C. (2014) The lithophile trace elements in enstatite chondrites. *Geochim. Cosmochim. Acta* **128**, 71-94.

Bédard J.H. (2006) Trace element partitioning in plagioclase feldspar. *Geochim. Cosmochim. Acta* **70**, 3717-3742.

Bindeman I.N. and Davis A.M. (2000) Trace element partitioning between plagioclase and melt: Investigation of dopant influence on partition behavior. *Geochim. Cosmochim. Acta* **64**, 2863-2878.

Bouvier A., Vervoort J.D. and Patchett P.J. (2008) The Lu–Hf and Sm–Nd isotopic composition of CHUR: Constraints from unequilibrated chondrites and implications for the bulk composition of terrestrial planets. *Earth Planet. Sci. Lett.* **273**, 48-57.

Chakhmouradian A.R. (2006) High-field-strength elements in carbonatitic rocks: Geochemistry, crystal chemistry and significance for constraining the sources of carbonatites. *Chem. Geol.* **235**, 138-160.

Curtis D.B. and Schmitt R.A. (1979) The petrogenesis of L-6 chondrites: insights from the chemistry of minerals. *Geochim. Cosmochim. Acta* **43**, 1091-1103.

Dauphas N. and Pourmand A. (2015) Thulium anomalies and rare earth element patterns in meteorites and Earth: Nebular fractionation and the nugget effect. *Geochim. Cosmochim. Acta* **163**, 234-261.

Davis A.M. (2006) Volatile evolution and loss. In *Meteorites and the Early Solar System II* (eds. Lauretta D.S. and McSween Jr. H.Y.). The University of Arizona Press, Tucson, pp. 295-307. in collaboration with Lunar and Planetary Institute, Houston.

Dunn T.L., Cressey G., McSween Jr H.Y. and McCoy T.J. (2010) Analysis of ordinary chondrites using powder X-ray diffraction: 1. Modal mineral abundances. *Meteorit. Planet. Sci.* **45**, 123-134.

Ebihara M. (1989) Rare earth and some other elements in acid-residues od unequilibrated ordinary chondrites. *Proc. NIPR Symp. Antract. Meteorites* **2**, 279-287.

Ebihara M. and Honda M. (1984) Distribution of rare earth elements and uranium in various components of ordinary chondrites. *Meteoritics* **19**, 69-77.

Ebihara M. and Honda M. (1987) Rare earth elements in Ca-phosphates of Allende carbonaceous chondrite. *Meteoritics* **3**, 179-190.

El Goresy A., Zinner E., Matsunami S., Palme H., Spettel B., Lin Y. and Nazarov M. (2002) Efremovka 101.1: a CAI with ultrarefractory REE patterns and enormous enrichments of Sc, Zr, and Y in Fassaite and Perovskite. *Geochim. Cosmochim. Acta* **66**, 1459-1491.

Green T.H. (1994) Experimental studies of trace-element partitioning applicable to igneous petrogenesis — Sedona 16 years later. *Chem. Geol.* **117**, 1-36.

Hewins R.H., Connolly H.C., Lofgren G.E. and Libourel G. (2005) Experimental constraints on chondrule formation. In *Chondrites and the Protoplanetary Disk* (eds. A.N. Krot, E.R.D. Scott and B. Reipurth). Astronomical Society of the Pacific, San Francisco, pp. 286–316.

Hezel D.C., Russell S.S., Ross A.J. and Kearsley A.T. (2008) Modal abundances of CAIs: Implications for bulk chondrite element abundances and fractionations. *Meteorit. Planet. Sci.* **43**, 1879-1894.

Huss G.R., Rubin A.E. and Grossman J.N. (2006) Thermal metamorphism in chondrites. In *Meteorites and the Early Solar System II* (eds. Lauretta D.S. and McSween Jr. H.Y.). The University of Arizona Press, Tucson, pp. 567-586. in collaboration with Lunar and Planetary Institute, Houston.

Jacquet E., Alard O. and Gounelle M. (2015) Trace element geochemistry of ordinary chondrite chondrules: The type I/type II chondrule dichotomy. *Geochim. Cosmochim. Acta* **155**, 47-67.

Jarosewich E. (1990) Chemical analyses of meteorites: A compilation of stony and iron meteorite analyses. *Meteoritics* **25**, 323-337.

Jones J.H. and Burnett D.S. (1979) The distribution of U and Pu in the St. Severin chondrite. *Geochim. Cosmochim. Acta* **43**, 1895-1905.

Jones R.H. and Layne G.D. (1997) Minor and trace element partitioning between pyroxene and melt in rapidly cooled chondrules. *American Mineralogist* **82**, 534-545.

Kallemeyn G.W., Rubin A.E., Wang D. and Wasson J.T. (1989) Ordinary chondrites: Bulk compositions, classification, lithophile-element fractionations, and composition-petrographic type relationships. *Geochim. Cosmochim. Acta* **53**, 2747-2767.

Kovach H.A. and Jones R.H. (2010) Feldspar in type 4–6 ordinary chondrites: Metamorphic processing on the H and LL chondrite parent bodies. *Meteorit. Planet. Sci.* **45**, 246-264.

Krot A.N., Keil K., Scott E.R.D., Goodrich C.A. and Weisberg M.K. (2003) Classification of meteorites. In *Meteorites, Comets, and Planets*, Treatise on Geochemistry (ed. Davis A.M.). Elsevier, Amsterdam, vol. 1, chap. 1.05, pp. 83-128.

Larimer J.W. and Ganapathy R. (1987) The trace element chemistry of CaS in enstatite chondrites and some implications regarding its origin. *Earth and Planet. Sci. Lett.* **84**, 123-134.

Lewis J.A. and Jones R.H. (2022) Exsolution in alkali feldspar in ordinary chondrites: Ubiquitous evidence for rapid cooling at high temperatures. *Geochim. Cosmochim. Acta* **321**, 293-310.

Lewis J.A., Jones R.H. and Brearley A.J. (2022) Plagioclase alteration and equilibration in ordinary chondrites: Metasomatism during thermal metamorphism. *Geochim. Cosmochim. Acta* **316**, 201-229.

Maeda R., Goderis S., Debaille V., Pourkhorsandi H., Hublet G. and Claeys P. (2021) The effects of Antarctic alteration and sample heterogeneity on Sm-Nd and Lu-Hf systematics in H chondrites. *Geochim. Cosmochim. Acta* **305**, 106-129.

Maeda R., Van Acker T., Vanhaecke F., Yamaguchi A., Debaille V., Claeys P. and Goderis S. (2023a) Quantitative elemental maps of chondritic meteorite samples using Laser Ablation-Inductively Coupled Plasma-

Time of Flight-Mass Spectrometry (LA-ICP-TOF-MS). *J. Anal. At. Spectrom.* **38**, 369-381.

Maeda R., Goderis S., Yamaguchi A., Van Acker T., Vanhaecke F., Debaille V. and Claeys P. (2023b) Fluid mobilization of rare earth elements (REEs), Th, and U during terrestrial alteration of chondrites. *Meteorit. Planet. Sci.* (accepted).

Martin C., Debaille V., Lanari P., Goderis S., Vandendael I., Vanhaecke F., Vidal O. and Claeys P. (2013) REE and Hf distribution among mineral phases in the CV–CK clan: A way to explain present-day Hf isotopic variations in chondrites. *Geochim. Cosmochim. Acta* **120**, 496-513.

Mason B. and Graham A.L. (1970) Minor and trace elements in meteoritic minerals. *Smithson. Contrib. Earth Sci.* **3**, 1-17.

McIntire W.L. (1963) Trace element partition coefficients—a review of theory and applocations to geology. *Geochim. Cosmochim. Acta* **27**, 1209-1264.

McSween Jr. H.Y., Bennett III M.E. and Jarosewich E. (1991) The mineralogy of ordinary chondrites and implications for asteroid spectroscopy. *Icarus* **90**, 107-116.

Middelburg J.J., van der Weijden C.H. and Woittiez J.R.W. (1988) Chemical processes affecting the mobility of major, minor and trace elements during weathering of granitic rocks. *Chem. Geol.* **68**, 253-273.

Miyamoto M. Fujii N. and Takeda H. (1981) Ordinary chondrite parent body: An internal heating model. *Proc. Lunar Planet. Sci.* **12**, 1145-1152.

Nielsen R.L., Ustunisik G., Weinsteiger A.B., Tepley III F.J., Johnston A.D. and Kent A.J. (2017) Trace element partitioning between plagioclase and melt: An investigation of the impact of experimental and analytical procedures. *Geochem. Geophys. Geosyst.* **18**, 3359-3384.

Ruzicka A., Floss C. and Hutson M. (2008) Relict olivine grains, chondrule recycling, and implications for the chemical, thermal, and mechanical processing of nebular materials. *Geochim. Cosmochim. Acta* **72**, 5530–5557.

Schaefer L. and Fegley Jr. B. (2010) Volatile element chemistry during metamorphism of ordinary chondritic material and some of its implications for the composition of asteroids. *Icarus* **205**, 483-496.

Shannon R.D. (1976) Revised effective ionic radii and systematic studies of interatomic distances in halides and chalcogenides. *Acta Cryst.* **A32**, 751-767.

Shinotsuka K. (1997) Abundances of rare earth elements, thorium and uranium in chondritic meteorites. Ph. D. Thesis, Tokyo Metropolitan University, Tokyo, Japan. DOI: 10.11501/3126008.

Shinotsuka K. and Ebihara M. (1995) A metamorphic sequence of ordinary chondrites based on the distribution of REE, Th and U. In *Lunar Plant. Sci.* **XXVI**, 1293-1294. Lunar and Planetary Institute, Houston (abstract).

Shinotsuka K. and Ebihara M. (1997) Migrational behaviors of rare-earth elements and actinoides during

thermal metamorphism of ordinary chondrites. *Meteorit. Planet. Sci.* **32**, A119-120.

Van Acker T., Van Malderen S.J.M., Van Helden T., Stremtan C., Šala M., van Elteren J.T. and Vanhaecke F. (2021) Analytical figures of merit of a low-dispersion aerosol transport system for high-throughput LA-ICP-MS analysis. *J. Anal. At. Spectrom.* **36**, 1201-1209.

Van Schmus W.R. (1969) The mineralogy and petrology of chondritic meteorites. *Earth Sci. Rev.* **5**, 145-184.

Wasson J.T. and Kallemeyn G.W. (1988) Compositions of chondrites. *Philos. Trans. R. Soc. Lond.*, A **325**, 535-544.

Chapter 6 "*Conclusions and future outlook of this research*"

Summary and Conclusions

In this PhD project, HCs displaying various metamorphic degrees from 3.3 to 7 as well as of different origins, falls and finds from cold and hot deserts, have been characterized in a comprehensive manner. This research supports the usefulness of Antarctic meteorites in this context, especially to improve our understanding of the effects of terrestrial alteration and thermal processing on the element distributions, with important consequences on isotope systematics, for example on the Sm-Nd and Lu-Hf systems in bulk chondrites. The five following considerations can be highlighted as the summary and conclusions of my PhD research.

(I) When we applied LA-ICP-TOF-MS mapping to our samples, a deposition of REEs, Th, and U in cracks was observed in weathered samples, providing important information regarding the underlying mechanism of terrestrial alteration. As a result of the detailed investigation of cracks in HCs using LA-ICP-SF-MS, **Chapter 4** highlights two remarkable features in cracks: the enrichments in unbound REEs, Th, and U, and the enrichment in Ce only. This observation demonstrates that the elemental mobilization occurred as a result of partial dissolution of Ca-phosphate phases taking place when fluids pass through the meteorite interiors during terrestrial weathering. The deposition of unbound REEs represents a transitional stage in the alteration sequence, while the positive Ce anomalies represent a later stage. However, the underlying mechanism of terrestrial alteration fundamentally occurs at the local scale only. **Chapter 2** demonstrates that the elemental and isotopic compositions in bulk Antarctic HCs appear generally unaffected even though the corresponding polished thick sections exhibit localized element mobilization and re-deposition. This confirms the utility of Antarctic meteorites even for radiogenic age determination, for example relying on the Sm-Nd and Lu-Hf systems. In the case that the partial dissolution of Ca-phosphate phases by fluids during terrestrial weathering was extensive, both the elemental and isotopic compositions of the sample are modified, in some cases accompanied by severe mineralogical alteration.

(II) In **Chapter 5**, the distributions of lithophile elements among the constituent minerals in UHCs and EHCs according to their metamorphic grades were studied in a systematic manner, mainly based on "well-preserved" Antarctic HCs. Overall, the elemental distributions in EHCs obtained in this work confirmed and refined those obtained in previous studies: *e.g.*, Y and REEs, except for Eu, are mainly hosted in Ca-phosphates, and Rb, Sr, Ba, and Eu in feldspar. As a resolvable difference is observed in the elemental distributions between UHCs and EHCs for many elements, this work contributes to understanding the geochemical evolution from UHCs to EHCs. Due to the growth of the constituent minerals in HCs during thermal metamorphism in the parent body(ies), the contribution of glass mesostasis in chondrules must be considered for the lithophile element distributions in the case of less metamorphosed samples. The glass mesostasis can host nearly half of the WR budgets of many lithophile elements, especially refractory lithophile elements (*e.g.*, Sc, REEs, and U). As a result of the occurrence and the recrystallizing of glass mesostasis during thermal metamorphism, re-distributions of lithophile elements must have occurred: *e.g.*, Sc and the REEs including Y (but excepting

Eu) are re-distributed from glass mesostasis to Ca-rich pyroxene and Ca-phosphates, respectively. The re-distributions of elements with a high-valence state such as Hf and U are more complicated, but they eventually migrated to their main host phase(s).

(III) This re-distribution scenario suggested in **Chapter 5** is entirely consistent with what we expected and discussed for the heterogeneity of the Sm-Nd and Lu-Hf systems in **Chapter 2**. The REEs and Hf are re-distributed from glass mesostasis to Ca-phosphates and Ca-rich pyroxene, respectively, resulting in larger nugget effects of these minerals in EOCs, especially in the case of Ca-phosphates due to their low modal abundances. As these two minerals are largely responsible for the Sm-Nd and Lu-Hf systems in bulk OCs, the use of EOCs displaying such larger nugget effects strengthens the scatter of the bulk Sm-Nd and Lu-Hf data. A similar influence may be observed for other radiogenic isotope systems related to lithophile elements such as Rb-Sr, Hf-W, and U-Th. Therefore, the use of UOCs should be preferred for the determination of well-constrained average isotopic compositions, such as CHUR values.

(IV) In **Chapters 2 and 4**, we quantitatively evaluated the weathering degree of samples on both bulk and PTSs using the Rb indicator and comprehensive petrographic observations, respectively. As described in these chapters, the classical ABC index system for Antarctic meteorites is largely subjective and more qualitative than the W0-W6 scale. In addition, terrestrial weathering may affect a sample in a heterogeneous manner, resulting in one fragment of the sample being heavily altered but another not to the same degree. As such, it is always ideal to quantitatively evaluate the weathering degrees of samples even though their ABC index or weathering degree has been evaluated in previous studies, especially when comparing their quantitative data with the weathering degrees. Moreover, because previous studies focusing on the weathering evaluation demonstrated to what degree a chondrite is affected by weathering depends on the group and that such an evaluation should be distinct for each group (*e.g.*, Ikeda and Kojima, 1991; Rubin and Huber, 2005), we must be careful when quantitatively comparing or determining the weathering degrees between different groups, even within the OCs.

(V) The potential of LA-ICP-TOF-MS for semi-quantitative elemental mapping is explained in **Chapter 3**. Compared with other more conventional mapping approaches applying EPMA, SEM-EDS, and μXRF, the strongest advantage of LA-ICP-TOF-MS mapping is the capability to detect nearly the entire elemental mass spectrum with a fast lateral scan speed (200 pixel/s), low LODs (a few ppm-hundreds of ppb level), and a high spatial resolution (5×5 μm) in a semi-quantitative manner. In terms of quantitative ability, the fast LA-ICP-TOF-MS mapping determines the major and trace element abundances in their primary host phase(s) with an accuracy approaching that of conventional spot analysis such as LA-ICP-SF-MS spot analysis. Moreover, no ablation effects in the regions studied using LA-ICP-TOF-MS mapping are observed on the BSE imaging, EPMA, and LA-spot analysis as only one shot per pixel was fired due to the fast mapping. Thus, LA-ICP-TOF-MS mapping constitutes a great screening tool for particular and precious geological samples, providing semi-quantitative information of elemental distributions including trace elements on such samples, and then a spot drilling approach can be applied to specific minerals of interest to obtain fully quantitative

information.

This work analyzed HCs only, but the conclusions obtained can be applied in a similar manner to other geological samples, especially meteorite samples: consideration (I) applies to Antarctic meteorites in general, consideration (II) is applicable to all groups of OCs, consideration (III) is relevant to all of the chondrite groups that underwent thermal metamorphism in their parent bodies, consideration (IV) is applicable to all meteorite finds, and consideration (V) applies to geological samples in general. And finally, answering the very first question addressed in the first page of this thesis "do we need a time machine to reveal the history of our Solar System?",

-YES

because meteorites can be considered time machines that deliver us to the early Solar System. As this PhD thesis demonstrates, we cannot drastically but only gradually reveal the formation and evolution of the Solar System using precious meteorite samples. However, if we could use a "real" time machine, quickly revealing its history, …although this could make us scientists lose our infinite passion for research.

Future outlook

The elemental distributions in chondrites

As described in **Chapter 1**, elements can be classified into lithophile and siderophile/chalcophile, in which their distributions are completely distinct in a chondrite. While the present studies reveal the distribution of lithophile elements in OCs, those of most siderophile/chalcophile elements have not been discussed. As these elements partition into metal and sulfide phases and the number of those phases in chondrites is commonly limited (*e.g.*, kamacite, taenite, and troilite in the case of OCs), it is expected that siderophile/chalcophile elements are mainly distributed in these phases only. In addition, some previous studies have already demonstrated their distributions in OCs, ECs, and CR chondrites and the thermal effects on them in the cases of OCs and ECs (Kong and Ebihara, 1997; Kong *et al.*, 1997, 1999). However, as they used a physical magnet separation, for example, their distributions between kamacite and taenite in OCs remain poorly understood. As such we can still contribute to the distributions of siderophile/chalcophile elements as the siderophile/chalcophile and several lithophile element abundances in kamacite and taenite for the same set of HCs as this PhD thesis have been already determined using LA-spot analysis at NIPR (quantified elements: Si, P, S, Ca, Cr, Fe, Co, Ni, Cu, Zn, Ga, Ge, As, Mo, Ru, Rh, Pd, Hf, W, Re, Os, Ir, Pt, Au, and Pb). In this case, additional measurements may be required to obtain the bulk siderophile/chalcophile abundances as we combined *in-situ* and bulk data for the distributions of lithophile elements. It would also be interesting to investigate the distributions of siderophile/chalcophile elements in the metallic-Fe-Ni-poor chondrite groups such as R chondrite and several groups of carbonaceous chondrites because of the lack of their metal phases and various other sulfide phases, but then first LA-spot analysis for sulfide phase needs to be developed.

The lithophile element distributions and the effects of the parent body process on the distribution in the chondrite groups that underwent thermal metamorphism (OCs, ECs, CK chondrites, and R chondrites) have fundamentally been documented in detail (**Chapter 5**; Martin *et al.*, 2013; Barrat *et al.*, 2014; Maeda *et al.*,

2017a, 2017b). On the other hand, the elemental distributions in the carbonaceous chondrite groups that underwent aqueous alteration in the parent bodies remain poorly understood. The elemental abundances and the Sm-Nd (both ^{147}Sm-^{143}Nd and ^{146}Sm-^{142}Nd) and Lu-Hf isotopic compositions in bulk CM chondrites have been determined at ULB, and the major element maps and the major element compositions in minerals of the CM chondrites have been obtained at NIPR. Hence, the investigation of the distribution in aqueously altered samples using CM chondrites can be initiated, as they also are the most abundant among the carbonaceous chondrite groups (Meteoritical Bulletin Database). However, we analyzed only four samples (A 09474, A 10014, A 12236, and Jbilet Winselwan) and one of them (A 09474) does not appear to be a CM chondrite but rather an L or LL chondrite based on the obtained results (yet as it is significantly less metamorphosed, another interesting sample!); hence more CM chondrites should be analyzed (ideally more than one of CM1 and CM2). Moreover, CM chondrites consist of significantly more matrix than OCs (~70 vol.% vs. 10-15 vol.%; Krot *et al.*, 2003) and their mineral grains contain many inclusions. Thus, LA-spot analysis for CM chondrites would be much more challenging than for OCs, indicating that we need to adjust the experimental conditions for LA-spot analysis to dedicate those to CM chondrites prior to measurement. Alternatively, the use of SIMS is another option for the CM chondrite analysis due to their lower LODs and higher spatial resolution than LA-ICP-SF-MS, although this prevents us from analyzing the entire suite of lithophile elements (*e.g.*, **Chapter 3**). LA-ICP-TOF-MS mapping may assist in revealing their distributions instead of struggling with spot analysis.

Sm-Nd and Lu-Hf isotopic compositions in Ca-phosphates of UHCs and EHCs

This PhD thesis emphasizes the re-distribution of REEs from glass mesostasis to Ca-phosphates in **Chapters 2 and 5**. As the re-distribution occurred in a closed system, their bulk Sm-Nd and Lu-Hf isotopic compositions remain the same between UHCs and EHCs. However, if we focused on a specific mineral, we may observe a trace of the re-distribution, *i.e.*, different isotopic compositions in the mineral between UHCs and EHCs. This has been suggested by Debaille *et al.* (2017) based on their diffusion model focusing on the Sm-Nd and Lu-Hf data in the silicate and Ca-phosphate phases of chondrites, with particular attention to Ca-phosphates. Yet, no study has been conducted focusing on the Sm-Nd and Lu-Hf isotopic compositions in bulk Ca-phosphates from unequilibrated samples to equilibrated samples in a systematic manner. As such, it would be interesting to apply physical mineral separation to the same set of HCs examined in this PhD thesis and then to analyze the Sm-Nd and Lu-Hf isotopic data in their bulk Ca-phosphates. Ideally, I would also like to obtain these data for bulk Ca-rich pyroxene, and at least 1 g of a sample is required for the mineral separation of bulk Ca-phosphates and the following isotope measurement in any case, which is a sufficient amount to obtain the data for bulk Ca-rich pyroxene as well. However, because the mineral grains in UHCs are generally smaller and contain more inclusions than those in EHCs, it would be challenging to separate pure Ca-phosphate grains in the case of UHCs. Probably, *in-situ* isotope measurement such as LA-MC-ICP-MS and LA-ICP-QQQ-MS is a more ideal way forward, at least in the case of UHCs (*e.g.*, Glorie *et al.*, 2022).

Further analytical development of LA-ICP-TOF-MS mapping

In **Chapter 3**, we demonstrate how fast LA-ICP-TOF-MS can be used to map relatively large sample area at 200 pixel/s with a high spatial resolution at 5×5 µm. However, the current scan speed is not optimal and our A&MS colleagues at Ghent University have been attempting to increase the laser repetition rate up to 1000 Hz

(Van Acker, 2023). As long as we can maintain the other experimental conditions such as the LODs and the spatial resolution, why should we not aim for a higher scan speed for the mapping? So far, no significant issues, such as losses in ionization efficiency, have not been observed at higher laser repetition rates. Thibaut Van Acker in the A&MS team led this work, but I include it here as one of my future aims, because we will apply this kHz mapping to Antarctic chondrites (a selection of examples from our chondrite set) and **Chapter 3** in this thesis largely relates to the kHz study. This state-of-the-art development could also contribute to the investigation of the elemental distribution in CM chondrites as described above.

Scientific contributions outside of this thesis

During my PhD research, I also contributed to other studies only distally related to the topics addressed in this thesis. One of the main outputs of such contributions so far is a study regarding an Antarctic micrometeorite that is isotopically anomalous in oxygen published in Soens *et al.* (2020), for which I have been included as a co-author. I determined the major and minor elemental compositions in the constituent phases of the micrometeorite using the EPMA at NIPR, and contributed to the overall interpretations in the paper. As such, I have also contributed to other micrometeorite studies being carried out by Flore Van Maldeghem in the AMGC team and Matthias van Ginneken at the University of Kent as similar EPMA analyses were conducted by me. These studies have been published in part as conference abstracts (Van Maldeghem *et al.*, 2022; van Ginneken *et al.*, 2022). I will also contribute to the interpretation in the respective future full articles.

During the NIPR International Internship Program for Polar Science 2021, I collaborated on two projects: one on the determination of trace lithophile element abundances in fine-grained portions of Juvinas, an eucrite, and the other on a comprehensive investigation of LL7 chondrites. The former study focuses on the trace lithophile element abundances, especially REEs, in fine-grained portions of Juvinas which are interpreted to have formed by partial melting (Takeda and Yamaguchi, 1991). This research is a part of the PhD thesis completed by Rei Kanemaru at NIPR (Kanemaru, 2021; my contribution is mainly included on pp. 141-144). In this dissertation, their elemental abundances were determined in segmented line scan mode using LA-ICP-SF-MS, which was mostly led by me, including the optimization of the experimental strategy. This contribution together with my assistance in the interpretation will be included in an article in the near future. In the other ongoing study, LL7 chondrites were characterized in terms of their chemical composition. This study has been led by Mitsuru Ebihara at Waseda University, and in part also conducted as a bachelor's thesis at Waseda University (Jun Sakuma, 2021). Fundamentally, the same experimental procedure as that described in **Chapter 5** without LA-ICP-TOF-MS mapping was applied to four LL7 chondrites and the trace elemental abundances in the constituent minerals, *i.e.*, Ca-phosphate and silicate phases, were determined using LA-spot analysis. I conducted the experimental procedure. According to the petrographic observation, not all samples seem to be actual type 7 based on the definition of type 7 which should be a part of the continuum of thermal metamorphism without evidence for shock melting or partial melting (*e.g.*, Kimura *et al.*, 2014). Yet, these non-type 7 samples appear to have been formed by an impact, providing us with a unique opportunity to study the difference in the elemental abundances between type 7 samples and impact-induced samples. Although the translation of this study into a journal article will take time because not even the data reduction has been done yet, I may be able to lead this study to publication.

References

Barrat J.A., Zanda B., Jambon A. and Bollinger C. (2014) The lithophile trace elements in enstatite chondrites. *Geochim. Cosmochim. Acta* **128**, 71-94.

Debaille V., Orman J.V., Yin Q.Z. and Amelin Y. (2017) The role of phosphates for the Lu–Hf chronology of meteorites. *Earth Planet. Sci. Lett.* **473**, 52-61.

Glorie S., Burke T., Hand M., Simpson A., Gilbert S., and Wade B. (2022) *In situ* Lu–Hf phosphate geochronology: Progress towards a new tool for space exploration. *Geoscience Frontiers* **13**, 101375.

Ikeda Y. and Kojima H. (1991) Terrestrial alteration of Fe-Ni metals in Antarctic ordinary chondrites and the relationship to their terrestrial ages. *Proc. NIPR Symp. Antract. Meteorites* **4**, 307-318.

Kanemaru R. (2021) Mineralogy of eucrite meteorites: the thermal and shock history of protoplanetary crusts. Ph. D. Thesis, The Graduate University for Advanced Studies (SOKENDAI), Tokyo, Japan. Link: id.nii.ac.jp/1013/00006145/

Kimura M., Yamaguchi A. and Friedrich J. (2014) Classification and petrologic features of chondrites of petrologic type 7. In *Japan Geosci. Union Met. 2014*, Japan Geosci. Union, Tokyo (abstract).

Kong P. and Ebihara M. (1997) The origin and nebular history of the metal phase of ordinary chondrites. *Geochim. Cosmochim. Acta* **61**, 2317-2329.

Kong P., Mori T. and Ebihara M. (1997) Compositional continuity of enstatite chondrites and implications for heterogeneous accretion of the enstatite chondrite parent body. *Geochim. Cosmochim. Acta* **61**, 4895-4914.

Kong P., Ebihara M. and Palme H. (1999) Distribution of siderophile elements in CR chondrites: Evidence for evaporation and recondensation during chondrule formation. *Geochim. Cosmochim. Acta* **63**, 2637-2652.

Krot A.N., Keil K., Scott E.R.D., Goodrich C.A. and Weisberg M.K. (2003) Classification of meteorites. In *Meteorites, Comets, and Planets*, Treatise on Geochemistry (ed. Davis A.M.). Elsevier, Amsterdam, vol. 1, chap. 1.05, pp. 83-128.

Maeda R., Shirai N. and Ebihara M. (2017a) Distribution of rare earth elements, Th and U in R chondrite. In *Lunar Plant. Sci.* **XLVIII**, #2370. Lunar and Planetary Institute, Houston (abstract).

Maeda R., Shirai N., Yamaguchi A. and Ebihara M. (2017b) Formation process and metamorphism on R chondrite parent body based on distribution of rare earth elements, Th and U. In *The Eighth Symposium on Polar Science*, #00258. National Institute of Polar Research, Tokyo (abstract).

Martin C., Debaille V., Lanari P., Goderis S., Vandendael I., Vanhaecke F., Vidal O. and Claeys P. (2013) REE and Hf distribution among mineral phases in the CV–CK clan: A way to explain present-day Hf isotopic variations in chondrites. *Geochim. Cosmochim. Acta* **120**, 496-513.

Rubin A.E. and Huber H. (2005) A weathering index for CK and R chondrites. *Meteorit. Planet. Sci.* **40**, 1123-1130.

Soens B., Suttle M.D., Maeda R., Vanhaecke F., Yamaguchi A., van Ginneken M., Debaille V., Claeys P. and Goderis S. (2020) Evidence for the presence of chondrule- and CAI-derived material in an isotopically anomalous Antarctic micrometeorite. *Meteorit. Planet. Sci*. **55**, 2703-2726.

Takeda H. and Yamaguchi A. (1991) Recrystallization and shock textures of old and new samples of Juvinas in relation to its thermal history. In the 54th Ann. Mtg. Met. Soc., p. 228. LPI Contribution No. 766, Lunar and Planetary Institute, Houston (abstract).

Van Acker T., Maeda R., Van Helden T., Van Malderen S.J.M., Goderis S. and Vanhaecke F. (2023: expected) Pushing the limits of elemental mapping via laser ablation – ICP-mass spectrometry with a nanosecond 193 nm kHz laser. In *European Winter Conference on Plasma Spectrochemistry 2023*, Ljubljana, Slovenia (abstract).

van Ginneken M., Goderis S., Maeda R., Wozniakiewicz P., Genge M., Folco L., Suttle M.D., Yamaguchi A. and Decrée S. (2022) A potential origin for ^{16}O-poor cosmic spherules: a near-Earth source and parentage with CY chondrites. In *Lunar Plant. Sci.* **LIII**, #2491. Lunar and Planetary Institute, Houston (abstract).

Van Maldeghem F., Soens B., van Ginneken M., Maeda R., Cordier C., Suttle M.D., Yamaguchi A., Claeys P. and Goderis S. (2022) Chromites in cosmic spherules: a unique perspective on the extraterrestrial flux to earth. In *the 85th Ann. Mtg. Met. Soc., #6267. LPI Contribution No. 2695, Lunar and Planetary Institute, Houston (abstract)*.

Addendum – List of publications

The following is a list of all scientific publications including conference abstracts, completed during my PhD duration.

International peer-reviewed articles (including submitted manuscripts)

1. Bastien Soens, Martin D. Suttle, **Ryoga Maeda**, Frank Vanhaecke, Akira Yamaguchi, Matthias van Ginneken, Vinciane Debaille, Philippe Claeys and Steven Goderis (2020) Evidence for the presence of chondrule- and CAI-derived material in an isotopically anomalous Antarctic micrometeorite. *Meteoritics & Planetary Science* **55** (12), 2703-2726. DOI: 10.1111/maps.13599.

2. **Ryoga Maeda**, Steven Goderis, Vinciane Debaille, Hamed Pourkhorsandi, Geneviève Hublet and Philippe Claeys (2021) The effects of Antarctic alteration and sample heterogeneity on Sm-Nd and Lu-Hf systematics in H chondrites. *Geochimica et Cosmochimica Acta* **305**, 106–129. DOI: 10.1016/j.gca.2021.05.005.

3. **Ryoga Maeda**, Thibaut Van Acker, Frank Vanhaecke, Akira Yamaguchi, Vinciane Debaille, Phillippe Claeys and Steven Goderis (2023) Quantitative elemental mapping of chondritic meteorites using Laser Ablation-Inductively Coupled Plasma-Time of Flight-Mass Spectrometry (LA-ICP-TOF-MS). *Journal of Analytical Atomic Spectrometry* **38**, 369-381. DOI: 10.1039/d2ja00317a.

4. **Ryoga Maeda**, Steven Goderis, Akira Yamaguchi, Thibaut Van Acker, Frank Vanhaecke, Vinciane Debaille and Phillippe Claeys (2023) Fluid mobilization of rare earth elements (REEs), Th, and U during the terrestrial alteration of chondrites. *Meteoritics & Planetary Science* (accepted).

5. **Ryoga Maeda**, Steven Goderis, Akira Yamaguchi, Thibaut Van Acker, Frank Vanhaecke, Vinciane Debaille and Phillippe Claeys (2023: expected) The distributions of lithophile elements and their re-mobilization during thermal metamorphism in the H chondrite parent body(ies). *Geochimica et Cosmochimica Acta* (submitted).

6. Vinciane Debaille, Maria Schönbächler, Maria Valdes, **Ryoga Maeda**, Steven Goderis, Philipp Heck, Manu Poudelet and Philippe Claeys (2023: expected) Detailed record of the BELARE 2022-2023 meteorite recovery expedition in the Sør Rondane area, East Antarctica. *Antarctic Record* (expected to be submitted shortly after the submission of this thesis).

Scientific report

1. Akira Yamaguchi, Naoki Shirai, Makoto Kimura, Naoya Imae, Makiko Haba, Vinciane Debaille, **Ryoga Maeda**, Steven Goderis, Philippe Claeys (2021) Meteorite Newsletter, Vol 28. Antarctic Meteorite Research Center, National Institute of Polar Research, Japan, 1-25.

Conference contributions (first author)

1. **Ryoga Maeda**, Steven Goderis, Vinciane Debaille, Geneviève Hublet, Hamed Pourkhorsandi and Philippe Claeys (2019) Rare Earth Element Distribution and Lu-Hf and Sm-Nd Isotope Systematics of Antarctic H Chondrites. *Poster presentation, 82nd Annual Meetings of the Meteoritical Society, Japan*.

2. **Ryoga Maeda**, Vinciane Debaille, Geneviève Hublet, Hamed Pourkhorsandi, Philippe Claeys and Steven Goderis (2019) Rare Earth Element Distribution and Lu-Hf and Sm-Nd Isotopic Effects in Antarctic H and CM Chondrites. *Poster presentation, Goldschmidt 2019, Spain*.

3. **Ryoga Maeda**, Steven Goderis, Thibaut Van Acker, Frank Vanhaecke, Akira Yamaguchi, Vinciane Debaille and Phillippe Claeys (2021) The effect of fluid mobilization on the budget and distribution of rare earth elements in Antarctic H chondrites. *Oral presentation: 12th Symposium on Polar Science, Japan (online)*.

4. **Ryoga Maeda**, Steven Goderis, Thibaut Van Acker, Frank Vanhaecke, Akira Yamaguchi, Vinciane Debaille and Phillippe Claeys (2022) The Effects of Thermal Processing on The Budget of Lithophile Elements in H Chondrites. *Oral presentation: 85th Annual Meetings of the Meteoritical Society, U.K.*

Conference contributions (contributing author)

1. Matthias van Ginneken, Steven Goderis, **Ryoga Maeda**, Penny Wozniakiewicz, Matthew Genge, Luigi Folco, Martin D. Suttle, Akira Yamaguchi and Sophie Decrée (2022) A potential origin for ^{16}O-poor cosmic spherules: a near-Earth source and parentage with CY chondrites. *53rd Lunar and Planetary Science Conference, U.S.* (peer-reviewed).

2. Matthias van Ginneken, Steven Goderis, **Ryoga Maeda**, Penny Wozniakiewicz, Matthew Genge, Luigi Folco, Martin D. Suttle, Akira Yamaguchi and Sophie Decrée (2022) A potential origin for ^{16}O-poor cosmic spherules: a near-Earth source and parentage with CY chondrites. *Sources and inventory of cosmic dust: From space to the Earth's surface, Royal Astronomical Society, U.K.*

3. Vinciane Debaille, **Ryoga Maeda**, Hamed Pourkhorsandi Steven Goderis, Geneviève Hublet and Philippe Claeys (2022) Effects of terrestrial alteration on meteorites from cold and hot deserts. *Goldschmidt 2022, U.S.*

4. Flore Van Maldeghem, Bastien Soens, Matthias van Ginneken, **Ryoga Maeda**, Carole Cordier, Martin D. Suttle, Akira Yamaguchi, Philippe Claeys and Steven Goderis (2022) Chromites in cosmic spherules: a unique perspective on the extraterrestrial flux to earth. *85th Annual Meetings of the Meteoritical Society, U.K.*

5. Thibaut Van Acker, **Ryoga Maeda**, Tom Van Helden, Stijn J.M. Van Malderen, Steven Goderis and Frank Vanhaecke (2023) Pushing the limits of elemental mapping via laser ablation – ICP-mass spectrometry with a nanosecond 193 nm kHz laser. *European Winter Conference on Plasma*

Spectrochemistry 2023, Slovenia.

6. Flore Van Maldeghem, Bastien Soens, **Ryoga Maeda**, Lisa Krämer Ruggiu, Matthias van Ginneken, Carole Cordier, Martin D. Suttle, Luigi Folco, Akira Yamaguchi, Philippe Claeys and Steven Goderis (2023: expected) CSI Solar System: Clues from chromites in cosmic dust. *Goldschmidt 2023, France.*

7. Matthias van Ginneken, Steven Goderis, Ralph P. Harvey, **Ryoga Maeda**, Jérôme Gattacceca, Akira Yamaguchi and Penny Wozniakiewicz (2023: expected) Meteoritic event recorded in Antarctic ice – Part 2: further exploring the BIT-58 debris layer and its implications for the impact record of Earth. *Impact Earth! Protecting the UK and Further Afield from Impacts by Near Earth Objects, Royal Astronomical Society, U.K.*